

Review

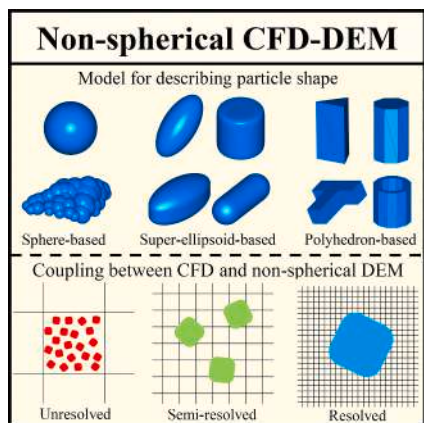
A review of recent development for the CFD-DEM investigations of non-spherical particles



Huaqing Ma, Lianyong Zhou, Zihan Liu, Mengyao Chen, Xiuhao Xia, Yongzhi Zhao *

Institute of Process Equipment, College of Energy Engineering, Zhejiang University, Hangzhou 310027, China

GRAPHICAL ABSTRACT



ARTICLE INFO

Keywords:
 DEM (Discrete Element Method)
 CFD (Computational Fluid Dynamics)
 CFD-DEM
 particle-fluid flow
 non-spherical particles

ABSTRACT

The coupling between fluid and granular materials is commonly encountered in nature and engineering practice. Moreover, the shape of granular materials in practical applications is normally non-spherical. Therefore, investigating the particle-fluid systems containing non-spherical particles for a deeper understanding of their underlying mechanisms and then for improving the performance of the related industrial processes should be an urgent necessity for practical needs. For investigating the intricate flow behaviors of particle-fluid systems, the numerical simulation method of coupling DEM (Discrete Element Method) with CFD (Computational Fluid Dynamics) has been widely recognized as a promising tool, and many efforts have been devoted to the CFD-DEM investigations of non-spherical particles in recent years. This paper aims to review development of the CFD-DEM investigations for non-spherical particles from theoretical models to applications in recent six years. It primarily represents three principal aspects: the theoretical foundations of DEM for modeling non-spherical particles, the coupling methodologies between CFD and DEM and the use of the non-spherical CFD-DEM coupling model in different applications involving particle-fluid flows. In the end, the conclusions and the outlooks for future investigations are given.

* Corresponding author.

E-mail address: yzzhao@zju.edu.cn (Y. Zhao).

1. Introduction

Granular materials have been presented very early in the history of human society in such forms as construction materials and cereal grains. Since entering the industrial society, granular materials are more involved, and it is commonly encountered in nature and industry such as chemical engineering, energy, agriculture, pharmaceuticals, environment, mining, ocean engineering, etc. For example, agriculture and food processing should be the biggest producers of final products in the form of granular materials [1], granular matter and particle technology represent 40% of the value added to the chemical industry [2], up to 80% of pharmaceuticals involve the particulate processes [3,4], and at least 50% of manufactured products sold worldwide are solid particles [5,6]. Furthermore, the influence of fluid (e.g., air and water) in granular systems often cannot be underestimated in nature and human activities. In other words, the particle-fluid multiphase systems that the coupling interaction between granular materials and fluid play a significant role extensively exist, such as the interactive movement of solid-fluid multiphase flow in chemical and energy equipment, rain-driven landslides, the interaction between a ship and broken ice, sediment in the river course, cleaning and segregation of bio-particulate matter, seepage of water in sand and gravel soil, etc. Therefore, a fundamental understanding for the underlying physics of particle-fluid systems is not only of academic interest but is also of significance for industrial applications [7].

Due to the intermediate state of granular materials between the solids, gases and liquids, granular systems are generally rather complicated, and it often presents many peculiar phenomena in motion evolution and even in a static state [1,8]. For particle-fluid systems, the complex interactions between fluid and solid particles should also be included, and it generally exhibits quite intricate multi-medium and multi-scale mechanical properties. Moreover, granular systems commonly encountered in practical applications are often comprised of non-spherical particles, where more than 70% of the raw materials are believed to contain non-spherical particles in modern industries [9,10]. And the non-spherical shape of particles should further increase the complexity of particle-fluid systems. Investigating particle-fluid systems involving non-spherical particles would be therefore of greater practical significance, and a better understanding of their very complicated underlying physics for the better design and control of related industrial processes should also be an urgent necessity for practical needs.

Because of the intricacy of particle-fluid systems, the investigations of particle-fluid systems cover multidisciplinary research areas, and it is undoubtedly an interdisciplinary study. Generally, experimental study, theoretical research and numerical simulation are three primary tools for investigating particle-fluid systems. Nevertheless, the abilities of experimental studies and theoretical researches in this area are rather limited. For instance, the experimental measurements for the interior behaviors of particles in 3D particle-fluid systems are fairly difficult because of their opaque nature [7]. With the increase in computing power and technology, therefore, numerical simulation has been a powerful tool for investigating granular systems. As far as the particle-fluid systems, CFD (Computational Fluid Dynamics) is an advanced and commonly used tool for exploring the complicated physics of solid-fluid multiphase flows. And concerning the way to treat particle phase, two different CFD-based approaches, *i.e.*, the Euler-Euler approach and the Euler-Lagrange approach, have been proposed, where the fluid phase is determinately solved by CFD in the Eulerian frame regardless of which approach you use. The Euler-Euler approach is typically represented by the so-called TFM (Two-Fluid Model) [11], in which the particle phase is also considered as the continuous medium just like the fluid phase and thus the fluid and particle phases are resolved with the balance equations of solving the single-phase flow. TFM is a quite computationally efficient approach. But it is yet a challenge to develop the suitable constitutive relations between the stress and strain tensors used to close the governing equations in TFM for accurately replicating

all typical flow regimes and transitions [9], and the discrete nature of granular systems is completely ignored that goes against the deep understanding of particle-fluid flows.

The Euler-Lagrange approach is typically represented by the CFD-DEM (Discrete Element Method) coupling model, where the particle phase is solved in the Lagrangian frame by DEM originally proposed by Cundall and Strack [12] in 1979, and the discreteness of granular systems can be effortlessly taken into account within the framework of DEM. Specifically, DEM is a powerful numerical simulation technique for modeling and reproducing discrete media flows based on Newton's laws of motion, particularly for dense granular flows. With the introduction of DEM, each individual particle in the particle-fluid systems will be tracked in the CFD-DEM simulations, and the abundant particle level information can be easily obtained, which is significant for understanding the underlying mechanisms of particle-fluid flows. In addition, there is no more need in CFD-DEM to develop the aforementioned complex constitutive relations used in the TFM model.

In the early stages, because the perfect symmetry of spheres can greatly ease the difficulty in establishing the CFD-DEM model and bring high computation efficiency, the CFD-DEM investigations mainly focused on spherical particles [13,14]. As discussed above, however, non-spherical particles should be mostly encountered in practical applications. In the meantime, particle shape not only affects the microscopic behaviors of particle systems, but also determines the macroscopic behaviors of granular materials. Additionally, particle shape will also significantly influence the fluid flow in particle-fluid systems and hence the interaction between fluid and particles. Therefore, investigating the non-spherical particles by CFD-DEM should be highly recommended for figuring out their complicated behaviors and the corresponding mechanisms.

On account of the superiority of CFD-DEM in modeling multiphase flows, the investigations involving CFD-DEM simulations for particle-fluid flows have been a hot research area [15]. Due to the flourish of CFD-DEM investigations, various review papers in this area can be accessed without difficulty, and then some of them published over the past few years will be briefly introduced below. Sarkar et al. [3] in 2017 outlined the different available process modeling techniques and the applications for the pharmaceutical industry, in which CFD-DEM is an element of this review, and the role of forces governing particle interactions was emphatically discussed. In 2017, Manjula et al. [16] and Wang et al. [17] introduced various CFD modeling methodologies and studies of pneumatic conveying, and CFD-DEM was a component part. Subsequently, Kuang et al. [9] in 2022 further published a rather comprehensive review for the CFD-DEM modellings and investigations of pneumatic conveying. Moreover, Kotzur et al. [18] in 2018 focused on the particle attrition mechanisms in horizontal lean phase pneumatic conveying systems, and some CFD-DEM applications were introduced as a constituent part of this review. Fitzgerald et al. [19] in 2019 reviewed multiscale simulations of elongated particles in fluidized beds, in which the related CFD-DEM investigations were introduced as a component part. Taking geotechnical engineering as background, Ibrahim and Meguid [20] in 2020 briefly reviewed the various modeling tools for particle-fluid systems, and CFD-DEM was introduced as a constituent part. Wang [21] in 2020 provided a comprehensive and pedagogical review for the various state-of-the-art CFD-based approaches in simulating the hydrodynamics of gas-solid fluidization technology, and CFD-DEM was involved as a component part. Alabaid et al. [22] in 2022 also comprehensively summarized the progress in CFD simulations of fluidized beds in chemical and energy engineering, where the CFD-DEM was included as a component part. Mangadoddy et al. [23] in 2020 provided a review about the applications of CFD modelling in particle-fluid dynamics and the performance prediction of hydrocyclone, dense medium cyclone and tumbling mill, and some concrete CFD-DEM applications were mentioned. Scherer et al. [24] in 2017 and Golshan et al. [25] in 2020 comprehensively reviewed the theory of the CFD-DEM model applied to chemical processes, and some CFD-DEM applications were

also introduced. In addition, Bérard et al. [2] in 2020 also briefly reviewed the CFD-DEM model and the related applications, and their main goal was to provide a tutorial review for beginners to understand the fundamentals behind CFD-DEM in chemical engineering. Similarly, Kieckhefen et al. [26] in 2021 also published a review to provide an overview of the CFD-DEM method for researchers with little background in process engineering. For agricultural applications, El-Emam et al. [15] and Zhao et al. [27] comprehensively reviewed the theoretical models [15] and applications [15,27] of CFD-DEM in 2021, in which the non-spherical particles were frequently encountered. Lu et al. [28] in 2022 reviewed the MFIX-based multi-scale CFD modellings for biomass fast pyrolysis, where the CFD-DEM was highlighted in this review. For ship-ice interaction problems, Xue et al. [29] in 2020 and Islam et al. [30] in 2021 systematically reviewed the existing modeling methods for level ice and broken ice, respectively, where CFD-DEM was introduced as one of the available numerical models. Subsequently, Li and Huang [31] in 2022 further presented a rather comprehensive review of CFD-DEM investigations for ship advancing in non-spherical broken ices. Wang et al. [32] in 2022 detailedly reviewed the coupling techniques between CFD and DEM, in which different CFD methods were introduced, such as conventional continuum-based CFD (e.g., using finite volume approximation), LBM (Lattice Boltzmann Method), SPH (Smoothed Particle Hydrodynamics), etc.

Lu et al. [7] in 2015 and Zhong et al. [10] in 2016 also provided two valuable reviews involving the non-spherical DEM. Unlike the reviews introduced in the last paragraph, however, the focuses of Lu et al. [7] and Zhong et al. [10] were not confined to a specific application, their research topics were for DEM modeling and investigations of non-spherical particles that the scientific publications involving the theoretical developments of non-spherical DEM/CFD-DEM and the related applications in different fields were systematically analyzed. And to our knowledge, there should be significant progress for the modelling and investigations of non-spherical CFD-DEM in recent years, where the non-spherical CFD-DEM model should become more sophisticated, and more implementations of the non-spherical CFD-DEM approach can be effortlessly found in various application areas. According to above discussions, however, it appears that there are no literatures focusing on the non-spherical CFD-DEM since the review of Zhong et al. [10] published in 2016, where either the recent reviews mainly concentrated on specific application areas or non-spherical particles were not the point. Therefore, providing a review for the state-of-the-art development of non-spherical CFD-DEM similar to the previously published reviews of Lu et al. [7] and Zhong et al. [10] should be highly necessary. Based on the above reasons, we hope to provide an overview of the progress of CFD-DEM investigations involving non-spherical particles in recent six years (mainly since 2016) that development for the CFD-DEM modeling of non-spherical particles and the applications of non-spherical CFD-DEM modeling in different areas rather than the specific application area will be reviewed. The remainder of this review is organized as follows. Section 2 and Section 3 concentrate on reviewing recent development of modeling that Section 2 outlines the theoretical foundations of the DEM in modelling non-spherical particles and the schemes for the coupling between CFD and DEM are reviewed in Section 3. In Section 4, the applications of non-spherical CFD-DEM in different areas involving particle-fluid systems (e.g., the fluidization, particle transport and particle separation) are reviewed. This review paper is finally concluded with perspectives of non-spherical CFD-DEM in Section 5. By introducing the model developments and numerous applications of non-spherical CFD-DEM in recent years, we hope this review can facilitate idea exchanges and attract new researchers to the fascinating and challenging field of non-spherical CFD-DEM.

2. Mathematical models of non-spherical DEM

Based on the way to process the particle deformation while two particles are in contact or collision, DEM technique can be generally

characterized as a soft-sphere approach [12] and a hard-sphere approach [33]. Fig. 1 schematically illustrates the primary differences between these two DEM modelling approaches. As shown in Fig. 1, the overlap between two contacting particles is allowed in the soft-sphere DEM, whereas the hard-sphere approach normally assumes that the collision between particles is instantaneous and there is no overlap. Generally, the hard-sphere approach is only suitable for modeling rather dilute granular flows due to its limited capability in processing multiple contacts. In contrast to the hard-sphere approach, however, the application range of the soft-sphere approach whose multiple contacts can be effortlessly handled is more extensive, where both the dilute and dense granular flows can be well simulated. Therefore, the soft-sphere approach is more commonly used in the DEM investigations of particulate systems [15,16,22,26]. For example, the currently available open-source and commercial software packages are mainly based on the soft-sphere model, e.g., PFC, EDEM, Rocky DEM, LIGGGHTS, DEMSLab, etc. In addition, the hard-sphere approach is typically used for spherical particles or the non-spherical particles composed of small spheres in the limited investigations [34–36], and it could be thought of as a simplified version of the soft-sphere approach by reducing the complexity in determining the particle-particle or particle-wall interactions [9]. Synthesizing the above, therefore, this review will mainly concentrate on the model framework of soft-sphere DEM in the following.

2.1. Particle motion equation

In DEM, the translational and rotational motions of every individual particle are determined by Newton's second law of motion, and it can be respectively formulated as:

$$m \frac{dv}{dt} = \mathbf{F}_c + \mathbf{F}_{coh} + \mathbf{F}_{pf} + mg \quad (1)$$

$$I \frac{d\omega}{dt} = \mathbf{T}_c + \mathbf{T}_f \quad (2)$$

in which t is time, and m , I , \mathbf{v} and ω represent the mass, inertia tensor, linear velocity and angular velocity of a single particle, respectively. \mathbf{F}_c is the contact force between contacting particles, \mathbf{F}_{coh} is the cohesion force, \mathbf{F}_{pf} is the interaction force between fluid and particle, \mathbf{g} is gravitational acceleration, \mathbf{T}_c is the contact torque, and \mathbf{T}_f is the torque caused by fluid.

In contrast to spheres, the exact calculation of particle orientation is the necessary prerequisite to accurately model the motion of non-spherical particles. For more clearly illustrating the rotation of an object, different representing methods were devised for describing the object orientation, e.g., the Euler angles and the Cardan angles. In the area of DEM, the Euler angles denoted as (ψ, θ, φ) should be the most widely used to the best of our knowledge. There are a total of twelve rotation conventions to define the Euler angles [38], and Fig. 2 further illustrates one of the commonly used rotation conventions called x -convention. In the first place, the local coordinate system x - y - z exactly coincides with the global coordinate system X - Y - Z (see Fig. 2a). Then, the x - y - z system rotates counterclockwise by the precession angle ψ about z -axis (see Fig. 2b). Subsequently, the x - y - z system rotates counterclockwise by the nutation angle θ about x -axis (see Fig. 2c). In the end, the x - y - z system rotates counterclockwise by the spin angle φ about z -axis (see Fig. 2d).

According to the convention of the Euler angles presented in Fig. 2, the orientation of a non-spherical particle in the global coordinate system X - Y - Z can be updated as follows [7,38]:

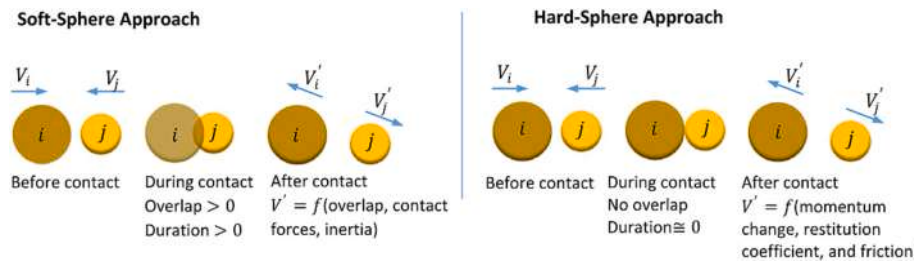


Fig. 1. Sketch diagram of the soft-sphere and hard-sphere approaches (adapted from [15], Copyright 2021, with kind permission from Springer Nature).

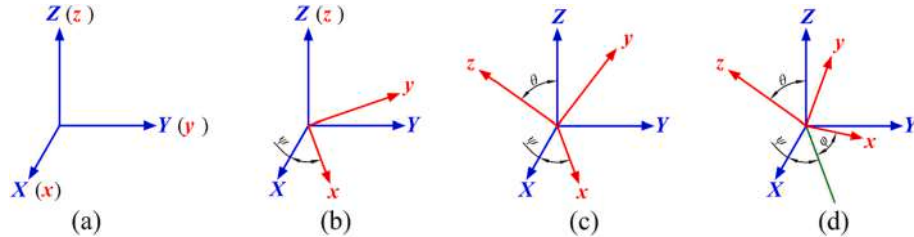


Fig. 2. Illustration of the rotation convention defining the Euler angles: the rotation in the (a) initial stage, (b) second stage, (c) third stage and (d) final stage (adapted from [37], Copyright 2018, with kind permission from Springer Nature).

$$\begin{cases} \frac{d\psi}{dt} = \omega_z - \cot\theta(\omega_x \sin\psi - \omega_y \cos\psi) \\ \frac{d\theta}{dt} = \omega_x \cos\psi + \omega_y \sin\psi \\ \frac{d\varphi}{dt} = \csc\theta(\omega_x \sin\psi - \omega_y \cos\psi) \end{cases} \quad (3)$$

where $\omega = (\omega_x, \omega_y, \omega_z)$ is the angular velocity of a particle in the global coordinate system X-Y-Z. However, the Euler angles cannot avoid singularities while $\theta = 0$ and $\theta = \pi$. This problem can be circumvented by the quaternion-based method, though it might increase the complexity of DEM model to a certain extent. Specifically, the quaternion \mathbf{q} can be described by four scalars $\mathbf{q} = (q_0, q_1, q_2, q_3)$ that can be derived from the Euler angles [39]:

$$\begin{cases} q_0 = \cos 0.5\theta \cos 0.5(\psi + \varphi) \\ q_1 = \sin 0.5\theta \cos 0.5(\psi - \varphi) \\ q_2 = \sin 0.5\theta \sin 0.5(\psi - \varphi) \\ q_3 = \cos 0.5\theta \sin 0.5(\psi + \varphi) \end{cases} \quad (4)$$

And the following equation for the quaternion is satisfied:

$$q_0^2 + q_1^2 + q_2^2 + q_3^2 = 1 \quad (5)$$

Accordingly, Eq. (3) can be reformulated in the form of the quaternion:

$$\begin{cases} \frac{dq_0}{dt} = -\frac{q_1\omega_x + q_2\omega_y + q_3\omega_z}{2} \\ \frac{dq_1}{dt} = \frac{q_0\omega_x - q_3\omega_y + q_2\omega_z}{2} \\ \frac{dq_2}{dt} = \frac{q_3\omega_x + q_0\omega_y - q_1\omega_z}{2} \\ \frac{dq_3}{dt} = \frac{-q_2\omega_x + q_1\omega_y + q_0\omega_z}{2} \end{cases} \quad (6)$$

where $\omega' = (\omega_x, \omega_y, \omega_z)$ is the local angular velocity, and it can be converted from the global angular velocity by:

$$\omega' = A\omega \quad (7)$$

The matrix A can be written in the form of Euler angles and quaternion:

$$A = \begin{bmatrix} \cos\psi \cos\varphi - \sin\psi \cos\theta \sin\varphi & \sin\psi \cos\varphi + \cos\psi \cos\theta \sin\varphi & \sin\theta \sin\varphi \\ -\cos\psi \sin\varphi - \sin\psi \cos\theta \cos\varphi & -\sin\psi \sin\varphi + \cos\psi \cos\theta \cos\varphi & \sin\theta \cos\varphi \\ \sin\psi \sin\theta & -\cos\psi \sin\theta & \cos\theta \end{bmatrix}$$

$$= \begin{bmatrix} q_0^2 + q_1^2 - q_2^2 - q_3^2 & 2(q_1 q_2 + q_0 q_3) & 2(q_1 q_3 - q_0 q_2) \\ 2(q_1 q_2 - q_0 q_3) & q_0^2 - q_1^2 + q_2^2 - q_3^2 & 2(q_2 q_3 + q_0 q_1) \\ 2(q_1 q_3 + q_0 q_2) & 2(q_2 q_3 - q_0 q_1) & q_0^2 - q_1^2 - q_2^2 + q_3^2 \end{bmatrix} \quad (8)$$

More details about the quaternion-based approach can be found in the previous investigations [7,39,40]. By incorporating the Euler angles and quaternions into DEM, the particle orientation can be subsequently updated in every time step. Note that the aforementioned approaches are not the only way for expressing the rotation of the particle or object, other approaches can also be found in published literatures [40–42].

The key difference between the spherical and non-spherical particles in determining the particle motion is the rotational motion [37], viz. the solution of Eq. (2). Specifically, the inertia tensor I in Eq. (2) is calculated by:

$$I = \rho_p \begin{pmatrix} \int (Y^2 + Z^2) dV_p & -\int XY dV_p & -\int XZ dV_p \\ -\int YX dV_p & \int (X^2 + Z^2) dV_p & -\int YZ dV_p \\ -\int ZX dV_p & -\int ZY dV_p & \int (X^2 + Y^2) dV_p \end{pmatrix} \quad (9)$$

where ρ_p and V_p are the density and volume of a particle, respectively. Due to the perfect symmetry of spheres, the non-zero entries for I only appear in the diagonal and I is invariant [7]. So the calculation of the rotational motion of spherical particles is quite effortless [12,43]. With regard to non-spherical particles, however, the off-diagonal entries for I are not necessarily equal to zero, and I is not a constant that depends on the chosen coordinate system. In other words, I is time-varying in the global coordinate system with the rotation of non-spherical particles. Therefore, the local coordinate system $x-y-z$ is necessarily introduced, and then Eq. (9) can be rewritten as:

$$\begin{aligned} \mathbf{I}' &= \begin{pmatrix} I_x & 0 & 0 \\ 0 & I_y & 0 \\ 0 & 0 & I_z \end{pmatrix} \\ &= \rho_p \begin{pmatrix} \int (y^2 + z^2) dV_p & 0 & 0 \\ 0 & \int (x^2 + z^2) dV_p & 0 \\ 0 & 0 & \int (x^2 + y^2) dV_p \end{pmatrix} \end{aligned} \quad (10)$$

in which the diagonal entries of the local inertial tensor \mathbf{I}' including I_x , I_y and I_z are constant, and they can be used to reformulate Eq. (2):

$$\left. \begin{aligned} I_x \frac{d\omega_x}{dt} + (I_z - I_y)\omega_y\omega_z &= T_x \\ I_y \frac{d\omega_y}{dt} + (I_x - I_z)\omega_z\omega_x &= T_y \\ I_z \frac{d\omega_z}{dt} + (I_y - I_x)\omega_x\omega_y &= T_z \end{aligned} \right\} \quad (11)$$

where $\mathbf{T}' = (T_x, T_y, T_z)$ is the sum of torque imposed on a particle in the local coordinate system.

According to Eq. (11), the torque obtained in the global coordinate system should be converted to the local coordinate system by the matrix \mathbf{A} :

$$\mathbf{T}' = \mathbf{AT} \quad (12)$$

Then, the local angular velocity $\boldsymbol{\omega}'$ can be determined by solving Eqs. (11) and (12). Subsequently, the global angular velocity $\boldsymbol{\omega}$ can be updated by Eq. (7).

So long as the force and torque imposed on the particles are determined, the kinetic behaviors of the non-spherical particle systems can be updated by Eqs. (1)-(12). For contact force \mathbf{F}_c and contact torque \mathbf{T}_c , various contact force models have been proposed (e.g., the linear spring-dashpot model and Hertz-Mindlin model), and the interested readers can be referred to the corresponding investigations [1,15,27,32]. Furthermore, the prerequisite for the use of the contact force model is the determination of contact parameters (e.g., the overlap, contact point and contact direction) that are closely related to the used particle shape model as well as contact detection algorithms, and the details will be discussed in Section 2.2. For other forces shown in Eqs. (1) and (2), the non-contact force \mathbf{F}_{nc} (e.g., the Van der Waals force and bridge force) and the interaction force between particle-fluid \mathbf{F}_{pf} will be outlined in Section 2.3 and Section 2.4, respectively.

2.2. Particle shape models and their contact detection algorithms

As is well-known, particle shape is of fundamental importance for determining the contact force between particles and then for accurately predicting the particle behaviors, since the contact details (e.g., the contact plane and contact point) are very sensitive to the geometric shape of the particle. Therefore, various particle models have been proposed for accurately describing the shape of the non-spherical particle, e.g., the multi-sphere model [44,45], super-ellipsoid model [46–49], polyhedral model [50–54], etc. With these proposed particle models, therefore, only achieving the precise modeling of particle shape should be theoretically not an unattainable goal. The essential difficulty for the DEM simulation of non-spherical particles lies in devising an accurate and efficient algorithm for detecting the contact between particles, considering the fact that resolving the contact can spend more than 80% computational time in the DEM simulations [55] and the contact details should directly influence the calculation of contact force.

In essence, detecting the contact for non-spherical particles is how to reasonably define or assume contact details. For spherical particles, as shown in Fig. 3, the determination of the contact details is quite straightforward and the contact parameters should be unique due to the perfect symmetry of their shape: the overlap δ is defined as the sum of

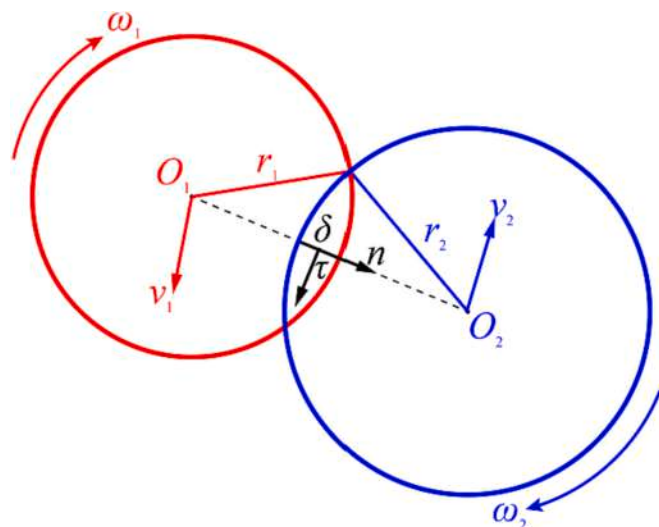


Fig. 3. Sketch map of the contact between spherical particles.

the radii of two contacting spheres minus the center distance of the two spheres, the contact point is the midpoint of the overlap, and the contact plane where the contact point is perpendicular to the line representing the overlap. For non-spherical particles, nevertheless, the question still remains and its determination is quite more complicated that the diversity of particle shapes is generally desperate for developing more intricate contact models beyond spherical shape. In general, the different physical concepts behind the contact models will provide the different contact parameters [56]. For example, “Geometric Potential (GP)” [57,58] and “Common Normal (CN)” [57,59] are two common methods for determining the contact between non-spherical particles, as shown in Fig. 4. It can be clearly seen that the contact parameters obtained from the GP method are different from the CN method for the same contact situation. Additionally, the numerical calculation for determining the contact of non-spherical particles is normally much more time-consuming compared with spherical particles.

By plugging the aforementioned contact parameters into the contact force model, the interaction force between the contacted particles can be then determined. In general, the well-developed contact force models originally devised for spherical particles [12,13,60] are used for non-spherical particles. Apparently, these contact force models should be not well suitable for non-spherical particles. As a consequence, some contact force models have been specially designed for calculating the contact force and torque of non-spherical particles in the past. For example, Feng et al. [61] proposed a contact force model for arbitrarily

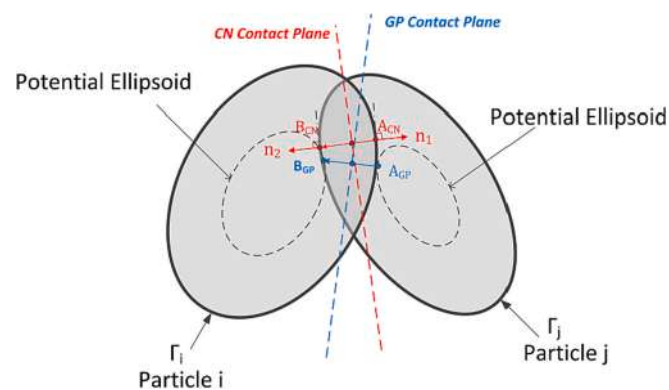


Fig. 4. Schematic illustration of the contact parameters determined by GP and CN method (adapted from [56], Copyright 2017, with kind permission from Elsevier).

shaped particles based on energy-conserving principle. In addition, other contact force models for specific particle model or particle shape can also be accessed [8,62,63]. In these contact force models, more contact details, e.g., the local curvature at the contact point, may also be required. To the best of our knowledge, nevertheless, there should be seemingly little progress in this research area in recent years. In the following of this section, therefore, introducing the contact force model is not the point, and the characteristics of the different particle models (e.g., the sphere-based, super-ellipsoid-based and polyhedron-based particle models) and the corresponding contact detection algorithms will be emphatically introduced. Additionally, the comparisons between some commonly used particle models are also presented in the end.

2.2.1. Sphere-based particle model

As mentioned above, the contact detection algorithm for spherical DEM has been well validated and has the advantages of high efficiency and strong robustness. For describing non-spherical particles, therefore, several particle models based on spherical particles have been proposed (e.g., the multi-sphere model for rigid particles, the bonded-sphere model for flexible and breakable particles, and directly using spherical particles by modifying some parameters), and the details will be discussed in the following.

2.2.1.1. Multi-sphere model. In the multi-sphere model, a solid object is created by assembling a certain number of spheres (referred to hereafter as “sub-sphere” or “sub-spheres”) together, and it permits to change the parameters of the sub-spheres (including the number, size and position) and then the amounts of overlaps between sub-spheres for describing a particle with arbitrary shape, as shown in Fig. 5. Once the multi-sphere particle is constructed, the particle behaves as a rigid body that the relative positions between the sub-spheres will remain unchanged during the DEM simulations. The resultant forces and torques for multi-sphere particles induced by the contact or collision between particles are the sum of the forces and torques acting on each sub-sphere and then accumulated on the mass center of the multi-sphere particle for the following calculation of particle motion. For more details, the interested readers can be referred to previous studies [64]. As a result, the contact detection for multi-sphere particles is essentially the determination of the contact for sub-spheres. Therefore, the conventional spherical contact detection algorithm can be conveniently extended to the multi-spheres, and its advantages of efficiency and robustness can be inherited by multi-sphere DEM simulations. For the above reasons, the multi-sphere model appears to be the most commonly used particle model in the DEM community at the moment [7,15].

The multi-sphere particles should belong to non-convex non-smooth

particles. In other words, the particle surface described by the multi-sphere model is generally “knobby” [66]. To ameliorate this surface irregularity while modeling smooth particles by the multi-sphere model, more sub-spheres should be required to approximate the real shape of the particles for increasing simulation accuracy. For instance, Fig. 6 presents the comparisons of repose angles of the particle pilings between the multi-sphere ellipsoids (labeled as “MS”) and true ellipsoids (labeled as “ellipse”) [65]. Obviously, the simulation accuracy will increase with the number of sub-spheres. However, the influence of the number of sub-spheres will be weakened as more sub-spheres are embedded in the multi-sphere particle. Furthermore, increasing the number of sub-spheres will also significantly damage the distinct advantage of computation efficiency for the multi-sphere model. Fig. 7 presents our previous studies about comparing the computational efficiency of using different particle models [67]. It can be clearly seen that the multi-sphere particles composed of more sub-spheres would consume more time, and hence the loss of computational efficiency. More importantly, increasing the number of sub-spheres would lead to the more serious issue of the occurrence of multiple contacts between two contacting particles, and hence resulting in some unphysical behaviors (e.g., excessive stiffness and damping). But for the modelling of large assemblies of non-spherical particles, Kruggel-Emden et. al. [66] indicated that the inaccuracy induced by the multiple contacts seemingly can be alleviated, where the number of sub-spheres appeared to affect the simulation results little.

For the multi-sphere model, more considerations are required for how to arrange the sub-spheres (including the optimal number of sub-spheres as well as their locations and sizes) while constructing a multi-sphere particle to balance the accuracy and efficiency of the DEM simulations. But synthesizing the above, the multi-sphere model should be still a valuable approach for modelling non-spherical particle systems, though it might be the “most primitive” method in modeling non-spherical particles within the DEM framework.

2.2.1.2. Bonded-sphere model. Similar to the multi-sphere model, the particle modeled by the bonded-sphere model is also generated by connecting a certain number of sub-spheres, in which the sub-spheres can either be of mono size or have a size distribution, and the overlap between sub-spheres is also allowed [68], as shown in Fig. 8. Therefore, the well-established contact detection algorithm for spherical particles can also be effortlessly used for determining the contact between the sub-spheres located in different bonded-sphere particles. The significant difference between the multi-sphere model and the bonded-sphere model is that the sub-spheres are glued together using bonds for the bonded-sphere model so that the interactions between the sub-spheres within the bonded-sphere particle must be considered (see Fig. 8(a)), whereas it is totally ignored in the multi-sphere model.

In the multi-sphere model, the sum of forces and torques acting on each sub-sphere will be simplified as a resultant force and torque imposing on the mass center of the particle for the following calculation of particle motion. Nevertheless, the motion for each individual sub-sphere within the bonded-sphere particle will be firstly determined using Newton's second law of motion based on the forces and torques acting on each sub-sphere. And the dynamics of the bonded-sphere particle are subsequently determined by the collective motion of the sub-spheres. During this process, the relative movement between the sub-spheres may occur and then lead to the deformation of bonds and also of the bonded-sphere particle. Therefore, the bonded-sphere model is a feasible way for the modeling of flexible particles. For example, Fig. 9(a) illustratively presents the DEM simulations of shear flow behaviors involving the flexible bonded-sphere particles with different bond bending modules.

As mentioned above, the bonded-sphere model can also be used to model the breakage of particles. For modeling particle breakage, there are generally two bonding models within the bonded-sphere particle, i.e.

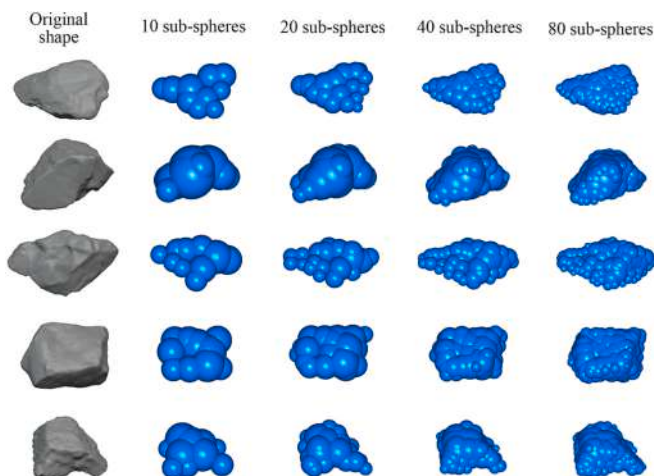


Fig. 5. Particles in different shapes described by multi-sphere model.

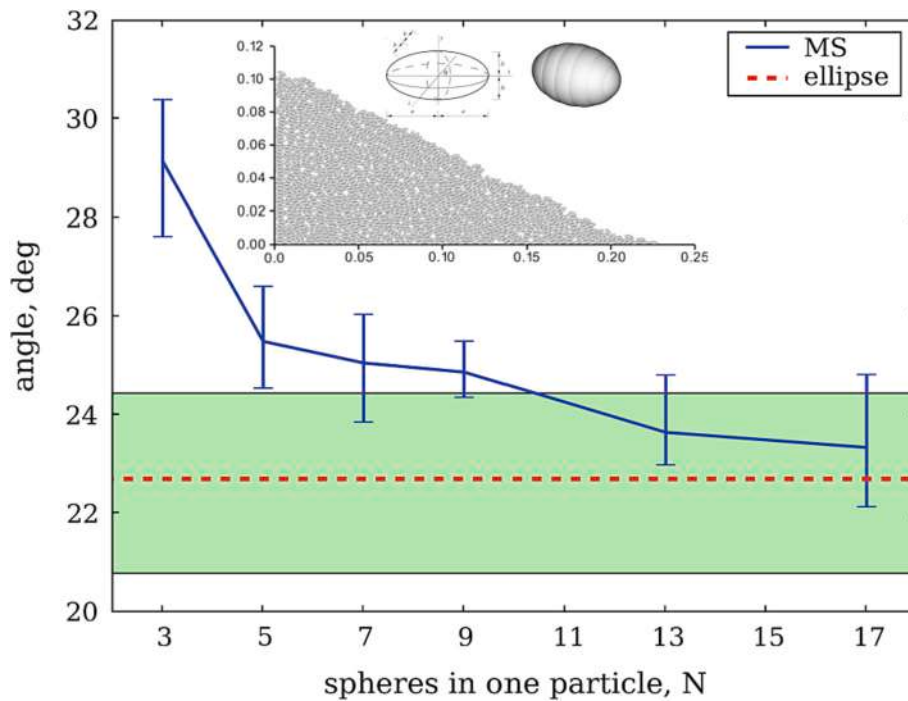


Fig. 6. Comparisons of the repose angles of particle pileings between the multi-sphere ellipsoids (MS) and true ellipsoids (ellipse) (adapted from [65], Copyright 2009, with kind permission from Springer Nature).

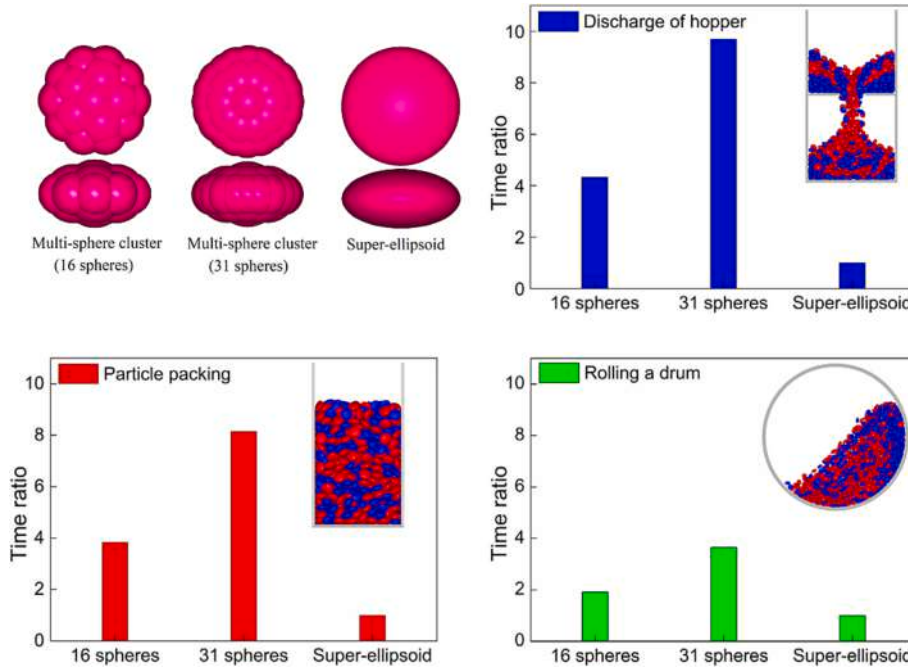


Fig. 7. Comparisons of the computational efficiency between different particle models (including the multi-sphere model and super-ellipsoid model, and the time ratio of the super-ellipsoid model is defined as 1) (adapted from [67], Copyright 2018, with kind permission from Elsevier).

e., the contact-bond model and parallel-bond model [68,69]. Fig. 8(b) presents the sketch map of these bonding models. The contact-bond model only acts on the contact point, and only the force can be transmitted; the parallel-bond model imposes on the circular cross-section lying between sub-spheres, and both the force and torque can be transferred. At present, the parallel-bond model should be the most used in modeling the breakage [8]. The existence of bond forces/torques can constrain the relative displacement between the sub-spheres. But while

the load acting on the particle exceeds the bond strength, the bond between the sub-spheres will be broken and then the breakage of the particle occurs. Fig. 9(b) shows an example about DEM simulations of the breakage of bonded-sphere particles.

It is conceivable that there is a defect inherent in the bonded-sphere model that the created particle possesses a bumpy surface just like in the multi-sphere model, leading to the inaccuracy in modeling the particle having a smooth surface. Though increasing the number of sub-spheres

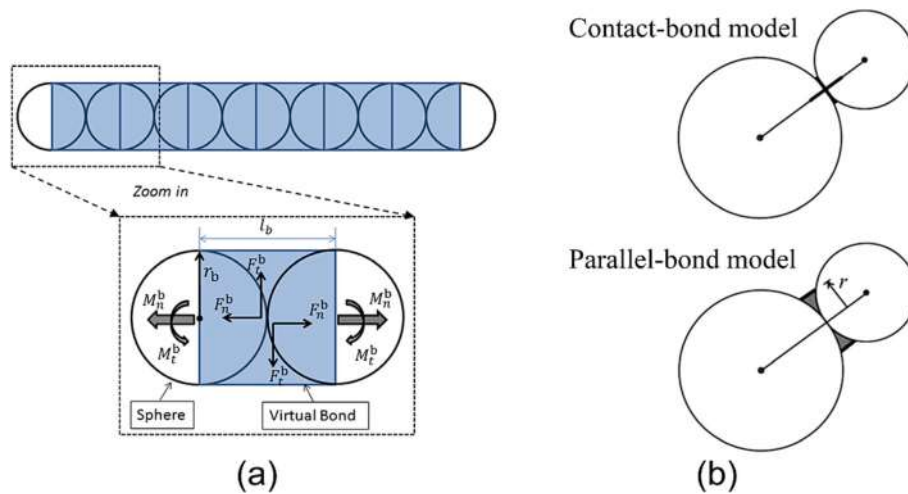


Fig. 8. Sketch map of the bonded-sphere model: (a) the interaction between sub-spheres (adapted from [68], Copyright 2013, with kind permission from Elsevier); (b) bonding model (adapted from [69], Copyright 2015, with kind permission from Central South University Press and Springer Nature).

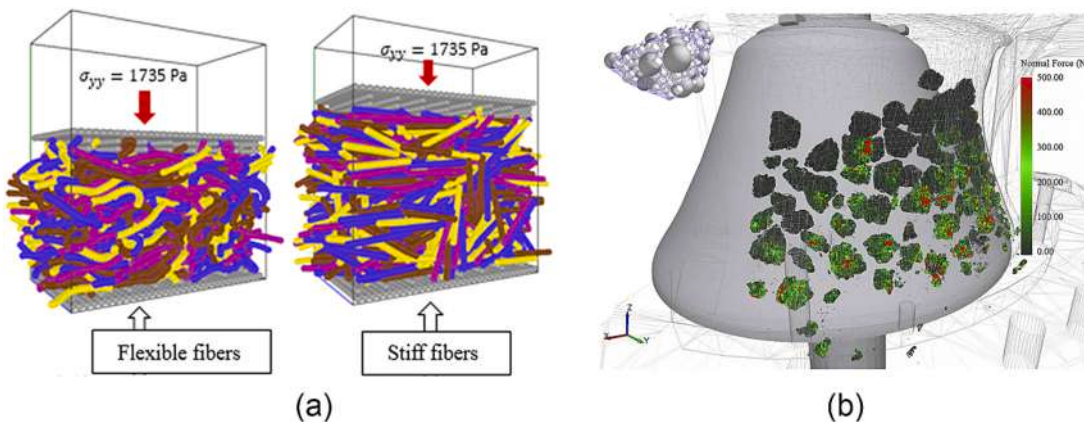


Fig. 9. DEM simulations of the behaviors of bonded-sphere particles: (a) the particle deformation in shear flows (adapted from [70], Copyright 2018, with kind permission from American Institute of Chemical Engineers); (b) the particle breakage in a cone crusher (adapted from [71], Copyright 2015, with kind permission from Elsevier).

can reduce the surface roughness of a bonded-sphere particle, the decrease in computational efficiency will be unavoidable. Therefore, the bonded-sphere model has been extended in that the composite elements of a bonded particle are replaced by other shaped elements, such as short cylinder [72] and prolate spheroids [73]. However, the complexity of the contact detection algorithms for non-spherical composite elements will be increased dramatically, and the computational efficiency will not be necessarily improved compared to the spherical composite elements. Synthesizing the above, the bonded-sphere model is still a worthwhile approach for modelling the deformation and breakage of particles.

2.2.1.3. Particle models based on single spherical particle. For particle models based on single spherical particle in this review, it means that the shape of the non-spherical particles is simplified as the idealized spherical shape for reproducing the behaviors of non-spherical particles by DEM. Among this type of model, the most widely used models should be the rolling friction model (generally for dynamic granular systems, e.g., the discharging and rotating drum) [74] and rolling resistance model (generally for pseudo-static granular systems, e.g., the penetration and shear bands) [75]. In general, it can be argued that the concept of rolling resistance can cover the rolling friction, but a precise definition of the terminology is out of the scope of this review. Additionally, both the rolling resistance model and rolling friction model obey the same framework and principle [76]. For simplicity, both the above models

will be therefore referred to as the rolling resistance model in the following.

In the rolling resistance model, the 'shape-like' performance for spherical particles is introduced by adjusting the rolling friction. The logic of this treatment is that spherical particles are generally more prone to roll than non-spherical particles due to the barriers of the non-spherical shape. And the rolling motion of spherical particles is mainly determined by the rolling friction between particle-particle or particle-wall. Therefore, there is a legitimate that artificially increasing the rolling friction of spherical particles, which is equivalent to imposing an additional torque at the contact points, could account for the effects arising from the non-circular or non-spherical shape to some extent. Following this train of thought, four different versions of rolling resistance models have been devised [76–78], including the elastic-plastic dashpot model [79], viscous model [74], directional constant torque model [74] and contact-independent model [78]. With these models, the spherical DEM models have successfully imitated the flow characteristics of non-spherical particles in various applications [77,80–83]. For example, Fig. 10 presents our previous investigations that use spherical particles with varying rolling friction coefficients (f_r in the figure) for replicating the behaviors of cube particles in the heap, discharging process, rotating drum and fluidization [77].

Besides using the rolling resistance model, Boyce et al. [84] proposed another way with introducing the concept of effective particle diameter.

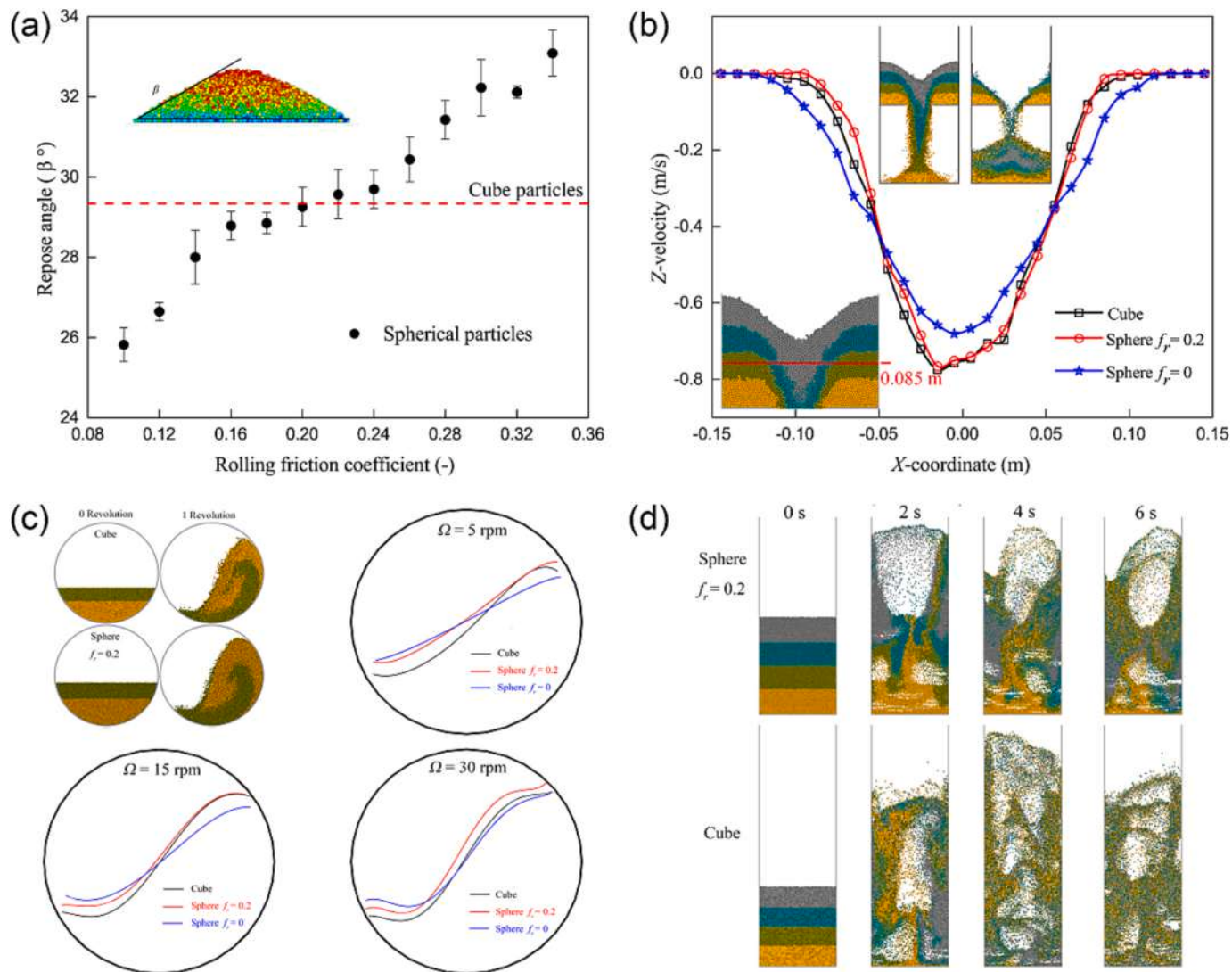


Fig. 10. DEM simulations of the cube particles and spherical particles with rolling resistance model: (a) the repose angle of the heap, (b) the vertical velocities of particles during the discharging process at a hopper height of 0.085 m, (c) the outlines of bed surfaces at different rotation speeds (Ω) of the rotating drum and (d) the fluidization behaviors in a fluidized bed (adapted from [77], Copyright 2019, with kind permission from Elsevier).

For modeling the fluidization of non-spherical kidney-bean-shaped poppy seed particles by spherical CFD-DEM in their investigations, the diameters of the spherical particles are different for different calculation purposes. For example, the particle diameter used for determining the contacts is $d_c = 1.07$ mm, and the diameter for calculating the voidage fraction of the CFD cell is $d_v = 1.00$ mm. While calculating the drag force, the diameter (d_d) significantly varies with the drag model, with $d_d = 1.20$ mm for the Gidaspow drag model [85], $d_d = 1.55$ mm for the drag mode proposed by Beetstra et al. [86] and $d_d = 2.10$ mm for the drag mode proposed by Tang et al. [87]. In this way, the spherical CFD-DEM can reproduce the fluidization behaviors of non-spherical poppy seeds more accurately than when a single particle diameter is applied by comparing with the corresponding MRI (Magnetic Resonance Imaging) experiments.

In summary, the particle model based on single spherical particle is an indirect but simple way to introduce the particle shape effects, and there is no doubt that this model is rather computational cost-effectiveness due to the high-efficiency and convenience in determining the contact between spheres in DEM. Nevertheless, there are still some open questions about these models. For example, the most important question for the rolling resistance model is the lack of a solid physical basis in selecting the rolling friction coefficient resulting in that

the rolling friction coefficient is considered as a “tunable parameter” [78]. Therefore, further efforts are still required for improving these models so that they can effortlessly take the non-sphericity of particles into account with a solid theoretical foundation.

2.2.2. Super-ellipsoid-based particle model

The super-ellipsoid-based particle model originates from superquadric method that is originally applied in computer graphics and is extended from the quadric equation. The standard formula of superquadric equation in three dimensions can be written as [37,49,88–90]:

$$f(x, y, z) = \left(\left| \frac{x}{a} \right|^{s_2} + \left| \frac{y}{b} \right|^{s_2} \right)^{\frac{s_1}{s_2}} + \left| \frac{z}{c} \right|^{s_1} - 1 = 0 \quad (13)$$

where a , b and c represent the semi-major axis lengths of a particle along its principal axes, respectively. The shape indices, s_1 and s_2 , decide the curvature of the particle edges, and the sharpness of the curvature increases with the shape indices. With the superquadric equation, various shapes can be effortlessly generated by adjusting three semi-major axis lengths (a , b and c) and two shape indices (s_1 and s_2), and it is statistically estimated that 80% of solid shapes can be described by the superquadric equation [50]. Fig. 11 presents the different particle

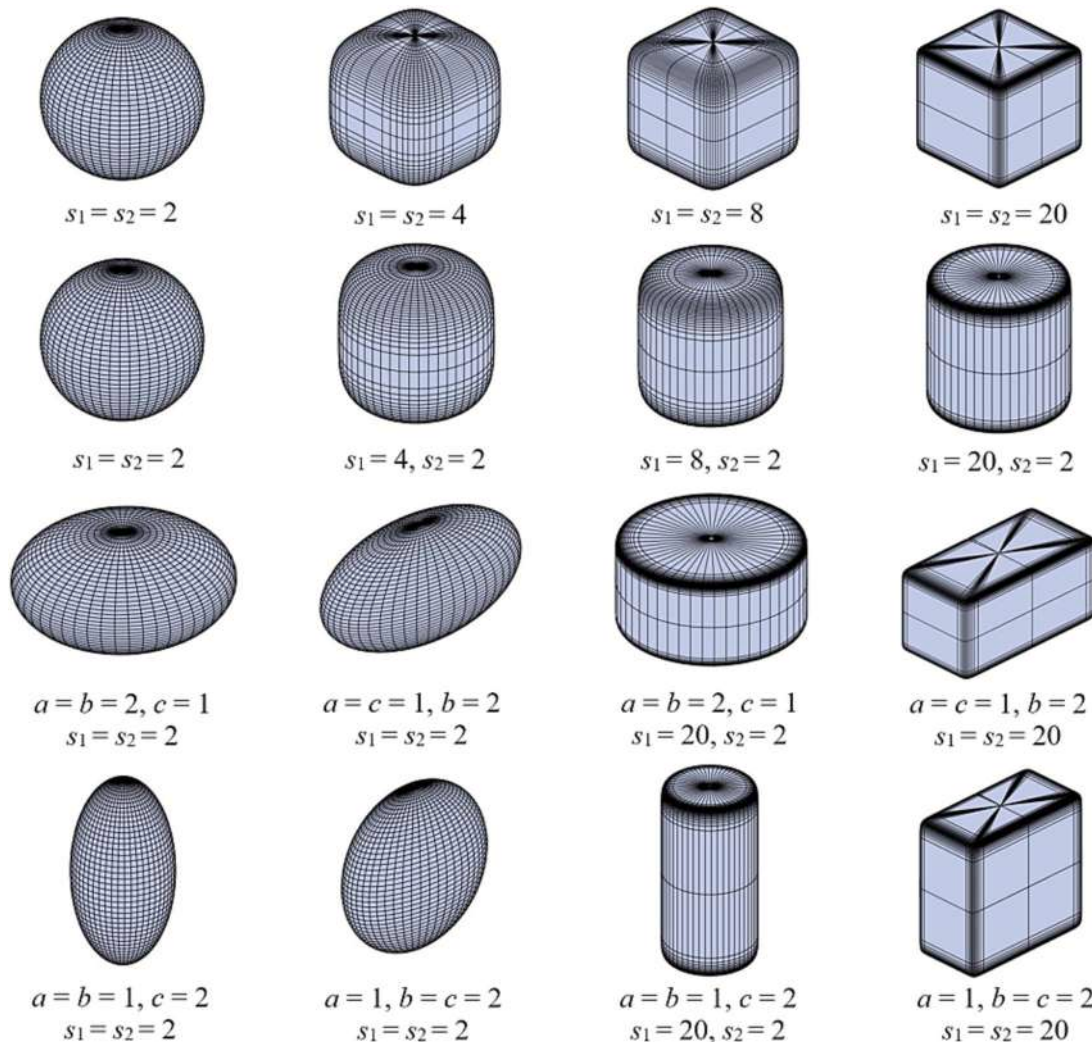


Fig. 11. Particles described by the super-ellipsoid model.

shapes by varying the aforementioned five tunable parameters in Eq. (13).

The superiority of the superquadric method in describing solid shape should agree well with the demand of the DEM simulation of non-spherical particles. The first application of the superquadric method in DEM was realized by Williams and Pentland [50] in 2D simulations, and then Cleary [51] successfully extended the method to three dimensions. DEM model incorporating the superquadric method can be effortlessly found in the published investigations now [8,49,91–93]. However, different terminologies for the particles modeled by the superquadric method were used, e.g., super-ellipsoid particles [49] and superquadric particles [93]. For convenience, all particles described by the superquadric method reviewed here are referred to as super-ellipsoid particles with the corresponding term of the super-ellipsoid model or super-ellipsoid particle model being adopted in the following. To the best of our knowledge, the super-ellipsoid-based particle model can be classified into two groups: the single-particle approach and the composite-particle approach. And the details will be presented below.

2.2.2.1. Single-particle approach. Frankly speaking, the single-particle approach mentioned here is the particle that is constructed by only one super-ellipsoid particle described by Eq. (14). For generating the super-ellipsoid particle, there is a prerequisite for using Eq. (14) that the center of the super-ellipsoid must coincide with the coordinate origin, and three major axes of the super-ellipsoid must coincide with the three

coordinate axes, which will be called the standard state for the super-ellipsoid in the following discussions. Therefore, it is necessary to define a super-ellipsoid particle with an optional position and orientation in the global coordinate system for practical use. Fig. 12 presents a sketch map of how a super-ellipsoid particle changes from its standard state to optional position and orientation. As shown in Fig. 12, the realization of this transformation is by translation operation (i.e., the change of centroid position of a particle) and rotation operation (i.e., the change of orientation of local coordinate system from x_l - y_l - z_l to x_g - y_g - z_g). Specifically, the coordinate transformation by the aforementioned matrix \mathbf{B} is performed for converting the position vector of the super-ellipsoid particle in the local coordinate system to the global coordinate system:

$$\mathbf{X} = \mathbf{B}\mathbf{x} + \mathbf{P} \quad (14)$$

where $\mathbf{x} = (x, y, z)^T$ and $\mathbf{X} = (X, Y, Z)^T$ are position vectors in the local and global coordinate system, respectively, $\mathbf{P} = (X_0, Y_0, Z_0)^T$ is the position vector of the particle centroid in the global coordinate system, and \mathbf{B} is the inverse of matrix \mathbf{A} :

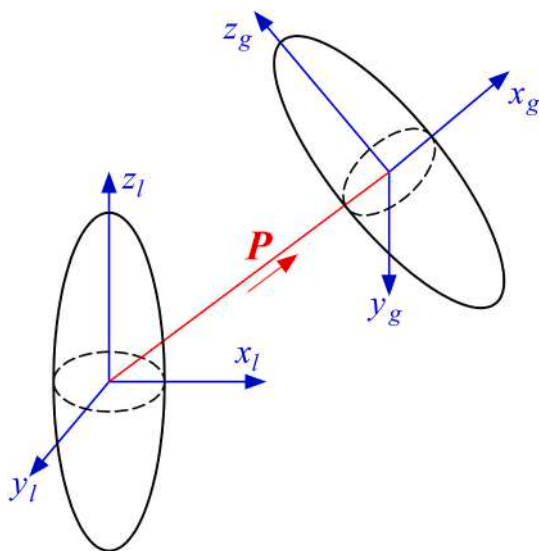


Fig. 12. Changing a super-ellipsoid particle from its standard state to an optional position and orientation.

$$\begin{aligned} B = A^{-1} &= \begin{bmatrix} \cos\varphi\cos\theta - \sin\varphi\cos\theta\sin\varphi & -\cos\varphi\sin\theta - \sin\varphi\cos\theta\cos\varphi & \sin\varphi\sin\theta \\ \sin\varphi\cos\theta + \cos\varphi\cos\theta\sin\varphi & -\sin\varphi\sin\theta + \cos\varphi\cos\theta\cos\varphi & -\cos\varphi\sin\theta \\ \sin\theta\sin\varphi & \sin\theta\cos\varphi & \cos\theta \end{bmatrix} \\ &= \begin{bmatrix} q_0^2 + q_1^2 - q_2^2 - q_3^2 & 2(q_1q_2 - q_0q_3) & 2(q_1q_3 + q_0q_2) \\ 2(q_1q_2 + q_0q_3) & q_0^2 - q_1^2 + q_2^2 - q_3^2 & 2(q_2q_3 - q_0q_1) \\ 2(q_1q_3 - q_0q_2) & 2(q_2q_3 + q_0q_1) & q_0^2 - q_1^2 - q_2^2 + q_3^2 \end{bmatrix} \end{aligned} \quad (15)$$

Then the formula of the super-ellipsoid particle in the global coordinate system can be obtained by plugging Eq. (14) into Eq. (13):

$$F(X, Y, Z) = \left(\frac{\left| B_{11}(X - X_0) + B_{21}(Y - Y_0) + B_{31}(Z - Z_0) \right|^{s_1}}{a} + \frac{\left| B_{12}(X - X_0) + B_{22}(Y - Y_0) + B_{32}(Z - Z_0) \right|^{s_2}}{b} + \frac{\left| B_{13}(X - X_0) + B_{23}(Y - Y_0) + B_{33}(Z - Z_0) \right|^{s_3}}{c} - 1 = 0 \right)^{\frac{1}{2}} \quad (16)$$

where B_{ij} ($i = 1, 2, 3; j = 1, 2, 3$) is the element of matrix B .

For calculating the contact details between the contacting super-ellipsoid particles, the researchers have proposed different contact detection algorithms. One representative algorithm can be referred to as the “deepest point method” [37,49,58,92,94] that should belong to the

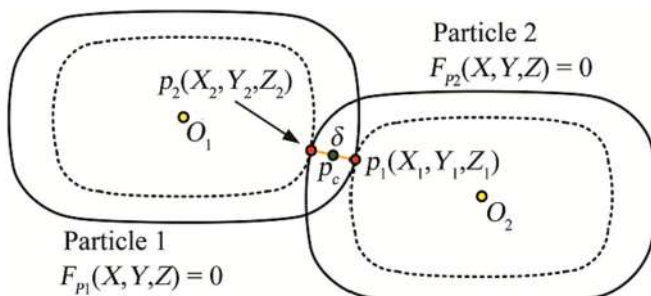


Fig. 13. Sketch map of the deepest point method for determining the contact between two super-ellipsoid particles (adapted from [49], Copyright 2019, with kind permission from Elsevier).

concept of the aforementioned GP method. As illustrated in Fig. 13, for two super-ellipsoid particles in the global coordinate system described by $F_{P1}(X, Y, Z) = 0$ and $F_{P2}(X, Y, Z) = 0$, respectively, the principle of this method is mainly to determine a point $p_1(X_1, Y_1, Z_1)$ on the surface of Particle 1 that can minimize the geometric potential of Particle 2 and vice versa. In other words, there must be a point $p_1(X_1, Y_1, Z_1)$ on the surface of Particle 1 that minimizes $F_{P2}(X_1, Y_1, Z_1)$ and vice versa. The minimum value is less than zero if Particles 1 and 2 are in contact. Otherwise, this minimum value will be greater than zero. Synthesizing the above, the deepest point method is primarily to calculate the deepest point p_1 in Particle 2 and the deepest point p_2 in Particle 1. Subsequently, p_1 and p_2 denote the deepest penetration of Particles 1 and 2 into each other. Synthesizing the above, the contact detection of super-ellipsoids can be transformed into solving the minimum value, i.e., solving the following equations:

$$\begin{cases} \text{Target equation : } \min F_{P2}(X, Y, Z) \\ \text{Constraint condition : } F_{P1}(X, Y, Z) \end{cases} \quad (17)$$

where the target function aims at finding the deepest point, and the constraint condition ensures that the deepest point is on the particle surface.

To resolve Eq. (17), the Lagrange multiplier method can be used:

$$L(X, Y, Z, \lambda) = F_{P2}(X, Y, Z) + \lambda F_{P1}(X, Y, Z) \quad (18)$$

where λ is the Lagrange multiplier. Then the following equations are obtained by taking the derivative of Eq. (18):

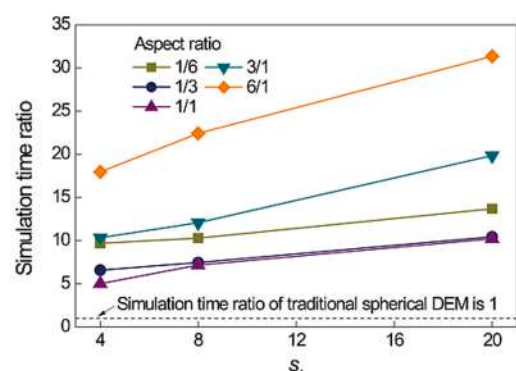
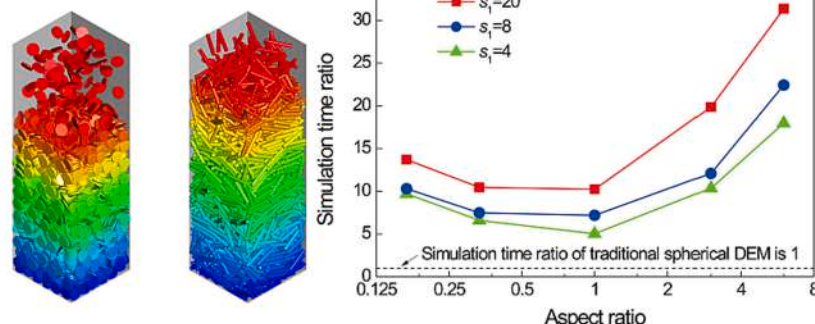
$$\begin{cases} \frac{\partial L}{\partial X} = \frac{\partial F_{P2}}{\partial X} + \lambda \frac{\partial F_{P1}}{\partial X} = 0 \\ \frac{\partial L}{\partial Y} = \frac{\partial F_{P2}}{\partial Y} + \lambda \frac{\partial F_{P1}}{\partial Y} = 0 \\ \frac{\partial L}{\partial Z} = \frac{\partial F_{P2}}{\partial Z} + \lambda \frac{\partial F_{P1}}{\partial Z} = 0 \\ \frac{\partial L}{\partial \lambda} = F_{P1}(X, Y, Z) = 0 \end{cases} \quad (19)$$

Eq. (17) can be resolved by solving Eq. (19). Then, the deepest point on the surface of Particle 1 can be obtained. Likewise, the deepest point on the surface of Particle 2 can also be calculated. Once these two deepest points are determined, the contact parameters between the contacting super-ellipsoids can be then defined. One rather straightforward definition is that the line segment joining two deepest points is the overlap δ , the action direction is parallel to the line segment, and the midpoint of the line segment denotes the effective contact point p_c . Subsequently, the contact force and torque can be calculated by plugging these determined contact parameters into the contact force model.

In general, the super-ellipsoid DEM will be less efficient as the shape of super-ellipsoid particles more and more deviates from the idealized sphere [49,95]. For example, our previous investigations compared the computational efficiency of super-ellipsoid particles with different shapes in the applications of box filling and rotating drum, as illustrated in Fig. 14. It can be clearly seen that the aspect ratio (defined as c/a here) and shape index of the particle significantly impact the computational efficiency that will be lower as the increase of shape index (s_1 here) or with the aspect ratio being farther from 1. But overall, the super-ellipsoid model is still quite efficient in modelling non-spherical particles. Taking the comparisons of different particle models illustrated in Fig. 7 as an example, the computation speed of the super-ellipsoid model is significantly faster than that of the multi-sphere model. In addition, the larger shape index or the aspect ratio farther from 1 can also deteriorate the robustness performance of the DEM model.

Note that there are also ways for the contact detection of super-ellipsoid particles. Besides Eq. (17), for example, an alternative equation set can be used to determine the minimum value:

Box filling



Rotating drum

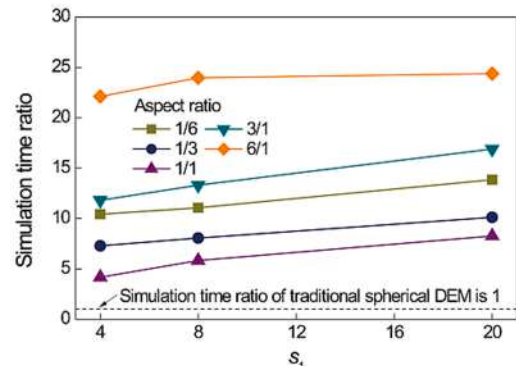
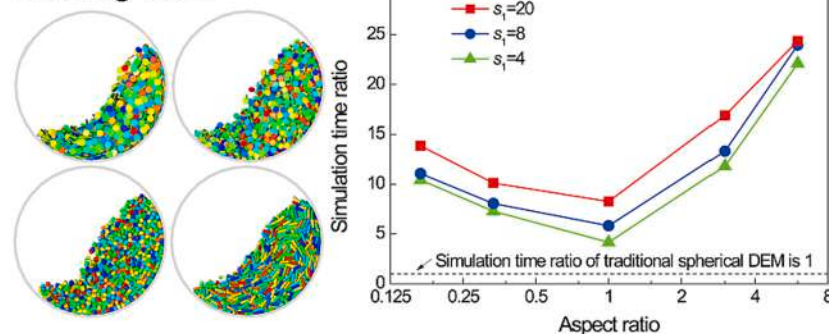


Fig. 14. Influence of the shape index (s_1 here) and the semi-axis lengths (mirrored by aspect ratio here) on the computational efficiency of the super-ellipsoid model (adapted from [49], Copyright 2019, with kind permission from Elsevier).

$$\begin{cases} \text{Target equation : } \min F_{P1}(X, Y, Z) + F_{P2}(X, Y, Z) \\ \text{Constraint condition : } F_{P1}(X, Y, Z) = F_{P2}(X, Y, Z) \end{cases} \quad (20)$$

More details about this way can be found in [93,96,97]. And the contact detection algorithms based on CN method have also been devised [59]. According to the characteristics of the above contact algorithms, furthermore, they all belong to CFR (Continuous Function Representation) that the particle can be represented by the continuous and smooth surface. To the best of our knowledge, the most robust algorithms for super-ellipsoids expressed by CFR can guarantee the convergence of DEM simulations with $s_1, s_2 \leq 40$ [98] and the range of aspect ratio being from 1/10 [99] to 30 [37]. In contrast to CFR, DFR (Discrete Function Representation) is also developed for determining the contact between super-ellipsoid particles that the surface of a super-ellipsoid is approximated by a certain number of discrete points with the relatively uniform distribution [55]. Lu et al. [58] further evaluated the performance of CFR and DFR by the DEM simulations. They found that the rather comparable results between these two approaches can be obtained if the number of discrete points in DFR is sufficient, and the computation efficiency of CFR should be slightly higher than that of DFR.

Additionally, for ellipsoidal particles that are a special case of super-ellipsoid particles with $s_1 = s_2 = 2$, it should be the frequently encountered non-spherical particles in DEM studies [8,53,100–104] and has attracted much attention. To determine the contact between ellipsoidal particles, various contact detection algorithms have been exclusively devised [7] (e.g., the intersection algorithm [105,106] and CN method [57]) besides the methods used for detecting the contact between super-ellipsoid particles, and the interested reader can be referred to the related investigations.

2.2.2.2. Composite-particle approach. As stated above, not all particle shapes can be described by the super-ellipsoid model, e.g., asymmetrically shaped particles. Inspired by the multi-sphere model, the composite-particle approach based on the super-ellipsoid model has also

been proposed for describing more particle shapes. For example, we put forward a composite approach called the multi-super-ellipsoid model in our previous investigations [107,108]. In the multi-super-ellipsoid model, the particle is formed by combining a certain number of super-ellipsoid particles with various amounts of overlaps, as shown in Fig. 15. Particularly for some specific applications, such as the drug tablets pharmaceutics, using the multi-super-ellipsoid model can effortlessly approximate the particle shape with fewer component particles and higher precision (see Fig. 15), and hence leading to more efficient and accurate DEM simulations as demonstrated in our previous investigations [108].

In addition, another composite-particle approach called the poly-superellipsoid approach was also proposed [96,109]. In this approach, the non-spherical particle is made up of eight eightths super-ellipsoid particles respectively located in eight quadrants, as illustrated in Fig. 16. According to Eq. (13), five parameters (a, b, c, s_1, s_2) are needed to describe a super-ellipsoid particle. So a total of forty parameters are required for eight super-ellipsoids in theory. But for the poly-superellipsoid particle, the parameters used for each sub-particle have some limitations because the surface of the composite particle needs to be continuous and smooth. To ensure the continuity of the composite particle surface, therefore, the semi-major axis lengths of adjacent sub-particles need to be equal in cross-sectional facets. For example, the lengths along the z-axis are the same for the four sub-particles ($k = 1, 2, 3$ and 4 in Fig. 16). What's more, in order to guarantee the smoothness of the surface at the junction of the sub-particles, the shape indexes for all eight sub-particles should also be the same. As a result, a poly-superellipsoid particle can be generated with only eight parameters, including the six semi-major axis lengths along the coordinate axis and two shape parameters. And then different asymmetrically shaped particles can be generated by adjusting these eight parameters just as shown in Fig. 16.

According to the characteristics of these two composite-particle approaches, the application area of the poly-superellipsoid approach might be limited due to the restrictions of the number and location of each

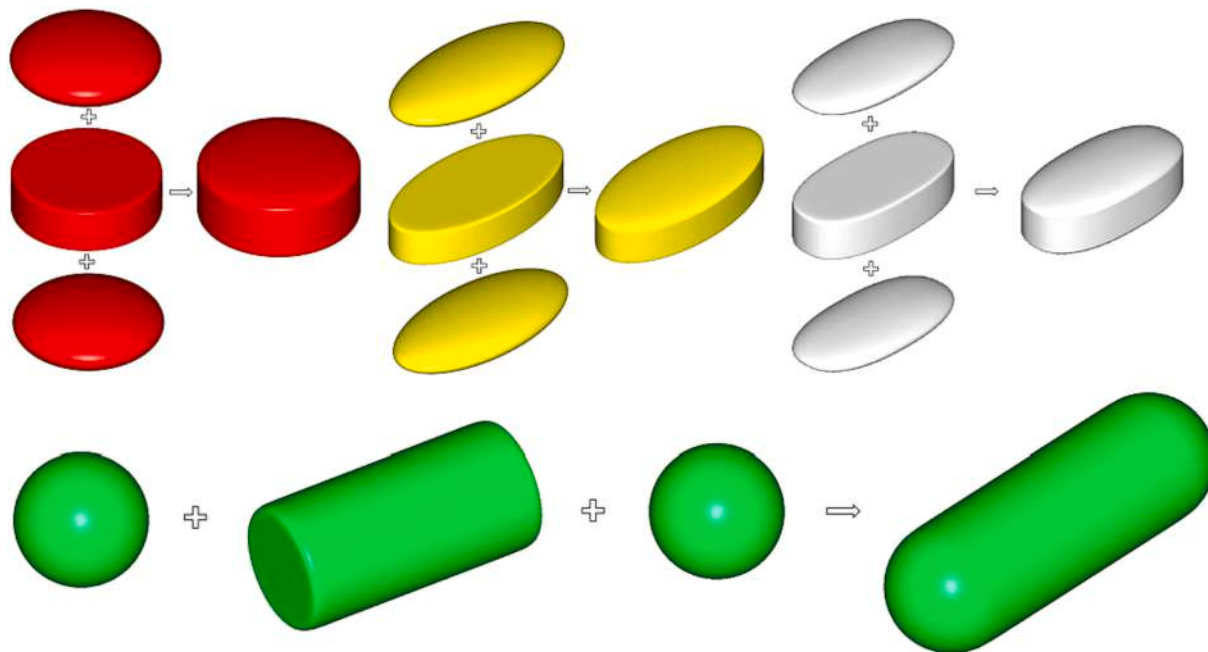


Fig. 15. Particles described by the multi-super-ellipsoid model (adapted from [107], Copyright 2019, with kind permission from Elsevier).

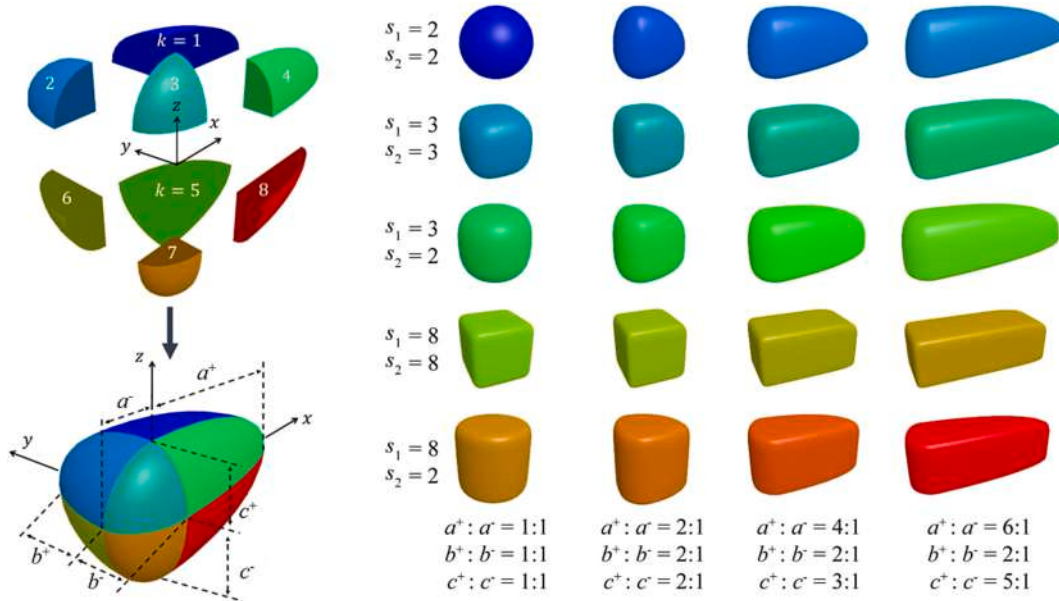


Fig. 16. Non-spherical particles described by poly-superellipsoid approach (adapted from [96], Copyright 2021, with kind permission from Springer Nature).

component super-ellipsoid particle. However, there should be theoretically no limit for the multi-super-ellipsoid model in determining the number and location of the element super-ellipsoid particles, which is more similar to the above-mentioned multi-sphere model. Therefore, the multi-super-ellipsoid model can describe the particles with arbitrary shapes.

2.2.3. Polyhedron-based model

In many areas like geotechnical and geological engineering, the solids possessing complex shape (e.g., ores and rocks) can be reasonably simplified as polyhedron particles that are composed of a certain number of planes, edges and vertexes. Due to the discontinuity of the surface of polyhedrons, therefore, the polyhedron particle model should be the most accurate way to construct the geometry of the polyhedron particles

among various particle models in DEM, as illustrated in Fig. 17. Apparently, the polyhedron particles can be constructed more accurately by including more planes, but more computational resources will be consumed.

For detecting the contact between the polyhedron particles, various methods have been put forward [7], such as the penetration edge method [110], shrunken edge method [111], shortest link method [112], incision body method [113], common plane method [114], fast common plane method [115], etc. Because of the space constraints of this review, nevertheless, this review will mainly introduce the energy-conserving contact interaction model that was proposed by Feng et al. [61] and has been widely used in the DEM modellings of polyhedron particles [108,116–120]. This theory obeys the energy-conservation principle for the elastic collisions between particles, and the contact

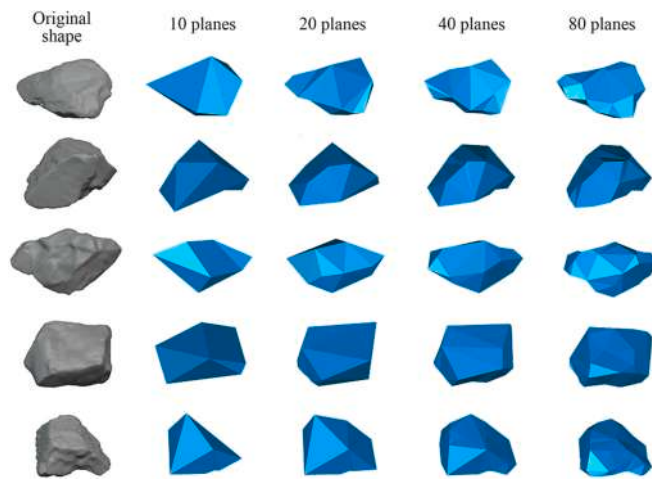


Fig. 17. Particles described by polyhedral model.

details are determined based on the overlapping volume between contacting particles. When two polyhedron particles are in contact, the overlap between them can be represented by a polyhedron block. Taking the simplest tetrahedral particles for instance, as presented in Fig. 18, there are three different contact types for the contacting polyhedrons: vertex-vertex contact, vertex-plane contact and edge-edge contact. For vertex-vertex contact (see Fig. 18(a)), A_i ($i = 1, 2$ and 3) is the plane area of polyhedron block $V_2P_1P_2P_3$, and \mathbf{n}_i ($i = 1, 2$ and 3) is the corresponding outward unit normal vector of the planes. Then the normal vector \mathbf{n} of block $V_2P_1P_2P_3$, which is normal to the contact plane, can be defined by the following formula [61]:

$$\mathbf{n} = (A_1\mathbf{n}_1 + A_2\mathbf{n}_2 + A_3\mathbf{n}_3)/\|A_1\mathbf{n}_1 + A_2\mathbf{n}_2 + A_3\mathbf{n}_3\| \quad (21)$$

Likewise, the unite normal vector \mathbf{n}' for polyhedron $V_1P_1P_2P_3$ can also be determined. As to vertex-plane contact (see Fig. 18(b)), the normal vector \mathbf{n} is the sum of the unit normal vectors \mathbf{n}_i ($i = 1, 2$, and 3) of three planes (i.e., $V_1P_2P_3$, $V_1P_1P_2$ and $V_1P_1P_3$), and the normal vector \mathbf{n}' is the unit normal vector of plane $P_1P_2P_3$. For edge-edge contact (see Fig. 18(c)), the normal vector \mathbf{n} is the sum of unit normal vectors of planes $P_2P_3P_4$ and $P_1P_2P_4$, and the normal vector \mathbf{n}' is the sum of the unit normal vectors of $P_1P_2P_3$ and $P_1P_3P_4$. Note that in this contact scenario, the relationship of $\mathbf{n} = -\mathbf{n}'$ is satisfied. For more details about this contact detection algorithm, the interested readers can also refer to the previous researches [108,116,118].

Generally, the polyhedron can be divided into two categories: the convex polyhedron and the concave polyhedron. The currently available contact detection algorithms are basically suitable for convex polyhedrons. In comparison with the convex polyhedrons, nevertheless, the contact detection for the concave polyhedrons is quite intricate due to the possible occurrence of multiple contacts between particles. The most

straightforward way to handle this challenging issue should be to split a concave polyhedron into several small convex polyhedrons [8]. Therefore, the contact interaction for the concave polyhedron can be subsequently determined by summing up of all component convex polyhedrons, just like the treatment for the multi-sphere model and the multi-super-ellipsoid model. Moreover, Feng [121] also proposed an approach for handling multiple contacts between concave particles. And then this approach was further incorporated into their DEM model based on an enhanced general energy-conserving contact theory for detecting the contact between concave polyhedrons [122], and the interested readers can refer to the investigation for more information.

The polyhedron model not only can construct the sharp-edged polyhedrons mentioned above, but can generate the smooth-edged polyhedrons with the necessary modification of the current polyhedron model [80,123–127], as illustrated in Fig. 19(a). One of the representative models is the polyhedron model based on the Minkowski sum (see Fig. 19(b)). In this modified polyhedron model, there are two sets of points A and B that denote the closed geometries in space, respectively, and their Minkowski sum can then be written as:

$$A \oplus B = \{x + y | x \in A, y \in B\} \quad (22)$$

in which x and y represent the points in sets A and B , respectively. In other words, $A \oplus B$ is the sum of position vectors of all points in sets A and B . Taking the presentation in Fig. 19(b) as an example, the above mathematical language can be briefly translated into that the polyhedrons with smooth edges are generated by replacing the sharp edges of polyhedrons with an infinite number spheres. For more details about the polyhedron model based on the Minkowski sum, the interested readers can refer to the previously published investigations [8,127].

2.2.4. Other particle models

Besides the aforementioned particle models, some other methods have also been developed for modelling non-spherical particles. For example, one representative model is the combined geometric element method that a particle is constructed by intersecting surfaces with arbitrary shapes. This method is appropriate for creating a particle with smooth surfaces or sharp edges. Fig. 20 presents some representative particles described by this method. As shown in this figure, the cylinder is constructed by a cylindrical band and two flat end planes, the bi-convex shaped tablet is composed of a cylindrical band and two cap surfaces (i.e., the two spherical parts), and the spherocylinder consists of a cylindrical band and two spheres. Nevertheless, the computational efficiency might be unsatisfactory that each possible contact scenario between particles, including the face-face, face-band, face-edge, band-band (parallel and skewed), band-edge and edge-edge (see Fig. 20), needs to be determined and all vertices, edges, and faces must be searched, resulting in the limited parallelism capability of large-scale computing [8]. In addition, other particle models not mentioned above, e.g., spherical harmonic-based approach that the particle shape

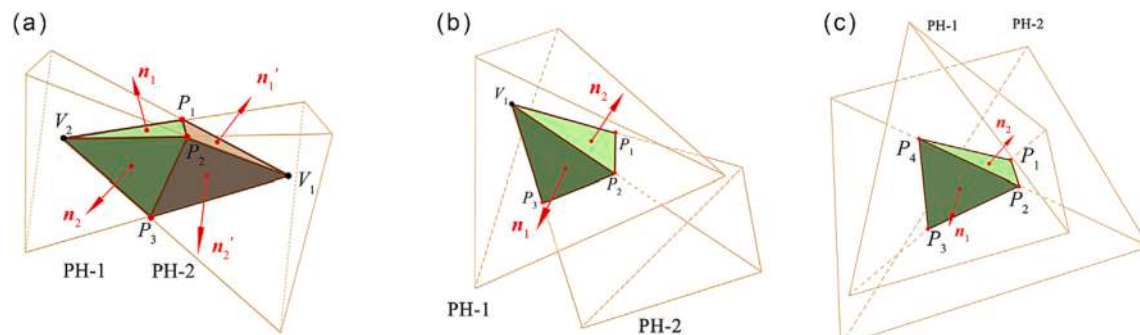


Fig. 18. Schematic of the contact between two polyhedron particles: (a) vertex-vertex contact, (b) vertex-plane contact and (c) edge-edge contact (Adapted from [116], Copyright 2020, with kind permission from Elsevier).

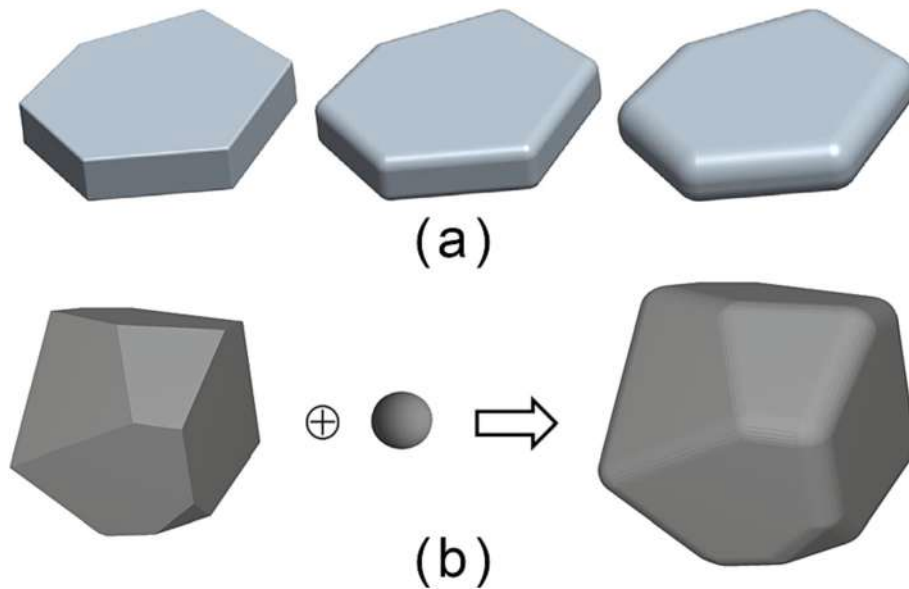


Fig. 19. Dilated polyhedral model: (a) the smooth-edged polyhedrons (adapted from [123], Copyright 2018, with kind permission from Springer Nature); (b) the polyhedron model based on Minkowski sum (adapted from [127], Copyright 2019, with kind permission from Springer Nature).

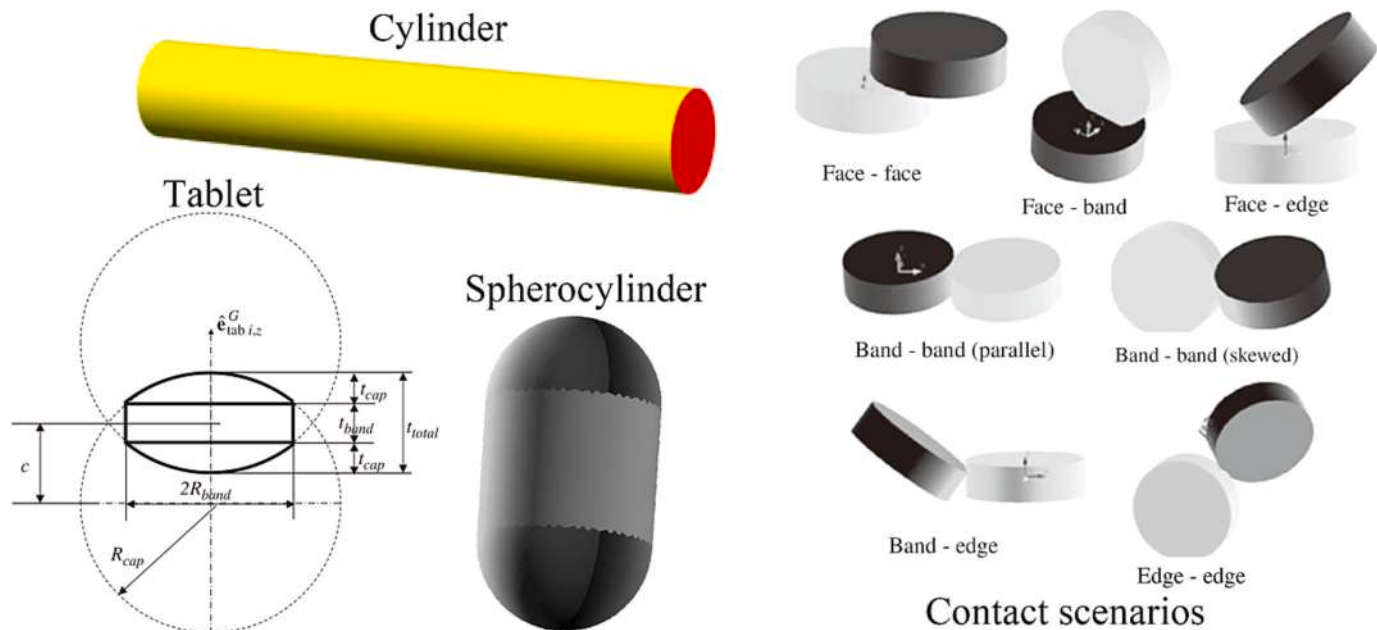


Fig. 20. Combined geometric element method (adapted from [136–138] with kind permissions from Cambridge University Press (Copyright 2012), Elsevier (Copyright 2010) and Elsevier (Copyright 2011)).

can be expressed by a higher order polynomial equation (*i.e.*, spherical harmonic function) [128,129], level set function model that the particle is approximated by a scalar-valued implicit function quantifying the distance from a point to an interface [130,131], potential particle model that the shape, surface normal and surface curvature of particles can be efficiently controlled by a well-designed function [132,133], virtual space method that the particle is constructed by a collection of pixels (2D) or voxels (3D) [134], and B-spline model that the particle is created by applying non-uniform rational B-Splines [135], can also be found effortlessly, and the interested readers can refer to the related literatures [7,8,10]. By the way, the larger a particle, the more important are geometric features like shape or inertial tensor. In other words, the influence of particle shape should be not significant for the particles with rather small dimensions, and the relatively comparable simulation

results may also be obtained by directly using spherical particles in some cases.

As mentioned above, the computational cost of contact detection for non-spherical particles is rather expensive that it generally spends more than 80% of the overall computational time [55]. Besides the conventional contact detection algorithms mentioned above, some novel methods were also proposed for improving the efficiency of DEM simulations. For example, Hwang et al. [139] introduced machine learning into the DEM model for determining the contact between particles just as shown in Fig. 21(a). Specifically, a large number of datasets directly generated by the conventional contact detection algorithms, such as the deepest point method for the super-ellipsoid model, are collected for the training of machine learning and then to correlate the contact parameters with the relative position and orientation of two particles. The

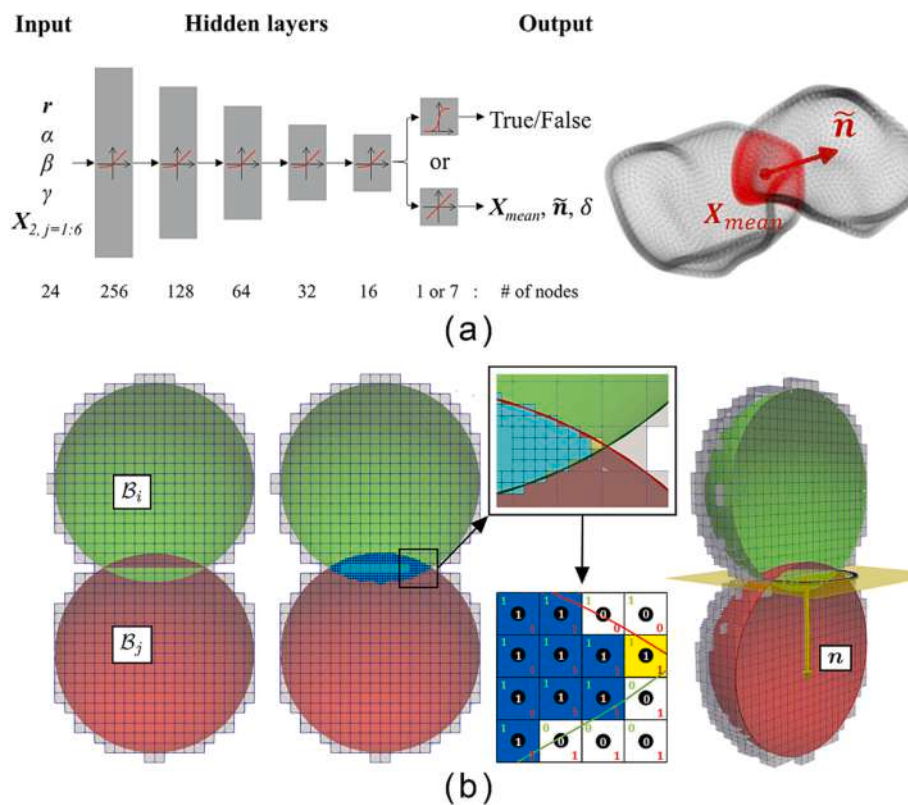


Fig. 21. Some other novel contact detection algorithms: (a) the detection algorithm based on machine learning (adapted from [139], Copyright 2022, with kind permission from Elsevier); (b) the virtual mesh algorithm (adapted from [140] with kind permission from the author).

Table 1
Comparisons between sphere-based, super-ellipsoid-based and polyhedron-based particle models

Category	Type	Shapes	Accuracy	Speed
Sphere-based model	Sphere	Spherical shape	High for spheres	Fast
	Multi-sphere	Any shapes	Low	Depend on the number of sub-spheres
	Bonded-sphere	Any deformable and breakable shapes	Low	Depend on the number of sub-spheres
Super-ellipsoid -based model	Super-ellipsoid	Sphere, ellipsoid, cylinder, cube, etc.	High	Medium
	Multi-super-ellipsoid	Any shapes (Especially tablets)	High	Depend on the number of super-ellipsoids
	Convex polyhedron	Any convex shapes	High	Depend on the number of planes
Polyhedron-based model	Concave polyhedron	Any concave shapes	High	Depend on the number of planes or polyhedrons

test results indicated that the machine learning based model is computationally efficient with high accuracy, which required less than a second for the determination of contact parameters for granular systems containing thousands of non-spherical particles. In addition, a few attempts have also been made to develop a general contact detection algorithm irrelevant to the particle shape or the used particle model. For instance, Studenik et al. [140] devised a method called the virtual mesh algorithm for efficiently detecting the contact just as shown in Fig. 21 (b). In this algorithm, the contact area was discretized into a number of uniformly distributed fine cube meshes. And then the required contact parameters including the overlap, contact normal and contact point are determined through the information of these fine cube meshes.

2.2.5. Comparisons between different particle models

There is no doubt that each of the aforementioned particle models has its own flaws and admirable points. For instance, Table 1 compares the advantages and disadvantages of the sphere-based, super-ellipsoid-based and polyhedron-based particle models. Generally, the particle model used for modeling non-spherical particles should be chosen carefully in solving different granular systems to trade off the accuracy and efficiency of DEM simulations.

Moreover, for the applications containing multiple particle types with different shapes, the researchers can consider using different particle models to describe different types of particles for the sake of taking full advantage of the characteristics of the particle models, so that it can maximize the accuracy and efficiency of DEM simulations. In other words, different particle models can be used simultaneously in the same simulation case, as illustrated in Fig. 22. For example, we have successfully developed the algorithms to detect the contact between the spheres and polyhedrons [117] as well as the super-ellipsoids and polyhedrons [116] for simulating the particulate systems containing multiple particle types, and the details will be presented below.

For the contact between sphere and polyhedron, the principle similar to the aforementioned “deepest point method” is adopted. As illustrated in Fig. 23, two types of contacts can be identified: edge-vertex contact and edge-edge contact. Taking 2D cases presented in Fig. 23 for example, the circle SP-1 and polygon PH-2 are in contact, and the circle SP-1 can be formulated as $F(x, y) = 0$. Therefore, the points satisfied $F(x, y) = 0$ are inside the circle SP-1. For the edge-vertex contact (see Fig. 23 (a)), the vertex of PH-2 (i.e., point p) that can minimize $F(x, y)$ is the

deepest point inside SP-1. The direction of the normal contact force is always parallel to line Op , and the intersection point q of the SP-1 and extension line Op is the deepest point inside the PH-2. For edge-edge contact (see Fig. 23(b)), the primary difference compared to the edge-vertex contact is that the deepest point p inside SP-1 is on the edge of PH-2 and the line Op is normal to the edge. The other procedures are identical to the edge-vertex contact. The above procedures can be effortlessly extended to 3D cases. Once these deepest points are obtained, the contact parameters and then the contact force can be determined.

The main idea behind the detection of the contact between a super-ellipsoid and a polyhedron is to transform the super-ellipsoid into a polyhedron. And then the contact detection between the super-ellipsoid and polyhedron can be therefore converted into the contact detection between two polyhedrons. Specifically, the standard formula of the super-ellipsoid model (i.e., Eq. (13)) can also be written in the form of spherical coordinates:

$$\begin{cases} x = a \cos^{\frac{2}{n}} \alpha \cos^{\frac{2}{n}} \vartheta \\ y = b \cos^{\frac{2}{n}} \alpha \sin^{\frac{2}{n}} \vartheta & \left(-\frac{\pi}{2} \leq \alpha \leq \frac{\pi}{2} \right) \\ z = b \sin^{\frac{2}{n}} \alpha & (-\pi \leq \vartheta \leq \pi) \end{cases}, \quad (23)$$

where ϑ and α are the angles of the super-ellipsoid in the x - y and x - z (or y - z) planes, respectively. For transforming the super-ellipsoid into a polyhedron, the increment of α is set as π/n and that of ϑ is $2\pi/n$, where n is the number of slices, as presented in Fig. 24. Then the contact parameters can be determined by the contact detection algorithms used for polyhedrons. In addition, other algorithms for determining the contact between super-ellipsoid and polyhedral can also be accessed in the published literature [141], and interested readers can refer to it for more details.

2.3. Cohesion force

Besides the contact force and gravitational force, the cohesion force should also be considered for the more accurate DEM simulations in some cases. For example, for dry granular systems with rather small particle diameters (< 0.1 mm), the cohesion between particles cannot be ignored that the van der Waals force might dominate the fine-grain

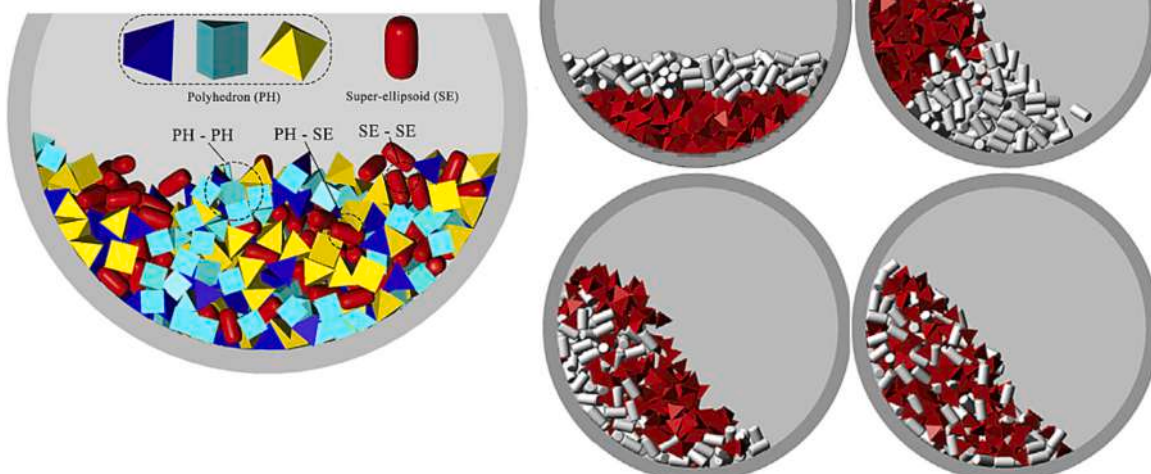


Fig. 22. Using polyhedron model and super-ellipsoid model together in a rotating drum (adapted from [116], Copyright 2020, with kind permission from Elsevier).

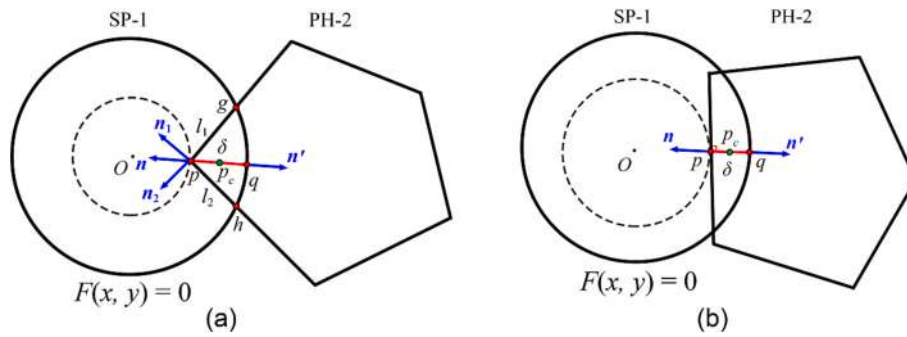


Fig. 23. Sketch map of the contact between a circle and a polygon: (a) edge-vertex contact and (b) edge-edge contact (adapted from [117], Copyright 2021, with kind permission from Elsevier).

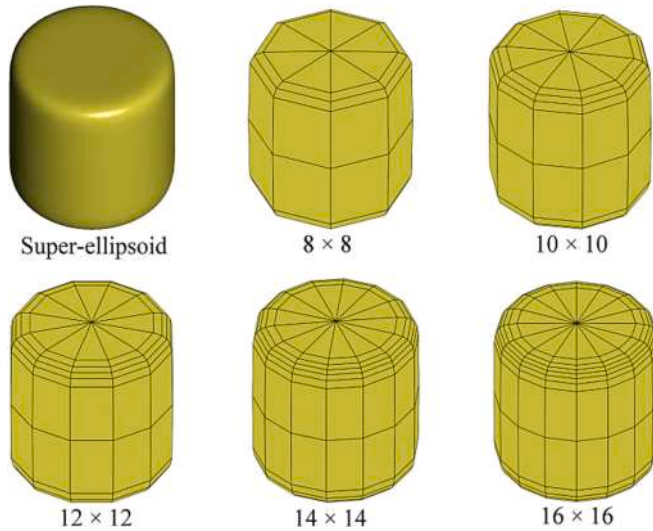


Fig. 24. Schematic of the transformation from a super-ellipsoid to a polyhedron with the different number of planes (adapted from [116], Copyright 2020, with kind permission from Elsevier).

granular flows [8,22]. In general, the cohesion force can be classed into forces with and without physical contact between particles. For example, the bridge force is the force with physical contact, whereas the van der Waals force and electrostatic force belong to the force without physical contact [142].

The van der Waals force that was first identified by van der Waals in 1873 is essentially an electromagnetic force between real gas atoms or molecules resulting from the interaction between dipole-dipole. This force can refer to the dipole-dipole interaction between atoms, molecules and surfaces and can occur between two microscopic molecules or two macroscopic objects (e.g. the interaction between particle-particle or particle-wall). The van der Waals force generally includes three main attractive intermolecular forces: the force induced by the interaction between two permanent dipoles, the force due to dipole-induced dipole and the force caused by two instantaneously induced dipoles [22]. Specifically, the force induced by the interaction between two permanent dipoles is an electrostatic force due to dipole-dipole interaction, the force due to the dipole-induced dipole is from the fast-changing of the atomic dipole, and the force caused by two instantaneously induced dipoles is generally referred to as the London force and roots in interacting molecules. The van der Waals force is normally affected by a number of factors (e.g., the surrounding fluid, contact deformation and roughness of particle surface) according to Hamaker theory [143].

The models to predict the van der Waals force for spherical particles have been well established by the Hamaker theory [143], in which the

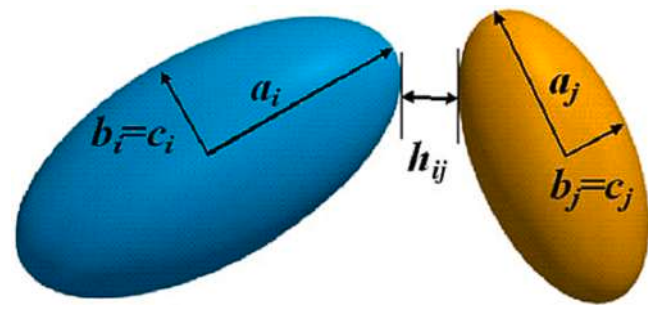


Fig. 25. Schematic of two interactive spheroids (adapted from [100], Copyright 2015, with kind permission from American Institute of Chemical Engineers).

model developed by Chen and Anandarajah [144] should be used rather popularly. Based on the work of Everaers and Ejtehadi [145], Gan et al. [100,103,146,147] further developed a van der Waals force model for ellipsoidal particles, and Fig. 25 presents the sketch map of two interactive ellipsoids. Specifically, the interaction potential U between two ellipsoidal molecules of arbitrary shape and size is derived through a systematic approximation of the Hamaker integral by Everaers and Ejtehadi [145]:

$$U = -\frac{A_{ij}}{36} \left(1 + 3\eta_{ij}\chi_{ij}\frac{\sigma}{h_{ij}} \right) \times \left(\frac{a_i}{a_i + h_{ij}/2} \right) \left(\frac{b_i}{b_i + h_{ij}/2} \right) \left(\frac{c_i}{c_i + h_{ij}/2} \right) \times \left(\frac{a_j}{a_j + h_{ij}/2} \right) \left(\frac{b_j}{b_j + h_{ij}/2} \right) \left(\frac{c_j}{c_j + h_{ij}/2} \right) \quad (24)$$

where a_i , b_i and c_i are the aforementioned semi-major axis lengths of the particle i , A_{ij} is the Hamaker constant, h_{ij} is the minimum surface separation, σ is the atomic/particle interaction radius, and $\eta_{ij}\chi_{ij}$ is a coefficient related to the position and orientation of the ellipsoid:

$$\eta_{ij}\chi_{ij} = \frac{2\sigma^{-1}}{\sqrt{\left(\frac{1}{R_i} - \frac{1}{R'_i}\right)\left(\frac{1}{R_j} - \frac{1}{R'_j}\right)\sin^2(\xi) + \left(\frac{1}{R_i} + \frac{1}{R'_i}\right)\left(\frac{1}{R_j} + \frac{1}{R'_j}\right)}}, \quad (25)$$

where R_i and R'_i are the two different principal radii of curvature at the point of closest approach, ξ is the relative angle that the principal axes of the two surfaces can be rotated relative to each other. Then the van der Waals force can be determined by differentiating the interaction potential U with regard to h_{ij} . For mono-sized ellipsoidal particles, the expression of calculating the van der Waals force can be simplified as:

$$F_{vdW} = -\frac{A_{ij}}{12} \frac{\eta_{ij}\chi_{ij}\sigma}{h_{ij}^2} \left(\frac{a}{a + h_{ij}/2} \right)^2 \left(\frac{b}{b + h_{ij}/2} \right)^2 \left(\frac{c}{c + h_{ij}/2} \right)^2, \quad (26)$$

Note that a minimum cut-off distance h_{min} needs to be set to avoid the singularity problem when h_{ij} equals to zero. On the other hand, a

maximum cut-off distance h_{max} is also required, where the van der Waals forces will be neglected for h_{ij} greater than h_{max} .

When there are bridge forces in granular systems (e.g., for wet granules), a physical bond will appear to connect two adjacent particles. Depending on the material properties of the physical bond between particles, two types of bridges can be distinguished: liquid bridge and solid bridge. When liquid (e.g., water) is presented in granular systems, the particle surfaces are wetted with a liquid film. The liquid bridge can be subsequently built while the distance between two particles falls below a threshold distance. For the solid bridge, it will be formed in the granular systems involving sintering, melt crystallization, thermochemical reaction, etc. The solid bridge connects two particles with a strong and permanent bond. In general, the bridge force is rather complicated, and it will be influenced by many factors, e.g., the bridge geometry, contact angle, filling angle, roughness of particle surface, temperature, etc. Researchers have proposed various force models for both the liquid bridge and the solid bridge. AlObaid et al. [22] had summarized the bridge force in detail, and the interested readers can refer to it.

Under the action of the electrostatic field as well as due to the collisions between particle-particle or particle-wall, the particle surface can be charged with a rather high possibility. Therefore, there will be the electrostatic force between particles that may have a significant influence on particle movements. In general, the electrostatic force for charged particles can be expressed by the typical Coulomb's law.

To date, the currently available cohesion force models are established primarily for spherical particles, whereas the corresponding investigations for non-spherical particles are very scarce. Therefore, a great deal of effort is still required in the future to develop the cohesion force models appropriate for non-spherical particles for more accurate DEM simulations of the flow of non-spherical particles.

2.4. Particle-fluid interaction forces

For accurately reproducing the particle behaviors in particle-fluid systems by DEM simulations, the interaction forces between particle-fluid (i.e., F_{pf} presented in Eq. (1)) must also be considered legitimately, namely the forces acting on particles imposed by the fluid should be calculated with rather high accuracy. In general, the particle-fluid interaction forces mainly include the drag force, lift force, pressure gradient force, virtual mass force, Basset force, etc. Among these forces, the drag force is generally the largest, and the other forces are usually rather small in comparison with the drag force [142], especially in gas-solid systems. For reducing the model complexity, therefore, only the drag force is normally accounted for in the simulations, while the other particle-fluid interaction forces are often neglected. The reasonable simulation results can still be obtained while only considering drag force. For example, in a gas-solid fluidized bed, the translational and rotation velocities of particles are usually not high so that the lift force can be reasonably ignored due to the relatively low gas superficial velocity [99,148]. With the development of society, however, there is a tendency that the operational conditions of industrial applications would become more extreme, e.g., the rather high fluid velocity for the gas-solid systems and using particles with quite complicated shapes. Under the circumstances, the other particle-fluid interaction forces besides the drag force should also be included for the more precise simulations and to enlarge the applicable areas of DEM.

2.4.1. Drag force

The drag force is the consequence of fluid acting on particles, which is caused by the difference in velocity of each phase and imposes on the direction of relative velocity between the fluid and particles. The drag force essentially acts on the particle surfaces, but it is often assumed to be effective at the center of the particle in the DEM simulations [20]. For an isolated particle, the drag force F_{D0} can be calculated by:

$$\mathbf{F}_{D0} = \frac{1}{6} \pi d_p^3 \beta (\mathbf{u} - \mathbf{v}), \quad (27)$$

where d_p is the diameter of the volume equivalent sphere, β is the interphase exchange coefficient, and \mathbf{u} is the fluid velocity. Due to the disturbance of neighboring particles, the prediction of drag force by Eq. (27) generally has a significant deviation. Therefore, the voidage fraction that is defined as the proportion of fluid is introduced to account for the flow and pressure effects from the neighboring particles, and then the drag force for dense granular systems is formulated as:

$$\mathbf{F}_D = \mathbf{F}_{D0} / (1 - \varepsilon), \quad (28)$$

where ε is the voidage fraction that will be detailedly discussed in Section 3.1 and Section 3.2.

For determining the interphase exchange coefficient β , various drag force models have been developed, and the prediction of the flow behaviors can be affected by the used drag force models. For example, Marchelli et al. [149] simulated the fluidization in a spout-fluid bed by CFD-DEM with different drag force models (including Wen and Yu [150], Gidaspow [85], Di Felice [151], Rong et al. [152], Beetstra et al. [86], Koch and Hill [153] and Tenneti et al. [154]). As illustrated in Fig. 26, the apparent differences in the fluidization behaviors of particles while using different drag force models can be observed.

Note that, however, the aforementioned drag force models are mainly used for spherical particles and cannot account for the shape effects of non-spherical particles. For non-spherical particles, the accurate prediction of drag force is more complicated because both the particle shape and orientation can significantly impact the flow field and hence the particle-fluid interaction. For example, Fig. 27 clearly illustrates the influence of particle orientation and shape (cube and spherocylinder here) on the flow field (streamlines here). For predicting the drag force of non-spherical particles, the researchers generally modify the correlations of calculating the drag coefficient C_D , and Table 2 further lists some of the general correlations for calculating the drag coefficient of non-spherical particles covering numerous shapes and orientations. According to Table 2, it can be apparently seen that some shape factors are introduced into the drag coefficient correlations to account for the shape effects, e.g., the regular sphericity ϕ that is the ratio between the surface area of the volume equivalent sphere and the surface area of the target particle, and the crosswise sphericity ϕ_{\perp} that is calculated by dividing the cross section area of the volume equivalent sphere by the projected cross section area of the real particle normal to the flow.

Using the general correlations to calculate the drag coefficient is quite convenient for evaluating the drag force of non-spherical particles, especially for granular systems containing particles with various shapes. However, the versatility of drag correlations may result in low-precision in calculating the drag force. For example, our previous investigations in modeling an isolated rod-like particle with an aspect ratio of 3 in the uniform flow by DNS (Direct Numerical Simulation) indicated that using Hölzer/Sommerfeld model [160] should lead to insufficiently accurate predictions of drag force [161], especially at low Reynolds number, as illustrated in Fig. 28. Besides the aforementioned general drag expressions, therefore, researchers have developed various drag coefficient correlations that are exclusively for the particles with fixed shapes, such as ellipsoids [162–174], cylinders [161,162,175,176], cubes [162,174,177,178], polyhedrons [179], spherocylinders [169,180] and other irregularly shaped particles [181,182]. Additionally, some researchers further introduced machine learning for more accurately correlating the shape and orientation of non-spherical particles and the flow conditions with the interaction force [182–184]. In summary, these customized correlations should provide more precise predictions, but at the expense of losing generality.

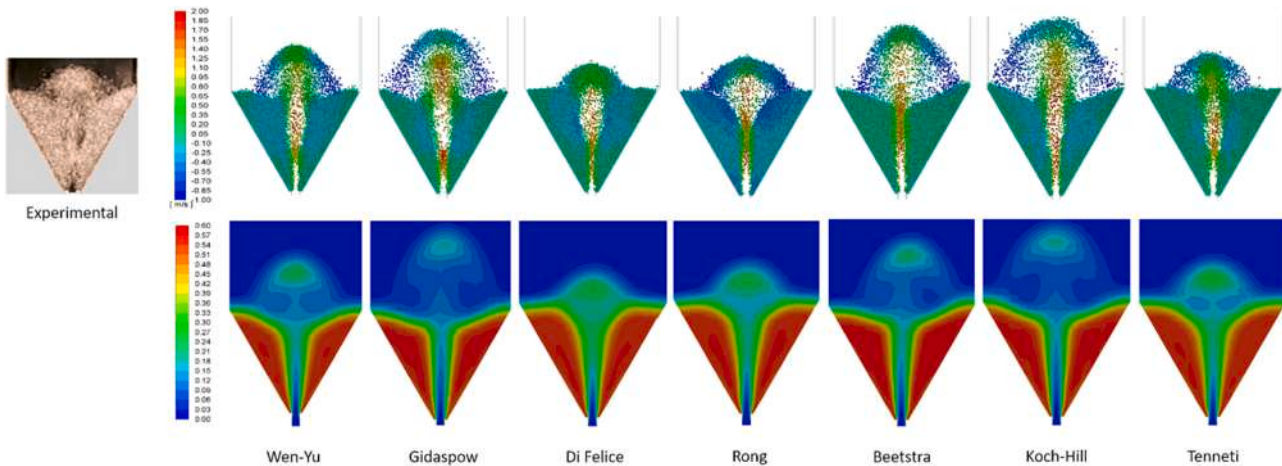


Fig. 26. Snapshots of particle behaviors (top) and time-averaged contour of the particle volume fraction (bottom) in a spout-fluid bed while using different drag force models (adapted from [149], Copyright 2019, with kind permission from Elsevier).

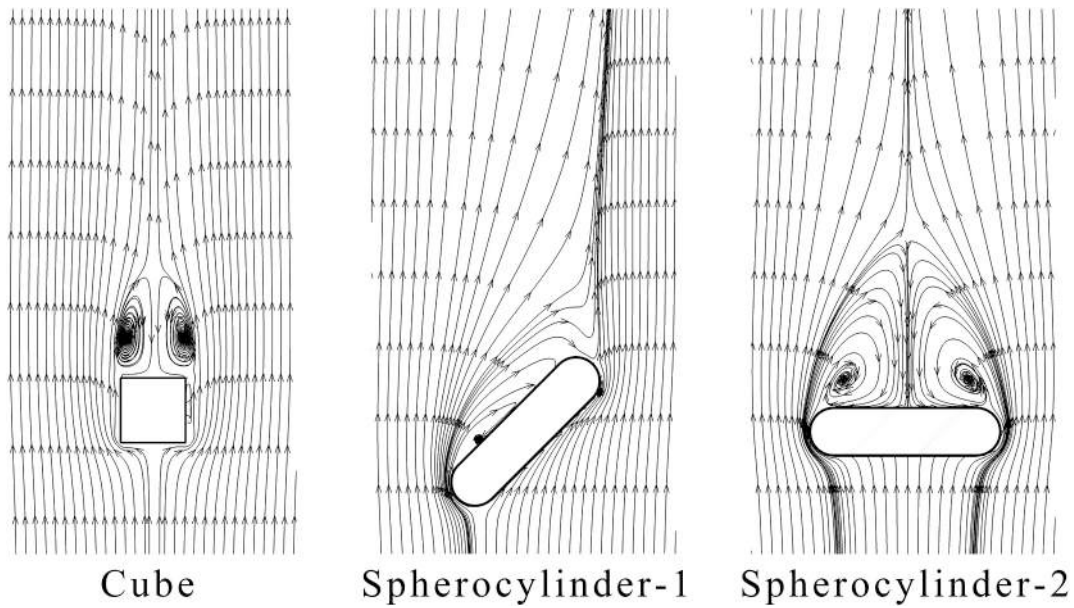


Fig. 27. Streamlines for the cube and spherocylinder with different orientations at $Re_p = 100$ (adapted from [155], Copyright 2019, with kind permission from Elsevier).

Table 2
General correlations for the drag coefficient C_D of non-spherical particles

References	Correlations
Haider and Levenspiel [156]	$C_D = 24 \left(1 + A_1 Re_p^{A_2} \right) / Re_p + A_3 / (1 + A_4 / Re_p),$ $A_1 = \exp(2.3288 - 6.4581\phi + 2.4486\phi^2),$ $A_2 = 0.0964 + 0.5565\phi$ $A_3 = \exp(4.905 - 13.8944\phi + 18.4222\phi^2 - 10.2599\phi^3)$ $A_4 = \exp(1.4681 + 12.2584\phi - 20.7322\phi^2 + 15.8855\phi^3)$
Ganser [157]	$\frac{C_D}{K_2} = \frac{24}{Re_p K_1 K_2} \left(1 + 0.1118 (Re_p K_1 K_2)^{0.6567} \right) + \frac{0.4305}{1 + 3305 / (Re_p K_1 K_2)}$ $K_1^{-1} = \frac{1}{3} + \frac{2}{3}\phi^{-0.5}, \log K_2 = 1.8148(-\log\phi)^{0.5743}, Re_p K_1 K_2 \leq 10^5$
Leith [158]	$C_D = \frac{8}{Re_p} \frac{1}{\sqrt{\phi_{\perp}}} + \frac{16}{Re_p} \frac{1}{\sqrt{\phi}}$
Tran-Cong et al. [159]	$C_D = \frac{3}{\sqrt{Re_p}} \frac{1}{\phi^{3/4}} + 0.42 \times 10^{0.4(-\log\phi)^{0.2}} \frac{1}{\phi_{\perp}}$
Hölzer and Sommerfeld [160]	$C_D = \frac{8}{Re_p} \frac{1}{\sqrt{\phi_{\perp}}} + \frac{16}{Re_p} \frac{1}{\sqrt{\phi}} + \frac{3}{\sqrt{Re_p}} \frac{1}{\phi^{3/4}} + 0.42 \times 10^{0.4(-\log\phi)^{0.2}} \frac{1}{\phi_{\perp}}$

where Re_p represents the particle Reynolds number.

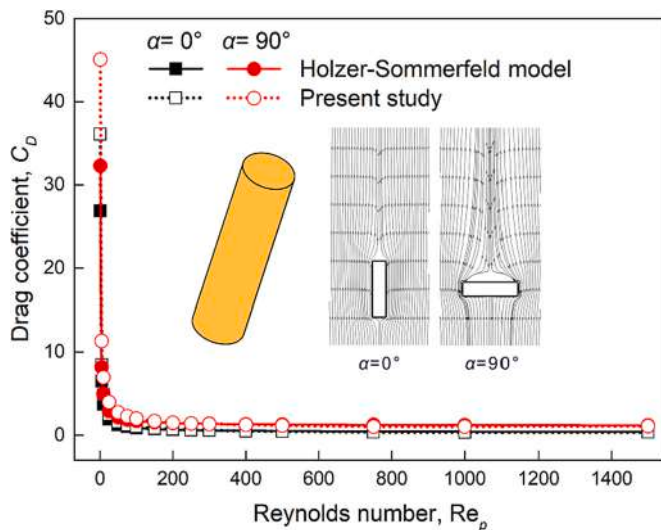


Fig. 28. Comparison of the drag coefficient for the flow over a rod-like particle with the aspect ratio of 3 (adapted from [161], Copyright 2019, with kind permission from Elsevier).

2.4.2. Lift force

The lift force mainly includes the Saffman force due to the fluid velocity gradient over a particle and the Magnus force caused by the rotational motion of particles. For a particle with a constant velocity moving, the different positions of the particle surfaces would experience different fluid velocities due to the existence of fluid velocity gradients. As a result, a pressure gradient is formed on the particle surface that a higher fluid velocity definitely leads to lower pressure. This pressure difference can drive the particles, and the corresponding resultant force is called the Saffman lift force. As for the Magnus force, the particle rotation will induce an inhomogeneous pressure distribution on the particle surface because of the difference in relative velocity between the particle surface and fluid. The resultant force due to the pressure difference is known as the Magnus force.

In comparison with spherical particles, the lift force should play a more significant role for non-spherical particles, especially for elongated particles. And there should be greater impacts for lift force with the increase of fluid velocity. In the DEM simulations, the magnitude of the lift force acting on a particle can be calculated by:

$$F_L = 0.5C_L\rho_f \frac{\pi}{4} d_p^2 |u - v|^2, \quad (29)$$

where C_L is the lift coefficient. To guarantee the lift force for a particle is properly oriented, the resultant lift force is formulated as [19,185,186]:

$$\hat{F}_L = F_L \hat{e}_L, \quad (30)$$

$$\hat{e}_L = \frac{\mathbf{n}_p \cdot \mathbf{u}_{fp}}{|\mathbf{n}_p \cdot \mathbf{u}_{fp}|} \frac{(\mathbf{n}_p \times \mathbf{u}_{fp}) \times \mathbf{u}_{fp}}{\|(\mathbf{n}_p \times \mathbf{u}_{fp}) \times \mathbf{u}_{fp}\|}, \quad (31)$$

where \mathbf{n}_p is the particle orientation vector, and \mathbf{u}_{fp} is the relative velocity of the fluid relative to the solid particle.

According to the equations listed above, the key issue for accurately calculating the lift force is to correctly evaluate the lift coefficient C_L that is closely related to the particle shape and orientation as well as the flow conditions. Therefore, various force models to calculate the lift force for non-spherical particles have been proposed [168,169,173–175,180,182], and some of them are listed in Table 3. Furthermore, the relevance of lift force for non-spherical particles has been demonstrated [185,186], and the numerical investigations of flow behaviors of non-spherical particles by CFD-DEM incorporating the lift force model can also be accessed in some recently published literatures [82,187–197].

2.4.3. Other forces

The virtual mass force is related to the fluctuation of particle velocity. The acceleration or deceleration of a particle will synchronously lead to the acceleration or deceleration of the surrounding fluid because of the cohesion to the particle surface. As a result, a wake vortex that the vorticity relies on the particle Reynolds number is generated. This additional form of resistance is referred to as the virtual mass force. The Basset force is also called the history force and is to addresses the viscosity effect of the fluid on the particle surface by the time delay in the development of the boundary layer. When a particle decelerates or accelerates relative to the fluid, the shape and volume of the boundary layer should undergo continuous changes. And the temporal delay of this development if there is a variation of the relative velocity is described by Basset force. The pressure gradient force imposing on the particle surface is relevant to the existence of a pressure gradient in the fluid that the pressure difference across the particle triggers the force acting over the volume of the particle, and it is in the opposite direction to the pressure gradient. A typical example of the pressure gradient force is the buoyancy governed by the Archimedes principle.

Table 3
Correlations of calculating the lift coefficient C_L for non-spherical particles

References	Correlations	Notes
Sanjeevi et al. [169]	$C_L = \left(\frac{a_1}{Re_p} + \frac{a_2}{Re_p^{0.25}} + \frac{a_4}{Re_p^{0.5}} \right) (\sin\alpha_L)^{1+a_6 Re_p^{0.7}} (\cos\alpha_L)^{1+a_8 Re_p^{0.9}}$	For spherocylinder and ellipsoid Valid when $0.1 \leq Re_p \leq 2000$
Zastawny et al. [180]	$C_L = \left(\frac{b_1}{Re_p^{0.5}} + \frac{b_3}{Re_p^{0.25}} \right) (\sin\alpha_L)^{b_5+b_6 Re_p^{0.7}} (\cos\alpha_L)^{b_8+b_9 Re_p^{0.10}}$	For spherocylinder and ellipsoid Valid when $0.1 \leq Re_p \leq 300$
Ouchene et al. [173]	$C_L = \left(F(w) Re_p^{0.25} + \frac{G(w)}{Re_p^{0.755}} \right) \cos\alpha_L (\sin\alpha_L)^{1.002 Re_p}$ $F(w) = 0.1944(w^{-0.93} - 1) \ln w + 0.2127(w - 1)^{0.47}$ $G(w) = 1.9183(w - 1)^{0.46} \ln w - 4.0573(w^{-1.61} - 1)$	For ellipsoid with $1 \leq w \leq 32$ Valid when $0.1 \leq Re_p \leq 240$
Cao and Tafti [175]	$C_L = \left(1.688 + \frac{6.617}{Re_p^{1.063}} \right) (\sin\alpha_L)^{0.8222} (\cos\alpha_L)^{0.9796}$	For cylinder with $w = 0.25$ Valid when $10 \leq Re_p \leq 300$
Richter and Nikrityuk [174]	$C_L = \frac{0.97}{Re_p^{0.25}} \sin(2\tilde{\alpha}_L) - \frac{0.0262}{Re_p^{0.25}} \cos(2\tilde{\alpha}_L)$ $\tilde{\alpha}_L = [(\alpha_L + 90)\text{mod}180] - 180 $	For ellipsoid with $w = 2$ Valid when $10 \leq Re_p \leq 200$
Richter and Nikrityuk [174]	$C_L = 0.0814 \sin(4\tilde{\alpha}_L)$ $\tilde{\alpha}_L = [(\alpha_L + 45)\text{mod}90] - 90 $	For cube Valid when $10 \leq Re_p \leq 200$

where α_L is the angle between the fluid velocity and particle orientation vector, the coefficients a_i and b_i are dependent on particle shape, and w denotes the particle aspect ratio.

3. Coupling scheme between CFD and DEM

For solving the fluid phase of particle-fluid systems, CFD is necessarily introduced. CFD solvers generally discretize the computational domains by the finite volume, finite difference or finite element approximations, and nonlinear flow equations, *i.e.*, the Navier-Stokes equations, are resolved with the iterative method. CFD used for solving fluid phase has made significant progress [32,198], and the related CFD models have been rather mature. At present, numerous commercial and open-source CFD software packages can be accessed easily, such as ANSYS Fluent, Siemens STAR-CCM+, OpenFOAM, MFix, etc. As mentioned above, the DEM modeling is at the individual particle scale, while the CFD solution of fluid flow is at the computational cell level. By coupling CFD and DEM, the flow behaviors of both the particles and fluid can be reasonably simulated. Since the pioneering study of Tsuji et al. [199] who firstly coupled CFD and DEM, the CFD-DEM coupling model has become a widely employed method for applications involving the interactions of the fluid and particles [10,13,14,142]. For example, numerous DEM software packages (*e.g.*, PFC, EDEM, Rocky DEM, DEMSLab and so on) provide a reliable interface for the coupling with CFD solvers (*e.g.*, ANSYS Fluent and OpenFOAM). On the other hand, some CFD software packages directly include the models based on DEM for simulating the particle phase, such as ANSYS Fluent and MFix.

Though the CFD-DEM model has solid theoretical foundations and has been extensively applied, it still has some fundamental limitations [32], *e.g.*, the treatment of complex boundaries and high parallelism capability. Besides the conventional CFD approach, therefore, some novel CFD methods (*e.g.* LBM [200] and SPH [201]) are also developed and can couple with DEM. LBM is a discrete mesoscopic approach that the Navier-Stokes equations are implicitly solved by resolving the linear kinetic gas theory equations. Therefore, the direct solutions of nonlinear partial differential Navier-Stokes equations can be avoided, which significantly simplifies the modeling process. Furthermore, the similarity of discrete nature between LBM and DEM gives them a natural superiority in coupling. As for SPH, it is an adaptive mesh free Lagrangian particle method for the simulation of fluid flow, which is markedly different from the conventional CFD using the Eulerian reference frame. Just like LBM, SPH can also replicate the fluid flow behaviors without resolving complicated Navier-Stokes equations, so that the computing procedure is greatly simplified. And the movement of fluid particles within the SPH framework also complies with Newton's laws of motion, just as the solid particles in DEM. Therefore, the practical programs of SPH and DEM possess highly consistent numerical algorithms and data

structures. Generally, the Lagrangian SPH should prevail over the conventional Eulerian CFD for simulating the fluid flow involving free liquid surface and surface tension. For example, Fig. 29 illustrates the SPH-DEM simulations of gas-liquid-particle dam break. It can be seen that the free liquid surface can be well captured by SPH.

Although the fluid flow can be resolved by different numerical solvers, the distinctions between the different particle-fluid coupling models are primarily the programming details of numerical models. In other words, whether for CFD-DEM, LBM-DEM, SPH-DEM or other particle-fluid coupling models, their coupling strategies between the fluid solver and DEM generally follow the same principle. Unless otherwise specified, therefore, the rest of this section in introducing the coupling of particle phase and fluid phase will focus on the CFD-DEM coupling model considering its employment should be the most extensive for now. The other coupling models for modeling the particle-fluid systems including LBM-DEM and SPH-DEM model also adopt the same logic frame, and the interested readers can refer to the related investigations for more details [8,32].

According to the ratio of CFD cell size ΔL to particle diameter d_p (referred to as size ratio in the following), three strategies for coupling CFD and DEM have been put forward, as illustrated in Fig. 30. As shown in Fig. 30, the size ratio is recommended to be greater than 3 for the unresolved CDE-DEM model, the size ratio is at most 1/10 of the particle diameter for the resolved CDE-DEM model, and the size ratio ranges from 1/10 to 3 for the semi-resolved CFD-DEM. Note that, however, the term "semi-resolved CFD-DEM" should be debatable to our knowledge that some researchers argued the unresolved CDE-DEM should cover the concept of semi-resolved CFD-DEM. Considering a precise definition and distinction of the above terminologies is out of the scope of this review, therefore, the semi-resolved CFD-DEM still falls into a separate category that differs from the unresolved CDE-DEM for convenience in this paper. And the details of these coupling strategies will be presented below.

3.1. Unresolved CFD-DEM model

The unresolved CFD-DEM model is also known as the particle-in-cell method based on its characteristic that one CFD cell usually contains a number of solid particles [204]. In the unresolved CFD-DEM model, the fluid flow is solved by the Navier-Stokes equations of particle-fluid multiphase coupling based on the concept of local average by incorporating the voidage fraction. Currently, two commonly used models are available, *i.e.*, Model A and Model B. These two models are mathematically equivalent but use different fluid pressure gradient terms that

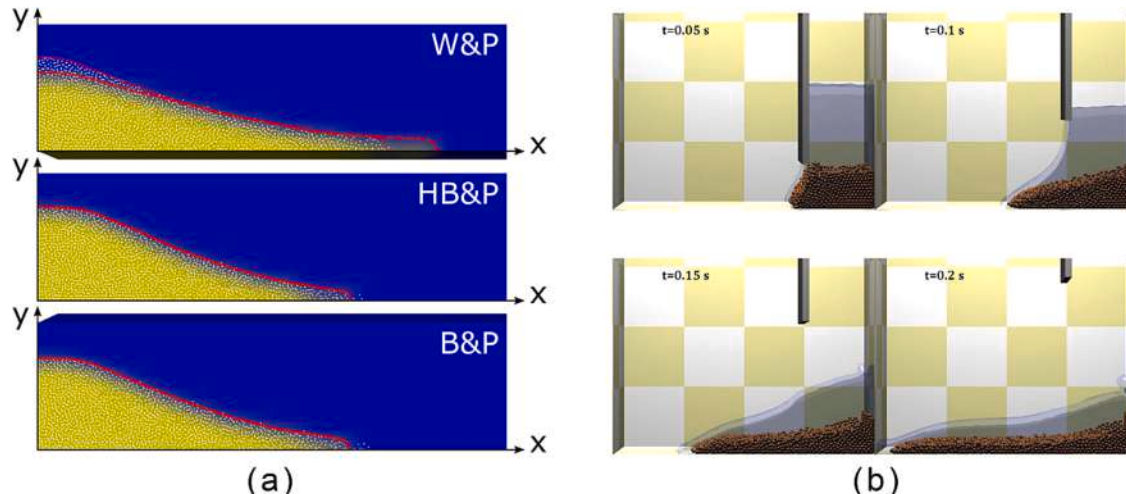


Fig. 29. Simulations of the gas-liquid-particle dam break using SPH-DEM: (a) simulated by Li and Zhao (the white dots represent the particle centers, and the yellow and blue regions are liquid and air, respectively; W, HB, B and P denote water, Herschel-Bulkley fluid, Bingham fluid and particles, respectively) (adapted from [202], Copyright 2018, with kind permission from Elsevier); (b) simulated by Sun et al. (adapted from [203], Copyright 2013, with kind permission from Elsevier).

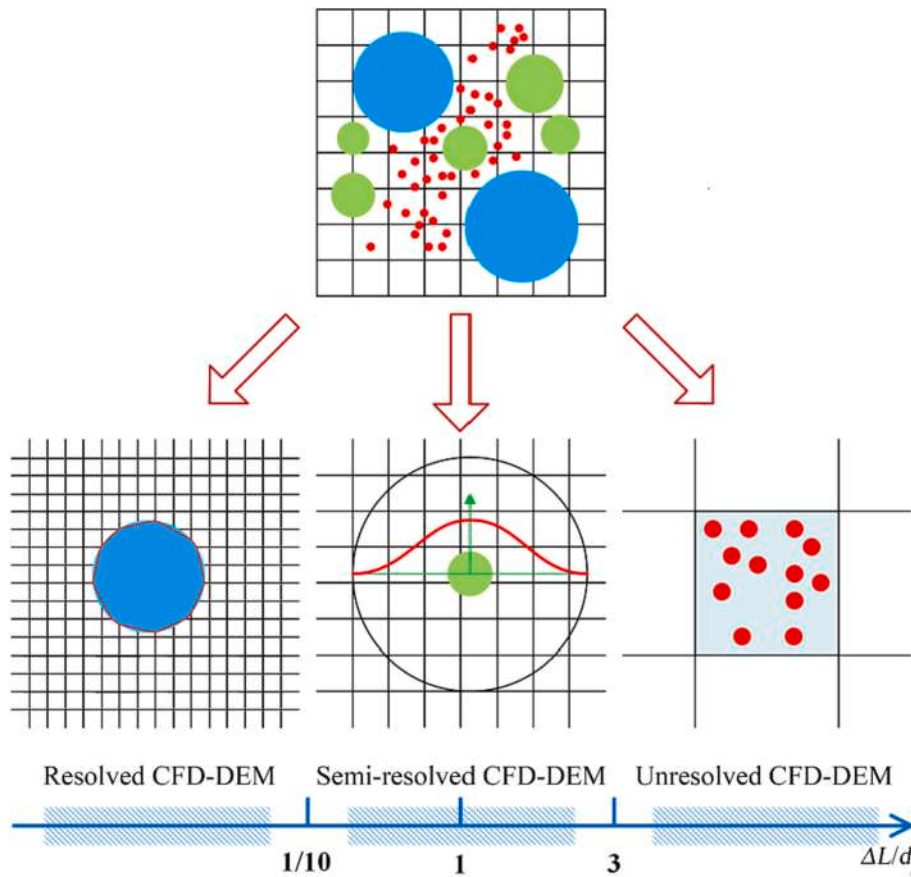


Fig. 30. Schematic illustration of the resolved CFD-DEM, semi-resolved CFD-DEM and unresolved CFD-DEM.

Model A assumes the pressure drop shares between the particle and fluid phases and Model B in the fluid phase only [13]. There are on-going debates about these two models [13]. However, this review does not intend to delve into this discussion, and only the correlations of Model B are presented here, in which the continuity equation and the momentum conservation equation are respectively formulated as:

$$\frac{\partial}{\partial t}(\epsilon\rho_f) + \frac{\partial}{\partial x_j}(\epsilon\rho_f u_j) = 0 \quad (32)$$

$$\frac{\partial}{\partial t}(\epsilon\rho_f u_i) + \frac{\partial}{\partial x_j}(\epsilon\rho_f u_j u_i) = -\frac{\partial p}{\partial x_i} + \frac{\partial}{\partial x_j} \left[\epsilon\mu_f \left(\frac{\partial u_i}{\partial x_j} + \frac{\partial u_j}{\partial x_i} \right) \right] + \mathbf{F}_s \quad (33)$$

in which u is the fluid velocity, p is the fluid pressure, x denotes the coordinates, and \mathbf{F}_s represents the source term interpreting the interaction between particle-fluid.

In the unresolved CFD-DEM model, DEM provides the particle-scale information at each time step, e.g., the velocity and position of each individual particle, for the subsequent evaluation of the voidage fraction and volumetric particle-fluid interaction force in each CFD cell. Subsequently, these data will be used by CFD to resolve the fluid flow, which then yields the particle-fluid interaction forces imposing on each individual particle. And then the motion of each individual particle for the next time step can be simulated by incorporating the resultant forces induced by fluid into DEM. Synthesizing the above process, the particle-fluid interaction is necessary to be evaluated properly for the successful coupling of CFD and DEM. Generally, the interaction between particle-fluid is characterized by the empirical force models, e.g., the drag force model and lift force model mentioned in Section 2.4. And the source term \mathbf{F}_s is the feedback force imposing on the fluid obtained by summing up the particle-fluid interaction forces acting on all particles in each control volume:

$$\mathbf{F}_s = -\frac{\sum_{i=1}^n \mathbf{F}_{pf,i}}{V_{cell}}, \quad (34)$$

where n is the total number of particles in a CFD cell, $\mathbf{F}_{pf,i}$ is the particle-fluid interaction force acting on particle i in the CFD cell, and V_{cell} is the volume of the CFD cell.

It is indisputable that the accurate calculation of particle-fluid interaction force, especially the drag force, is vital for accurately simulating particle-fluid systems by the unresolved CFD-DEM model. Taking the drag force as an example, the drag force models as discussed in Section 2.4.1 are generally related to the voidage fraction and relative velocity between particle-fluid. For the proper evaluation of voidage fraction and relative velocity, as mentioned above, the CFD cell size is recommended to be at least three times larger than the particle size, otherwise the prediction ability of the drag force models will be degraded [205,206]. Note that the threshold size ratio of 3 is more suitable for spheres, and a higher size ratio might be used for non-spherical particles [204].

According to the above discussions, one of the key steps while using the unresolved CFD-DEM model is to accurately evaluate the voidage fraction due to its important role played in determining the drag force and solving the local averaged Navier-Stokes equations. Traditionally, the particle is considered as entirely included in the fluid cell while the particle is mapped into the corresponding CFD cell just as shown in Fig. 31(a), i.e., this voidage fraction scheme is formulated by:

$$\epsilon = 1 - \frac{\sum_{i=1}^n V_{p,i}}{V_{cell}}, \quad (35)$$

in which $V_{p,i}$ is the volume of particle i within the CFD cell. Due to the

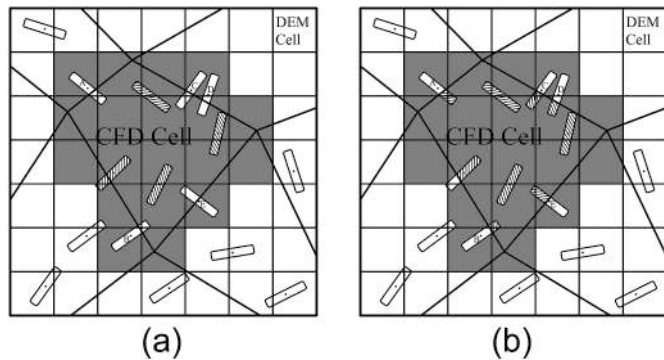


Fig. 31. Sketch map of calculating the voidage fraction: (a) PCM and (b) the improved method (adapted from [207], Copyright 2018, with kind permission from Elsevier).

characteristics of this scheme, it is generally known as the particle centroid method (PCM). PCM is computationally inexpensive as only particle centroid host cell is required to search. However, the use of PCM may result in large errors of calculating the voidage fraction, especially when the cell size to particle size ratio is relatively small. As illustrated in Fig. 31(a), PCM would include the total volume of the particles marked by oblique lines to calculate the voidage fraction of the CFD cell. In effect, part of the volume of Particles A, B, C, D and E should be theoretically included, which is completely ignored in PCM. On the other hand, some of the particles entirely belonging to the CFD cell should be shared by two or more CFD cells. In addition, the above drawback of PCM will also cause the jump of the voidage fraction as the particles cross the CFD cells, which may reduce the smoothness in the voidage fraction field. And generally, the derivative of voidage fraction in the local averaged Navier-Stokes equations requires the smooth field of voidage fraction to guarantee the robustness and accuracy of resolving the particle-fluid flow behaviors [10,208]. Synthesizing the above, PCM needs to be improved for the rational evaluation of voidage fraction just as shown in Fig. 31(b), and Eq. (35) should be changed to:

$$\varepsilon = 1 - \frac{\sum_{i=1}^n \zeta_{p,i} V_{p,i}}{V_{cell}}, \quad (36)$$

where $\zeta_{p,i}$ is the spatial weight representing the volume fraction of particle i .

Some attempts have been made toward the analytical calculation of voidage fraction [205,209–211]. However, these analytical methods are usually only practicable for spherical (or circular in 2D) particles and structured CFD meshes (e.g., the cube cells), as shown in Fig. 32. And the implementation of the analytical method for non-spherical particles and unstructured CFD cells (e.g., Fig. 31(a)), which should be the most commonly encountered in practical problems, will become extremely difficult or even impossible [208]. Therefore, various alternative non-analytical methods have been put forward, and the details of some methods based on the divided concept will be presented below.

A rather straightforward way is using the sphere-based model that the particles are constructed by connecting a certain number of sub-spheres with small overlap [187,213,214], which can be considered as that the particle is divided into several spherical entities. The calculation of particle-fluid interaction force is based on each individual sub-sphere, as illustrated in Fig. 33(a). Subsequently, two different concepts respectively based on the bonded-sphere model [187,213] and the multi-sphere model [214] are used for determining the following particle motions. Specifically, the forces will be imposed on each sub-sphere in the bonded-sphere principle, whereas the force will be summed and then applied to the mass center of the particle in the multi-sphere principle.

In the so-called “divided particle volume method” [211,212,215], in which the shape of the particle is approximated by some simple geometric approach (such as a cube) and then the portions of the volume of the particle are assigned to several nearby fluid cells. Fig. 33(b) sketches the principle of the “satellite point method” [212,215,216]. In this method, the particle i is divided into $N_{total,i}$ smaller entities. Then the center of each entity inside the particle i and CFD cell j can be identified for obtaining the number of centroids $N_{i,j}$. Thus the voidage fraction can be subsequently determined by defining the spatial weight $\zeta_{p,i}$ as:

$$\zeta_{p,i} = N_{i,j} / N_{total,i}, \quad (37)$$

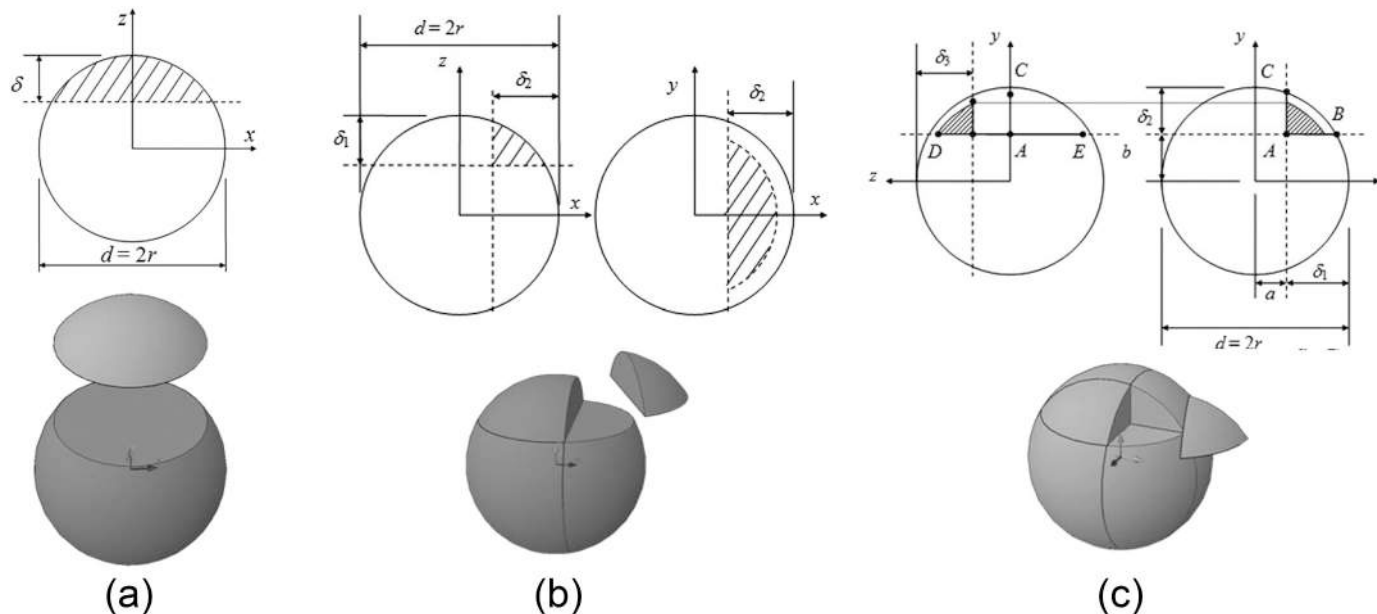


Fig. 32. Sketch map of the analytic method in calculating the voidage fraction: (a) the sphere intersecting with a single bin face, (b) the sphere intersecting with two faces and an edge and (c) the sphere intersecting with three faces and a corner (adapted from [209], Copyright 2010, with kind permission from American Institute of Chemical Engineers).

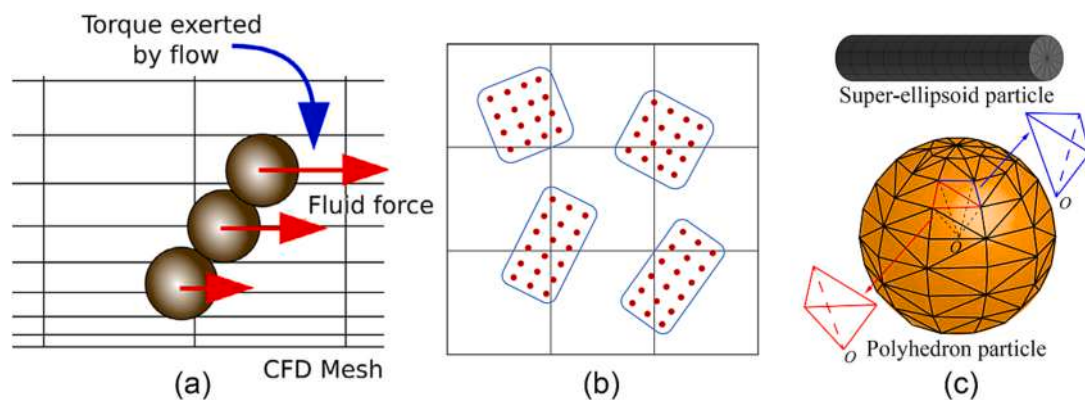


Fig. 33. Sketch map of the non-analytic method in calculating the voidage fraction: (a) the calculation based on sphere-based particle model (adapted from [187], Copyright 2017, with kind permission from Elsevier); (b) satellite point method (adapted from [212], Copyright 2022, with kind permission from Elsevier); (c) the calculation for super-ellipsoid particle and polyhedron particle (adapted from [118,207] with kind permissions from Multidisciplinary Digital Publishing Institute (Copyright 2021) and Elsevier (Copyright 2018).

In our previous investigations, we also proposed the methods similar to the satellite point method for particles described by the super-ellipsoid model and polyhedron model [118,207], as illustrated in Fig. 31(b). For the super-ellipsoid model, the particle is equally divided into 12 parts along both the axial and circumference directions, namely 144 smaller entities are created inside the particle [207]; for the polyhedron model, the particle surface is constructed by a certain number of triangular planes, and several smaller tetrahedron entities can be then obtained by connecting the particle mass center with triangular planes [118]. Subsequently, these smaller entities rather than the entire super-ellipsoid particle or polyhedron particle are used to evaluate the voidage fraction. Apparently, a smoother and more accurate porosity could be obtained as the particles being divided more small entities (*i.e.*, higher division accuracy of the particles) for the above methods. However, the influence of further increasing the division accuracy might be weakened as the number of small entities being rather high. Meanwhile, this should consume more computing resources. Therefore, a suitable number of small entities should be used in CFD-DEM simulations.

By the above non-analytical method, the calculation accuracy of the voidage fraction should be improved, and a smoother voidage fraction field can be obtained. For example, Fig. 34 presents the comparisons of solid fraction (equal to one minus the voidage fraction) filed while using different methods in our previous CFD-DEM investigations involving the

fluidization of rod-like particles in a fluidized bed with immersed tube [207], in which both PCM and the improved method devised for super-ellipsoid particles mentioned above were used to determine the voidage fraction. It can be clearly seen that the improved method can obtain a smoother voidage fraction. For instance, the local solid fraction calculated by PCM reaches up to 0.8 while the solid fraction using the improved method is no more than 0.6. As an aside, other methods for more reasonably calculating the voidage fraction, such as the statistical kernel method [215,217] and Monte Carlo method [218], can also be accessed in the published literatures, and the interested readers can refer to the related investigations.

Synthesizing the above, the unresolved CFD-DEM model does not resolve the particle boundary, and hence it has a superior computational convenience in modeling particle-fluid systems. It is precisely because of the above reasons, the model used in the majority of the current CFD-DEM investigations is the unresolved CFD-DEM model [7,10,13,14], especially for the particle-fluid systems containing a large number of particles. And this is also the focus while reviewing the applications of CFD-DEM in Section 4. Therefore, the unresolved CFD-DEM is referred to simply as CFD-DEM for convenience in the following, unless otherwise specified.

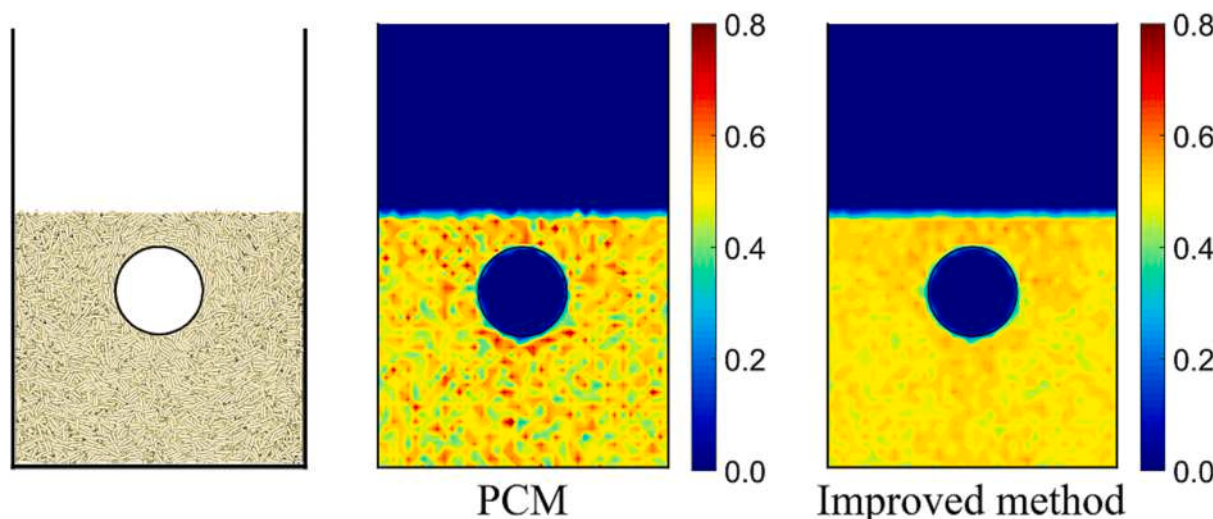


Fig. 34. Solid fraction fields calculated by PCM and the improved method developed for super-ellipsoid particles (adapted from [207], Copyright 2018, with kind permission from Elsevier).

3.2. Semi-resolved CFD-DEM model

As mentioned above, it remains a gap between the resolved fashion and the unresolved fashion when the grid size is comparable to or somewhat smaller than the particle size, which conflicts with the requirement of unresolved CFD-DEM that the grid size should be larger enough to represent the local voidage and the demand of resolved CFD-DEM because of the insufficient grid refinement. In this case, if the unresolved method is still used, some cells will have unrealistically magnitudes of voidage fractions, and the quite sharp changes in the voidage fraction field across the cells will appear when the particles cross the cell boundaries. Consequently, the drag force evaluated from empirical correlations will be unbounded and the solution of Navier-Stokes equations tends to be singular, resulting in the reduced accuracy and robustness of the numerical integration, even more, the crash of the calculation. A feasible solution to release this dilemma is to adopt the aforementioned semi-resolved CFD-DEM model. As the name implies, the semi-resolved CFD-DEM is the intermediate between the resolved CFD-DEM and unresolved CFD-DEM. In essence, the main concept of semi-resolved CFD-DEM is the same as that of the unresolved CFD-DEM, but the fluid domain used to determine the voidage fraction and background fluid velocity is expanded from the local cell to the neighboring cells to break through the limit of grid size in unresolved CFD-DEM.

For the calculation of cell voidage and background velocity, there are three methods in the framework of semi-resolved fashion, including the two-grid method [219], kernel-based method [206] and diffusion-based method [220]. In the two-grid method, two separate grids are taken into account that the fine grids (*i.e.*, the fluid grids) are used to calculate the fluid dynamics, and the coarse grids (referred to as the particle grids) composed of multiple fine grid cells are used to determine the voidage and background velocity, as shown in Fig. 35. The fluid velocities calculated on the fluid cells are averaged over the particle grid cell, and this averaged velocity serves as the background velocity used to calculate the drag force exerting on each particle in this particle cell. Specifically, the voidage fraction is calculated on the particle grid cell as follows:

$$\epsilon = 1 - \frac{\sum_{i=1}^n V_{p,i}}{V_{pg}}, \quad (38)$$

where V_{pg} is the volume of the particle grid cell. Once the voidage fraction in the particle grid cell is calculated, the simplest way to

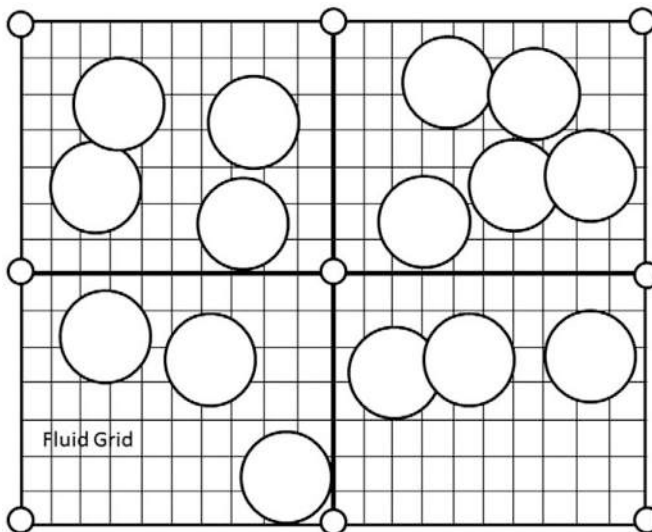


Fig. 35. Illustration of the fine grid and coarse grid in two-grid method (adapted from [219], Copyright 2013, with kind permission from Elsevier).

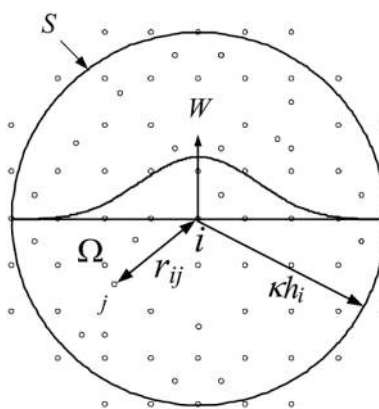


Fig. 36. Schematic of the kernel-based method (adapted from [206], Copyright 2019, with kind permission from Elsevier).

determine the voidage fraction in the fluid cells is by mapping the same magnitude of voidage to all fluid cells located in this particle grid cell, *i.e.*, $\epsilon_{fluid_cell} = \epsilon$.

In terms of the kernel-based method (see Fig. 36), the background velocity is estimated in the support region (*i.e.*, the circle in this figure) by using a kernel-based approximation. Specifically, a kernel function W is adopted to calculate the velocity at point i using the weighted sum over point j within the support region with a cut-off distance of kh_i (k is a scale factor depending on the specific kernel function, and h is the initial point spacing). Therefore, the background velocity, *i.e.*, the velocity at point i , can be calculated by:

$$\mathbf{u} = \frac{\sum_{j=1}^N \mathbf{u}(\mathbf{r}_j) W(\mathbf{r}_i - \mathbf{r}_j, h) \Delta V_j}{\sum_{j=1}^N W(\mathbf{r}_i - \mathbf{r}_j, h) \Delta V_j}, \quad (39)$$

where j is the index of the fluid cell with the volume of ΔV_j , and \mathbf{r}_i and \mathbf{r}_j are the position vectors of point i and point j , respectively. A frequently used kernel function is Gaussian kernel, written as:

$$W(\mathbf{r}_i - \mathbf{r}_j, h) = \exp \left[-\frac{|\mathbf{r}_i - \mathbf{r}_j|^2}{2(kh)^2} \right], \quad (40)$$

where h is usually taken as the diameter of the particle. Note that the support region in the kernel-based method is a circular or spherical region, and the diameter of which is determined by the specific value of k . Once the background velocity is calculated, the corrected relative velocity is written as:

$$\mathbf{u}_r = \mathbf{u}_p - \mathbf{u} = \mathbf{u}_p - \frac{\sum_{j=1}^N \mathbf{u}(\mathbf{r}_j) \exp \left[-|\mathbf{r}_i - \mathbf{r}_j|^2 / 2(kh)^2 \right] \Delta V_j}{\sum_{j=1}^N \exp \left[-|\mathbf{r}_i - \mathbf{r}_j|^2 / 2(kh)^2 \right] \Delta V_j}, \quad (41)$$

Similarly, the corrected voidage is calculated in the support region, given as:

$$\epsilon = 1 - \frac{\sum V_{p,i}}{\sum V_{c,j}}, \quad (42)$$

where $V_{c,j}$ is the volume of the fluid cell j within the support region. Note that, just like in this semi-resolved CFD-DEM model, the kernel function is also used in SPH to serve as weight allocation. However, there are mainly two differences between SPH and semi-resolved CFD-DEM. Firstly, the kernel function in SPH embodies the influence of surrounding elements on the target element while the kernel function in semi-resolved CFD-DEM reflects how the target element affects surrounding elements. Secondly, the smoothing length in SPH is variable, where the smoothing length can be the function of time and space. In

semi-resolved CFD-DEM, the smoothing length is constant, usually 2-3 times the size of the particle diameter.

In the diffusion-based method, a homogeneous diffusion equation for a period of pseudo-time is solved to smooth the coarse voidage field calculated by PCM. The diffusion equation for $\varepsilon(x, \tau)$ can be written as:

$$\frac{\partial \varepsilon}{\partial \tau} = \nabla^2 \varepsilon, \tau > 0, \quad (43)$$

$$\varepsilon(x, 0) = \varepsilon_0(x), \quad (44)$$

where x is the spatial coordinates, τ is the pseudo-time, and ε_0 is the coarse voidage field. Note that the derivation above is also valid for fluid velocity. The diffusion equation is independently solved for each fluid cell, and the final result is the superposition of each component, as illustrated in Fig. 37.

When the particle-fluid systems contain non-spherical particles, especially for particles with an extreme aspect ratio, the kernel-based method should possess insufficient accuracy to describe the actual fluid field around the particles, since the support region is circular or spherical with a diameter of $k d$. As depicted in Fig. 38, Particles C1, C2 and C3 are completely covered by their support regions, whereas Particles C4, C5 and C6 are partly beyond the support regions. Therefore, the corrected background velocity and voidage fraction obtained from the support region fail to consider the fluid information at both ends of Particles C4, C5 and C6. To alleviate this issue, a particle shape enlargement method is proposed [204]. As shown in Fig. 39, the support region is defined by the enlarged particle shape with a scale factor k , instead of the circular or spherical region with a diameter of $k d$. Based on this method, the background velocity is calculated as:

$$\mathbf{u} = \frac{\sum_{j=1}^N \mathbf{u}(r_j) \exp \left[-|r_i - r_j|^2 / 2(kR_\perp)^2 \right] \Delta V_j}{\sum_{j=1}^N \exp \left[-|r_i - r_j|^2 / 2(kR_\perp)^2 \right] \Delta V_j}, \quad (45)$$

where R_\perp is the local radius of the particle in the direction of $r_i - r_j$ just as shown in Fig. 39. The corrected relative velocity can be written as:

$$\mathbf{u}_r = \mathbf{u}_p - \mathbf{u} = \mathbf{u}_p - \frac{\sum_{j=1}^N \mathbf{u}(r_j) \exp \left[-|r_i - r_j|^2 / 2(kR_\perp)^2 \right] \Delta V_j}{\sum_{j=1}^N \exp \left[-|r_i - r_j|^2 / 2(kR_\perp)^2 \right] \Delta V_j}, \quad (46)$$

3.3. Resolved CFD-DEM model

In contrast to the unresolved and semi-resolved CFD-DEM models using the empirical interaction force model, the particle-fluid interaction force in the resolved CFD-DEM model is generally determined by the exact particle-fluid interaction process along the boundary surface of the particle. The resolved CFD-DEM method is theoretically appropriate for arbitrary particle shapes to determine the interaction between a particle and the surrounding fluids. For the sake of accurately resolving particle boundary, a very fine CFD cell is required that the CFD cell size should be at most 1/10 of the particle size guaranteeing the numerical

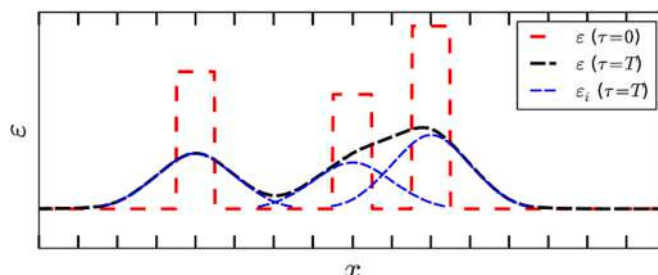


Fig. 37. Solution to the diffusion equation with an initial condition $v(\tau = 0)$ (adapted from [220], Copyright 2015, with kind permission from Elsevier).

error to be less than 1% [221]. Since the CFD cell size is much smaller than the particle size in the resolved model, the fluid flow can be fully resolved on the whole boundary surface of the particle that the detailed flow field around the particle can be effortlessly determined just as shown in Fig. 40, and the particle-fluid interaction force imposing on the particle can be calculated simultaneously. Based on the above discussions, the resolved CFD-DEM method should be exactly in the category of the DNS method. And the governing equations of solving fluid flow in the resolved model can be regarded as the simplified version of Eqs. (32) and (33) that the term of voidage fraction ε is removed. For the source term F_s in Eq. (33), whether to remove it depends on the used fluid-structure interaction model in processing the solid particles. For example, the source term F_s will be retained while using immersed boundary method.

In order to implement the resolved CFD-DEM simulations, the high quality of CFD mesh should be desired for the fast and stable convergence of numerical solutions. Because of the complicity of contact between particle-particle or particle-wall, however, there are some difficulties in discretizing the fluid domain, particularly for dense granular systems. In other words, the contacts should pose a great challenge for simulations. In the vicinity of the contact regions, the inferior CFD cells (e.g., large skewness, low aspect ratio, etc.) are always created and hence resulting in the divergences of numerical solutions [223,224]. Unlike the ideal spherical particles with only including point contacts, the line and area contacts are also involved for non-spherical particles just as shown in Fig. 41(a), which further increases the complexity of the meshing process [223,225].

For meshing the fluid domain close to the contact regions with high quality, the contact modification methods including global modifications and local modifications have been devised, as illustrated in Fig. 41. In the global modifications, all particles are either expanded [228] or shrunk [229] by a certain amount of size, and hence leading to overlaps and gaps between particles, respectively. However, the global modification would cause a drastic change in the porosity and structure of the granular bed, and then the transport phenomena are significantly impacted. Therefore, the local modifications including necks [230], bridges [231] and caps [227] are further devised by changing the bed structure only near the contact regions. Specifically, both the necks and bridges methods introduce a cylinder replacing the fluid to link the neighboring particles, and the caps method will flatten the particle surfaces in the vicinity of the contacting point so that a gap filled with fluid cells with a specified width is formed. The distinct difference between the necks and bridges is that the cylinders are regarded as part of the packing with the same thermal properties as the necks, whereas the bridges are treated as separate regions with assuming different thermal properties. Due to the superiority of local modifications in discretizing the fluid domain, it has been extended to non-spherical particles (see Fig. 41(b) of the schematic of bridges for cylinders), and the related simulations for the solid-fluid systems involving non-spherical particles have been successfully carried out [183,223,225,226], as illustrated in Fig. 42.

Note that the above contact modification methods were originally proposed for pure CFD solutions of solid-fluid systems. In other words, CFD and DEM are decoupled that DEM is normally applied to generate the particle bed, and the CFD simulations are subsequently carried out based on the generated structure of the particle bed, where the solid particles are regarded as the solid boundaries in the fluid domain. But apparently, these contact modification methods can be reasonably incorporated into the resolved CFD-DEM model for meshing the fluid domain, especially for dense granular systems where the particle contacts occur rather frequently.

For dynamic granular systems, however, using the aforementioned contact modification methods will involve the frequent update of the CFD mesh, which should significantly deteriorate the computational efficiency. Therefore, the resolved CFD-DEM model based on the contact modification methods should be more applicable to static granular

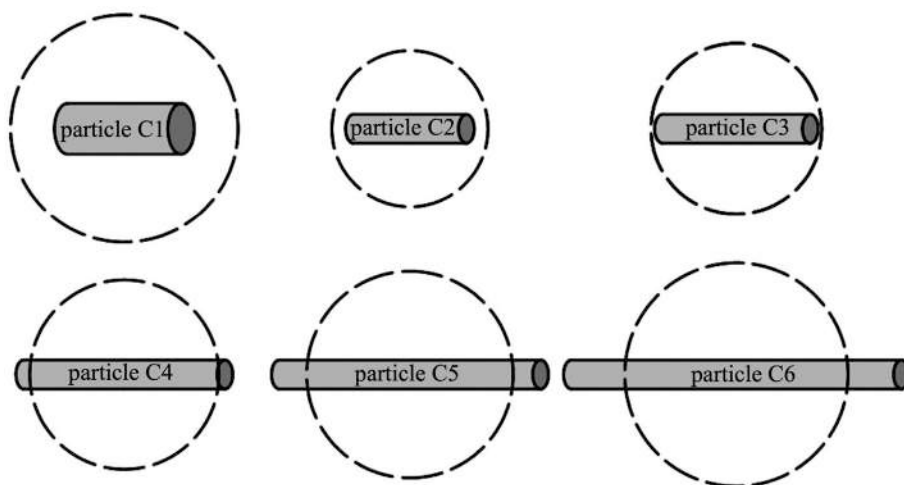


Fig. 38. Non-spherical particles with different aspect ratios and the associated support regions (indicated by the dashed lines) (adapted from [204], Copyright 2021, with kind permission from Elsevier).

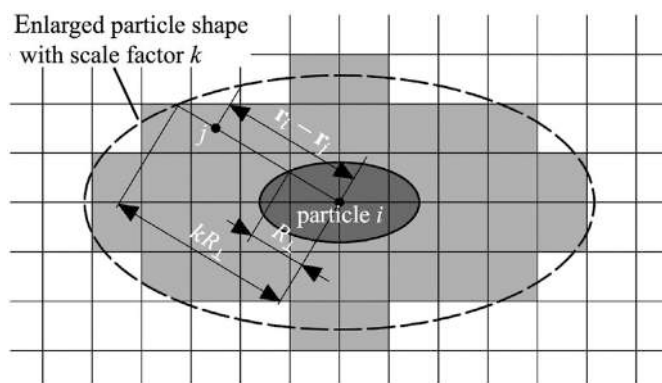


Fig. 39. Illustration of the virtual fluid domain created by the particle shape enlargement method (adapted from [204], Copyright 2021, with kind permission from Elsevier).

systems (e.g., the packed bed) to avoid the remeshing of the CFD domain. As an alternative, IBM (Immersed Boundary Method) [232,233] can be integrated into the resolved CFD-DEM model for simulating the dynamic granular systems. The principle of IBM is to approximate the solid boundary by a certain number of uniformly distributed marker points on the boundary surface that impacts the fluid flow via the force field, as illustrated in Fig. 43. In IBM, the solid boundary is mimicked by incorporating the source term into the Navier-Stokes equations, *i.e.*, the force source term F_s in Eq. (33). Specifically, the mathematical basis of IBM is a Lagrangian system and an Eulerian system [200]. As shown in Fig. 43, the Lagrangian system is an ensemble of marked points distributed rather uniformly on the boundary surface (the solid circles in the figure); the Eulerian system is denoted by an ensemble of fixed grids (the hollow circles in the figure) where the fluid lives and the Navier-Stokes equations are resolved. The solution of the solid-fluid interactions can be therefore transformed into the determination of interactions between the Lagrangian and Eulerian points. In effect, there is not real solid boundary while using IBM, and the fluid exists on both sides of the IBM boundary surface that the solid particles processed by IBM are also filled with fluid. Therefore, the time-consuming remeshing process of the computational domain can be avoided by incorporating the IBM into the resolved CFD-DEM model for the simulation of dynamic granular systems [218,234,235].

The resolved CFD-DEM approach should be theoretically deemed to be the most precise way and might be the only theoretical tool capable of

investigating the non-linear complicated phenomena of particle-fluid systems [10,236]. But it is clear that the computational cost of resolved CFD-DEM model is very expensive due to the huge number of CFD cells. Synthesizing the above, the resolved CFD-DEM model should be more applicable to the particle-fluid systems involving no more than a few hundred of particles and to the fundamental investigations of multi-phase flow as well as multi-physical field, *e.g.*, for deriving the empirical drag force model for non-spherical particles with higher prediction accuracy.

4. Applications of the non-spherical CFD-DEM

In this section, an effort is made to collect and then review the related literatures published in recent years for the applications of non-spherical CFD-DEM. Note that, the focus of this review is on the non-spherical CFD-DEM rather than on a specific application, so the CFD-DEM investigations in different areas are reviewed in the following. Specifically, we will illustratively review the fluidization, particle transport and particle separation in the following. Besides these three application areas, additionally, other applications relevant to the non-spherical CFD-DEM investigations will also be reviewed in this section. At the end of each sub-section, a brief summary for the corresponding applications is also provided. We hope this section can play a role in the research field of CFD-DEM to some degree that can help researchers quickly find the related applications or the use of non-spherical CFD-DEM in a certain application area. In addition, due to the flourish of related studies, this section does not intend to present the detailed introductions for the majority of investigations, and generally only some concise statements are presented.

4.1. Fluidization

Fluidization technology is one of the most important and extensively-used technologies in industry because of its excellent mass and heat transfer characteristics, high fluid and solids throughput and continuous powder handling ability [21]. Therefore, numerically investigating the fluidization of non-spherical particles (*e.g.*, in the packed bed, bubbling fluidized bed, spout-fluid bed, etc.) by CFD-DEM has been gradually popular in recent years for a deeper understanding of fluidization properties and then for the control, design and optimization of related industrial processes.

Various scholars have successfully developed the CFD-DEM model for investigating the fluidization behaviors of particles with different shapes in different types of the fluidized bed. For example, we carried

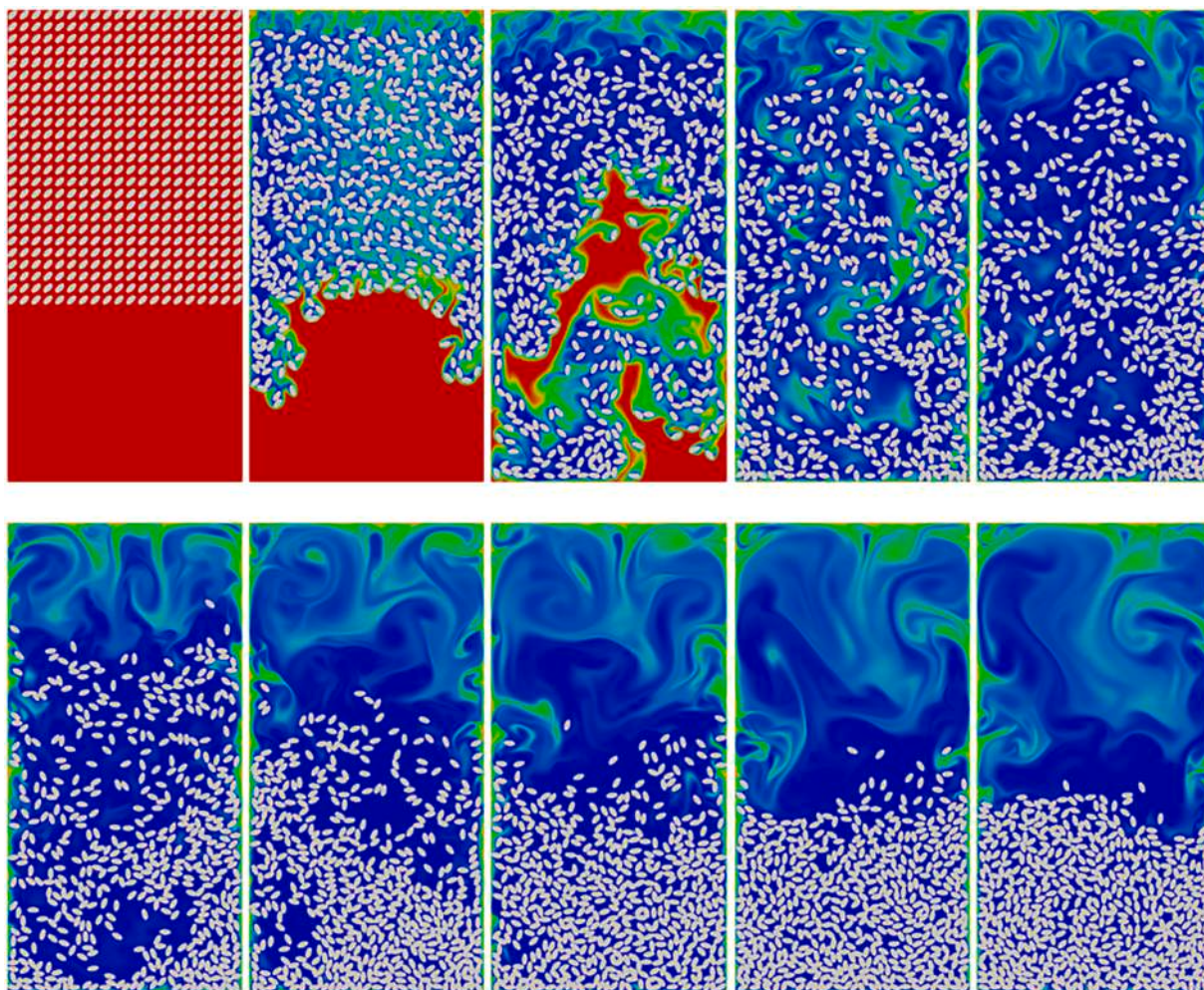


Fig. 40. Simulations of the suspension of settling elliptic particles by the resolved CFD-DEM (adapted from [222], Copyright 2019, with kind permission from Elsevier).

out a series of numerical investigations for the fluidization of cylindrical particles (rod-like and disk-like particles) in the bubbling fluidized bed by our self-developed CFD-DEM model [99,148,237,238], where the super-ellipsoid model for describing non-spherical particles and a modified method for the coupling between DEM and CFD with the unstructured mesh were incorporated [207]. As shown in Figs. 44(a) and (b), the influence of aspect ratio on the fluidization of particles (including rod-like particles with aspect ratio from 1 to 6 and disk-like particles with aspect ratio from 1/10 to 1) was investigated [99,148]. The simulation results indicated that as the aspect ratio closer to 1, both the rod-like and disk-like particles possessed smaller minimum fluidization velocity, more violent fluidization behaviors and higher particle mixing rate for rod-like particles as well as higher mixing degree in the horizontal direction for disk-like particles. The wall effect on particle orientation could be apparently observed that in the vicinity of the walls, the longest axis of rod-like particles with a larger aspect ratio was more prone to be parallel to the vertical direction, and the cross section of disk-like particles with smaller aspect ratio had more tendency to be parallel to the wall. Farivar et al. [239] also found apparent phenomena of wall effect while investigating the fluidization of rod-like multi-sphere particles in a bubbling fluidized bed by CFD-DEM. In the investigation carried out by Nan et al. [240], where the fluidization of rod-like multi-sphere particles in a bubbling fluidized bed was simulated, the effects of the particle aspect ratio on the fluidizations behaviors (e.g., the minimum fluidization velocity, flow pattern and particle orientation) were also discussed in detail.

As for the fluidization behaviors of cylindrical particles in a spout-fluid bed, our previous CFD-DEM investigation for rod-like particles indicated that both increasing fluidization gas velocity and spout gas velocity could be conducive to particle mixing, but the fluidization gas velocity should have a greater influence [238]. As the aspect ratio of rod-like particles increased, the particle mixing degree firstly decreased and then increased, and the particles possessed more consistent particle orientation. Liu et al. [241] also numerically investigated the flow characteristics of cylindrical particles with the aspect ratio changing from 0.25 to 3.0 in a spout-fluid bed. They found that the distributions of particle orientation were different in different regions of the spout-fluid bed that the particles inclined to align their larger dimension to be parallel to the flow direction in the spout region while the orientation tendency was contrary in the annulus region. Furthermore, such a difference in particle orientation would be more obvious for cylinders with longer or flatter shapes. The shape effects of cylindrical particles (including long rod-like particles and short disk-like particles) on bubble dynamics in both the spout-fluid bed and the bubbling fluidized bed were investigated by Shrestha et al. [242]. According to simulation results, the bubble size, shape and velocity exhibited a significant difference for short and long cylinders compared to spheres.

In our previous investigation about the fluidization of the binary mixtures containing rod-like particles representing the biomass and spherical particles representing bed materials (see Fig. 44(c)) [237], the mixing rate between the rods and spheres would be accelerated with the increase of superficial velocity and the decrease of the volume fraction

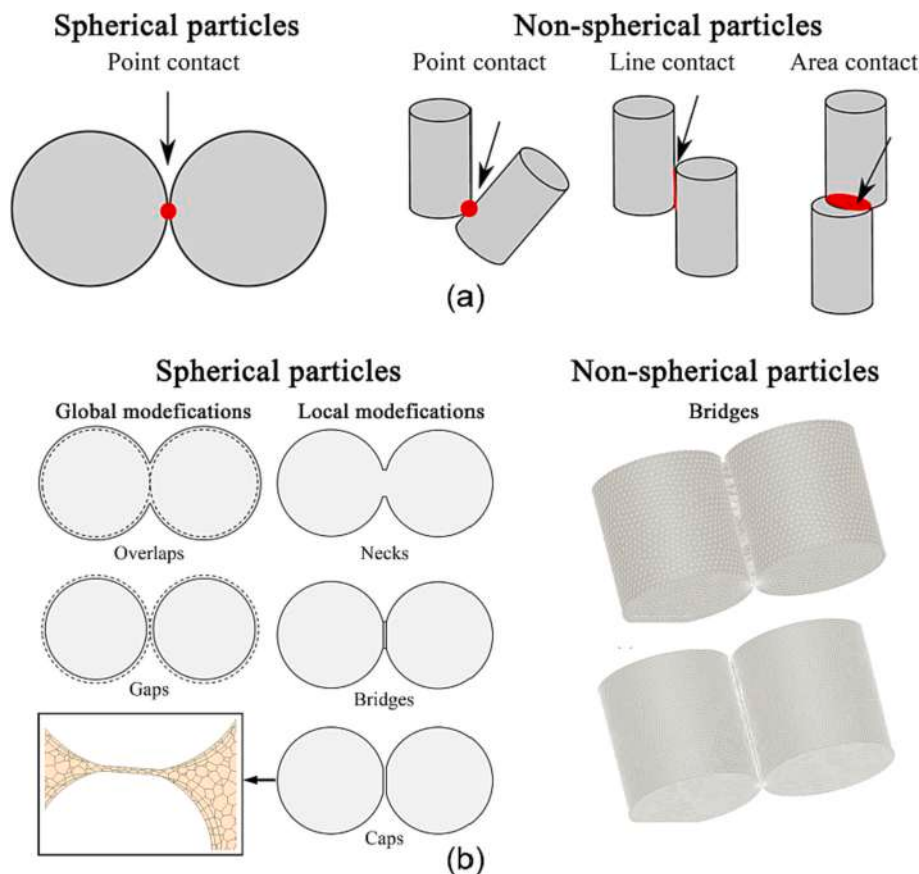


Fig. 41. Contact problems related to the discretization of the fluid domain by fine CFD cells: (a) the sketch of contact modes (adapted from [223], Copyright 2017, with kind permission from American Chemical Society); (b) the schematic of contact modification method (adapted from [224,226,227] with kind permissions from Elsevier (Copyright 2020), Elsevier (Copyright 2010) and Elsevier (Copyright 2017)).

of the rod-like particles. In comparison with the monodisperse rod-like particle system, the longest axis of rod-like particles preferred to be in vertical direction in the binary granular systems. And the apparent wall effect on the orientation of rod-like particles could also be observed. In the work of Wang et al. [243], they also focused on the mixing behaviors of binary particle systems containing spherical and rod-like particles in a bubbling fluidized bed. They found that there was a higher mixing degree with minor density difference between particles, and the larger size of rod-like particles should suppress the mixing. Besides the hydrodynamics behaviors, Zhong et al. [244–248] also comprehensively explored the thermodynamics characteristics of binary mixtures containing cylindrical biomass particles and spherical sand (or coal) particles in a bubbling fluidized bed, where the cylinders were approximated by multi-sphere model. Based on the research results, the addition of cylindrical particles should go against particle mixing. For thermodynamics behaviors, the temperature of cylindrical particles was generally lower than that of the spherical particles, and the temperature drop rate for cylinders was slower compared with the spheres.

For the fluidization of spherocylindrical particles, Padding et al. [185,186,197,249,250] carried out a series of numerical CFD-DEM investigations. They found that the spherocylindrical particles were prone to interlocking behaviors, and the spherocylindrical particles possessed higher mixing degree and mixing rate in comparison with the spherical particles. Moreover, the impacts of lift force and hydrodynamic torque on the fluidization behaviors were also explored that their influences for spherocylindrical particles cannot be ignored. Specifically, the lift force would greatly affect the particle velocities parallel to the direction of gravity, and the particle orientation was closely related to hydrodynamic torque. Esgandari et al. [251] reported a similar research for spherical and elongated spherocylindrical particles with an aspect ratio

of 4 but in a spout-fluid bed. According to the comparison results, the spherocylindrical particles had larger bubble size, lower leakage fraction of the bubble, lower solid circulation rate, smaller spout diameter and lower probability of particles transition into the spout in comparison with the spherical particles. During the spouting process, the spherocylindrical particles preferred to orient nearly perpendicularly against the fluid velocity, whereas they inclined to align almost horizontally in the annulus region. Zhang et al. [252] applied the multi-sphere and bonded-sphere models to simulate the fluidization of spherocylindrical particles in a bubbling fluidized bed. And the differences in predicting the fluidization between these two particle models were highlighted. To explore the mobility effects in gas-particle fluidized systems, Rosemann et al. [253] conducted an investigation of flow through both static and freely moving particle assemblies by the LBM-DEM model based on the resolved principle, where two different particle shapes, including spheres and multi-sphere spherocylinders, were involved. The simulation results indicated that the capability of the existing empirical correlations originally derived from the static systems should be quite limited for predicting drag and lift forces in dynamic gas-particle flow systems.

Other applications involving spherocylindrical particles can also be found in the published literatures. For example, the fluidization of mono-sized and binary granular systems containing spherocylindrical particles in a bubbling fluidized bed was numerically investigated by He et al. [35,254]. The results indicated that the bubble boundaries for non-spherical particle systems were not as clear as for spherical particles [35]. For the binary mixture, the translational and rotational granular temperatures would increase with the volume fraction of the spherocylindrical particles, and the addition of the spherical particles would also promote the spherocylinders to be in vertical orientation [254].

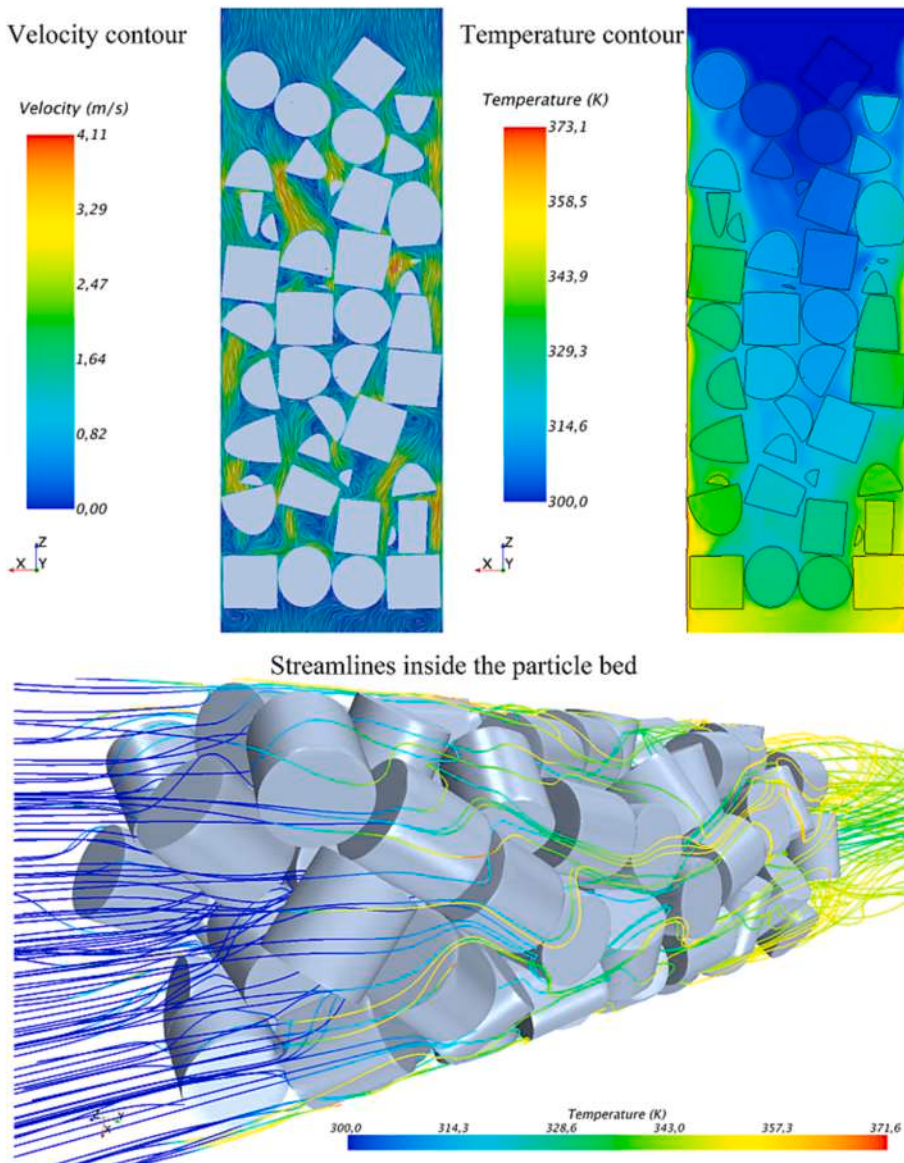


Fig. 42. Simulations of the solid-fluid systems involving non-spherical particles by integrating the contact modification methods (adapted from [223], Copyright 2017, with kind permission from American Chemical Society).

Moreover, both elongated spherocylindrical and cylindrical particles were included in the investigation of Baran et al. [255] for examining the effects of particle sharp edge on the fluidization behaviors in a bubbling fluidized bed. The simulation results suggested that there would be a lower packing density, higher initial bed height, higher minimum fluidization velocity and longer time required to reach the quasi-steady state with the increase of the aspect ratio of the spherocylinders. For cylinders, they possessed similar variations but of lesser degree.

For the fluidization of ellipsoidal particles, the rather comprehensive CFD-DEM investigations have been conducted by Zhou et al. [103,146,256–263]. Based on the simulation results, they elucidated the impacts of different forces (e.g., the van der Waals force, particle-fluid interaction force, and contact force) on the formation of expanded beds with fine ellipsoidal particles in a bubbling fluidized bed [146], as presented in Fig. 45(a). For the micro-scale flow and structure of fine ellipsoidal particles, their simulations revealed that there is a vortex flow structure, which is more significant for oblate ellipsoids [103]. And during the fluidization, the ellipsoids inclined to align their orientation with small projected area relative to the direction of fluid flow to

decrease the flow resistance. As to the liquid fluidization, the ellipsoidal particles had a tendency to enter the freeboard region and the entrainment may appear, and the oblate ellipsoids would expand more dramatically than the spherical particles and prolate ellipsoids [256]. In their further studies about the mixing of binary mixtures involving ellipsoidal and spherical particles in both gas and liquid fluidizations (see Fig. 45(b)), the results suggested that the addition of ellipsoids to spherical particles should go against the particle mixing, and the mixing degree would decrease with the particle aspect ratio diverging from 1 [257,258]. Subsequently, they also emphasized on the bubble dynamics of ellipsoidal particles in the bubbling fluidized bed and spout-fluid bed [259–263], as illustrated in Fig. 45(c). The research results revealed that the ellipsoidal particles possessed asymmetrical bubble patterns with two or more circulation vortices, while the bubbles for spherical particles generated at the bed center and moved upward through the bed center [259,260]. The bubble size was found to increase with the particle shape deviating from the sphere, where the bubbles became more circular for spherical particles [260,261]. While investigating the combined influence of particle shape and the van der Waals force, they found that the bubble dynamics were greatly affected by the aspect ratios of

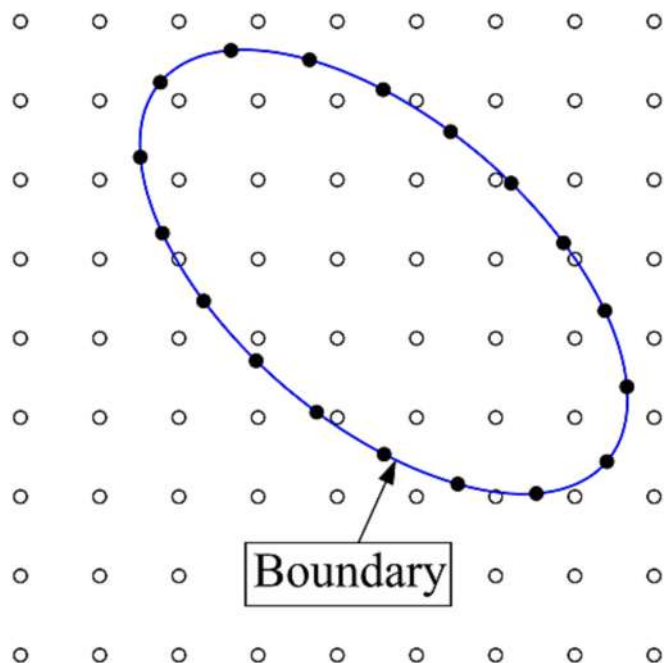


Fig. 43. Schematic diagram of the IBM (the Lagrangian and Eulerian points are represented by the hollow and solid circles, respectively).

ellipsoids under the impact of the van der Waals force [262]. The bubble would significantly impact the particle orientation of ellipsoids that the orientation evolved with bubble progression and preferred to align vertically or horizontally depending on the bubble position [263].

Besides the above, the fluidization of ellipsoidal particles has also been numerically investigated by other researchers. For example, Yang et al. [264] studied the mixing and dispersion behaviors of ellipsoid particles with aspect ratios varying from 0.5 to 2.0 in a bubbling fluidized bed. The results demonstrated that the minimum fluidization velocity increased with the aspect ratio, and the ellipsoids with higher sphericity would lead to a lower mixing degree and a larger solid dispersion intensity. Peng et al. [265] carried out a multi-sphere CFD-DEM investigation in a solid-liquid riser. They found that the ellipsoidal particles possessed a greater slip coefficient than spherical particles, and the ellipsoids with an aspect ratio of 1.5 reached the greatest. E et al. [266] focused on the heat transfer characteristics of ellipsoidal multi-sphere particles in a spout-fluid bed. According to the simulation results, the oblate ellipsoid assembly had better heat performance, whereas the performance was poor for prolate ellipsoids.

The fluidization behaviors of flexible fibers were also numerically studied. For example, both dry and wet granular systems in a bubbling fluidized bed were investigated by Guo et al. [267,268], where the flexible particles were constructed by bonded-sphere model, as presented in Fig. 46. The influences of initial bed height, fiber flexibility and degree of cohesion on fluidization characteristics had been comprehensively discussed. Wu et al. [269,270] also investigated the flow characteristics of flexible ribbon particles in a bubbling fluidized bed by bonded-sphere CFD-DEM. Subsequently, the influence of process parameters (e.g., the gas superficial velocity and bed height) on the dynamic behaviors of flexible ribbon particles (e.g., the particle residence time distribution) was explored.

As concerning the fluidized bed spray coating, CFD-DEM has been applied as a powerful tool for the related studies. By introducing the discrete droplet model used to model spray droplets into the previously developed CFD-DEM model [239], Farivar et al. [192] successfully reproduced the spray coating process in a Wurster fluidized bed, as shown in Fig. 47. Two granular systems were involved in their investigation: an assembly of spherical particles and a mixture of rod-like and

spherical particles. According to the simulation results, both COVs (coefficient of variation) that can mirror the quality of the coating process for two granular systems were inversely proportional to the square root of the coating time, and the particle shape affected the COV little as all particles had the comparable cross-section area. In terms of residence time distributions, the optimal configurations of spray zones that account for most of the particle-droplet contacts should be different for these two granular systems. Also for simulating the coating process in a Wurster fluidized bed, Jiang et al. [271] devised a CFD-DEM coupling model in combination with the Monte Carlo approach used to model the deposition and splashing of spray droplets on the particle surfaces. In their investigations, only the particles with slight irregularity were considered, and the shape effects were reflected by the rolling resistance model. Subsequently, the coating coverage, residence time distribution, cycle time distribution, uniformity of porosity and layer thickness distributions on each individual particle and in the particle population were detailedly discussed.

As the core equipment in ironmaking, the blast furnace has also attracted much attention. As illustrated in Fig. 48, Wei et al. [272–275] performed a series of CFD-DEM investigations for the microstructure and heat transfer characteristics in blast furnaces with different structures, where the particles were created by the multi-sphere model. For ellipsoidal particles, they argued that the raceway size would decrease with the aspect ratio that the prolate and oblate ellipsoids possessed the smallest and the largest raceway sizes, respectively [274], and the burden descending rate for oblate ellipsoids was faster than the prolate ellipsoids [273]. As to the thermodynamics, the heating rate should be more efficient for ellipsoids possessing larger surface area than the sphere [274], and the oblate ellipsoids presented better heating performance than the prolate ellipsoids during the initial heating process [273]. In addition, the heating process was also affected by the voidage [273]. For polyhedral particles, the closer the aspect ratio to 1, the bigger the raceway size would be [275]. The tetrahedron-like particles generally possessed a stronger interlocking efficiency and hence a smaller raceway size [272]. In addition, the octahedron-like particles possessed the highest average temperature while the average temperature of spherical particles is lower than polyhedral particles [272].

Also for ironmaking, You et al. [276] applied the CFD-DEM approach to investigate how the shape of coke particles affects the burden profile and gas flow in a melter gasifier, where the particles were described by the multi-sphere model (cf. Fig. 49(a)). As illustrated in Fig. 49(b), a stable packed bed was firstly formed by the fall of particles under gravity, and the air with the velocity smaller than the minimum fluidization velocity was injected into the bottom of the bed. The simulation results indicated that the pressure drop was basically constant when the non-convexity shape factor was less than 0.4, but further increasing the shape factor would make the pressure drop decline sharply. In addition, the pressure drop of multi-sized particle beds was generally higher than that of mono-sized particle beds. For evaluating the sintering process of iron ore particles, Nyembwe et al. [277] numerically investigated the pressure drop across the packed bed. As listed in Table 4, the influences of the particle shape were examined by performing CFD-DEM simulations involving the spheres, rounded polygons and polyhedrons. The results predicted that the irregularity of particle shape went against the formation of a dense packing so that the pressure drop across granular beds would increase with the increase in particle sphericity and the decrease in particle angularity.

In order to explore the heat transfer, combustion and gasification behaviors of particles in the packed bed with deeper insight, the mass and heat transfer models have been incorporated into the CFD-DEM model to account for macroscopic transport of quantities such as momentum, heat, mass, radiation intensity, etc. Wu et al. [279] numerically investigated the radiative heat transfer behaviors in a nuclear packed pebble bed. For examining the shape effects, four different non-spherical particles, including prolate ellipsoid, oblate ellipsoid, cylinder and cube, described by the super-ellipsoid model were taken into

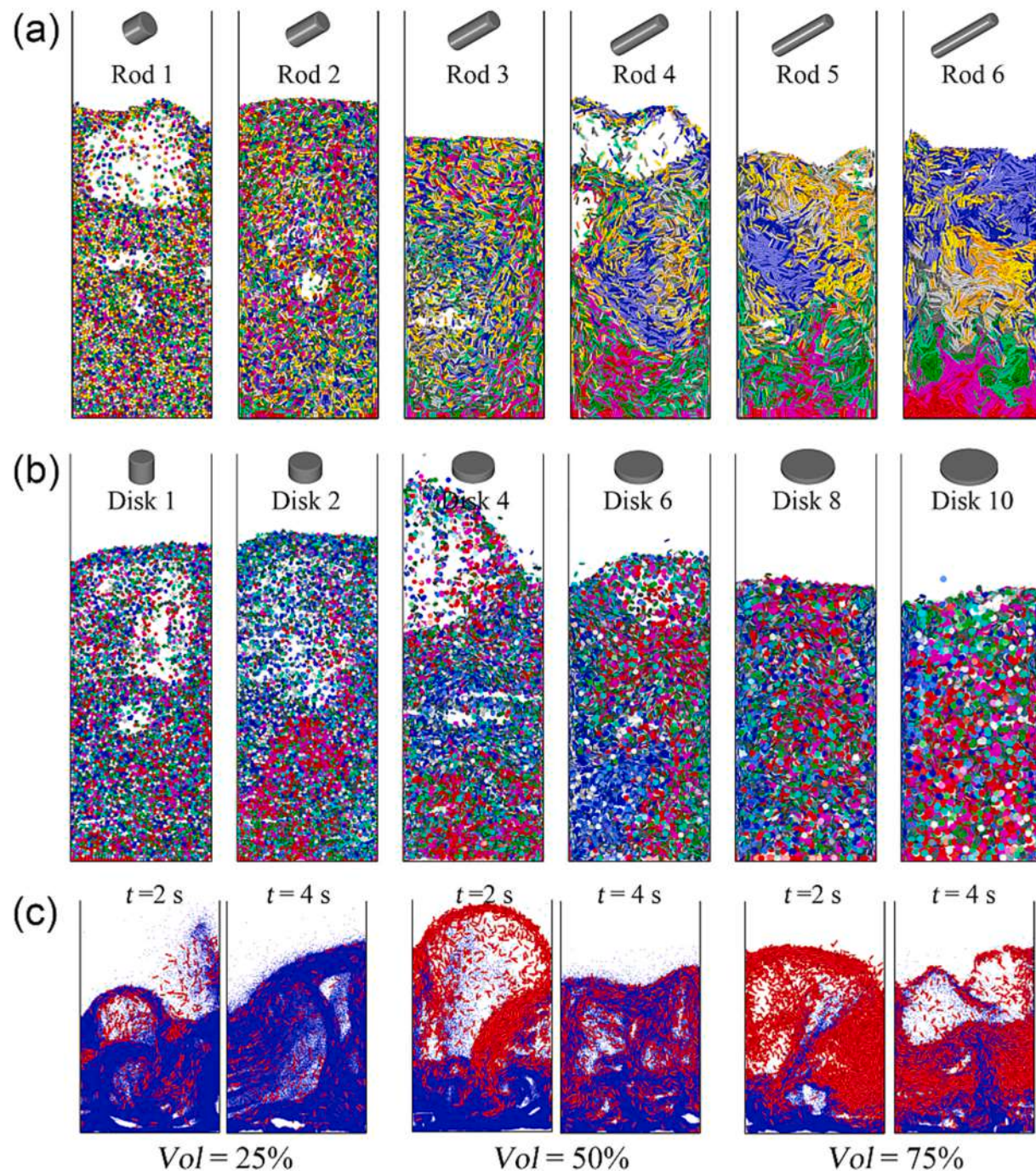


Fig. 44. Snapshots of the flow behaviors of particles in a bubbling fluidized bed: (a) the fluidization of rod-like particles (adapted from [148], Copyright 2016, with kind permission from Elsevier); (b) the fluidization of disk-like particles (adapted from [99], Copyright 2018, with kind permission from Elsevier); (c) the fluidization of binary mixtures containing rod-like and spherical particles (adapted from [237], Copyright 2018, with kind permission from Elsevier).

account. The numerical results revealed that the radiative conductivity was inversely proportional to the packing density and particle sphericity while the particles were in the bulk region without wall effect. With the previously established super-ellipsoid CFD-DEM model [280], Gao et al. [281] simulated biomass pyrolysis in a packed bed pyrolyzer. The simulations with and without the particle-scale model predicting intra-particle phenomena inside an individual particle were compared, and the influences of the particle-fluid heat transfer models were examined. For reproducing the continuously changing assemblies of reacting particles, a shrinking model was further integrated for modeling particle shrinking. Mohseni et al. [282] studied the biomass conversion by CFD-DEM, where the biomass particles were modeled as cylinders. The heat-

up, drying, pyrolysis, gasification and combustion were all considered in their work, and a shrinking model was devised for evaluating the impact of particle shrinkage. Furthermore, the resolved CFD-DEM model was also adopted by some researchers, where the non-spherical particles were approximated as a certain number of triangulated surfaces. For instance, Buss et al. [283] simulated the combustion of spherocylindrical straw pellet particles in the static and agitated beds and Wiese et al. [278] reproduced the combustion of cylindrical polyhedron particles in a pellet stove, as shown in Fig. 50. And the corresponding experiments had been carried out for verifying the applicability of their established CFD-DEM models.

Due to the complexity of non-spherical CFD-DEM, the spherical

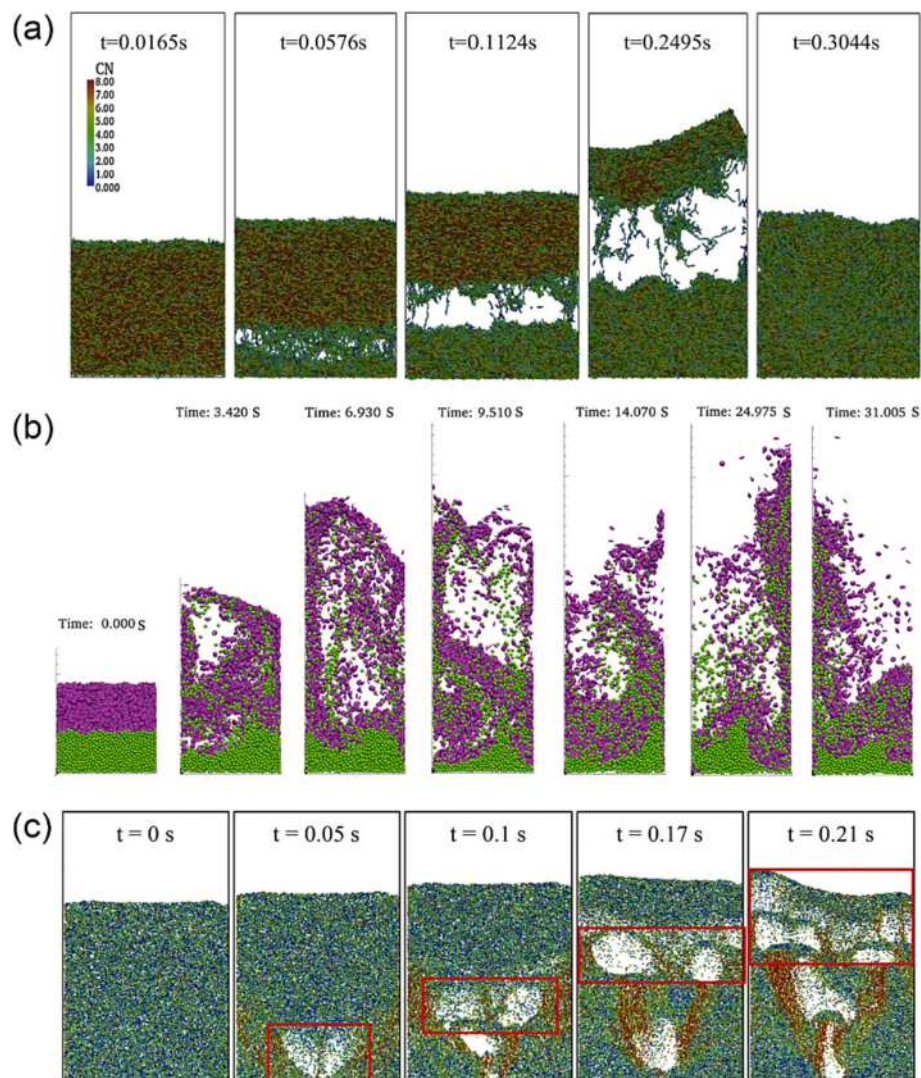


Fig. 45. Snapshots of the fluidization behaviors of ellipsoidal particles: (a) the formation of bed expansion (adapted from [103], Copyright 2017, with kind permission from Elsevier); (b) the mixing/segregation behaviors of binary mixtures in gas fluidizations (adapted from [257], Copyright 2018, with kind permission from Elsevier); (c) the bubble dynamics (adapted from [263], Copyright 2019, with kind permission from Elsevier).

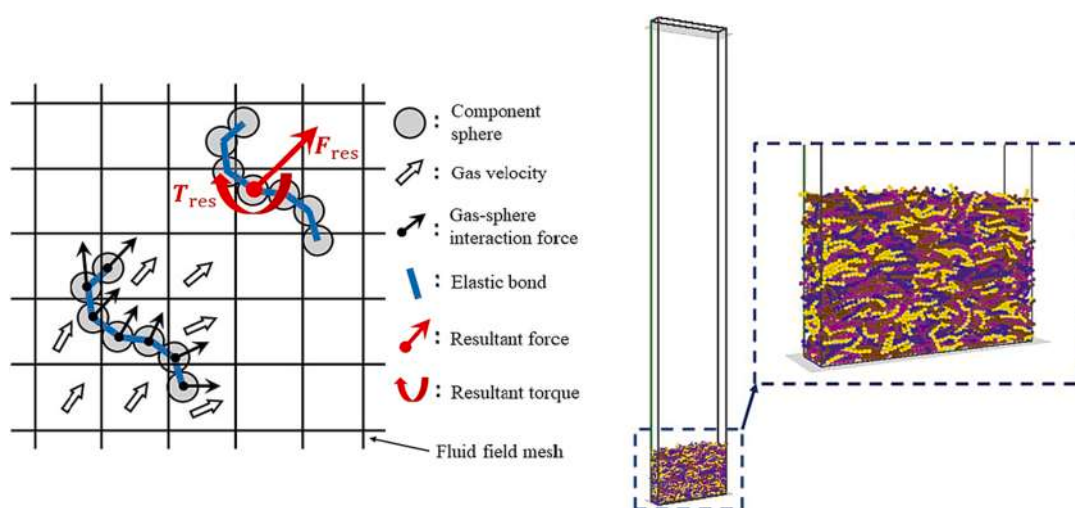


Fig. 46. Schematic representation of the hydrodynamic forces imposing on the flexible bonded-sphere particle and the initial state of the fluidized bed containing flexible fibers (adapted from [267], Copyright 2022, with kind permission from Elsevier).

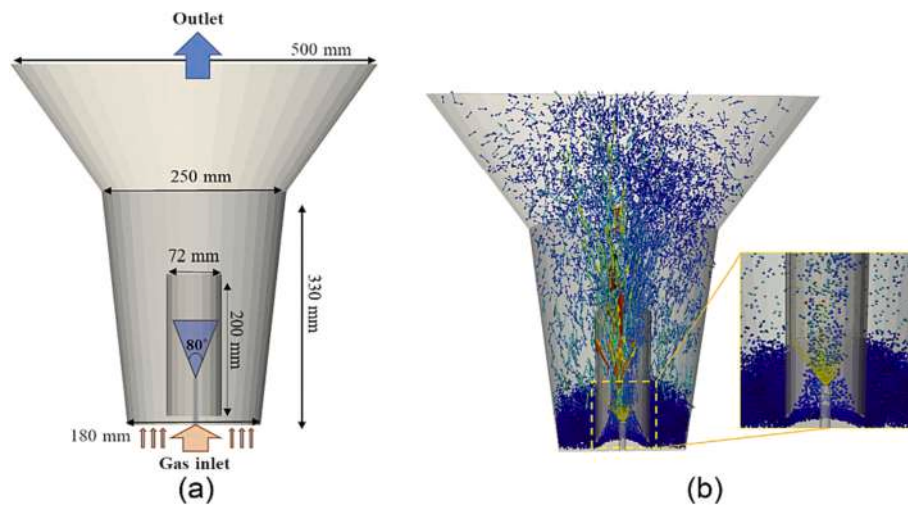


Fig. 47. CFD-DEM simulations of the coating process in a Wurster fluidized bed coater: (a) the simplified geometry of Wurster coater and (b) the velocity vectors of particles (adapted from [192], Copyright 2020, with kind permission from Elsevier).

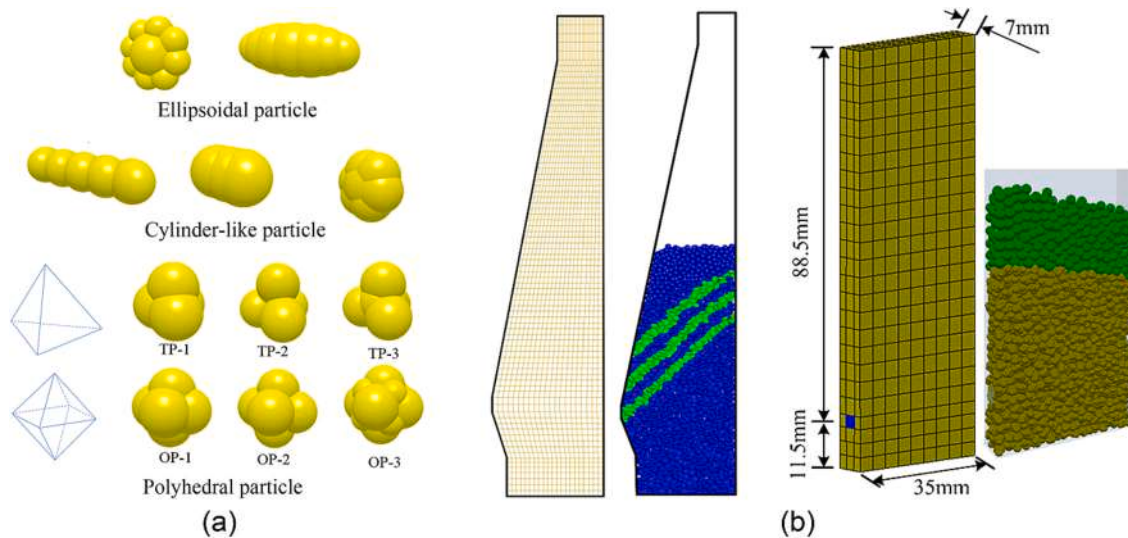


Fig. 48. CFD-DEM investigations of the blast furnace: (a) the non-spherical multi-sphere particles (TP and OP denote the tetrahedron-like and octahedron-like particles) (adapted from [272,273,275] with kind permissions from Elsevier (Copyright 2019), Elsevier (Copyright 2020) and Elsevier (Copyright 2022)); (b) the schematic of the blast furnaces with different geometries (adapted from [272,273] with kind permissions from Elsevier (Copyright 2019) and Elsevier (Copyright 2020)).

particles were also used to imitate the non-spherical particles in some investigations by introducing particle sphericity or rolling friction. For example, Ostermeier et al. [284] developed a CFD-DEM model incorporating the coarse grain model for simulating the biomass gasification in a bubbling fluidized bed, where the particle sphericity were accounted for the shape effects in the momentum exchange computation with the fluid phase. Subsequently, the simulation results, e.g., the bed pressure drop, product gas composition and conversion time, were analyzed and then compared with the literature correlations as well as experimental observations for proving the capacity of the established CFD-DEM model. In addition, they also simulated the fluidization in a dense fluidized bed, where the particles with the sphericity of 0.8 were used, for comparing the performance between different numerical models such as TFM and CFD-DEM [285]. Xu et al. [286] integrated the rolling friction model with coarse-grained CFD-DEM of spherical particles, aiming to reproduce the macroscopic flow behaviors of irregular-shaped sand particles. Subsequently, the proposed model was proved to have satisfactory accuracy through the comparison between

simulation results and experimental measurements in terms of the pressure drops along the bed height in a cylindrical fluidized bed. Marchelli et al. [287] investigated the effects of density, diameter and sphericity of particles on the minimum spouting velocity, where the shape effect was quantified by the particle sphericity in determining the drag force. They found that the minimum spouting velocity would be approximately proportional to the square root of particle density, cube root of particle diameter and fourth power of particle sphericity.

Generally, the calculation of particle-fluid interactions (e.g., the drag force) will be different while using different particle-fluid interaction models (e.g., drag models), and then affects the CFD-DEM predictions of the flow behaviors of particle-fluid systems. For evaluating the influence of particle-fluid interaction models, therefore, some numerical investigations have been performed. For example, Olatunde and Fasina [288] simulated the flow behaviors of biomass particles in a fluidized bed with using different drag equations, where the shape effects were mainly mirrored by particle sphericity, for exploring the influence of drag models on fluidization behaviors. In order to accurately replicate

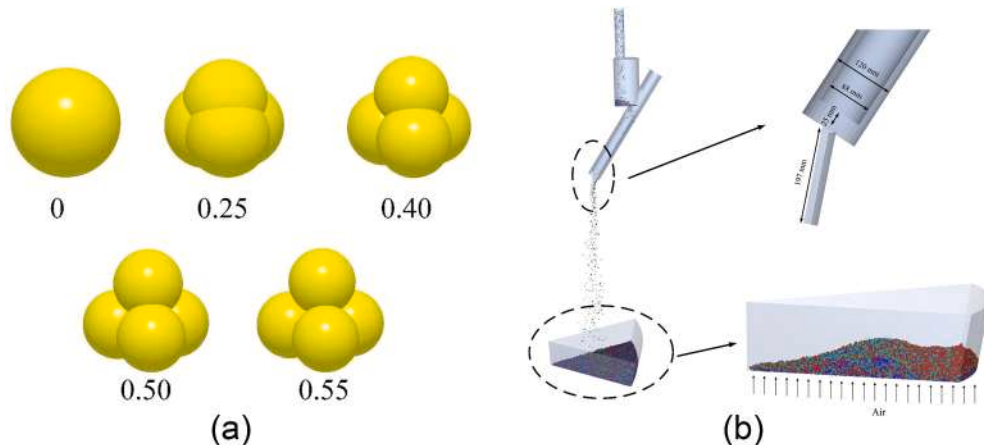


Fig. 49. CFD-DEM investigations of the packed bed in a melter gasifier: (a) the multi-sphere particles with different shape factors and (b) the simulated set-up of melter gasifier (adapted from [276], Copyright 2019, with kind permission from Elsevier).

Table 4

Examined shape of the DEM particles (adapted from [277], Copyright 2019, with kind permission from Elsevier).

Shape	Sphere	Rounded polygons	Rounded polyhedrons
Number of corners	∞	25	4
Order of angularity		\longrightarrow	

the preferred particle orientation and thus the applicability of the apparatus design for coating processes, Atxutegi et al. [289] conducted a similar research for the fluidization of spherical and ellipsoidal particles in conical and prismatic spout-fluid beds by super-ellipsoid CFD-DEM

with utilizing various drag models. Besides the drag force, moreover, the lift force and Nusselt number were also involved in the work of Kravets et al. [290] with introducing different particle-fluid interaction models into CFD-DEM. Subsequently, the simulation results between the particle resolved DNS and CFD-DEM for the flow through the homogenous ensembles of stationary spherical and non-spherical particles are compared.

Besides the above-mentioned literatures, the CFD-DEM investigations of fluidization of non-spherical particles for other particle shapes or research purposes could also be effortlessly accessed. For instance, our group developed a CFD-DEM model based on the polyhedron particle model, and then the fluidization of polyhedron particles in a bubbling fluidized bed was investigated [118], as shown in Fig. 51. The simulations predicted that the polyhedron particles had stronger motion and higher mixing degree than the equivalent volume spheres. Wang and Shen [212] carried out the CFD-DEM simulations for the

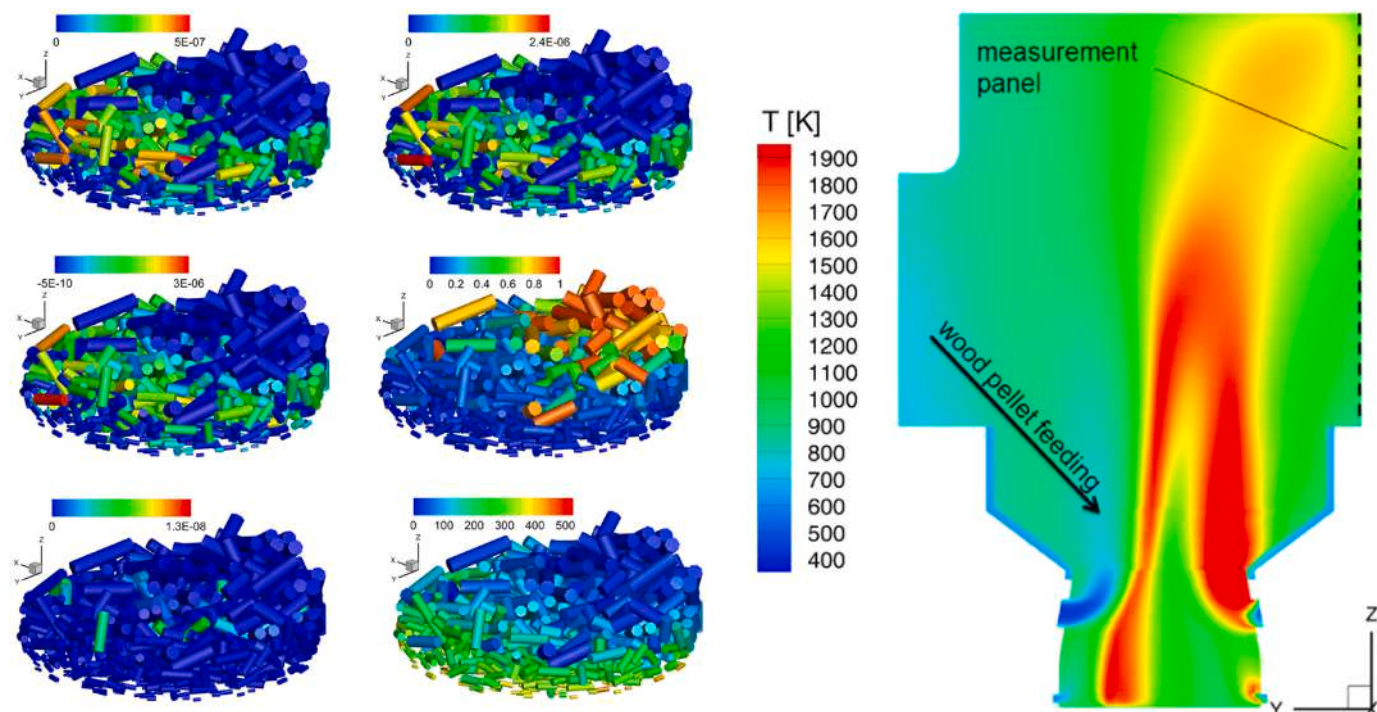


Fig. 50. Simulations of the combustion of cylindrical polyhedron particles in a pellet stove by the resolved CFD-DEM approach (adapted from [278], Copyright 2016, with kind permission from Elsevier).

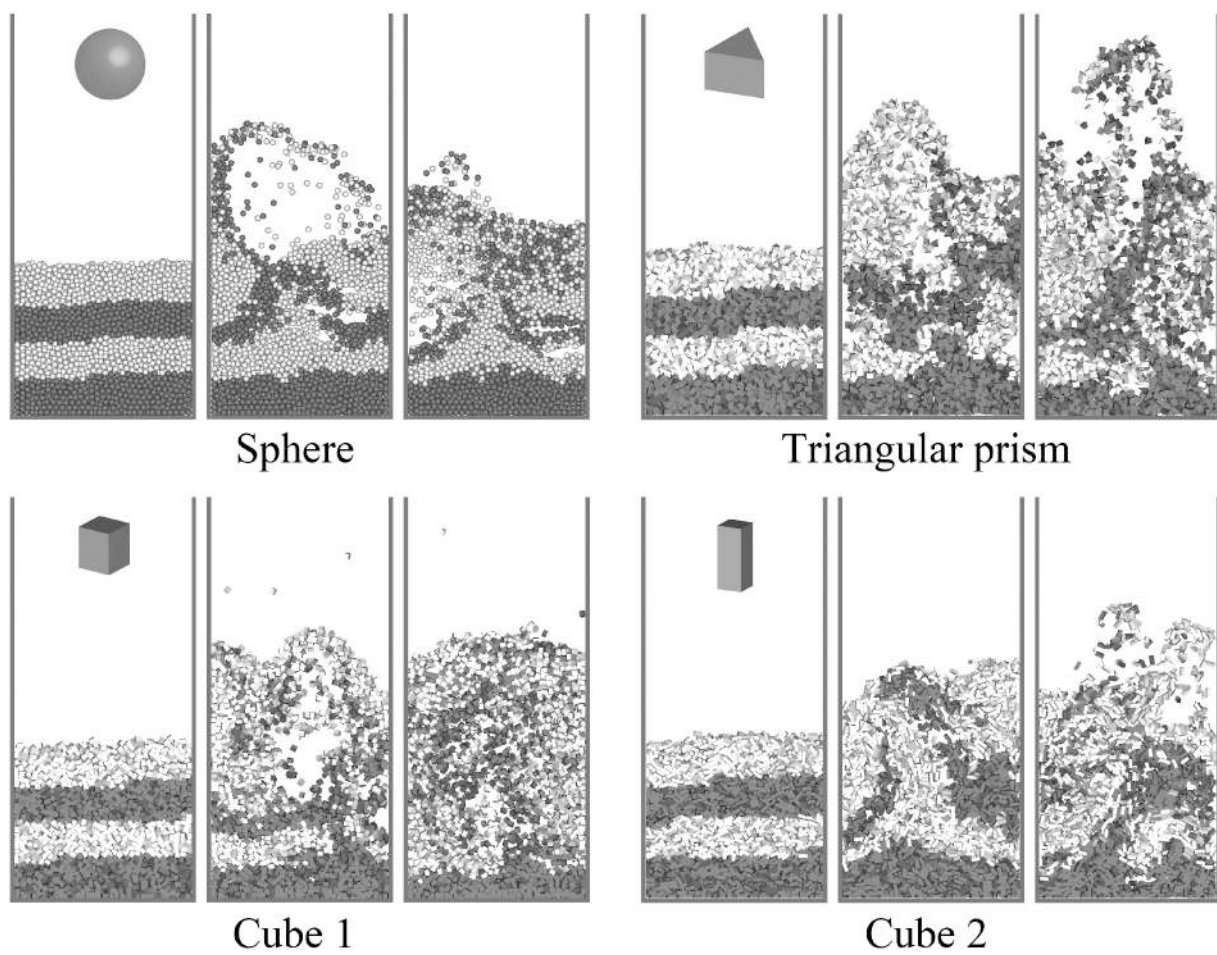


Fig. 51. Snapshots of the fluidization behaviors of spherical and polyhedral particles in a bubbling fluidized bed (adapted from [118], Copyright 2021, with kind permission from Multidisciplinary Digital Publishing Institute).

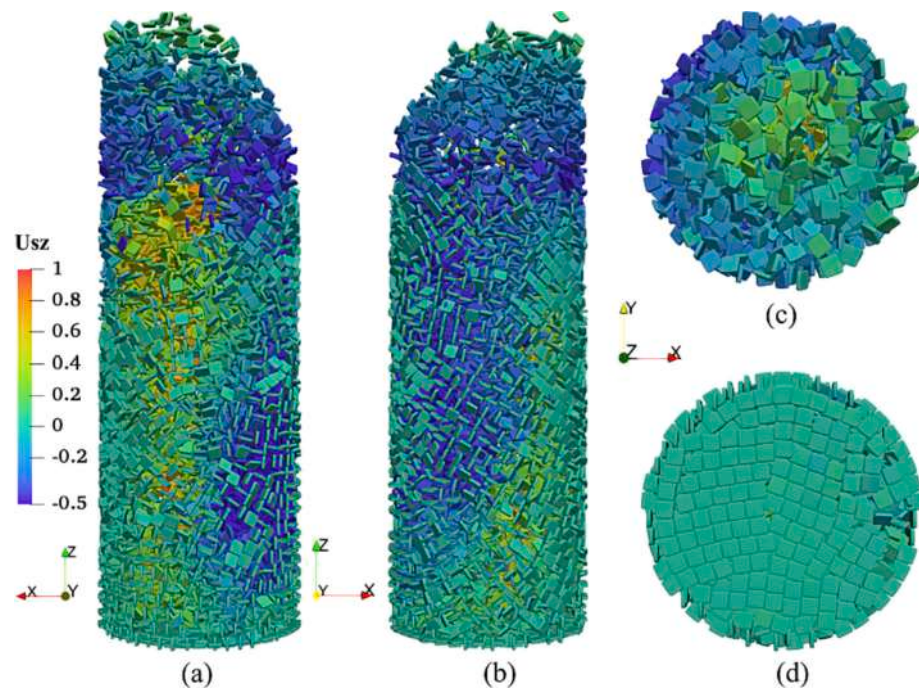


Fig. 52. Snapshots of the fluidization behaviors for the chip-like particles with $AR = 4$: (a) right view, (b) left view, (c) top view and (d) bottom view (adapted from [212], Copyright 2022, with kind permission from Elsevier).

fluidization of chip-like super-ellipsoid particles with the aspect ratio of 1, 2 and 4 in a cylindrical fluidized bed, as shown in Fig. 52. The also found apparent wall effect that the arrangement of particle orientation was more ordered near the wall (see Fig. 52). Moreover, increasing the aspect ratio could trigger a higher pressure drop and a larger particle dispersion coefficient reflecting the solid transportation intensity. Also in a cylindrical fluidized bed, Prakotmak and Wangchai [291] investigated the fluidization of corn kernel particles, where the particles were approximated by the multi-sphere model. The results revealed that increasing the number of sub-spheres would lead to a higher minimum fluidization velocity, larger pressure drop and lower heat transfer rate between the particle and gas phases. For the design and testing of newly designed solutions to operational problems encountered in a coffee roaster, Hłosta et al. [292] reported an application of the multi-sphere CFD-DEM for modeling the flow of coffee beans in a laboratory scale fluidized bed coffee roaster. Aided by CFD-DEM, Wang et al. [34] focused on contributing to a deep understanding of the instability mechanisms for the fluidization of non-spherical particles in a spout-fluid bed, and efforts had been made to determine the relationship between the instability and the motion of micro-scale particles and bubbles. The fluidization in a dual-chamber fluidized bed was simulated by CFD-DEM in the investigation of Vollmari and Kruggel-Emden [293] mainly for studying the particle residence times, where three different particle shapes, including spheres, cubes and cylinders, were considered. To gain a deeper understanding of the influence of particle shape on the mixing of mono- and bidisperse particulate systems, Vollmari et al. [294] further investigated the fluidization of differently shaped particles in a bubbling fluidized bed by CFD-DEM and experiments, where spheres, plates, cubes and elongated cuboids were included.

According to the studies and findings mentioned above, it can be found that the particle shape can affect the dynamic behaviors of fluidization significantly, and the non-spherical particles generally possess preferred orientation (particularly for elongated and flat particles) in the fluidization systems. Despite the fact that numerous CFD-DEM investigations have been successfully performed for the fluidization of irregular particles, nevertheless, still more efforts are required due to the complicity of fluidization involving non-spherical particles. For example, the current related CFD-DEM studies focus more the gas fluidization in the bubbling fluidized bed and spout-fluid bed, whereas the researches for the fluidization involving the liquid flow or in other types of fluidized beds (*e.g.*, the circulating fluidized bed) is relatively few. In addition, the fluidization of non-spherical particles involving heat transfer is also little investigated.

4.2. Particle transport

Many kinds of granular materials in industry need to be transported from one place to another. And in many cases, the interactions between the fluid and solid particles cannot be ignored during the transport process, or even the solid particles are directly driven by the fluid. One of the typical examples is pneumatic conveying that uses either negative or positive (or the combination of the two) pressure of gas and has been widely used to transport solid materials in industry. Therefore, numerous academic researches with the aid of CFD-DEM for investigating particle transport have been reported.

At present, the most commonly encountered fluid medium in the process of particle transport should be gas. To evaluate and improve the performance of sowing in agriculture, for example, CFD-DEM has been

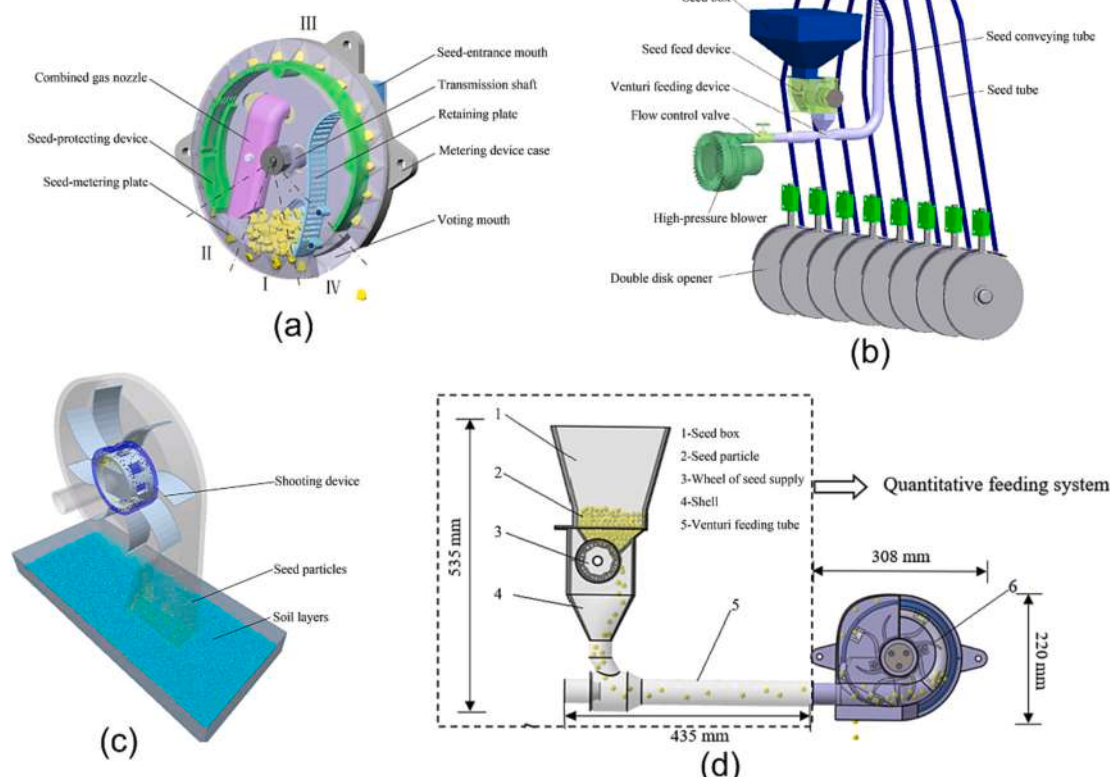


Fig. 53. Simplified geometry of the seeding device: (a) the inside-filling air-blowing seed metering device (adapted from [295], Copyright 2018, with kind permission from Elsevier); (b) the air-assisted centralized seed-metering device (adapted from [296], Copyright 2018, with kind permission from Elsevier); (c) the self-suction wheat shooting device (adapted from [297], Copyright 2021, with kind permission from Elsevier); (d) the pneumatic seed metering device with the Venturi feeding tube (adapted from [298], Copyright 2020, with kind permission from Elsevier).

gradually used to simulate the flow and transport behaviors of seed particles in the gas flows in various sowing machineries as well as their subcomponents [295–312], as shown in Fig. 53. In general, the non-spherical bio-particles were modeled by the multi-sphere approach in these investigations. Aided by CFD-DEM, they were devoted to studying the influence of working parameters (e.g., the air velocity and pressure, geometry of the device, feeding rate of the seed particles and rotation speed of the seeding device with rotating part) and particle shape on the flow and transport behaviors of bio-particles and hence could evaluate the performance as well as the applicability of the sowing machinery. For instance, Wang et al. [297] numerically study the influences of operation parameters (the rotation speed of the shooting device, window length and width of directional seed delivery wheel) on the transport behaviors of seed particles in a self-suction wheat shooting device. Li et al. [299] numerically investigated the flow and transport behaviors of seed particles in an air-blown seed metering device. Du et al. [300] used CFD-DEM to investigate the flow characteristics of rice seed particles in the pneumatic conveying with elbow that is the core part deciding the performance of the pneumatic metering device. They found that the difference in the particle velocity profile between the spherical and non-spherical particles was tiny, but the non-spherical rice particle rope would disperse more slowly than the spherical particle rope. Cui et al. [295,298,306–309] comprehensively investigated the sowing of maize grains in different seeding devices such as inside-filling air-blown seed metering device [295,308,309], air suction seed metering device [307], pneumatic seed metering device with the Venturi feeding tube [298,306], etc. And the efforts had been made to find the optimal combination of operational parameters for the different seeding devices. Lei et al. [296,310–312] mainly concentrated on the air-assisted centralized seed-metering device for spherical rapeseeds and ellipsoidal wheat by CFD-DEM. They primarily studied the flow behaviors of seed particles in different subcomponents of the seeding device, including the seed conveying tube [310], pressurized tube [311], distribution head [296] and seed feeding device [312], for examining and then improving the sowing performance.

As mentioned above, the pneumatic conveying in the pipeline with and without elbow is a common scenario for the transport of particles, and the related researches can be effortlessly accessed. To increase the working efficiency of the road sweeper, for example, the multi-sphere CFD-DEM investigations of pneumatic conveying of rod-like particles with different densities and aspect ratios in a pipeline were performed by Liu et al. [313]. The results suggested that the particle suction efficiency would decrease with increasing the particle density, and the aspect ratio of particles had little influence on the efficiency. Aiming to quantify the predictive capability of the developed CFD-DEM model, Ebrahimi et al. [314] carried out the experiments with the help of laser Doppler anemometry and CFD-DEM simulations of the horizontal pneumatic conveying of spherical and short cylindrical particles for comparisons, where the cylinders were approximated by multi-sphere model. With using CFD-DEM, Liu et al. [315] simulated the conveying

process of two different shaped particles (the tablet-shaped and cylinder-shaped particles) modeled by the multi-sphere approach in a Venturi powder ejector, as presented in Fig. 54. The simulations predicted that both the number of particle-wall and particle-particle collisions of cylinder-shaped particles were larger than tablet-shaped particles, and the cylinder-shaped particles possessed a higher magnitude of collision force. Therefore, the Venturi powder ejector was not recommended for cylinder particles for reducing the impact breakage. Aided by the experiments and CFD-DEM simulations, Kabeel et al. [316] studied the jet of solid particles into turbulent cross gas flow in a pipeline, where the irregularity of particles was quantified by the sphericity in calculating the drag force for the coupling of CFD and DEM. Then the effects of conveying velocity and solid loading ratios on the flow characteristics were examined. Olaleye et al. [317] experimentally and numerically investigated the pneumatic conveying of cohesive dairy powder in a stainless steel pipe, where the particle shape was quantified by the so-called Corey's shape factor [10] within the CFD-DEM. Subsequently, the effects of operating conditions (i.e., the gas velocity and solid loading) on the dynamics of particle flow were explored. Moreover, the pneumatic conveying of flexible bonded-sphere particles in a pipe bend was numerically investigated by Markauskas et al. [318]. And then the effects of some important parameters such as particle stiffness and bond damping on pneumatic particle transport behaviors were revealed.

The erosion of pipelines and the breakage of particles in the pneumatic conveying were also investigated by some scholars. Zhou et al. [319–321] focused on investigating the influences of particle shape and swirling intensity on elbow erosion and particle breakage by applying the multi-sphere and bonded-sphere CFD-DEM models, as presented in Fig. 55. For elbow erosion [319], the simulation results uncovered that the average erosion rate usually changed with the particle sphericity in an almost inclined "S" pattern and generally decreased with the swirling intensity first quickly and then slowly. For particle breakage where the particles were constructed by the bonded-sphere model [320], the non-spherical agglomerate particles were more inclined to be broken compared to sphere agglomerate, and the agglomerate integrality ratio would increase with the swirling number and particle sphericity. Moreover, they argued that the pipeline bending direction radius also impacted the particle breakage [321]. Jägers et al. [191] incorporated a numerical degradation model on the basis of the so-called selection and breakage functions into the CFD-DEM model to simulate the wood pellet breakage and the formation of fine, in which the wood pellet particles were approximated as spherocylinders, as illustrated in Fig. 56. According to simulation results, increasing the air flow rates (i.e., the higher particle velocities), decreasing the pellet mass flows and reducing the elbow radii accelerated the breakage of particles. Chen et al. [322] carried out the CFD-DEM simulations of the flow of stiff shotcrete materials modeled by multi-sphere approach in the pipeline with elbow. Then the flow characteristics of materials and the wear degree at the pipe elbow were analyzed. Zeng et al. [323] investigated the erosion of pipeline elbow during the transportation process of sulfur particles by CFD-DEM, where the sulfur particles were approximated by four kinds of polyhedral particles (tetrahedron, hexahedron, octahedron and dodecahedron) described by the multi-sphere model. The results suggested that the erosion rate would firstly decrease and then increase with the particle sphericity. The impact velocity and angle had more significant influence on the erosion rate when the particle sphericity was less than 0.77, otherwise the erosion rate was primarily influenced by the impact concentration. Liu et al. [324] numerically investigated the erosion characteristics at 90° elbow while conveying the rod-like multi-sphere catalyst particles with the aspect ratio varying from 3 to 9. The results uncovered that the erosion area of elbow was mainly in the middle part of the outer wall, and the erosion rate and impact density of particles decreased while the impact velocity increased with the aspect ratio.

The applications and investigations for the particle transport behaviors in the gas flow can also be found in other areas. To improve the drug delivery efficiency, for instance, Zhao et al. [325] carried out the

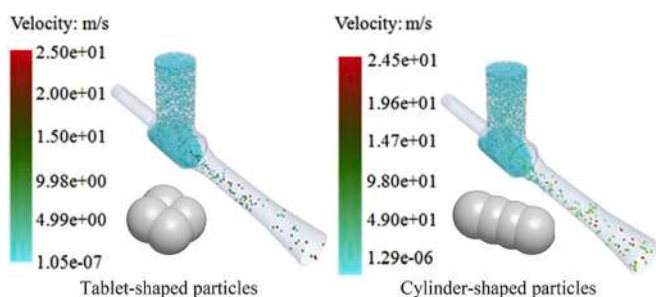


Fig. 54. Distribution of the particle velocity while conveying the particles in an ejector (adapted from [315], Copyright 2016, with kind permission from Elsevier).

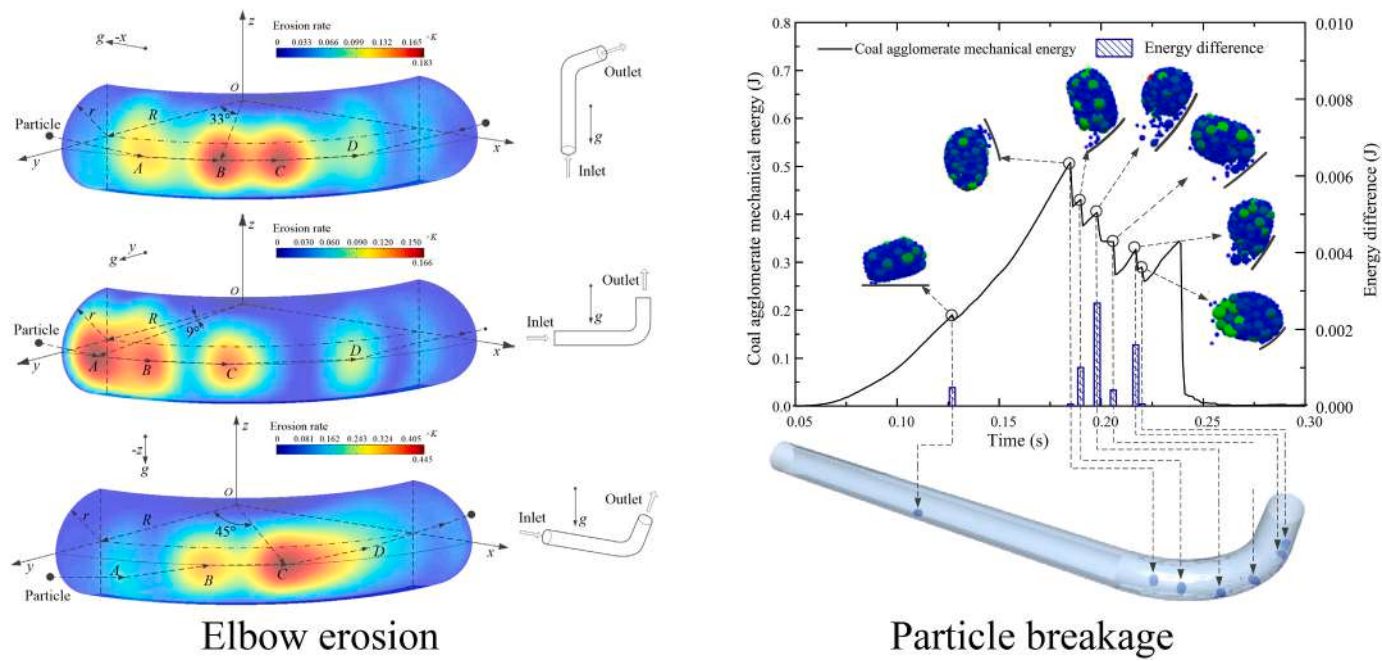


Fig. 55. Illustration of the simulated erosion elbow and particle breakage in the pneumatic conveying (adapted from [319,320] with kind permissions from Elsevier (Copyright 2017) and Elsevier (Copyright 2017)).

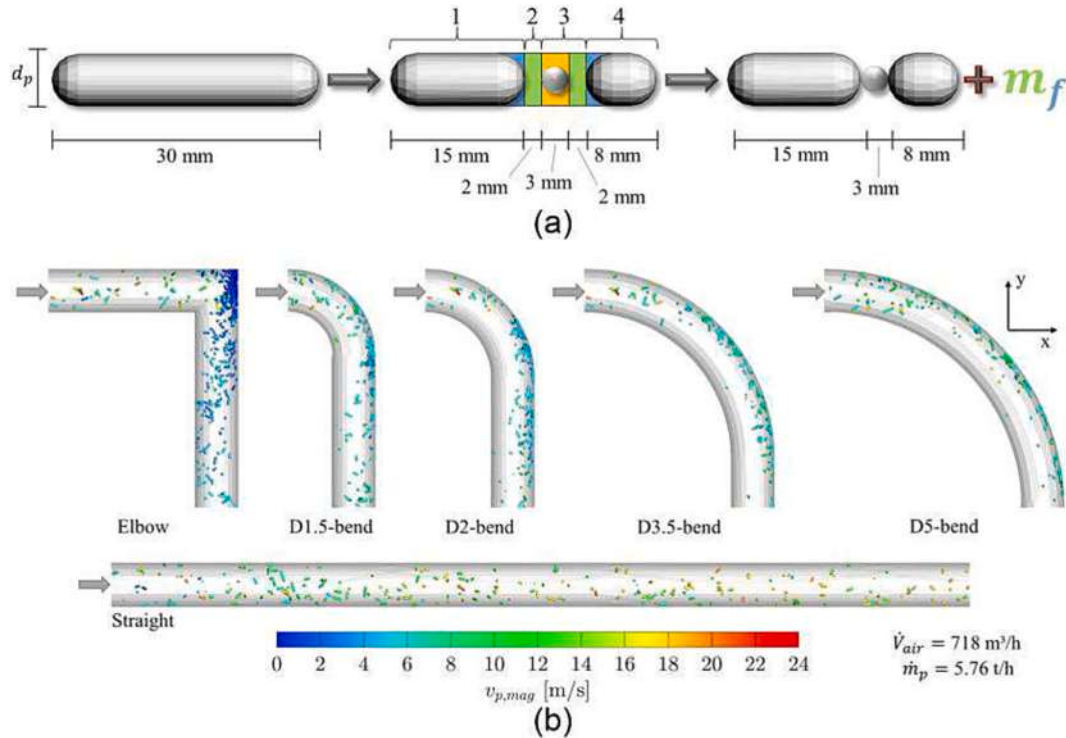


Fig. 56. Illustrating the CFD-DEM simulations of particle behaviors in the pneumatic conveying: (a) the schematic of particle degradation model and (b) the snapshots of particle flow patterns in different shaped pipes (adapted from [191], Copyright 2021, with kind permission from Elsevier).

CFD-DEM simulations for predicting the transport, interaction and deposition of API (Active Pharmaceutical Ingredient) particles and spherocylindrical lactose carrier particles with different aspect ratios in the flow channels of two DPIs (Dry Powder Inhalers) into a 3D human respiratory system, as shown in Fig. 57. According to the numerical results, the shape of lactose carrier particles could greatly affect the DPI delivery efficiency, but its influence was not significant for the lung

deposition patterns of the API. Moreover, Ohsaki et al. [326] also carried out a similar CFD-DEM investigation for the conveying of drug particles in the human respiratory system. The simulation results further indicated that the smaller-, lower-density and larger aspect ratio particles possessed higher reachability into the depth of the respiratory system. Using the CFD-DEM, Dauphin et al. [327] simulated the clogging behaviors of particles while transporting suspended particles in a

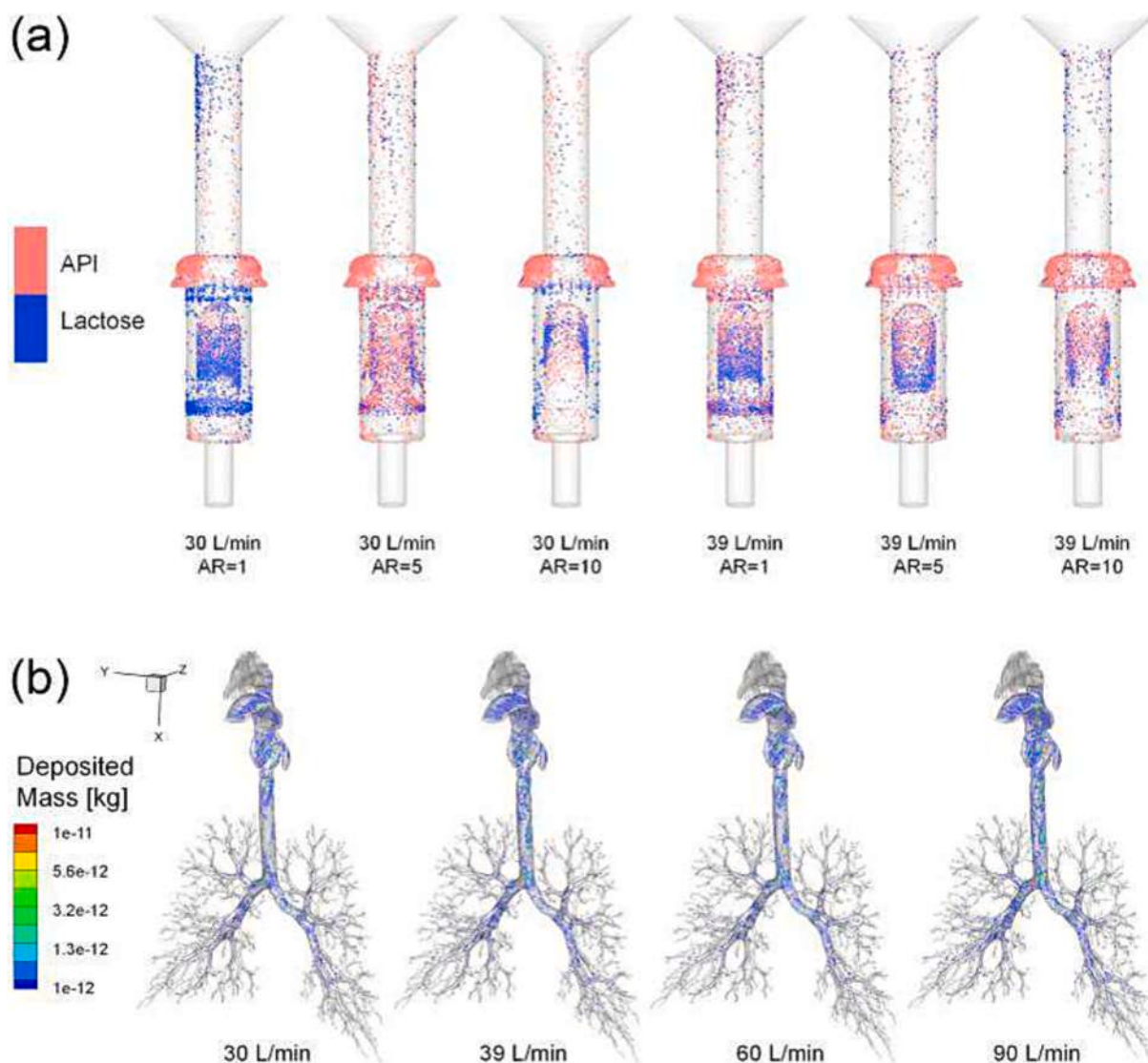


Fig. 57. Snapshots of the flow patterns in (a) the DPI and (b) the human respiratory system (adapted from [325], Copyright 2021, with kind permission from Elsevier).

microchannel with sudden contraction, where the triplet multi-sphere particles were considered. The results indicated that the cohesion energy density should be the only factor that could qualitatively affect the clog formation. And as for the particle orientation, the cluster formed at the channel contraction appeared to keep the uniform distribution imposed at the entrance. To improve the unfavorable design of the mixed-flow dryer for the drying of grains, Weigler et al. [328] numerically studied the flow and transport behaviors of non-spherical multi-sphere grain particles as well as the air flows in a mixed-flow dryer. And the effects of dryer geometry and air duct arrangements were subsequently investigated.

Besides the gaseous phase mentioned above, the transport of particles in the liquid medium is also relatively common. The transport of flows with solid particles by pumps is a typical case, such as in mining and coal as well as chemical and metallurgical processes [329,330]. With the multi-sphere CFD-DEM model, Zhao et al. [330–332] carried out a series of investigations of the erosion behaviors in different types of pumps for transporting particle-laden flows, as Fig. 58 presents the schematic representation of the centrifugal pump. Fig. 59 further presented the erosion rates on the different components of the pump. According to the results of the predicted erosions, the relation between the erosions and particle sizes was nonlinear that there would be the

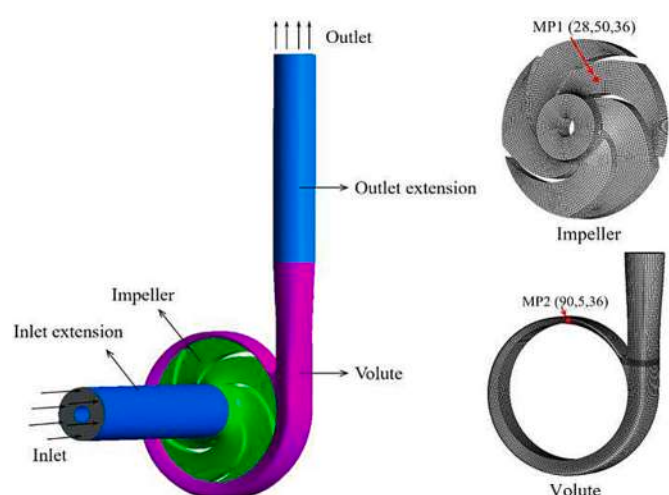


Fig. 58. Simplified geometry of the centrifugal pump and the contours of erosion rate (adapted from [330], Copyright 2021, with kind permission from Multidisciplinary Digital Publishing Institute).

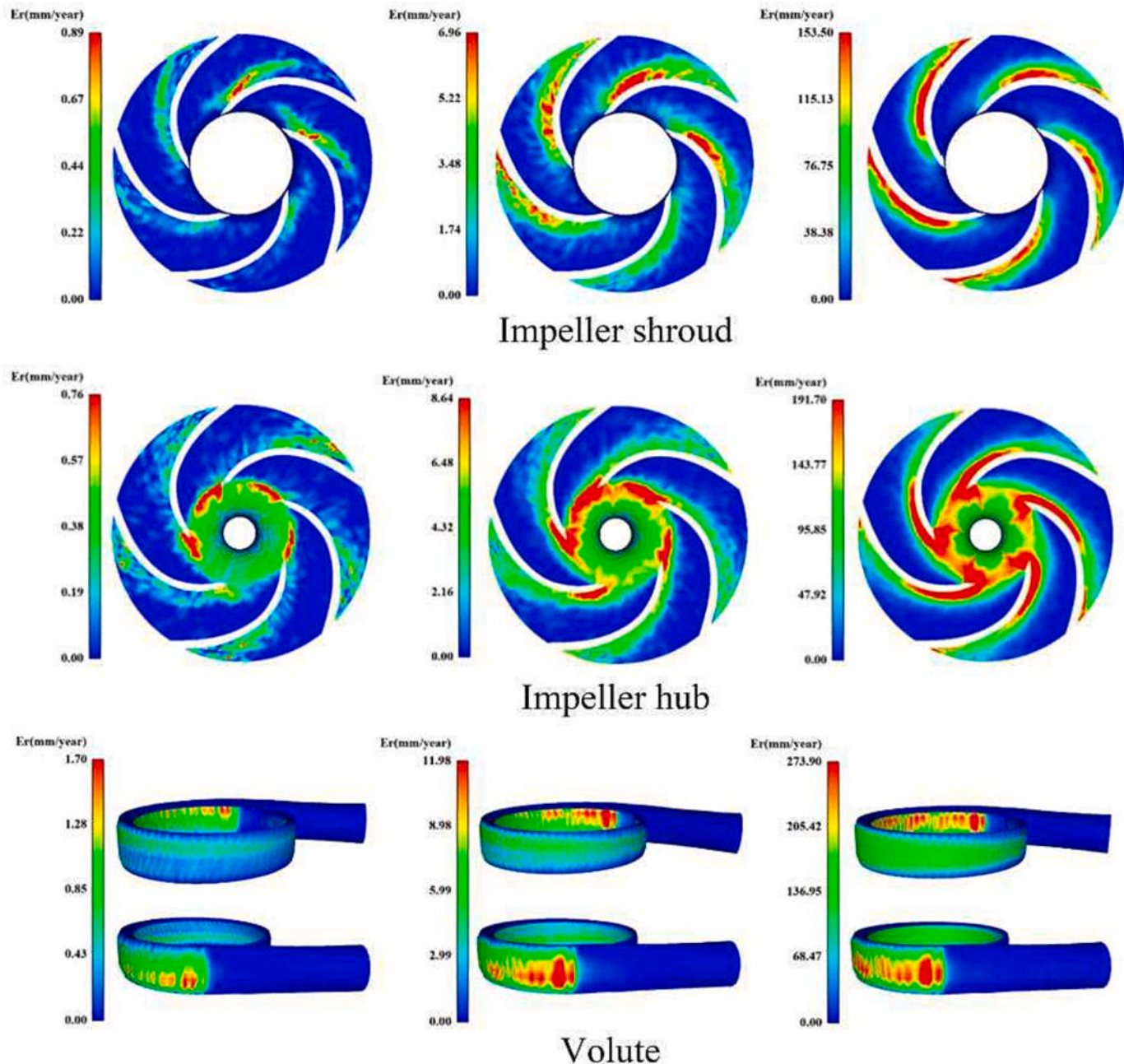


Fig. 59. Contours of the annual erosion rates on the surfaces of different components of the pump (adapted from [330], Copyright 2021, with kind permission from Multidisciplinary Digital Publishing Institute).

maximum erosion in the pump for particles with the size of 1 mm, and the particles with sharper edges would cause more severe pump erosion. Moreover, Tang et al. [333] investigated the wear characteristics (including abrasive and impact wear) of a centrifugal pump. Four regular polyhedron particles described by the multi-sphere model and the spherical particles possessing the same volume were considered. The results indicated that the overall impact wear rate firstly decreased and then increased with the increase of particle sphericity, while the overall abrasive wear rate grew rather stably. In addition, Guan et al. [334] numerically investigated the backflow performance of ore particles in a deep-sea mining slurry pump, in which differently shaped multi-sphere particles were included. According to the analysis results, the backflow performance of non-spherical particles was inferior to that of spherical particles, which should increase the complexity in designing the slurry pump.

Similar to the pneumatic conveying, the transport of solid particles in the pipeline but with the liquid medium should also be often encountered. As shown in Fig. 60, for example, Chen et al. [189] numerically studied the influence of particle shape in a horizontal slurry pipeline transport, in which three different shaped multi-sphere particles (*i.e.*, the spherical particles, square platens particles and line-shaped particles) were involved. The effects of particle shape on the flow regimes, concentration distributions, particle forces and transport stabilities at different velocities conditions were systematically explored. Chara et al. [335] carried out a similar investigation in water channel flow, where both the spherical particles and spherocylindrical multi-sphere particles were involved. Subsequently, the shape effects on the averaged particle height and the slope of the moving particle bed surface were emphatically discussed. Qu et al. [336] focused on the effects of particle shape on blockage in the slurry pipeline transportation. The simulation results

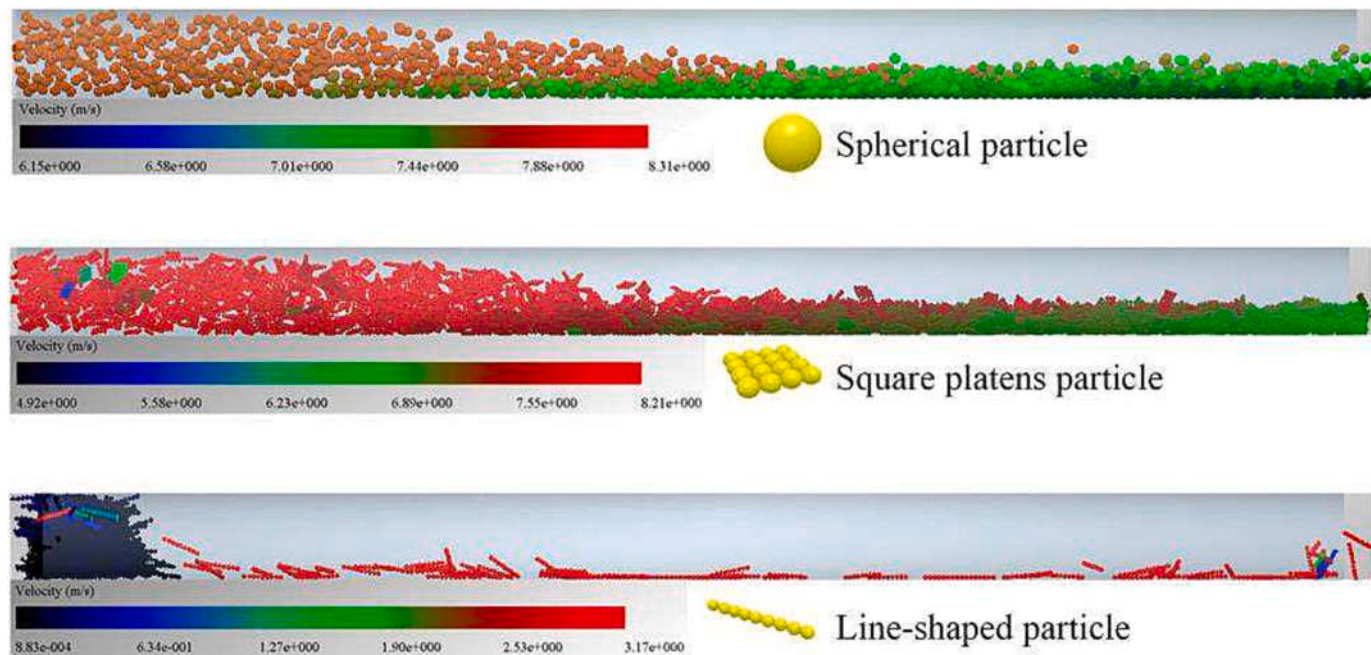


Fig. 60. Flow states of the differently shaped particles in a horizontal slurry pipeline (adapted from [189], Copyright 2019, with kind permission from Taylor & Francis).

revealed that the particles with higher sphericity could cause blockage with a higher possibility. Wang et al. [337] primarily investigated the flow characteristics of non-spherical multi-sphere ballasts in a slurry pipe. And then the effects of particle size, ballast volumetric concentration and slurry flow rates were examined. For evaluating the performance of solid-liquid flow behaviors in a newly designed pipeline transport system with a tangential jet inlet (see Fig. 61), Qi et al. [338] carried out a CFD-DEM investigation, where three types of non-spherical multi-sphere particles (the ellipsoids, cylinders and tetrahedrons) were included besides the spherical particles. The focus of this investigation was on the effect of different tangential flow proportions on the velocity distribution, total pressure, vorticity, concentration and drag force of differently shaped particles. As concerning the influence of particle shape specifically, the axial drag forces for cylindrical particles and spherical particles were the largest and smallest, respectively, and the ellipsoids and tetrahedrons possessed comparable force magnitudes. But the above difference could be narrowed by the influence of swirling flow. Ibrahim et al. [339] applied the CFD-DEM to simulate the conveying process of the food solid-liquid system in a bent horizontal pipe, in which the food particles were modeled as cubes using the multi-sphere model. And then the effects of flow velocities and particle mass concentrations were briefly discussed. Besides the flow behaviors, Zhao et al. [340] also numerically investigated erosion process in a 90° bend

for the transportation of dilute particle-liquid flows, and the particle shape effects were accounted for by the sphericity and the proposed particle shape coefficient. The results revealed bend erosion increased continuously as the mass loading of particles was increased to 10% in volume fraction, and the sharper particle would lead to less erosion at the given particle volume and concentration.

The process of well drilling encountered in various industries (e.g., the mining and petroleum industries) is also a common scenario for the particle transport involving the liquid flow. Taking the coal bed methane as the research background, Shao et al. [341–344] investigated the particle transport in the well drilling by the multi-sphere CFD-DEM model. The results suggested that the rather good transport performance happened to spherical particles while the cubic particles behaved worse, and the platy particles took the second place [341,344]. Moreover, they also investigated the double-circulation system for the transport of non-spherical cuttings [343]. In order to contribute deeper insight into the transport mechanisms during the well drilling process frequently encountered in petroleum industry, Akhshik et al. [82,195,196] developed the CFD-DEM model for carrying out the related numerical investigations, as illustrated in Fig. 62(a). Both the multi-sphere model and rolling resistance method were incorporated to account for the shape effects of particles and then for evaluating the performances of these two approaches. The evaluation results suggested that the multi-

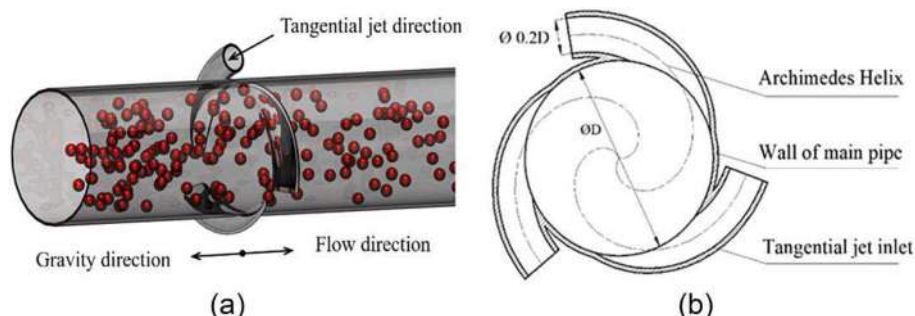


Fig. 61. Sketch map of the newly designed pipeline with a tangential jet inlet: (a) the spatial structure of the pipeline, and (b) the plane distribution of the tangential inlet (adapted from [338], Copyright 2021, with kind permission from Multidisciplinary Digital Publishing Institute).

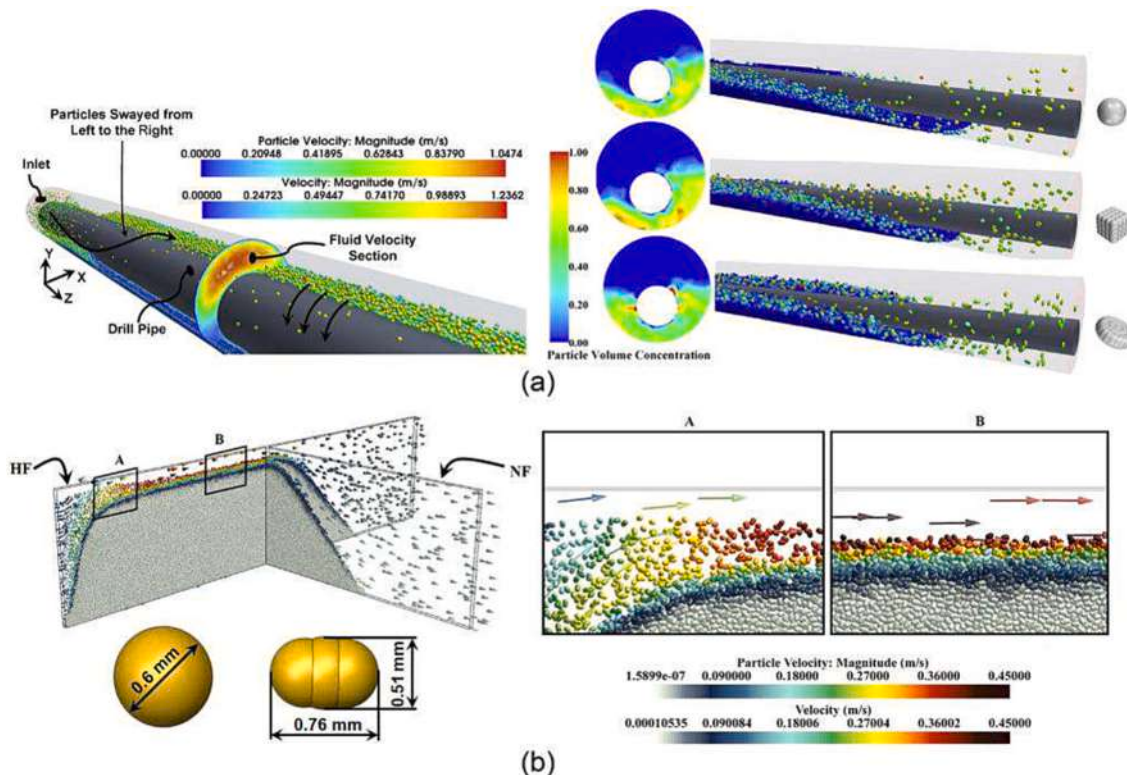


Fig. 62. Schematic of the particle transport behaviors encountered in the well drilling: (a) the particle behaviors in wellbores (adapted from [195], Copyright 2015, with kind permission from Elsevier); (b) the proppant transports in HF-NF intersection (adapted from [194], Copyright 2022, with kind permission from Elsevier).

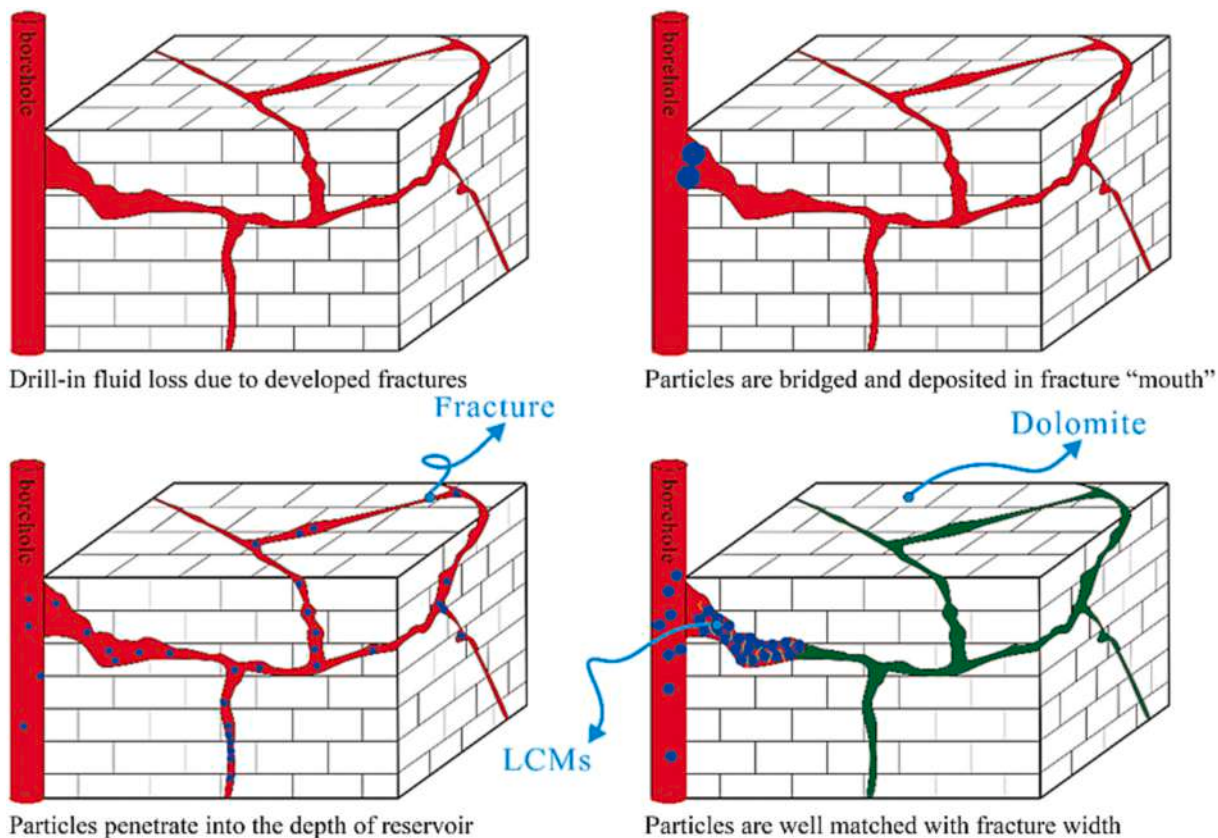


Fig. 63. Schematic representation of the bridging and plugging process of granular LCM in the fracture (adapted from [345], Copyright 2018, with kind permission from Taylor & Francis).

sphere model with larger number of component sub-spheres could replicate the transport behaviors of particles with higher accuracy, and the rolling resistance method can reduce the inaccuracy in predicting the particles hold-up and could be an alternative approach for reducing the computation cost. With the developed CFD-DEM model, the effects of particle shape (the spheres, disks and cubes) on the flow behaviors in the non-Newtonian fluid were further studied [195,196]. The results suggested that the particles with lower sphericity exhibited higher concentrations than the spheres at higher well inclination angles, whereas it is the opposite at low inclination angles that the particle concentration for spherical particles was slightly higher. In addition, the cleaning efficiency at the highly deviated hole and low fluid inlet velocities would be lower as the particle sphericity deviated from unity.

In the drilling process, there are also other issues should be considered. For example, Akhshik et al. [194] reported a CFD-DEM investigation for the proppant transport at the intersection of HF (hydraulic fracture) and NF (natural fracture) of wellbores, as shown in Fig. 62(b). The results revealed that the particle shape, fluid velocity, HF-NF intersection type and NF aperture could affect the flow characteristics and quality of blockage occurrence. For the particle shape effects specifically, the equilibrium bed height and repose angle would increase slightly with reducing the particle sphericity. Aided by CFD-DEM, Zhu et al. [345] simulated the transport behaviors of granular LCM (Lost Circulation Material) used for fracture plugging in the fracture, where the shape effect was account for by the rolling resistance model, as shown in Fig. 63. The simulation results suggested that the drill-in fluid loss rate would be impacted by the plugging process, structure of the plugging zone and particle size distribution. Moreover, the bridging probability would significantly increase with non-spherical particles.

Based on the immersed boundary method, Balachandran Nair et al. [234,346] developed a resolved CFD-DEM model for simulating the transport behaviors of deformable RBCs (Red Blood Cell) in blood flow, where the deformable RBCs were constructed by bonded-sphere model. For validation purposes, the CFD-DEM solver was subsequently applied to simulate the micro-scale flows with single and multiple RBCs. And an industrial application of CFL (Cell-Free Layer) enhancement for plasma separation was also simulated to examine the computational efficiency of the developed solver [234].

The particle transport in the gas-liquid-solid flow systems was also investigated by some scholars. For example, Alihosseini and Thamsen [347,348] reported a CFD-DEM investigation of the sediment transport in a sewer pipe, where the sediments were represented by multi-sphere particles and VOF (Volume of Fluid) was incorporated into the CFD to track the interface between the gas and liquid phases. According to the research findings, the critical velocity required to initiate the motion of the sediment bed would increase with the sediment size and bed roughness. But overall, the sediment size affected the critical velocity more than the bed roughness.

Just like the investigations of fluidization reviewed in Section 4.1, the effects of particle shape on the particle transport behaviors are also explored by many scholars. But the respect of shape effects for the applications of particle transport should be declined. In this research field, researchers often times omit the comparisons between the differently shaped particles, and the particles close to the realistic particle shape encountered in the practical applications are directly adopted. Moreover, the investigations for the internal mechanisms of particle transport are seemingly relatively few. In the future, more studies for revealing the underlying physics of particle transport should be conducted.

4.3. Particles separation

The separation of particle mixtures can be widely encountered in nature and industry. Usually, the achievement of particle separation should be essentially by making use of the differences in the inherent properties of particles (such as size, density and shape). Sometimes, particle separation can also be a problem in some solids handling

industries because of the requirement of homogeneity. Due to the complexity of the separation process (especially when the particle-fluid interactions are involved) and its wide application in industry, understanding the inherent mechanism of particle separation has drawn researchers' attention.

For separating the biological particles (e.g., the separation of grains and stalks), there are usually two approaches: air-and-screen cleaning and airflow cleaning [349]. Both cleaning approaches are intricate gas-solid two-phase flow systems. The air-and-screen cleaning device cleans bio-particles through a combination of the fan and vibrating screen, and one of the common applications is used on the combine harvesters. In order to provide a basis for improving the design of air-and-screen cleaning devices, a number of related CFD-DEM investigations with bio-particles generally approximating by the multi-sphere model have been conducted [350–359]. For the influence of the vibrating screen, the investigations conducted by Zhao et al. [350] (see Fig. 64(a)) revealed that the addition of a vibrating screen could decrease the trash rate of rice, but the entrained loss rate would increase accordingly. Wang et al. [351] further evaluated the cleaning performance of using different types of vibrating screens (including woven screen and shell screen). In the work of Dai et al. [352], they firstly compared the suspension characteristics of flax grains, capsules, short stalks and capsule husks in a vertical pipe for validating the proposed CFD-DEM model. And then the migration behaviors of flax threshing materials in an air-and-screen cleaning unit were investigated [353], as shown in Fig. 64(b). Xu et al. [354] simulated the movements of ternary threshed mixture containing grains, stems and light impurities in a multi-duct cleaning unit designed by themselves, as shown in Fig. 64(c). For ease of predicting the cleaning performance, they had made an attempt to mathematically derive a relationship to correlate the particle centroid velocity and dispersion degree with the measured cleaning performance based on the simulation results. Li et al. [355] designed a novel screen with sliding fingers and ladders for reducing the particle accumulation existing on the traditional planar-linear screen, as shown in Fig. 64(d). Then the separation performance of using the traditional and novel screen was evaluated according to the CFD-DEM simulation results. Feng et al. [356] applied CFD-DEM to study the particle motion at different stages of screening and the influence of airflow velocity above the sieve on the dispersion degree of particles. They argued that the research results could provide a theoretical foundation for improving cleaning performance. In the investigations of Li et al. [357] (see Fig. 64(e)), they further indicated that increasing the inlet airflow velocity could improve vibrating screen processing power, but the grain losses would also increase. Furthermore, Zhao et al. [350] analyzed the effects of inclination angle and device structure on the cleaning performance as well as the flow of particles and fluid. In contrast to the above scholars, a cylindrical sieve was used in the investigations of Yuan et al. [358,359], as shown in Fig. 64(f). And then the effects of inlet airflow velocity as well as the diameter, rotating speed aperture and deflectors of cylindrical screen on the movement rules and the separation effect of threshed rice mixtures components containing grains, shriveled grains and short stalks were systematically investigated with the help of CFD-DEM.

For the grain separating cleaning adopting the principle of airflow cleaning, one of the representative devices is the cyclone separator, as shown in Fig. 65. The cyclone separator should be the most common device applied in the agricultural processing industry, and it has been judged as one of the major cheapest and simplest devices for the segregation of gas-particulates matter [360,361]. Nevertheless, the cyclone separator has an intricate flow pattern phenomenon. Therefore, CFD-DEM simulations involving the separation of non-spherical bio-particles in a cyclone has been reported by some researchers. For example, El-Emam et al. [360–363] carried out a series of investigations for the separation of binary mixtures of real heterogeneous bio-particles (jojoba seeds and their leaves), where the bio-particles were treated as the polyhedrons. In their impressive investigations, both the standard and inverse-flow cyclone separator as well as the influences of

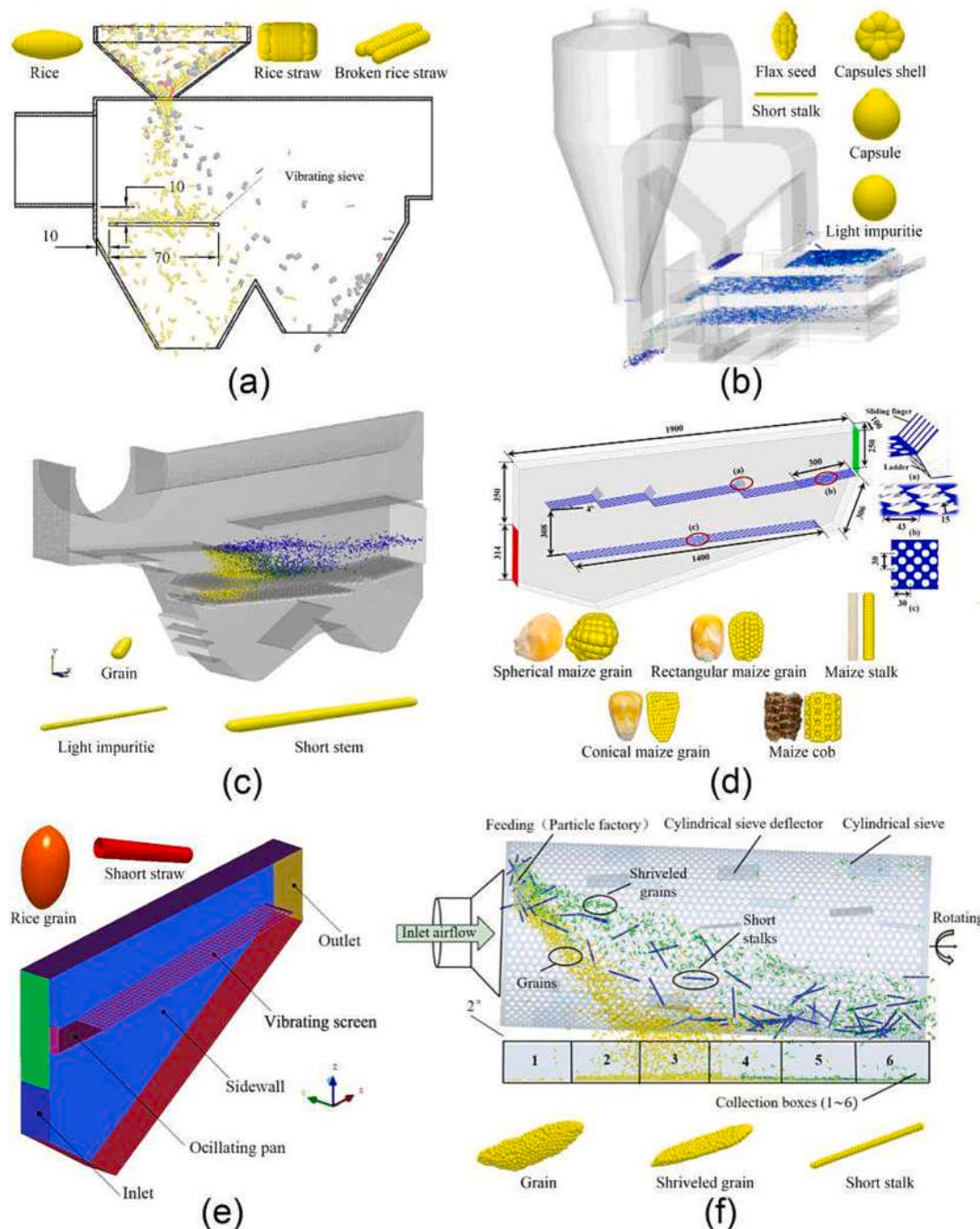


Fig. 64. Schematic representations of the simulated air-and-screen cleaning devices: (a) Zhao et al. (adapted from [350], Copyright 2022, with kind permission from Multidisciplinary Digital Publishing Institute); (b) Dai et al. (adapted from [353], Copyright 2021, with kind permission from International Journal of Agricultural and Biological Engineering); (c) Xu et al. (adapted from [354], Copyright 2019, with kind permission from Elsevier); (d) Li et al. (adapted from [355], Copyright 2021, with kind permission from Elsevier); (e) Li et al. (adapted from [357], Copyright 2012, with kind permission from Elsevier); (f) Yuan et al. (adapted from [359], Copyright 2019, with kind permission from Taylor & Francis).

operational parameters (e.g., the leaves mass loading to seeds ratios, cylindrical and conical lengths, and position and dimension of the involute inlet portions and cyclone diameter) were seriously studied, and the performances between these two types of cyclone separators were compared. Dang et al. [364] further investigated the influences of inlet and outlet airflow velocities on the cleaning performance while they simulated the movement of the soybeans and straw in a bucket-free cyclone separator by the multi-sphere CFD-DEM model. In addition, Dai et al. [365] also conducted a CFD-DEM research for the separating cleaning process of flax threshing materials and then for evaluating the working performance of the cyclone separator.

Besides the cyclone separators, other airflow cleaning devices have also attracted attention from scholars. Using the device sketched in Fig. 64(a) where the vibrating screen was removed, Ma et al. [366] numerically investigated the migration law and separation behavior of rice and its impurities under different airflow velocities and airflow inclined angles. Hu et al. [367] investigated the movement characteristics and separation mechanism of safflower petals and their impurities in a safflower sorting device by multi-sphere CFD-DEM, and the effects of dust remover angle, inlet airflow velocity and airflow inclined angle on the cleaning performance were examined. In the CFD-DEM investigation performed by Jiang et al. [368] about the separation of non-

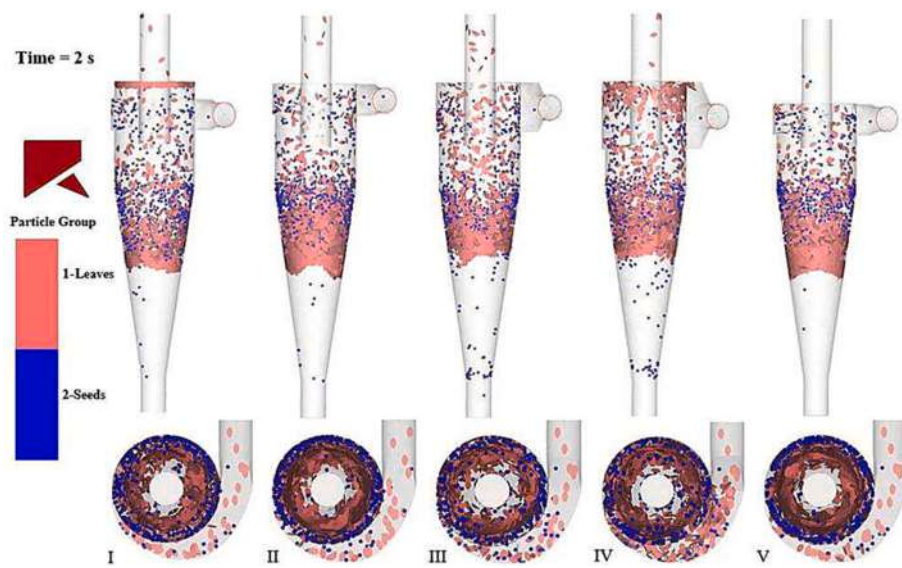


Fig. 65. Schematic illustration of the simulated cyclone separator (adapted from [360], Copyright 2019, with kind permission from Elsevier).

spherical grains and short straws in the inertia separation chamber of combine harvester threshing prior to cutting, they demonstrated that increasing the airflow velocity could improve the performance of chamber separating and cleaning grain, while there would be more severe turbulence phenomenon in the rear of the chamber and then the pressure drop would be elevated. For the sake of clarifying and improving the working performance of the tapered threshing device for plot breeding, Dai et al. [369] reported a CFD-DEM research for the motion process and separation behaviors of threshed materials containing wheat and their stalks in the longitudinal-axial tapered cylinder

threshing and transmission device. Almeida et al. [370,371] developed a CFD-DEM model for simulating the pneumatic separation of sugarcane bagasse particles. In the numerical investigation of Pieper et al. [372], a new prediction approach on the basis of particle tracking was devised and then incorporated into their multi-sphere CFD-DEM model for simulating an optical belt sorter of peppercorns, coffee beans and maize grains with higher accuracy.

In addition to the above, there are also other applications involving particle separation in the air flow. For example, Petit et al. [375] numerically evaluated the performance of the cross-flow air classifier in

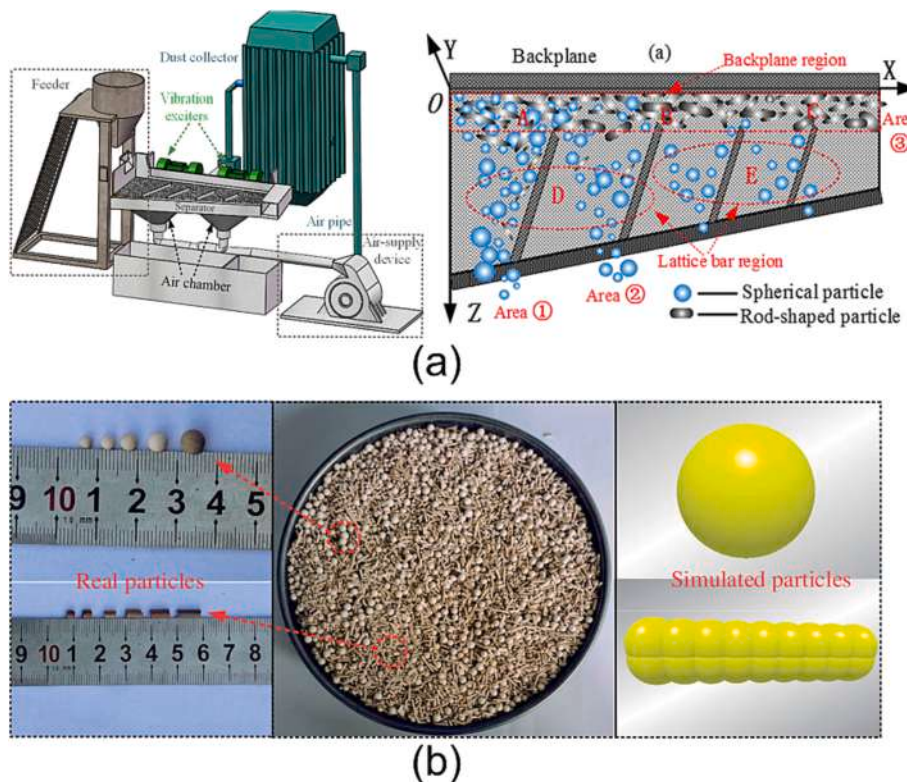


Fig. 66. Investigating the separation of waste catalysts in a separator: (a) the schematic of compound dry separation system (adapted from [373], Copyright 2020, with kind permission from Elsevier); (b) the raw materials and simulated particles in DEM (adapted from [374], Copyright 2018, with kind permission from Taylor & Francis).

the manufactured sand processing by CFD-DEM, where the shape effects were considered as particles with the sphericity of 0.7. Subsequently, the influences of air inlet velocity on the particle size distribution and mass production were assessed, and they argued that air classification was applicable for replacing the traditional washing process. For better recycling of the waste catalysts in petroleum industry, the particle behaviors and separation mechanism of waste catalysts in a compound dry separator were numerically investigated using CFD-DEM by Qiao et al. [373,374] (see Fig. 66(a)). As illustrated in Fig. 66(b), the raw materials were composed of spherical particles and rod-like particles in their investigations, in which the rod-like particles approximated by the multi-sphere model in DEM. The simulation results indicated that the rod-like particles and spherical particles would incline to distribute in different regions of the separator. The importance of both single factor and factor combination was examined. And then the optimal operational conditions and structures of the separator were determined to maximize the separation efficiency.

In practice, the separation of particles in the liquid-particle flow systems should also be often encountered. To our knowledge, for instance, the solid-liquid filtration is the separation of particles from the fluid by filter media, and some related CFD-DEM investigations can be available in the published literatures. For the static surface filtration, the particles deposit on the surface of the filter medium, where the filter cake would be formed due to the accumulation of solid particles, and the so-called bridging that the pores are blocked by the accumulated particles would be created, as sketched in Fig. 67(a). Hund et al. [376] performed the corresponding CFD-DEM investigations for better understanding the bridging mechanism, as shown in Fig. 67(b). Both the spheres and spherocylinders constructed by the multi-sphere model were considered in their study for determining the influence of particle shape. In comparison with spherical particles, the formation of bridging for spherocylindrical particles would be finished earlier. Deshpande et al. [377] further investigated the formation of filter cake during the filtration of suspension with non-spherical particles by multi-sphere CFD-DEM. The intricate interdependencies of the particle sphericity, voidage fraction and pressure drop of the filter cake for a wide range of fluid conditions were subsequently analyzed. To gain bionic inspiration from biological filtration for improving the traditional filters, Zhu et al. [378] numerically studied the filtering mechanism in balaenid whale filter feeding, where the spherical and non-spherical multi-sphere prey particles were contained for examining the shape effects, as presented in Fig. 68. The influences of fringe layer permeability, size and shape of the food particles as well as particle incident direction were earnestly explored. As concerning the effect of prey shape, there were no obvious differences in the number of prey at each location for different types of

incident directions, but the variation of the particle distribution for non-spherical prey particles was not as smooth as for the sphere case.

So far, numerous CFD-DEM researches for the particle separation involving non-spherical particles have been reported. Nevertheless, there should be still many issues that are require to be studied by non-spherical CFD-DEM in the future. For instance, the investigations for the internal mechanisms of governing the separation behaviors in the fluid-particle systems containing non-spherical particles should be not sufficiently abundant, especially when comparing with the flourish of researches involving spherical particles or particulate systems without the influence of fluid.

4.4. Other applications

In addition to the aforementioned processes, efforts have also been made to employ the CFD-DEM approach to investigate other applications. For the sediment of a single particle, Lv et al. [379] experimentally and numerically investigated the dynamic behaviors of fine kaolinite particle sedimentation. Within the CFD-DEM framework, only the sphericity in calculating the drag force was used to quantify the irregularity of kaolinite particles. Subsequently, the influences of particle size, liquid velocity and liquid viscosity on the sedimentation characteristics were investigated. Moreover, the fully resolved CFD-DEM model was also developed for investigating the single particle sediment. As illustrated in Fig. 69, Ma et al. [218] focused on the sediment of an isolated ellipsoid particle generated by the multi-sphere model with assembling 49 sub-spheres in the viscous fluid. The investigations indicated that the ellipsoid presented large “wiggles” down the square tube at 45° angle, and the “wiggles” would gradually decrease in a time due to the influence of fluid viscosity dissipation.

With the experiments and CFD-DEM simulations, Yang et al. [190] investigated the suspension behaviors of a single non-spherical particle in a vertical pipeline, where the non-spherical particles were constructed by the multi-sphere model, as presented in Fig. 70. The results indicated that the flow field greatly affected the particle rotation only when the particle size was large. And the rotation of large non-spherical particles in the vertical flow field could reduce the particle suspension velocity. For the suspension behaviors of granular assemblies, Mahajan et al. [380] numerically investigated the rheology of suspensions of high-inertia spherocylindrical particles with an aspect ratio of 4 subjected to shear flow, as shown in Fig. 71. While the fluid medium was air, it presented the similar scaling as compared to dry granular simulations except for the lower stress values. Whereas there would be the remarkable change while the fluid medium was water. But in all cases, the spherocylindrical particles possessed a strong alignment in the shear

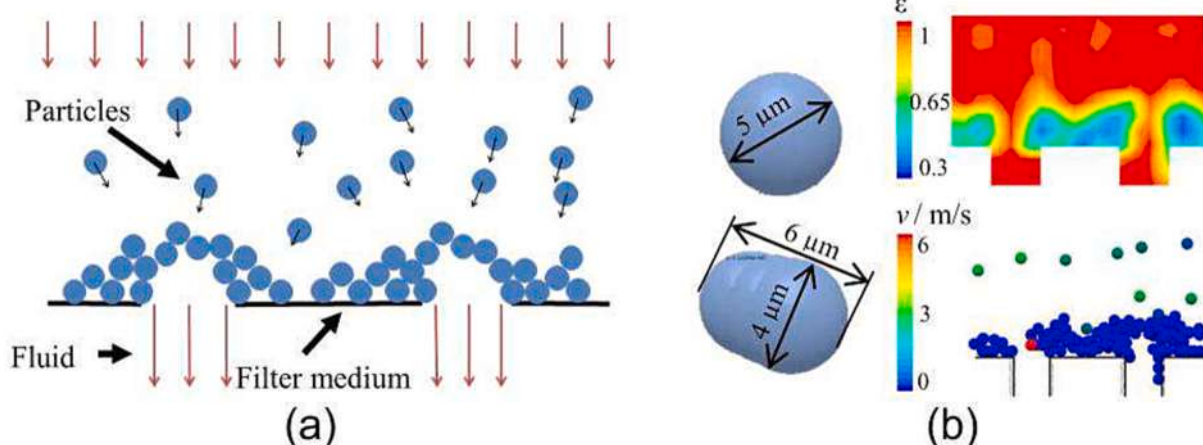


Fig. 67. Illustration of the solid-liquid filtration: (a) the schematic of the bridging mechanism and (b) the CFD-DEM studies of the bridging mechanism (adapted from [376], Copyright 2017, with kind permission from EPJ Web of Conferences).

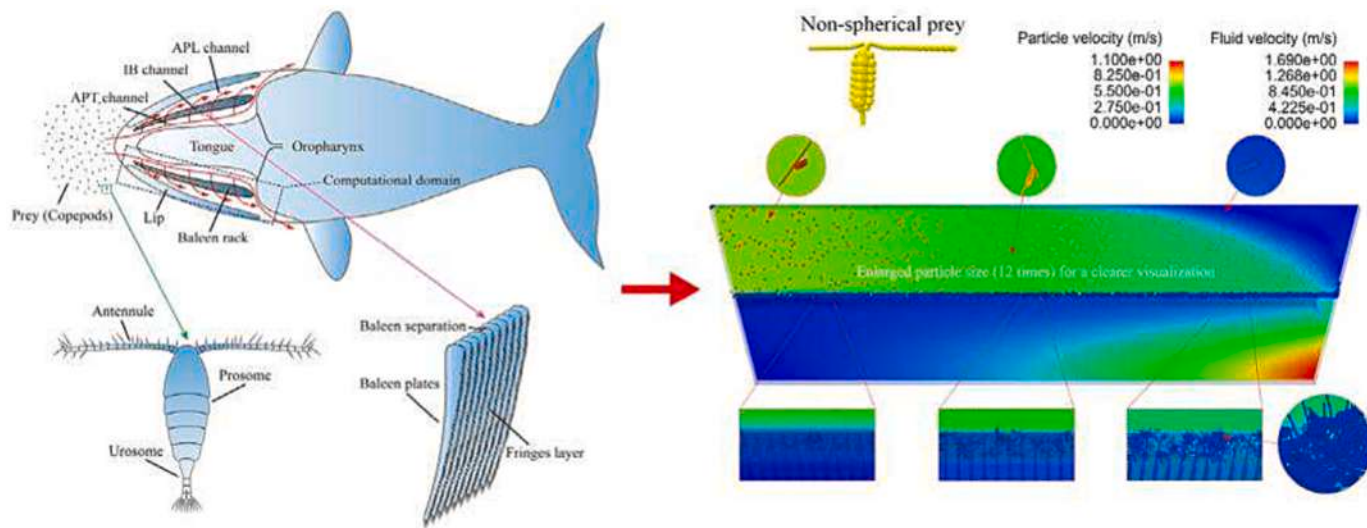


Fig. 68. Illustration of the simulated solid-liquid separation in the balaenid whale filter feeding (adapted from [378], Copyright 2021, with kind permission from Elsevier).

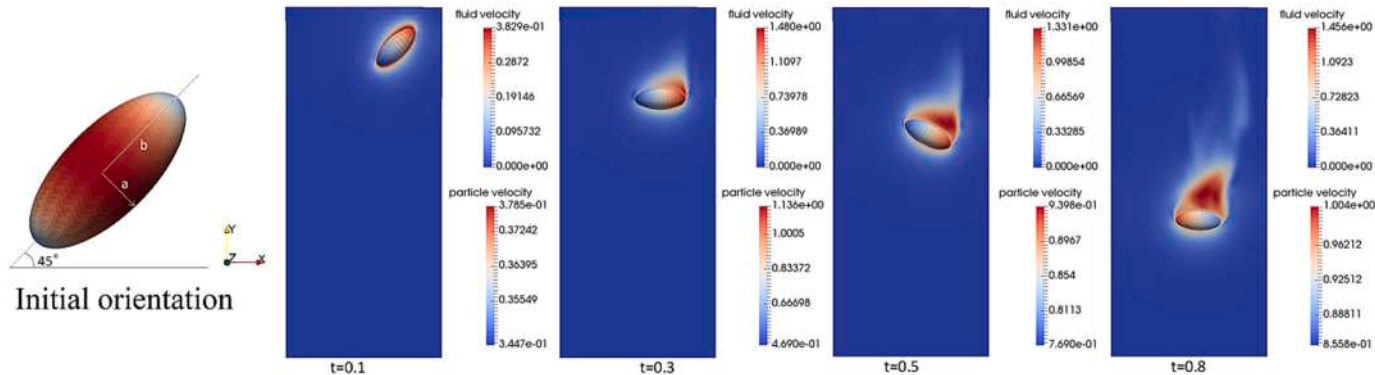


Fig. 69. Contours of the velocity magnitude for the sediment of an ellipsoid (adapted from [218], Copyright 2017, with kind permission from Taylor & Francis).

direction. Redlinger-Pohn et al. [381,382] applied the CFD-DEM to investigate the solid-liquid suspension behaviors of non-spherical fiber particles in a coiled tube, where the fibers were represented as spherocylinders and prolate ellipsoids. Moreover, Isoz et al. [235,383] developed a fully resolved CFD-DEM model for simulating the arbitrarily-shaped particles. And then the suspensions as well as the depositions were simulated for testing the capabilities of their in-house CFD-DEM solver.

Xiong et al. [384] reported a CFD-DEM investigation for examining the influence of particle shape on the suffusions that should be the most common cause of hydraulic geological structure failures, in which the shapes of fine particles were spherical and the coarse particles were represented by polyhedrons with different aspect ratios, as illustrated in Fig. 72(a). According to the numerical results, the particle shape should have an inhibitory effect on the erosion, and more fines were lost in the upper layer while the particle shape was closer to the sphere. Moreover, the influence of particle angularity on the suffusions was further numerically investigated by Qian et al. [385], where the coarse particles were considered as quasi-spherical polyhedrons with different angularities, as shown in Fig. 72(b). They argued that the angularity could also intensify the erosion resistance as the fines loss decreased greatly with the angularity. Furthermore, the soil peak strength and friction angle were approximately linearly correlated with angularity.

The CFD-DEM approach could also be employable in ship engineering. One typical application is to solve the ship-ice interaction

problems, as shown in Fig. 73. For example, Seo and Wang [386] applied the CFD-DEM to predict the ice resistance and broken ice behaviors around the hull, where VOF was introduced to resolve the gas-liquid two phase problem and the ice particles were modeled by the polyhedron approach. And then the sensitivity studies to friction and restitution coefficients were performed. For simulating the ship advancing in floating ice floes, Huang et al. [387] put forward a high-fidelity CFD-DEM model with integrating the VOF, which should be the pioneering research of successfully achieving the modeling of ship-wave-ice interactions. With this established CFD-DEM model, they subsequently simulated three different types of ships with varying environmental and operational conditions to derive an empirical correlation for the quick prediction of the influence of ice floes on ship resistance [388]. With CFD-DEM, Guo et al. [389] proposed a virtual mass method to evaluate the total resistance for the ice-going ship in the floe ice region. And then they conducted the following research by the established method to investigate the ship-ice interaction behaviors (e.g., the virtual mass coefficients and total resistance for ice-going ships) on the random and fixed distributions of floe ices in the different ice concentrations [390]. In the investigation of Luo et al. [391], an ice-strengthened bulk carrier navigates through brash ice channel was numerically studied by CFD-DEM-VOF, where two representative ice shapes (tetrahedron and polyhedron) described by multi-sphere model were included. Subsequently, the performance of ship resistance and the mechanism of ship-ice-water interactions in brash ice channels were explored. Besides the ship-ice

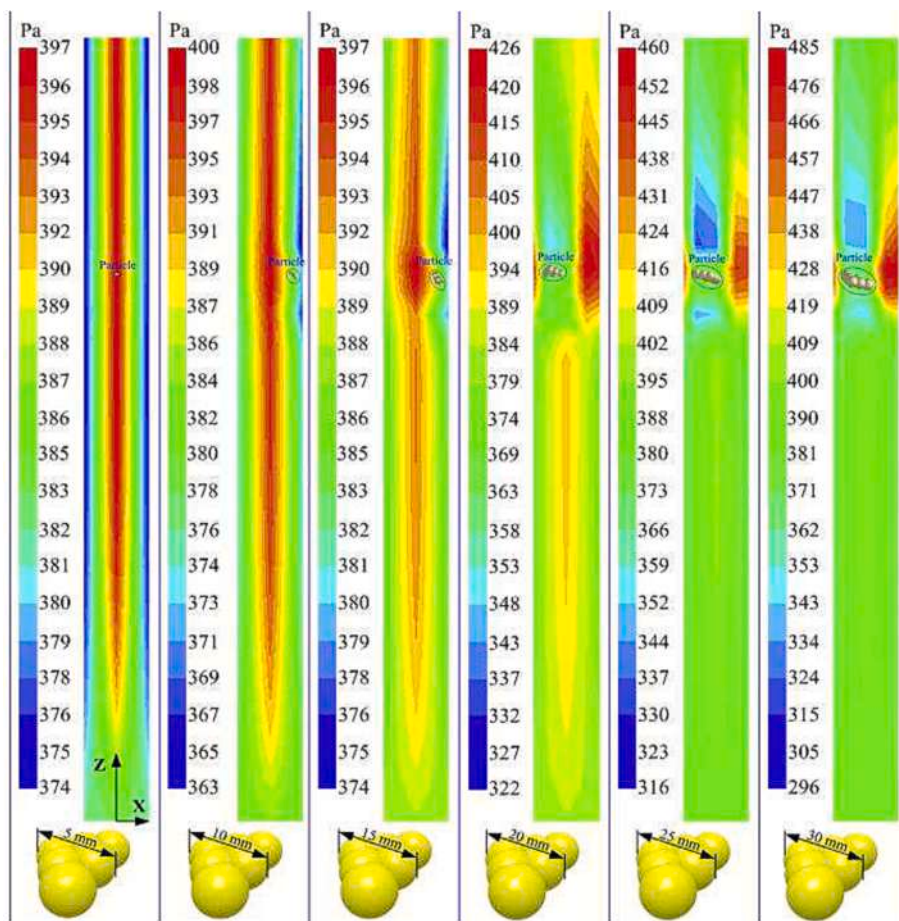


Fig. 70. Instantaneous dynamic pressure of the flow field in a vertical pipeline (adapted from [190], Copyright 2019, with kind permission from Elsevier).

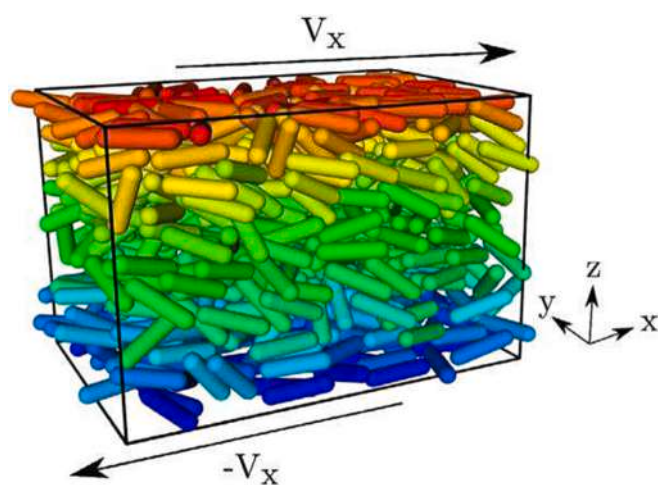


Fig. 71. Snapshot of the particle suspension behaviors under the shear flow (adapted from [380], Copyright 2019, with kind permission from Elsevier).

interaction problems, Nan et al. [392] also developed a multiphase fluid-solid solver by coupling CFD, DEM and VOF for studying the dynamic behaviors of the drifting boat with different densities, where the hull was approximated by the multi-sphere model (see Fig. 74). They found that the hull weight would impact the ship drifting motion significantly.

For investigating the particle-fluid flow behaviors containing dust particles more deeply, the CFD-DEM approach has also been introduced. In order to provide a theoretical foundation for dust protection and

cleaning in a Martian dust storm, for example, Hou et al. [393] investigated the creeping behaviors of non-spherical Martian dust particles by CFD-DEM, where the shapes of dust particles were analyzed by fractal theory and then approximated as multi-sphere particles. Subsequently, the effect of wind speed on the speed of non-spherical Martian dust particles and the dust removal rates of different particles were analyzed. Also aided by multi-sphere CFD-DEM approach, Hu et al. [394] investigated the formation mechanism of brownout in a full-scale helicopter. Based on the simulation results, the impact of the ground effect flow field on the state of the dust particles and the formation mechanism of dust clouds were explored.

The primary purpose of the following introductions is to review the applications that the non-spherical CFD-DEM approach were used, but there was only a tiny number of researchers to carry out the corresponding CFD-DEM studies. Based on the fluid medium, the CFD-DEM investigations involving the gas medium are presented in this paragraph, and the related studies for the liquid medium will be reviewed in the next paragraph. By CFD-DEM, Gou et al. [395] modeled the densification of uniform tetrahedron multi-sphere particles under the air impact, as presented in Fig. 75(a). The influence of air impact on packing structures, including packing density, radial distribution function and coordination number, were examined. And the densification mechanism was also explored for a deeper understanding of the densification process. Using the resolved multi-sphere CFD-DEM and pure CFD approaches, Baghban et al. [396] numerically studied the effective thermal conductivity of the geothermal pavement system when constructed using construction and demolition materials, as shown in Fig. 75(b). The results demonstrated that the CFD-DEM should possess high prediction accuracy than the CFD simulations. Furthermore, they also found that decreasing the voidage fraction, gravel content and

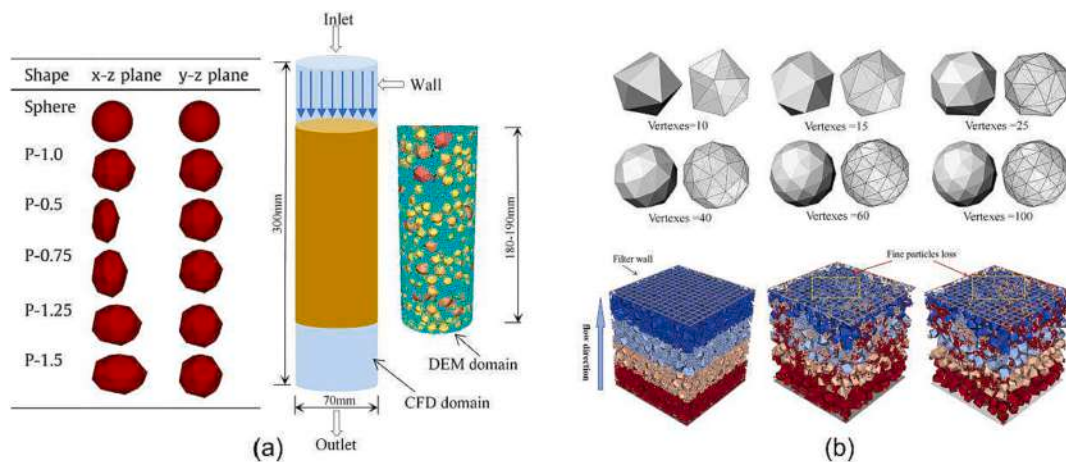


Fig. 72. Illustration of the suffusion process: (a) Xiong et al. (adapted from [384], Copyright 2021, with kind permission from Elsevier); (b) Qian et al. (adapted from [385], Copyright 2021, with kind permission from Elsevier).

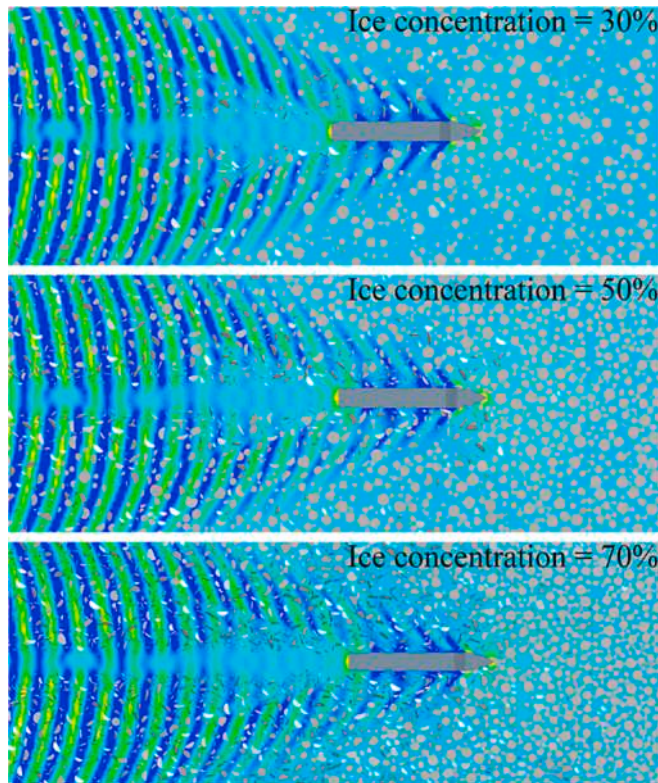


Fig. 73. Illustration of the simulated ship advancing in floating ice floes with different ice concentrations (adapted from [387], Copyright 2020, with kind permission from Elsevier).

particle aspect ratio could increase the effective thermal conductivity. Boehling et al. [188] developed a high-fidelity CFD-DEM model incorporating the heat and mass transfer model as well as coating model for reproducing the tablet coating process in a GEA ConsiGma® coater, in which the tablet particles were modeled by combined geometric element method. Subsequently, the prediction accuracy of the established CFD-DEM model was validated by comparing with the experimental outcomes. Wang et al. [193] developed a multi-sphere CFD-DEM framework for modeling the granular flows with charged particles under the action of the electric field. Subsequently, the dynamic flow behaviors of charged particles in a gas insulated switchgear were numerically investigated.

As the continuation of the last paragraph, this paragraph focuses on particle-fluid systems involving the liquid medium. Guo et al. [397,398] studied the particle shape effects on soil erodibility under the water flow by CFD-DEM, in which the non-spherical soil particles were represented by prolate ellipsoidal multi-sphere particles, as shown in Fig. 76(a). The results indicated that the erosion rate was linearly proportion to the flow velocity, and the irregularity of particles would intensify the erosion resistance that would increase with the aspect ratio of ellipsoids. Zhou et al. [399] reported a CFD-DEM study on the flow of chip-like multi-sphere particles in a stirred tank filled with liquid for the graphene production process. During the liquid-stirring process, the particles inclined to accumulate in the vicinity of the bottom wall, and the particles would stay in the accumulation area for a long time. Jayathilake et al. [400] used CFD-DEM to study the rod-like bacterial twitching on the surface under shear flow conditions, where the rod-like bacterial was described as a certain number of spherical particles, as shown in Fig. 76(b). The impacts of surface topography and fluid flow rate on the twitching motility were explored in this study. Zhang and Tahmasebi [131] simulated the collapse processes of dry granular systems by DEM and wet granular systems by resolved CFD-DEM, as presented in Fig. 76(c), in which the level set function model was used to describe the particles. The simulation results revealed that the particle shape had an important influence, but the shape effects could be significantly ameliorated by the presence of liquid due to the impacts of viscous and lubrication effects of liquid. Song et al. [401] numerically investigated the flow, clogging and unclogging dynamic behaviors of ellipsoidal and spherical particles, in which the ellipsoids were described by the multi-sphere model, as shown in Fig. 76(d). The simulation results demonstrated that the unclogging pressure gradient for ellipsoids was significantly higher than spheres, the clogging arches of ellipsoidal assembly possessed much higher stability than that of spherical assembly that the orientations of ellipsoids could greatly affect the strength of clogging arches. For investigating the pressure dip phenomenon within the conical sandpiles, Wang et al. [83] simulated the formation process of sandpiles in both dry and submerged conditions, as shown in Fig. 76(e). In the simulations, non-spherical multi-sphere particles and spherical particles with and without rolling resistance were considered. The simulation results indicated that the sandpiles in the submerged condition usually possessed more homogeneous internal fabric structures, thereby alleviating the pressure dip. And the presence of water could lead to a flat pattern of sandpiles for spherical particles, but it affected non-spherical particles little.

Besides the CFD-DEM approach, the SPH-DEM coupling model has also been applied to simulate the dynamic behaviors of non-spherical particles involving liquid flows due to the superiority of SPH in

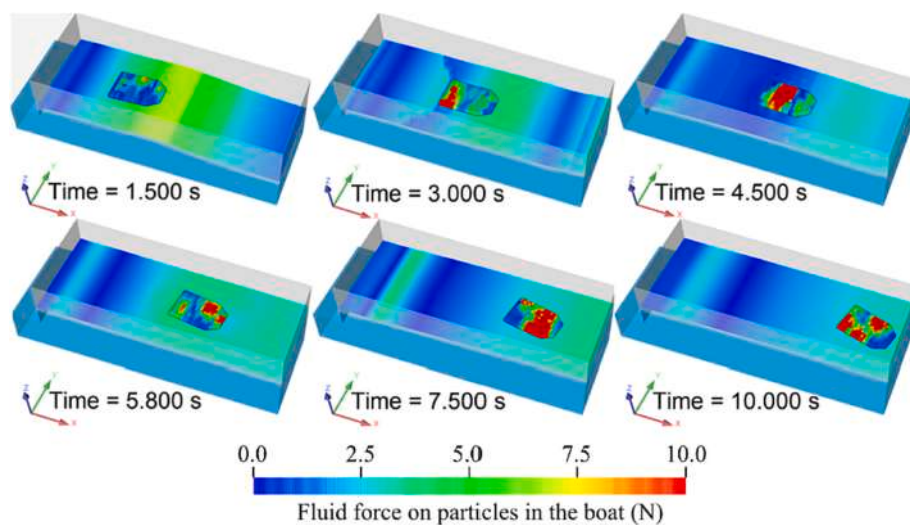


Fig. 74. Motion of the hull on the water surface (adapted from [392], Copyright 2022, with kind permission from Elsevier).

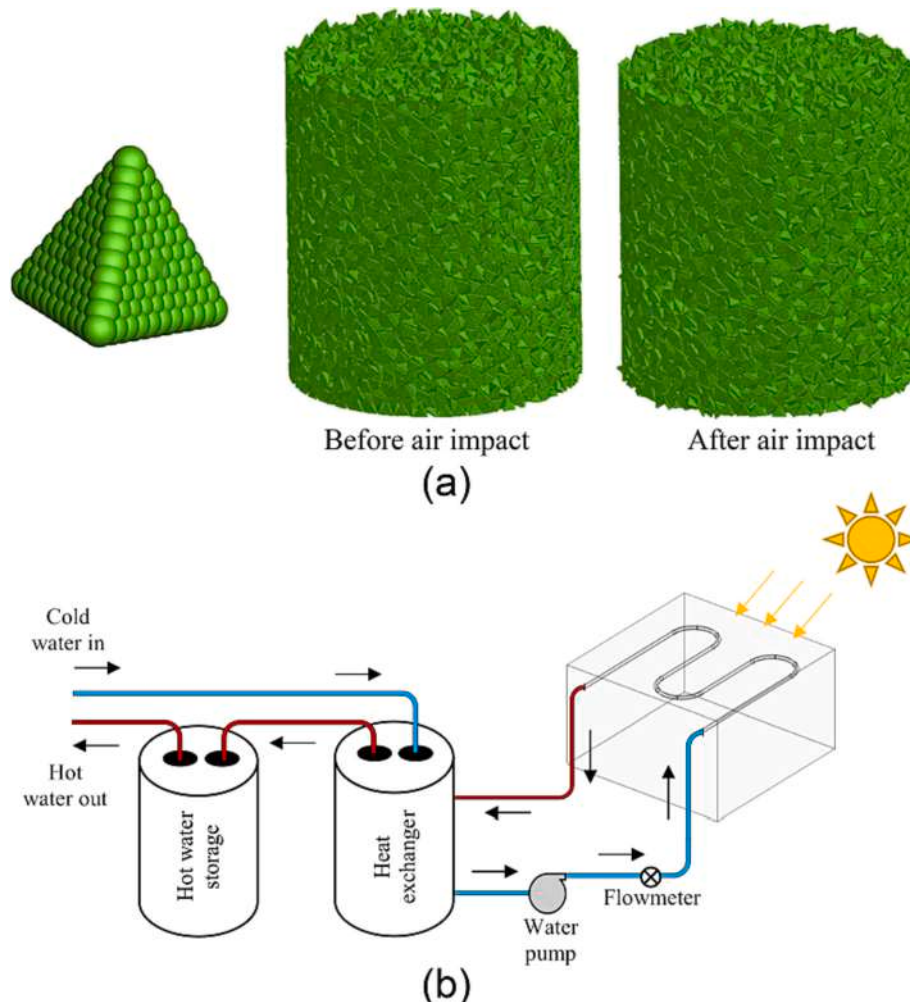


Fig. 75. Schematic illustrations of the simulated particle-gas systems: (a) the densification process (adapted from [395], Copyright 2020, with kind permission from Elsevier); (b) the geothermal pavement system (adapted from [396], Copyright 2021, with kind permission from Springer Nature).

modelling free surface behaviors [402–414]. For example, Cleary et al. [402–406] successfully developed a SPH-DEM model with using the super-ellipsoid model to describe non-spherical particles. With the SPH-DEM model, various industrial processes containing the liquid phase

were simulated and investigated, including the food processing operations (the solid particulate blending in a ribbon blender, liquid mixing in a planetary mixer, sieving of fine cohesive flour, particle size reduction of almonds fragmented in a food processor, delivery of post-mix soft

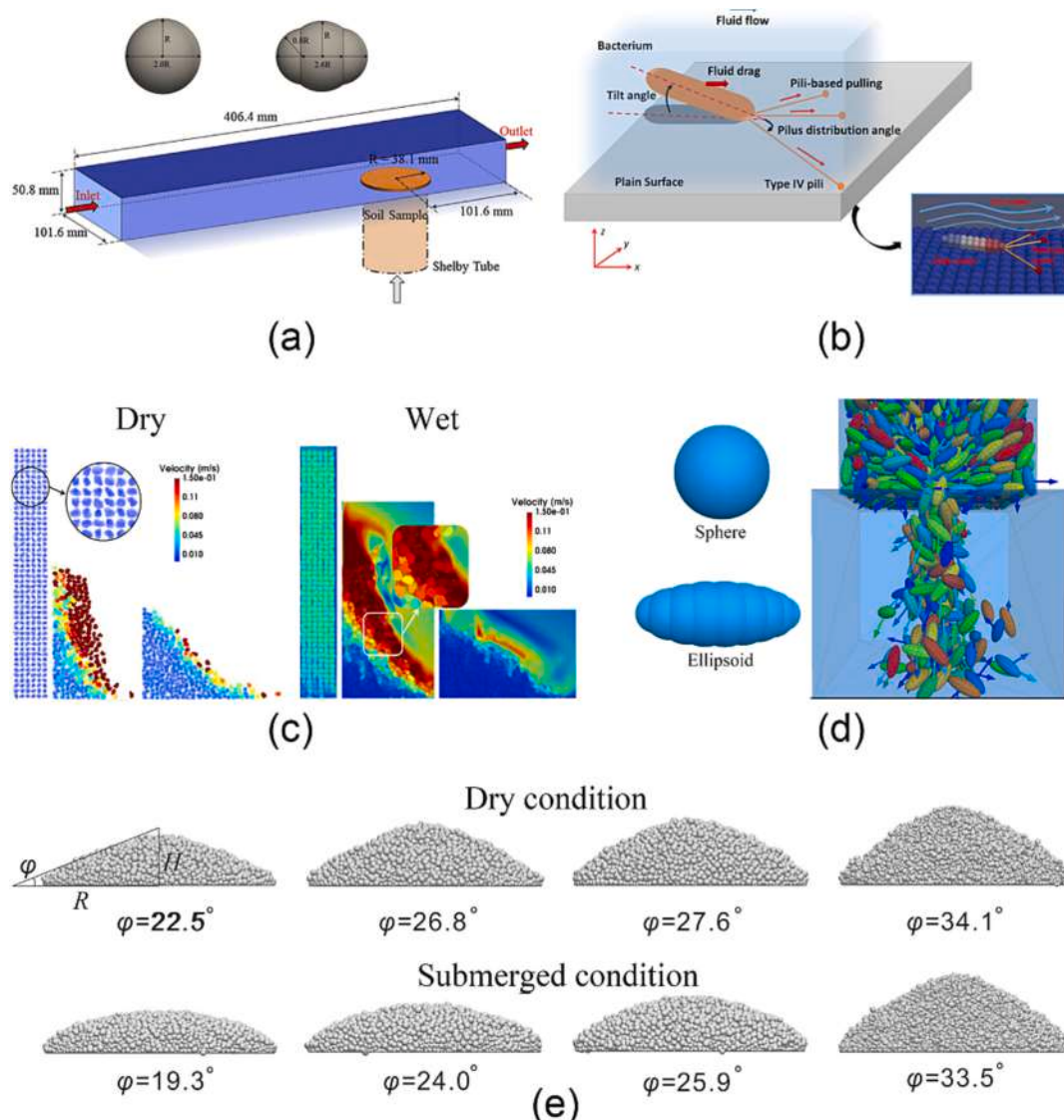


Fig. 76. Schematic illustrations of the simulated particle-fluid flows involving the liquid medium: (a) the dimensions of the soil erosion simulation model (adapted from [398], Copyright 2018, with kind permission from Elsevier); (b) the bacterial twitching model (adapted from [400], Copyright 2019, with kind permission from Springer Nature); (c) the collapse process of particle assemblies in the dry and wet particle systems (adapted from [131], Copyright 2021, with kind permission from Elsevier); (d) the flow and clogging dynamic behaviors of particles (adapted from [401], Copyright 2021, with kind permission from Elsevier); (e) the conical sandpiles and their repose angles (adapted from [83], Copyright 2022, with kind permission from Elsevier).

drink and multiphase flow of ice and liquid in a Slushie machine) [403], water and particulate mixing in a feed box [404], flow and breakage of particles in a semi-autogenous mill [405] and laser powder bed fusion additive manufacturing process for Ti-6Al-4V [406], as presented in Figs. 77(a) and (b). Natsui et al. [413] also incorporated the multi-sphere model into SPH-DEM, and the molten slag trickle flow in coke bed was then studied. Furthermore, the polyhedron model was integrated into the SPH-DEM model by some other scholars such as Sizkow and El Shamy [411], Nassauer et al. [412], etc. Sizkow and El Shamy [411] further analyzed the dynamic response and liquefaction of saturated level and gently sloped granular deposits based on the SPH-DEM simulation of the liquefaction of saturated granular deposits during the violent seismic ground motions. In the studies of Ji et al. [407–410], both dilated polyhedron model and super-ellipsoidal model were incorporated into their SPH-DEM model, and the model capability was demonstrated by the example applications such as dam break, water entry process of particles and particle-liquid coupling in a rotating drum. Subsequently, the rock dumping process for evaluating whether the rock particles could provide enough constraints to submarine pipe or cable

was investigated [409], as presented in Fig. 77(c). In addition, Peng et al. [414] put forward a SPH-DEM model based on the resolved concept for studying heterogeneous suspensions with arbitrary particle shape.

Based on the studies listed above, it can be found that the application range of non-spherical CFD-DEM approach has been extended compared with just a few years ago, though there might be only one available CFD-DEM investigations for some applications. This should also better prove the capability of CFD-DEM approach in modeling non-spherical particle systems in different scenarios. In addition, this might encourage researchers to carry out more CFD-DEM investigations for the applications that the CFD-DEM approach is seldom or even never used in the past. Then the application range of CFD-DEM can be further extended in the future, and the CFD-DEM could play a more important role in academia and industry.

5. Conclusions and outlook

This paper is designed to furnish a relatively comprehensive and

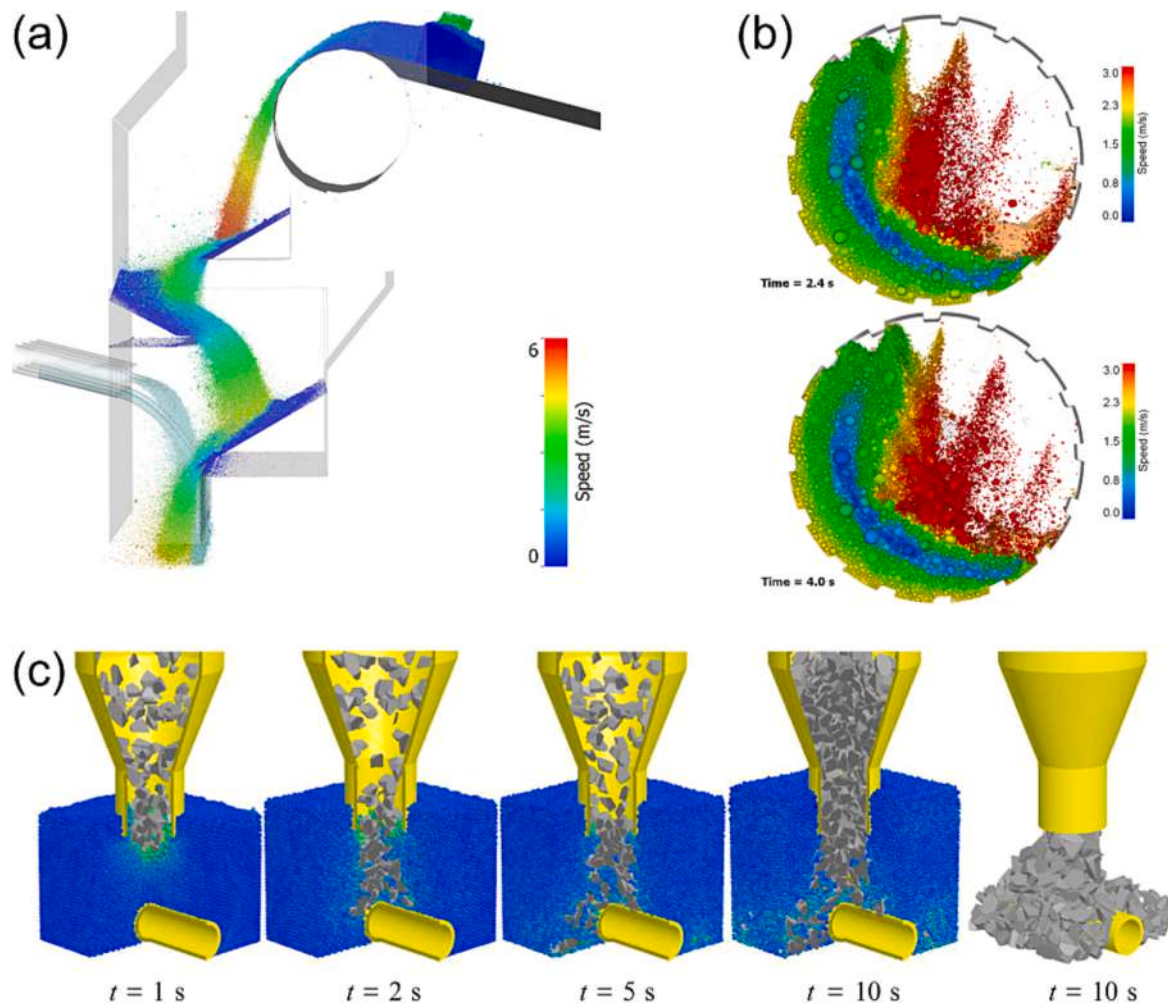


Fig. 77. Schematic representation of the SPH-DEM simulations: (a) the flow of particles through the entire feed box (the solid particles are colored by speed, and the SPH fluid is colored by light blue) (adapted from [404], Copyright 2017, with kind permission from Elsevier); (b) the flow behaviors of particles in a semi-autogenous mill (adapted from [405], Copyright 2020, with kind permission from Elsevier); (c) the rock dumping process (adapted from [409], Copyright 2020, with kind permission from Elsevier).

state-of-the-art review by collecting the literatures published in recent years that used the CFD-DEM coupling approach as a research tool for modeling and investigating the particle-fluid systems, limited to non-spherical particles. Toward this goal, the theoretical foundations of DEM for modeling non-spherical particles are firstly reviewed, including the principle of governing the particle motion, the particle models for describing non-spherical particles as well as the corresponding contact detection algorithms for detecting the contact between particles, the cohesion forces and the particle-fluid interaction forces (e.g., the drag force and lift force). Subsequently, the strategies for the coupling of CFD and DEM are introduced. According to the ratio of CFD cell size ΔL to particle size d_p , there are three coupling schemes: the unresolved CFD-DEM coupling model that ΔL is much greater than d_p and the particle-fluid interaction force is determined by the empirical force models using the local flow field data, the resolved CFD-DEM coupling model that ΔL is far less than d_p and the particle-fluid interaction forces are directly solved by the exact particle-fluid interaction process along the particle boundary surface, and the semi-resolved CFD-DEM coupling model that ΔL is comparable to d_p and the particle-fluid interaction forces are also predicted by the empirical force models but using the flow field data in the local and neighboring CFD cells. In the end, the use of the CFD-DEM approach for investigating the flow behaviors of non-spherical particles in different application areas (including the fluidization of particles, particle transport, particle separation and some

other applications) is reviewed.

Benefiting from the collective effort of numerous scholars, the CFD-DEM approach in modeling and investigating the non-spherical particle has made significant progress in recent years. However, there are still some limitations for the current non-spherical CFD-DEM approach. In our view, the CFD-DEM model for non-spherical particles can be improved from the two aspects of accuracy and efficiency:

1. Accuracy: Currently, the CFD-DEM approach for modeling spherical particles is rather accurate and mature, but it is not the truth for non-spherical CFD-DEM. Specifically, many sub-models required in the CFD-DEM model for accurately simulating the flow of non-spherical particles are still imperfect or even non-existent.

1) For calculating the contact force between the contacting non-spherical particles, the contact force models originally developed for spherical particles are commonly applied at present, e.g., the linear spring-dashpot model and Hertz-Mindlin model. However, this should go against the prediction accuracy of non-spherical particles while using some contact force models (such as the Hertz-Mindlin model) that, for example, the determination of the size of the contact plane would be significantly simplified for non-spherical particles.

2) The current cohesion force models are developed primarily for spherical particles, whereas there are rare scientific investigations for non-spherical particles. To our knowledge, for example, only Zhou et al. [100,103,146] ever incorporated the van der Waals force model into

their in-house CFD-DEM model for investigating the flow behaviors of ellipsoidal particles. In addition, some theories (e.g., the DMT theory [415] and JKR theory [416]) can also be used for predicting the cohesion force of non-spherical particles. For example, Nan et al. [417] used the JKR theory in their DEM simulations of the packing of rod-like particles. However, the non-spherical particles were generally constructed by the sphere-based model (e.g., the multi-sphere model), and the use of these theories for non-spherical particles is essentially on the base of spherical particles.

3) Among the various particle-fluid interaction forces, the fundamental researches for drag force and then for deriving the empirical drag force correlations for non-spherical particles should be rather abundant. Due to the complicity of interactions between the fluid and non-spherical particles induced by the irregular particle shape, however, the general drag force correlations suitable for numerous particle shapes may not well predict the drag force for the specific particle shape. On the other hand, the non-universal drag force correlations proposed for the specific particle shape seemingly cannot cover the sufficiently large range of working conditions (e.g., the high Reynolds number and more particle shapes). Therefore, more related researches involving the non-spherical particles are still necessary for extending the database of the drag force and then for developing the more powerful drag force model. For lift force, though several models for non-spherical particles have been devised and were also incorporated into the CFD-DEM model in some investigations, the corresponding investigations for lift force are quite scarce as ever, especially compared to the drag force. For the other particle-fluid interaction forces, the related force models for non-spherical particles are much rarer.

4) Heat transfer occurring in the granular systems is also of paramount significance in industry, such as the environmental, energy, food, mineral, chemical and process industries, although it is not detailed in this review. However, only limited number of CFD-DEM investigations involve the heat transfer of non-spherical particles. For example, the heat transfer model based on spherical particles was modified for ellipsoidal particles containing the conduction and radiation [104,147] or was directly used for multi-sphere particles involving the conduction [266,273,274], and a conductive heat transfer model without considering the heat transfer through the fluid medium was devised for particles described by polyhedron model [418]. For convective heat transfer, the fundamental researches similar to the aforementioned investigations of drag force have also been performed by some researchers for developing the convective heat transfer model, namely correlating the Nusselt number with the particle properties (e.g., the shape and orientation) and fluid flow conditions (e.g., the Reynolds number and Prandtl number). However, the current researches for establishing a convective heat transfer model with quite high accuracy suitable for arbitrarily-shaped particles should be far from adequate. In addition, many proposed convective heat transfer models appear to overlook the effect from the neighboring particles, i.e., the term of voidage fraction is not incorporated into the convective heat transfer model.

5) In comparison with the resolved and unresolved coupling models, more researches should be done for improving the semi-resolved CFD-DEM model. Within the framework of the semi-resolved model, for example, the optimal size of the virtual fluid domain for the system containing non-spherical particles remains unknown, and the interpolation operation, that is, how to allocate interphase forces back to each fluid cell in the virtual fluid domain has not been fully discussed. In addition, the particulate systems encountered in practical applications often possess a wide particle size distribution, namely the particle size can vary significantly. Under such circumstances, the combination of two or three of the above-mentioned coupling models should be a favorable way for successful CFD-DEM simulations. However, there should be so far no related investigations.

Besides the above, there are also other sub-models that are not yet fully developed for non-spherical particles (e.g., the wear model). Moreover, whether for spherical particles or non-spherical particles, the

simulations of the granular systems involving the highly viscous non-Newtonian fluid and highly compressible fluid by the current CFD-DEM approach are still difficult. Therefore, more efforts are still required for improving or establishing these models and then for improving the prediction accuracy of CFD-DEM models in replicating the flow behaviors of non-spherical particles.

2. Efficiency: For simulating the industrial-scale particulate systems where the number of particles usually exceeds 10^9 [419], the corresponding DEM simulations will be very computationally demanding. Particularly for the non-spherical particles, the computation speed is normally much slower than the spherical particles. Furthermore, the coupling with CFD will further reduce the computational efficiency. So the number of particles for the granular systems simulated by non-spherical CFD-DEM is generally no more than 10^6 as far as we know. Therefore, improving the computational efficiency of the non-spherical CFD-DEM approach should be of significant importance for practical applications. From our perspective, the computational efficiency can be improved by reducing the computational cost and increasing the computation speed, and the details are presented below.

1) One representative way to reduce the computational cost is to integrate the CGM (Coarse-Grain Method) into the CFD-DEM model. The main idea behind the CGM is to substitute the actual particles with a certain number of representative parcels, where each parcel is composed of a specified number of original particles. So the computational overhead of CGM-CFD-DEM can be greatly reduced due to the decrease in the number of particles used in the simulations. However, there should be few researches focused on the CGM for non-spherical particles at the moment. As a result, the investigations in this field need to be intensified in the upcoming years. Another way to reduce the computational effort is to develop general scaling theories. By this way, the particle flow characteristics for the large-scale particulate systems can be deduced from the small-scale systems through the scaling theories. Therefore, only the small-scale CFD-DEM simulations are required, and hence the computational cost can be significantly reduced.

2) To increase the computation speed, the most efficient way should be to use parallel computing. With the development of modern computer technology, parallel computing has shown enormous potential in accelerating computer simulations by applying multi-core CPU (Central Processing Unit) and GPU (Graphics Processing Unit). Especially for GPU-based parallel computing, it should be one of the most promising technologies for accelerating the DEM simulations. Nevertheless, the simulation of the granular flows by DEM using GPU-based parallel computing should be as ever a fairly new technique [10], especially when CFD is introduced for the coupling with DEM. As a consequence, the investigations for developing the CFD-DEM solver adopting GPU-based parallel computing technique are strongly recommended in the coming years.

3) As is well-known, LBM possesses quite excellent parallel performance compared to the conventional CFD approach (e.g., based on the finite volume method). And although LBM is memory-intensive, this limitation should be gradually less significant with the development of computer hardware. So using the LBM-DEM coupling model should be promising that could take full advantage of the parallel-processing capability of multi-core CPU or GPU more easily in resolving both fluid flow and particle phase. In addition, there are also other merits of using LBM such as the ease of treating complex solid boundaries. However, the current LBM-DEM coupling models are developed mainly for spherical particles, and the investigations involving non-spherical particles are quite rare at present. Therefore, developing the LBM-DEM coupling model for simulating and investigating the non-spherical particles is recommended in the future.

In summary, we are firmly convinced that the non-spherical CFD-DEM coupling approach will further progress in the years ahead. With the advances in non-spherical CFD-DEM approach, CFD-DEM will become a more crucial tool enabling both researchers and practitioners to obtain valuable insights and understandings of particle-fluid systems,

especially for open problems that still exist in non-spherical multi-phase particulate systems.

Declaration of Competing Interest

The authors declare that they have no known competing financial interests or personal relationships that could have appeared to influence the work reported in this paper.

Data availability

No data was used for the research described in the article.

Acknowledgments

This research is financially supported by the National Natural Science Foundation of China (No. 22078283), Foundation of State Market Regulatory Administration (No. 2019MK154) and China Postdoctoral Science Foundation (No. 2021M702792).

References

- [1] J. Horabik, M. Molenda, Parameters and contact models for DEM simulations of agricultural granular materials: a review, *Biosyst. Eng.* 147 (2016) 206–225.
- [2] A. Bérard, G.S. Patience, B. Blais, Experimental methods in chemical engineering: unresolved CFD-DEM, *Can. J. Chem. Eng.* 98 (2020) 424–440.
- [3] S. Sarkar, R. Mukherjee, B. Chaudhuri, On the role of forces governing particulate interactions in pharmaceutical systems: a review, *Int. J. Pharm.* 526 (2017) 516–537.
- [4] F.J. Muzzio, T. Shinbrot, B.J. Glasser, Powder technology in the pharmaceutical industry: the need to catch up fast, *Powder Technol.* 124 (2002) 1–7.
- [5] J. Bridgwater, The dynamics of granular materials - towards grasping the fundamentals, *Granul. Matter* 4 (2003) 175–181.
- [6] B. Blais, D. Vidal, F. Bertrand, G.S. Patience, J. Chaouki, Experimental methods in chemical engineering: discrete element method-DEM, *Can. J. Chem. Eng.* 97 (2019) 1964–1973.
- [7] G. Lu, J. Third, C. Müller, Discrete element models for non-spherical particle systems: from theoretical developments to applications, *Chem. Eng. Sci.* 127 (2015) 425–465.
- [8] S. Ji, L. Liu, Computational Granular Mechanics and its Engineering Applications, Springer, New York, USA, 2020.
- [9] S. Kuang, M. Zhou, A. Yu, CFD-DEM modelling and simulation of pneumatic conveying: a review, *Powder Technol.* 365 (2020) 186–207.
- [10] W. Zhong, A. Yu, X. Liu, Z. Tong, H. Zhang, DEM/CFD-DEM modelling of non-spherical particulate systems: theoretical developments and applications, *Powder Technol.* 302 (2016) 108–152.
- [11] T.B. Anderson, R. Jackson, Fluid mechanical description of fluidized beds, *Ind. Eng. Chem. Fundam.* 6 (1967) 527–539.
- [12] P.A. Cundall, O.D. Strack, A discrete numerical model for granular assemblies, *Geotechnique*. 29 (1979) 47–65.
- [13] H. Zhu, Z. Zhou, R. Yang, A. Yu, Discrete particle simulation of particulate systems: theoretical developments, *Chem. Eng. Sci.* 62 (2007) 3378–3396.
- [14] H. Zhu, Z. Zhou, R. Yang, A. Yu, Discrete particle simulation of particulate systems: a review of major applications and findings, *Chem. Eng. Sci.* 63 (2008) 5728–5770.
- [15] M.A. El-Emam, L. Zhou, W. Shi, C. Han, L. Bai, R. Agarwal, Theories and applications of CFD-DEM coupling approach for granular flow: a review, *Arch. Comput. Methods Eng.* 28 (2021) 4979–5020.
- [16] E.V.P.J. Manjula, W.K.H. Ariyaratne, C. Ratnayake, M.C. Melaaen, A review of CFD modelling studies on pneumatic conveying and challenges in modelling offshore drill cuttings transport, *Powder Technol.* 305 (2017) 782–793.
- [17] Y. Wang, K. Williams, M. Jones, B. Chen, CFD simulation methodology for gas-solid flow in bypass pneumatic conveying - a review, *Appl. Therm. Eng.* 125 (2017) 185–208.
- [18] B.A. Kotzur, R.J. Berry, S. Zigan, P. García-Trinanes, M.S.A. Bradley, Particle attrition mechanisms, their characterisation, and application to horizontal lean phase pneumatic conveying systems: a review, *Powder Technol.* 334 (2018) 76–105.
- [19] B.W. Fitzgerald, A. Zarghami, V.V. Mahajan, S.K.P. Sanjeevi, I. Memm, V. Verma, Y.M.F. El Hasadi, J.T. Padding, Multiscale simulation of elongated particles in fluidised beds, *Chem. Eng. Sci. X*. 2 (2019), 100019.
- [20] A. Ibrahim, M.A. Meguid, On the development and challenges of particulate flow modeling in geotechnical engineering: a review, *GeoVirtual 2020* (2020). Calgary, Canada.
- [21] J. Wang, Continuum theory for dense gas-solid flow: a state-of-the-art review, *Chem. Eng. Sci.* 215 (2020), 115428.
- [22] F. Allobaid, N. Almohammed, M. Massoudi Farid, J. May, P. Rößger, A. Richter, B. Epple, Progress in CFD simulations of fluidized beds for chemical and energy process engineering, *Prog. Energy Combust. Sci.* 91 (2022), 100930.
- [23] N. Mangadoddy, T.R. Vakamalla, M. Kumar, A. Mainza, Computational modelling of particle-fluid dynamics in comminution and classification: a review, *Miner. Process. Ext. Metall.* 129 (2020) 145–156.
- [24] V. Scherer, S. Wirtz, B. Krause, F. Wissing, Simulation of reacting moving granular material in furnaces and boilers an overview on the capabilities of the discrete element method, *Energy Procedia* 120 (2017) 41–61.
- [25] S. Golshan, R. Sotudeh-Gharebagh, R. Zarghami, N. Mostoufi, B. Blais, J.A. M. Kuipers, Review and implementation of CFD-DEM applied to chemical process systems, *Chem. Eng. Sci.* 221 (2020), 115646.
- [26] P. Kieckhefen, S. Pietsch, M. Dosta, S. Heinrich, Possibilities and limits of computational fluid dynamics-discrete element method simulations in process engineering: a review of recent advancements and future trends, *Annu. Rev. Chem. Biomol. Eng.* 11 (2020) 397–422.
- [27] H. Zhao, Y. Huang, Z. Liu, W. Liu, Z. Zheng, Applications of discrete element method in the research of agricultural machinery: a review, *Agriculture*. 11 (2021) 425.
- [28] L. Lu, X. Gao, J.-F. Dietiker, M. Shahnam, W.A. Rogers, MFix based multi-scale CFD simulations of biomass fast pyrolysis: a review, *Chem. Eng. Sci.* 248 (2022), 117131.
- [29] Y. Xue, R. Liu, Z. Li, D. Han, A review for numerical simulation methods of ship-ice interaction, *Ocean Eng.* 215 (2020), 107853.
- [30] M. Islam, J. Mills, R. Gash, W. Pearson, A literature survey of broken ice-structure interaction modelling methods for ships and offshore platforms, *Ocean Eng.* 221 (2021), 108527.
- [31] F. Li, L. Huang, A review of computational simulation methods for a ship advancing in broken ice, *J. Mar. Sci. Eng.* 10 (2022) 165.
- [32] T. Wang, F. Zhang, J. Furtney, B. Damjanac, A review of methods, applications and limitations for incorporating fluid flow in the discrete element method, *J. Rock Mech. Geotech. Eng.* 14 (2022) 1005–1024.
- [33] B.P.B. Hoomans, J.A.M. Kuipers, W.J. Briels, W.P.M.V. Swaaij, Discrete particle simulation of bubble and slug formation in a two-dimensional gas-fluidised bed: a hard-sphere approach, *Chem. Eng. Sci.* 51 (1996) 99–118.
- [34] T. Wang, Q. Gao, A. Deng, T. Tang, Y. He, Numerical and experimental investigations of instability in a spouted bed with non-spherical particles, *Powder Technol.* 379 (2021) 231–240.
- [35] T. Wang, Y. He, T. Tang, Y. Zhao, Numerical investigation on particle behavior in a bubbling fluidized bed with non-spherical particles using discrete hard sphere method, *Powder Technol.* 301 (2016) 927–939.
- [36] D. Wu, N. Gui, Comparison of collision dynamics of non-spherical particles between the hard-particle model and soft-particle model, *Appl. Phys. A* 105 (2017) 97–102.
- [37] H. Ma, Y. Zhao, Investigating the flow of rod-like particles in a horizontal rotating drum using DEM simulation, *Granul. Matter* 20 (2018) 41.
- [38] H. Goldstein, C. Poole, J. Safko, Classical Mechanics, Addison Wesley, Boston, USA, 2002.
- [39] D.J. Evans, S. Murad, Singularity free algorithm for molecular dynamics simulation of rigid polyatomics, *Mol. Phys.* 34 (1977) 327–331.
- [40] P.A. Langston, M.A. Al-Awamleh, F.Y. Fraige, B.N. Asmar, Distinct element modelling of non-spherical frictionless particle flow, *Chem. Eng. Sci.* 59 (2004) 425–435.
- [41] A. Džugys, B. Peters, An approach to simulate the motion of spherical and non-spherical fuel particles in combustion chambers, *Granul. Matter* 3 (2001) 231–266.
- [42] A. Janota, V. Šimák, D. Nemec, J. Hrbček, Improving the precision and speed of euler angles computation from low-cost rotation sensor data, *Sensors*. 15 (2015) 7016–7039.
- [43] B. Xu, A. Yu, Numerical simulation of the gas-solid flow in a fluidized bed by combining discrete particle method with computational fluid dynamics, *Chem. Eng. Sci.* 52 (1997) 2785–2809.
- [44] Z. Ning, R. Boerefijn, M. Ghadiri, C. Thornton, Distinct element simulation of impact breakage of lactose agglomerates, *Adv. Powder Technol.* 8 (1997) 15–37.
- [45] H. Kruggel-Emden, F. Elskamp, Modeling of screening processes with the discrete element method involving non-spherical particles, *Chem. Eng. Technol.* 37 (2014) 847–856.
- [46] M.A. Hopkins, Polyhedra faster than spheres? *Eng. Comput.* 31 (2014) 567–583.
- [47] B. Nassauer, T. Liedke, M. Kuna, Polyhedral particles for the discrete element method, *Granul. Matter* 15 (2013) 85–93.
- [48] D. Höhner, S. Wirtz, V. Scherer, A study on the influence of particle shape on the mechanical interactions of granular media in a hopper using the discrete element method, *Powder Technol.* 278 (2015) 286–305.
- [49] Y. Zhao, L. Xu, P.B. Umbanhowar, R.M. Lueptow, Discrete element simulation of cylindrical particles using super-ellipsoids, *Particuology*. 46 (2019) 55–66.
- [50] J.R. Williams, A.P. Pentland, Superquadrics and modal dynamics for discrete elements in interactive design, *Eng. Comput.* 9 (1992) 115–127.
- [51] P.W. Cleary, Large scale industrial DEM modelling, *Eng. Comput.* 21 (2004) 169–204.
- [52] J. Hilton, L. Mason, P. Cleary, Dynamics of gas-solid fluidised beds with non-spherical particle geometry, *Chem. Eng. Sci.* 65 (2010) 1584–1596.
- [53] H. Ma, Y. Zhao, Modelling of the flow of ellipsoidal particles in a horizontal rotating drum based on DEM simulation, *Chem. Eng. Sci.* 172 (2017) 636–651.
- [54] Y. Zhao, H. Xiao, P.B. Umbanhowar, R.M. Lueptow, Simulation and modeling of segregating rods in quasi-2D bounded heap flow, *AICHE J.* 64 (2018) 1550–1563.
- [55] J.R. Williams, R. O'connor, Discrete element simulation and the contact problem, *Arch. Comput. Methods Eng.* 6 (1999) 279–304.

- [56] K. Kildashti, K. Dong, B. Samali, Q. Zheng, A. Yu, Evaluation of contact force models for discrete modelling of ellipsoidal particles, *Chem. Eng. Sci.* 177 (2018) 1–17.
- [57] X. Lin, T.-T. Ng, Contact detection algorithms for three-dimensional ellipsoids in discrete element modelling, *Int. J. Numer. Anal. Methods Geomech.* 19 (1995) 653–659.
- [58] G. Lu, J. Third, C. Müller, Critical assessment of two approaches for evaluating contacts between super-quadratic shaped particles in DEM simulations, *Chem. Eng. Sci.* 78 (2012) 226–235.
- [59] C. Wellmann, C. Lillie, P. Wriggers, A contact detection algorithm for superellipsoids based on the common-normal concept, *Eng. Comput.* 25 (2008) 432–442.
- [60] A. Di Renzo, F.P. Di Maio, Comparison of contact-force models for the simulation of collisions in DEM-based granular flow codes, *Chem. Eng. Sci.* 59 (2004) 525–541.
- [61] Y.T. Feng, K. Han, D.R.J. Owen, Energy-conserving contact interaction models for arbitrarily shaped discrete elements, *Comput. Methods Appl. Mech. Eng.* 205–208 (2012) 169–177.
- [62] V.L. Popov, *Contact Mechanics and Friction*, Springer, Berlin, Germany, 2010.
- [63] Q.J. Zheng, Z.Y. Zhou, A.B. Yu, Contact forces between viscoelastic ellipsoidal particles, *Powder Technol.* 248 (2013) 25–33.
- [64] J. Favier, M. Abbaspour-Fard, M. Kremmer, A. Raji, Shape representation of axisymmetrical, non-spherical particles in discrete element simulation using multi-element model particles, *Eng. Comput.* 16 (1999) 467–480.
- [65] D. Markauskas, R. Kačianauskas, A. Džiugys, R. Navakas, Investigation of adequacy of multi-sphere approximation of elliptical particles for DEM simulations, *Granul. Matter* 12 (2010) 107–123.
- [66] H. Kruggel-Emden, S. Rickelt, S. Wirtz, V. Scherer, A study on the validity of the multi-sphere Discrete Element Method, *Powder Technol.* 188 (2008) 153–165.
- [67] Y. You, Y. Zhao, Discrete element modelling of ellipsoidal particles using super-ellipsoids and multi-spheres: a comparative study, *Powder Technol.* 331 (2018) 179–191.
- [68] Y. Guo, C. Wassgren, B. Hancock, W. Ketterhagen, J. Curtis, Validation and time step determination of discrete element modeling of flexible fibers, *Powder Technol.* 249 (2013) 386–395.
- [69] L. Gao, Q. Luo, Y. Xu, G.-Q. Jing, H.-K. Jiang, Discrete element method of improved performance of railway ballast bed using elastic sleeper, *J. Cent. South Univ.* 22 (2015) 3223–3231.
- [70] Y. Guo, K. Buettner, V. Lane, C. Wassgren, W. Ketterhagen, B. Hancock, J. Curtis, Computational and experimental studies of flexible fiber flows in a normal-stress-fixed shear cell, *AICHE J.* 65 (2019) 64–74.
- [71] J. Quist, C.M. Evertsson, Cone crusher modelling and simulation using DEM, *Miner. Eng.* 85 (2016) 92–105.
- [72] F. Geng, Y. Li, X. Wang, Z. Yuan, Y. Yan, D. Luo, Simulation of dynamic processes on flexible filamentous particles in the transverse section of a rotary dryer and its comparison with ideo-imaging experiments, *Powder Technol.* 207 (2011) 175–182.
- [73] R.F. Ross, D.J. Klingenberg, Dynamic simulation of flexible fibers composed of linked rigid bodies, *J. Chem. Phys.* 106 (1997) 2949–2960.
- [74] Y.C. Zhou, B.D. Wright, R.Y. Yang, B.H. Xu, A.B. Yu, Rolling friction in the dynamic simulation of sandpile formation, *Physica A.* 269 (1999) 536–553.
- [75] M.J. Jiang, H.S. Yu, D. Harris, A novel discrete model for granular material incorporating rolling resistance, *Comput. Geotech.* 32 (2005) 340–357.
- [76] J. Ai, J.-F. Chen, J.M. Rotter, J.Y. Ooi, Assessment of rolling resistance models in discrete element simulations, *Powder Technol.* 206 (2011) 269–282.
- [77] C. Xie, H. Ma, Y. Zhao, Investigation of modeling non-spherical particles by using spherical discrete element model with rolling friction, *Eng. Anal. Bound. Elem.* 105 (2019) 207–220.
- [78] C.M. Wensrich, A. Katterfeld, Rolling friction as a technique for modelling particle shape in DEM, *Powder Technol.* 217 (2012) 409–417.
- [79] K. Iwashita, M. Oda, Rolling resistance at contacts in simulation of shear band development by DEM, *J. Eng. Mech.* 124 (1998) 285–292.
- [80] W. Chen, T. Donohue, A. Katterfeld, K. Williams, Comparative discrete element modelling of a vibratory sieving process with spherical and rounded polyhedron particles, *Granul. Matter* 19 (2017) 81.
- [81] D. Markauskas, Á. Ramírez-Gómez, R. Kačianauskas, E. Zdancvičius, Maize grain shape approaches for DEM modelling, *Comput. Electron. Agric.* 118 (2015) 247–258.
- [82] S. Akhshik, M. Behzad, M. Rajabi, Simulation of the interaction between nonspherical particles within the CFD-DEM framework via multisphere approximation and rolling resistance method, *Part. Sci. Technol.* 34 (2016) 381–391.
- [83] H. Wang, Y. Zhou, B. Zhou, W. Zheng, An investigation of the pressure dip phenomenon within conical sandpiles using CFD-DEM, *Powder Technol.* 398 (2022), 117152.
- [84] C.M. Boyce, A. Ozel, N.P. Rice, G.J. Rubinstein, D.J. Holland, S. Sundaresan, Effective particle diameters for simulating fluidization of non-spherical particles: CFD-DEM models vs., MRI measurements. *AICHE J.* 63 (2017) 2555–2568.
- [85] D. Gidaspow, *Multiphase Flow and Fluidization*, Academic Press, San Diego, USA, 1994.
- [86] R. Beetstra, M.A. Van Der Hoef, J.A.M. Kuipers, Drag force of intermediate Reynolds number flow past mono- and bidisperse arrays of spheres, *AICHE J.* 53 (2007) 489–501.
- [87] Y. Tang, E.A.J.F. Peters, J.A.M. Kuipers, S.H.L. Kriebitzsch, M.A. Van Der Hoef, A new drag correlation from fully resolved simulations of flow past monodisperse static arrays of spheres, *AICHE J.* 61 (2015) 688–698.
- [88] A.H. Barr, Superquadrics and angle-preserving transformations, *IEEE Comput. Graph. Appl.* 1 (1981) 11–23.
- [89] X. Xia, L. Zhou, H. Ma, C. Xie, Y. Zhao, Reliability study of super-ellipsoid DEM in representing the packing structure of blast furnace, *Particuology.* 70 (2022) 72–81.
- [90] H. Sun, H. Ma, Y. Zhao, DEM investigation on conveying of non-spherical particles in a screw conveyor, *Particuology.* 65 (2022) 17–31.
- [91] P.W. Cleary, DEM prediction of industrial and geophysical particle flows, *Particuology.* 8 (2010) 106–118.
- [92] X. Gao, J. Yu, R.J.F. Portal, J.-F. Dietiker, M. Shahnam, W.A. Rogers, Development and validation of SuperDEM for non-spherical particulate systems using a superquadric particle method, *Particuology.* 61 (2022) 74–90.
- [93] A. Podlozhnyuk, S. Pirker, C. Kloss, Efficient implementation of superquadric particles in Discrete Element Method within an open-source framework, *Comput. Part. Mech.* 4 (2017) 101–118.
- [94] Y. You, M. Liu, H. Ma, L. Xu, B. Liu, Y. Shao, Y. Tang, Y. Zhao, Investigation of the vibration sorting of non-spherical particles based on DEM simulation, *Powder Technol.* 325 (2018) 316–332.
- [95] Z. Cui, Y. Chen, Y. Zhao, Z. Hua, X. Liu, C. Zhou, Study of discrete element model for non-sphere particles base on super-quadric, *Chin. J. Comput. Mech.* 30 (2013) 854–859.
- [96] S. Wang, S. Ji, Poly-superquadric model for DEM simulations of asymmetrically shaped particles, *Comput. Part. Mech.* 9 (2022) 299–313.
- [97] B. Soltanbeigi, A. Podlozhnyuk, S.-A. Papanicolopoulos, C. Kloss, S. Pirker, J. Y. Ooi, DEM study of mechanical characteristics of multi-spherical and superquadric particles at micro and macro scales, *Powder Technol.* 329 (2018) 288–303.
- [98] S. Wang, Y. Fan, S. Ji, Interaction between super-quadric particles and triangular elements and its application to hopper discharge, *Powder Technol.* 339 (2018) 534–549.
- [99] H. Ma, Y. Zhao, Investigating the fluidization of disk-like particles in a fluidized bed using CFD-DEM simulation, *Adv. Powder Technol.* 29 (2018) 2380–2393.
- [100] J. Gan, Z. Zhou, A. Yu, CFD-DEM modeling of gas fluidization of fine ellipsoidal particles, *AICHE J.* 62 (2016) 62–77.
- [101] Z.Y. Zhou, D. Pinson, R.P. Zou, A.B. Yu, Discrete particle simulation of gas fluidization of ellipsoidal particles, *Chem. Eng. Sci.* 66 (2011) 6128–6145.
- [102] Z.Y. Zhou, R.P. Zou, D. Pinson, A.B. Yu, Dynamic simulation of the packing of ellipsoidal particles, *Ind. Eng. Chem. Res.* 50 (2011) 9787–9798.
- [103] J. Gan, Z. Zhou, A. Yu, Micromechanical analysis of flow behaviour of fine ellipsoids in gas fluidization, *Chem. Eng. Sci.* 163 (2017) 11–26.
- [104] J. Gan, Z. Zhou, A. Yu, Particle scale study of heat transfer in packed and fluidized beds of ellipsoidal particles, *Chem. Eng. Sci.* 144 (2016) 201–215.
- [105] H. Ouadfel, L. Rothenburg, An algorithm for detecting inter-ellipsoid contacts, *Comput. Geotech.* 24 (1999) 245–263.
- [106] L. Rothenburg, R.J. Bathurst, Numerical simulation of idealized granular assemblies with plane elliptical particles, *Comput. Geotech.* 11 (1991) 315–329.
- [107] Z. Liu, Y. Zhao, Multi-super-ellipsoid model for non-spherical particles in DEM simulation, *Powder Technol.* 361 (2020) 190–202.
- [108] Z. Liu, H. Ma, Y. Zhao, Comparative study of discrete element modeling of tablets using multi-spheres, multi-super-ellipsoids, and polyhedrons, *Powder Technol.* 390 (2021) 34–49.
- [109] S. Zhao, J. Zhao, A poly-superellipsoid-based approach on particle morphology for DEM modeling of granular media, *Int. J. Numer. Anal. Methods Geomech.* 43 (2019) 2147–2169.
- [110] W. Chen, H. Zheng, Y.M. Cheng, X. Ge, Detection of 3D rock block contacts by penetration edges, *Chin. J. Rock Mech. Eng.* 23 (2004) 565–571.
- [111] J. Wang, S. Li, C. Feng, A shrunken edge algorithm for contact detection between convex polyhedral blocks, *Comput. Geotech.* 63 (2015) 315–330.
- [112] E.G. Nezami, Y.M.A. Hashash, D. Zhao, J. Ghaboussi, Shortest link method for contact detection in discrete element method, *Int. J. Numer. Anal. Methods Geomech.* 30 (2006) 783–801.
- [113] J. Wang, G. Lin, J. Liu, Analysis and improvement of scheme to detect contacts in system composed of 3 D convex polyhedral blocks, *Chin. J. Rock Mech. Eng.* 25 (2006) 2247–2257.
- [114] P.A. Cundall, Formulation of a three-dimensional distinct element model-Part I. A scheme to detect and represent contacts in a system composed of many polyhedral blocks, *Int. J. Rock Mech. Min. Sci. Geomech.* 25 (1988) 107–116.
- [115] E.G. Nezami, Y.M.A. Hashash, D. Zhao, J. Ghaboussi, A fast contact detection algorithm for 3-D discrete element method, *Comput. Geotech.* 31 (2004) 575–587.
- [116] C. Xie, T. Song, Y. Zhao, Discrete element modeling and simulation of non-spherical particles using polyhedrons and super-ellipsoids, *Powder Technol.* 368 (2020) 253–267.
- [117] C. Xie, H. Ma, T. Song, Y. Zhao, DEM investigation of SAG mill with spherical grinding media and non-spherical ore based on polyhedron-sphere contact model, *Powder Technol.* 386 (2021) 154–165.
- [118] Z. Liu, H. Ma, Y. Zhao, CFD-DEM simulation of fluidization of polyhedral particles in a fluidized bed, *Energies.* 14 (2021) 4939.
- [119] N. Govender, D.N. Wilke, C.-Y. Wu, U. Tuzun, H. Kureck, A numerical investigation into the effect of angular particle shape on blast furnace burden topography and percolation using a GPU solved discrete element model, *Chem. Eng. Sci.* 204 (2019) 9–26.
- [120] N. Govender, R. Rajamani, D.N. Wilke, C.-Y. Wu, J. Khinast, B.J. Glasser, Effect of particle shape in grinding mills using a GPU based DEM code, *Miner. Eng.* 129 (2018) 71–84.

- [121] Y.T. Feng, An energy-conserving contact theory for discrete element modelling of arbitrarily shaped particles: basic framework and general contact model, *Comput. Methods Appl. Mech. Eng.* 373 (2021), 113454.
- [122] Y. Feng, A generic energy-conserving discrete element modeling strategy for concave particles represented by surface triangular meshes, *Int. J. Numer. Methods Eng.* 122 (2021) 2581–2597.
- [123] L. Liu, S. Ji, Ice load on floating structure simulated with dilated polyhedral discrete element method in broken ice field, *Appl. Ocean Res.* 75 (2018) 53–65.
- [124] D. Höhner, S. Wirtz, V. Scherer, Experimental and numerical investigation on the influence of particle shape and shape approximation on hopper discharge using the discrete element method, *Powder Technol.* 235 (2013) 614–627.
- [125] L. Liu, S. Ji, A fast detection algorithm based on the envelope function of dilated polyhedron, *Sci. Sin.-Phys. Mech. Astron.* 49 (2019), 064601.
- [126] S.A. Galindo-Torres, D.M. Pedroso, D.J. Williams, L. Li, Breaking processes in three-dimensional bonded granular materials with general shapes, *Comput. Phys. Commun.* 183 (2012) 266–277.
- [127] L. Liu, S. Ji, Bond and fracture model in dilated polyhedral DEM and its application to simulate breakage of brittle materials, *Granul. Matter* 21 (2019) 41.
- [128] R. Capozza, K.J. Hanley, A hierarchical, spherical harmonic-based approach to simulate abradable, irregularly shaped particles in DEM, *Powder Technol.* 378 (2021) 528–537.
- [129] B. Zhou, J. Wang, H. Wang, Three-dimensional sphericity, roundness and fractal dimension of sand particles, *Geotechnique*. 68 (2018) 18–30.
- [130] R. Kawamoto, E. Andò, G. Viggiani, J.E. Andrade, Level set discrete element method for three-dimensional computations with triaxial case study, *J. Mech. Phys. Solids*. 91 (2016) 1–13.
- [131] X. Zhang, P. Tahmasebi, Coupling irregular particles and fluid: complex dynamics of granular flows, *Comput. Geotech.* 143 (2022), 104624.
- [132] G.T. Housby, Potential particles: a method for modelling non-circular particles in DEM, *Comput. Geotech.* 36 (2009) 953–959.
- [133] C.W. Boon, G.T. Housby, S. Utili, A new contact detection algorithm for three-dimensional non-spherical particles, *Powder Technol.* 248 (2013) 94–102.
- [134] X. Jia, R. Williams, A packing algorithm for particles of arbitrary shapes, *Powder Technol.* 120 (2001) 175–186.
- [135] K.W. Lim, J.E. Andrade, Granular element method for three-dimensional discrete element calculations, *Int. J. Numer. Anal. Methods Geomech.* 38 (2014) 167–188.
- [136] Y. Guo, C. Wassgren, W. Ketterhagen, B. Hancock, B. James, J. Curtis, A numerical study of granular shear flows of rod-like particles using the discrete element method, *J. Fluid Mech.* 713 (2012) 1–26.
- [137] M. Kodam, R. Bharadwaj, J. Curtis, B. Hancock, C. Wassgren, Cylindrical object contact detection for use in discrete element method simulations. Part I - contact detection algorithms, *Chem. Eng. Sci.* 65 (2010) 5852–5862.
- [138] M. Kodam, J. Curtis, B. Hancock, C. Wassgren, Discrete element method modeling of bi-convex pharmaceutical tablets: contact detection algorithms and validation, *Chem. Eng. Sci.* 69 (2012) 587–601.
- [139] S. Hwang, J. Pan, A.A. Sunny, L.-S. Fan, A machine learning-based particle-particle collision model for non-spherical particles with arbitrary shape, *Chem. Eng. Sci.* 251 (2022), 117439.
- [140] O. Studenik, M. Kotouč Sourek, M. Isoz, Octree-generated virtual mesh for improved contact resolution in CFD-DEM coupling, in: Topical Problems of Fluid Mechanics, 2022. Prague, Czech.
- [141] D. Peng, K.J. Hanley, Contact detection between convex polyhedra and superquadratics in discrete element codes, *Powder Technol.* 356 (2019) 11–20.
- [142] C. Zhou, Y. Zhao, Discrete element method and its applications in fluidization, *CIESC J.* 65 (2014) 2520–2534.
- [143] H.C. Hamaker, The London-van der Waals attraction between spherical particles, *Physica*. 4 (1937) 1058–1072.
- [144] J. Chen, A. Anandarajah, Van der Waals attraction between spherical particles, *J. Colloid Interface Sci.* 180 (1996) 519–523.
- [145] R. Everaerts, M.R. Ejtehadi, Interaction potentials for soft and hard ellipsoids, *Phys. Rev. E* 67 (2003), 041710.
- [146] J. Gan, Z. Zhou, A. Yu, Flow and force analysis on the formation of expanded beds in gas fluidization of fine ellipsoids, *Powder Technol.* 357 (2019) 291–304.
- [147] J. Gan, Z. Zhou, A. Yu, Effect of particle shape and size on effective thermal conductivity of packed beds, *Powder Technol.* 311 (2017) 157–166.
- [148] H. Ma, L. Xu, Y. Zhao, CFD-DEM simulation of fluidization of rod-like particles in a fluidized bed, *Powder Technol.* 314 (2017) 355–366.
- [149] F. Marchelli, Q. Hou, B. Bosio, E. Arato, A. Yu, Comparison of different drag models in CFD-DEM simulations of spouted beds, *Powder Technol.* 360 (2020) 1253–1270.
- [150] C.Y. Wen, Y.H. Yu, Mechanics of fluidization, *Chem. Eng. Prog. Symp. Ser.* 62 (1966) 100–111.
- [151] R. Di Felice, The voidage function for fluid-particle interaction systems, *Int. J. Multiphase Flow* 20 (1994) 153–159.
- [152] L.W. Rong, K.J. Dong, A.B. Yu, Lattice-Boltzmann simulation of fluid flow through packed beds of uniform spheres: effect of porosity, *Chem. Eng. Sci.* 99 (2013) 44–58.
- [153] D.L. Koch, R.J. Hill, Inertial effects in suspensions and porous-media flows, *Annu. Rev. Fluid Mech.* 33 (2001) 619–647.
- [154] S. Tenneti, R. Garg, S. Subramaniam, Drag law for monodisperse gas-solid systems using particle-resolved direct numerical simulation of flow past fixed assemblies of spheres, *Int. J. Multiphase Flow* 37 (2011) 1072–1092.
- [155] H. Ma, Y. Zhao, An approach to distribute the marker points on non-spherical particle/boundary surface within the IBM-LBM framework, *Eng. Anal. Bound. Elem.* 108 (2019) 254–266.
- [156] A. Haider, O. Levenspiel, Drag coefficient and terminal velocity of spherical and nonspherical particles, *Powder Technol.* 58 (1989) 63–70.
- [157] G.H. Ganser, A rational approach to drag prediction of spherical and nonspherical particles, *Powder Technol.* 77 (1993) 143–152.
- [158] D. Leith, Drag on nonspherical objects, *Aerosol Sci. Technol.* 6 (1987) 153–161.
- [159] S. Tran-Cong, M. Gay, E.E. Michaelides, Drag coefficients of irregularly shaped particles, *Powder Technol.* 139 (2004) 21–32.
- [160] A. Hölzer, M. Sommerfeld, New simple correlation formula for the drag coefficient of non-spherical particles, *Powder Technol.* 184 (2008) 361–365.
- [161] H. Ma, Y. Zhao, Convective heat transfer coefficient for a rod-like particle in a uniform flow, *Int. J. Heat Mass Transf.* 147 (2020), 118742.
- [162] C. Zhou, J. Su, H. Chen, Z. Shi, Terminal velocity and drag coefficient models for disc-shaped particles based on the imaging experiment, *Powder Technol.* 398 (2022), 117062.
- [163] H. Zhang, B. Xiong, X. An, C. Ke, G. Wei, Prediction on drag force and heat transfer of spheroids in supercritical water: a PR-DNS study, *Powder Technol.* 342 (2019) 99–107.
- [164] J. Fu, S. Chen, P. Chen, C. Wen, Particle-resolved simulation on viscous flow past random and ordered arrays of hot ellipsoidal particles, *Int. J. Multiphase Flow* 142 (2021), 103736.
- [165] C. Ke, S. Shu, H. Zhang, H. Yuan, Particle scale numerical simulation on momentum and heat transfer of two tandem spheroids: an IB-LBM study, *Adv. Appl. Math. Mech.* 10 (2018) 1497–1526.
- [166] H. Zhang, B. Xiong, X. An, C. Ke, G. Wei, Numerical investigation on the effect of the incident angle on momentum and heat transfer of spheroids in supercritical water, *Comput. Fluids* 179 (2019) 533–542.
- [167] K.E. Buettner, J.S. Curtis, A. Sarkar, Fluid-particle drag force measurements from particle-resolved CFD simulations of flow past random arrays of ellipsoidal particles, *Chem. Eng. Sci.* 235 (2021), 116469.
- [168] S.K.P. Sanjeevi, J.T. Padding, On the orientational dependence of drag experienced by spheroids, *J. Fluid Mech.* 820 (2017) R1.
- [169] S.K.P. Sanjeevi, J.A.M. Kuipers, J.T. Padding, Drag, lift and torque correlations for non-spherical particles from Stokes limit to high Reynolds numbers, *Int. J. Multiphase Flow* 106 (2018) 325–337.
- [170] C. Ke, S. Shu, H. Zhang, H. Yuan, D. Yang, On the drag coefficient and averaged Nusselt number of an ellipsoidal particle in a fluid, *Powder Technol.* 325 (2018) 134–144.
- [171] C. Ke, S. Shu, H. Zhang, H. Yuan, Drag coefficient and averaged Nusselt number of a scalene prolate ellipsoid, *Appl. Math. Model.* 64 (2018) 556–571.
- [172] Z. Cao, D.K. Tafti, M. Shahnam, Development of drag correlation for suspensions of ellipsoidal particles, *Powder Technol.* 369 (2020) 298–310.
- [173] R. Ouchene, M. Khalij, B. Arcen, A. Tanière, A new set of correlations of drag, lift and torque coefficients for non-spherical particles and large Reynolds numbers, *Powder Technol.* 303 (2016) 33–43.
- [174] A. Richter, P.A. Nikrityuk, New correlations for heat and fluid flow past ellipsoidal and cubic particles at different angles of attack, *Powder Technol.* 249 (2013) 463–474.
- [175] Z. Cao, D.K. Tafti, Investigation of drag, lift and torque for fluid flow past a low aspect ratio (1:4) cylinder, *Comput. Fluids* 177 (2018) 123–135.
- [176] Z. Cao, D.K. Tafti, Fluid forces and torques in suspensions of oblate cylinders with aspect ratio 1:4, *Int. J. Multiphase Flow* 131 (2020), 103394.
- [177] Y. Chen, J.R. Third, C.R. Müller, A drag force correlation for approximately cubic particles constructed from identical spheres, *Chem. Eng. Sci.* 123 (2015) 146–154.
- [178] N. Agarwal, R.P. Chhabra, Settling velocity of cubes in Newtonian and power law liquids, *Powder Technol.* 178 (2007) 17–21.
- [179] H. Zhang, B. Xiong, X. An, C. Ke, J. Chen, Numerical prediction on the drag force and heat transfer of non-spherical particles in supercritical water, *Powder Technol.* 361 (2020) 414–423.
- [180] M. Zastawny, G. Mallouppas, F. Zhao, B. Van Wachem, Derivation of drag and lift force and torque coefficients for non-spherical particles in flows, *Int. J. Multiphase Flow* 39 (2012) 227–239.
- [181] Y. Wang, L. Zhou, Q. Yang, Hydro-mechanical analysis of calcareous sand with a new shape-dependent fluid-particle drag model integrated into CFD-DEM coupling program, *Powder Technol.* 344 (2019) 108–120.
- [182] S. Hwang, J. Pan, L.-S. Fan, A machine learning-based interaction force model for non-spherical and irregular particles in low Reynolds number incompressible flows, *Powder Technol.* 392 (2021) 632–638.
- [183] S.-N. Yan, T.-Y. Wang, T.-Q. Tang, A.-X. Ren, Y.-R. He, Simulation on hydrodynamics of non-spherical particulate system using a drag coefficient correlation based on artificial neural network, *Pet. Sci.* 17 (2020) 537–555.
- [184] K. Luo, D. Wang, T. Jin, S. Wang, Z. Wang, J. Tan, J. Fan, Analysis and development of novel data-driven drag models based on direct numerical simulations of fluidized beds, *Chem. Eng. Sci.* 231 (2021), 116245.
- [185] I. Memä, V.V. Mahajan, B.W. Fitzgerald, H. Kuipers, J.T. Padding, Effect of lift force on dense gas-fluidised beds of non-spherical particles, in: 12th International Conference on CFD in Oil & Gas, Metallurgical and Process Industries. Trondheim, Norway, 2017.
- [186] I. Memä, V.V. Mahajan, B.W. Fitzgerald, J.T. Padding, Effect of lift force and hydrodynamic torque on fluidisation of non-spherical particles, *Chem. Eng. Sci.* 195 (2019) 642–656.
- [187] R. Sun, H. Xiao, H. Sun, Realistic representation of grain shapes in CFD-DEM simulations of sediment transport with a bonded-sphere approach, *Adv. Water Resour.* 107 (2017) 421–438.

- [188] P. Boehling, D. Jacevic, F. Detobel, J. Holman, L. Wareham, M. Metzger, J. G. Khinast, Validating a numerical simulation of the ConsiGma(R) Coater, AAPS PharmSciTech 22 (2020) 10.
- [189] Q. Chen, T. Xiong, X. Zhang, P. Jiang, Study of the hydraulic transport of non-spherical particles in a pipeline based on the CFD-DEM, Eng. Appl. Comput. Fluid Mech. 14 (2020) 53–69.
- [190] D. Yang, B. Xing, J. Li, Y. Wang, N. Hu, S. Jiang, Experiment and simulation analysis of the suspension behavior of large (5–30 mm) nonspherical particles in vertical pneumatic conveying, Powder Technol. 354 (2019) 442–455.
- [191] J. Jägers, M. Brömmer, E. Illana, S. Wirtz, V. Scherer, DEM-CFD simulation of wood pellet degradation by particle-wall impact during pneumatic conveying, Powder Technol. 391 (2021) 385–402.
- [192] F. Farivar, H. Zhang, Z.F. Tian, A. Gupte, CFD-DEM -DDM model for spray coating process in a Wurster coater, J. Pharm. Sci. 109 (2020) 3678–3689.
- [193] Z. Wang, M. Liu, X. Yang, A four-way coupled CFD-DEM modeling framework for charged particles under electrical field with applications to gas insulated switchgears, Powder Technol. 373 (2020) 433–445.
- [194] S. Akhshik, M. Rajabi, Simulation of proppant transport at intersection of hydraulic fracture and natural fracture of wellbores using CFD-DEM, Particuology. 63 (2022) 112–124.
- [195] S. Akhshik, M. Behzad, M. Rajabi, CFD-DEM simulation of the hole cleaning process in a deviated well drilling: the effects of particle shape, Particuology. 25 (2016) 72–82.
- [196] S. Akhshik, M. Behzad, M. Rajabi, CFD-DEM model for simulation of non-spherical particles in hole cleaning process, Part. Sci. Technol. 33 (2015) 472–481.
- [197] I. Mema, J.T. Padding, Spherical versus elongated particles - numerical investigation of mixing characteristics in a gas fluidized bed, Chem. Eng. Sci. X. 8 (2020), 100079.
- [198] J.H. Ferziger, M. Perić, R.L. Street, Computational Methods for Fluid Dynamics, fourth ed., Springer, New York, USA, 2020.
- [199] Y. Tsuji, T. Kawaguchi, T. Tanaka, Discrete particle simulation of two-dimensional fluidized bed, Powder Technol. 77 (1993) 79–87.
- [200] T. Krüger, H. Kusumaatmaja, A. Kuzmin, O. Shardt, G. Silva, E.M. Viggen, The Lattice Boltzmann Method: Principles and Practice, Springer International Publishing, Switzerland, 2017.
- [201] C.A.D. Fraga Filho, Smoothed Particle Hydrodynamics: Fundamentals and Basic Applications in Continuum Mechanics, Springer Nature, Basel, Switzerland, 2019.
- [202] X. Li, J. Zhao, Dam-break of mixtures consisting of non-Newtonian liquids and granular particles, Powder Technol. 338 (2018) 493–505.
- [203] X. Sun, M. Sakai, Y. Yamada, Three-dimensional simulation of a solid-liquid flow by the DEM-SPH method, J. Comput. Phys. 248 (2013) 147–176.
- [204] L. He, Z. Liu, Y. Zhao, An extended unresolved CFD-DEM coupling method for simulation of fluid and non-spherical particles, Particuology. 68 (2022) 1–12.
- [205] Z. Peng, E. Doroodchi, C. Luo, B. Moghtaderi, Influence of void fraction calculation on fidelity of CFD-DEM simulation of gas-solid bubbling fluidized beds, AICHE J. 60 (2014) 2000–2018.
- [206] Z. Wang, Y. Teng, M. Liu, A semi-resolved CFD-DEM approach for particulate flows with kernel based approximation and Hilbert curve based searching strategy, J. Comput. Phys. 384 (2019) 151–169.
- [207] H. Ma, Y. Zhao, Y. Cheng, CFD-DEM modeling of rod-like particles in a fluidized bed with complex geometry, Powder Technol. 344 (2019) 673–683.
- [208] Z. Peng, B. Moghtaderi, E. Doroodchi, A modified direct method for void fraction calculation in CFD-DEM simulations, Adv. Powder Technol. 27 (2016) 19–32.
- [209] B. Freireich, M. Kodam, C. Wassgren, An exact method for determining local solid fractions in discrete element method simulations, AICHE J. 56 (2010) 3036–3048.
- [210] F. Chen, E.C. Drumm, G. Guiochon, Coupled discrete element and finite volume solution of two classical soil mechanics problems, Comput. Geotech. 38 (2011) 638–647.
- [211] C.L. Wu, J.M. Zhan, Y.S. Li, K.S. Lam, A.S. Berrouk, Accurate void fraction calculation for three-dimensional discrete particle model on unstructured mesh, Chem. Eng. Sci. 64 (2009) 1260–1266.
- [212] S. Wang, Y. Shen, Super-quadratic CFD-DEM simulation of chip-like particles flow in a fluidized bed, Chem. Eng. Sci. 251 (2022), 117431.
- [213] S. Xiong, S. Chen, M. Zang, T. Makoto, Development of an unresolved CFD-DEM method for interaction simulations between large particles and fluids, Int. J. Comput. Methods. 18 (2021) 2150047.
- [214] M.A. Romero-Valle, C. Goniva, H. Nirschl, Modeling of non-spherical particle flows: movement and orientation behavior, Powder Technol. 382 (2021) 351–363.
- [215] D.A. Clarke, A.J. Sederman, L.F. Gladden, D.J. Holland, Investigation of void fraction schemes for use with CFD-DEM simulations of fluidized beds, Ind. Eng. Chem. Res. 57 (2018) 3002–3013.
- [216] A. Hobbs, Simulation of an aggregate dryer using coupled CFD and DEM methods, Int. J. Comput. Fluid Dyn. 23 (2009) 199–207.
- [217] H.P. Zhu, A.B. Yu, Averaging method of granular materials, Phys. Rev. E 66 (2002), 021302.
- [218] S. Ma, Z. Wei, X. Chen, CFD-DEM combined the fictitious domain method with Monte Carlo method for studying particle sediment in fluid, Part. Sci. Technol. 36 (2018) 920–933.
- [219] S. Deb, D.K. Tafti, A novel two-grid formulation for fluid-particle systems using the discrete element method, Powder Technol. 246 (2013) 601–616.
- [220] R. Sun, H. Xiao, Diffusion-based coarse graining in hybrid continuum-discrete solvers: theoretical formulation and a priori tests, Int. J. Multiphase Flow 77 (2015) 142–157.
- [221] M. Uhlmann, An immersed boundary method with direct forcing for the simulation of particulate flows, J. Comput. Phys. 209 (2005) 448–476.
- [222] K. Walayat, Z. Zhang, K. Usman, J. Chang, M. Liu, Fully resolved simulations of thermal convective suspensions of elliptic particles using a multigrid fictitious boundary method, Int. J. Heat Mass Transf. 139 (2019) 802–821.
- [223] G.D. Wehinger, C. Fütterer, M. Kraume, Contact modifications for CFD simulations of fixed-bed reactors: cylindrical particles, Ind. Eng. Chem. Res. 56 (2017) 87–99.
- [224] M. Pichler, B. Haddadi, C. Jordan, H. Norouzi, M. Harasek, Effect of particle contact point treatment on the CFD simulation of the heat transfer in packed beds, Chem. Eng. Res. Des. 165 (2021) 242–253.
- [225] T. Eppinger, G.D. Wehinger, A generalized contact modification for fixed-bed reactor CFD simulations, Chem. Ing. Tech. 93 (2021) 143–153.
- [226] B. Partopour, A.G. Dixon, An integrated workflow for resolved-particle packed bed models with complex particle shapes, Powder Technol. 322 (2017) 258–272.
- [227] T. Eppinger, K. Seidler, M. Kraume, DEM-CFD simulations of fixed bed reactors with small tube to particle diameter ratios, Chem. Eng. J. 166 (2011) 324–331.
- [228] A. Guardo, M. Coussirat, M.A. Larrayoz, F. Recasens, E. Egusquiza, CFD flow and heat transfer in nonregular packings for fixed bed equipment design, Ind. Eng. Chem. Res. 43 (2004) 7049–7056.
- [229] A.G. Dixon, M. Nijemeisland, CFD as a design tool for fixed-bed reactors, Ind. Eng. Chem. Res. 40 (2001) 5246–5254.
- [230] S. Ookawara, M. Kuroki, D. Street, K. Ogawa, High-fidelity DEM-CFD modeling of packed bed reactors for process intensification, in: Proceedings of European Congress of Chemical Engineering (ECCE-6), Copenhagen, Netherlands, 2007.
- [231] A.G. Dixon, M. Nijemeisland, E.H. Stitt, Systematic mesh development for 3D CFD simulation of fixed beds: contact points study, Comput. Chem. Eng. 48 (2013) 135–153.
- [232] C.S. Peskin, Numerical analysis of blood flow in the heart, J. Comput. Phys. 25 (1977) 220–252.
- [233] C.S. Peskin, The immersed boundary method, Acta Numer. 11 (2002) 479–517.
- [234] A.N. Balachandran Nair, S. Pirker, M. Saedipour, Resolved CFD-DEM simulation of blood flow with a reduced-order RBC model, Comput. Part. Mech. 9 (2022) 759–774.
- [235] M.K. Šourek, M. Isoz, Y. Haroun, Estimating rheological properties of suspensions formed of arbitrarily-shaped particles via CFD-DEM, in: Topical Problems of Fluid Mechanics, Prague, Czech, 2022.
- [236] H.H. Hu, Direct simulation of flows of solid-liquid mixtures, Int. J. Multiphase Flow 22 (1996) 335–352.
- [237] H. Ma, Y. Zhao, CFD-DEM investigation of the fluidization of binary mixtures containing rod-like particles and spherical particles in a fluidized bed, Powder Technol. 336 (2018) 533–545.
- [238] H. Ma, Y. Zhao, CFD-DEM investigation on mixing of rod-like particles in spout-fluid bed, J. Zhejiang Univ. 54 (2020) 1347–1354.
- [239] F. Farivar, H. Zhang, Z.F. Tian, A. Gupte, CFD-DEM simulation of fluidization of multisphere modelled cylindrical particles, Powder Technol. 360 (2020) 1017–1027.
- [240] W. Nan, Y. Wang, J. Wang, Numerical analysis on the fluidization dynamics of rodlike particles, Adv. Powder Technol. 27 (2016) 2265–2276.
- [241] X. Liu, J. Gan, W. Zhong, A. Yu, Particle shape effects on dynamic behaviors in a spouted bed: CFD-DEM study, Powder Technol. 361 (2020) 349–362.
- [242] S. Shrestha, Z. Zhou, Effect of particle shape on bubble dynamics in bubbling fluidized bed, EPJ Web Confer. 249 (2021) 06012.
- [243] L.-J. Wang, G.-C. Wei, S.-P. Duan, Q.-F. Hou, CFD-DEM study on the mixing characteristics of binary particle systems in a fluidized bed of refuse-derived fuel, Part. Sci. Technol. 37 (2019) 51–59.
- [244] H. Wang, Z. Zhong, P. Zhao, J. Wang, Z. Wang, X. Wang, L. Zhu, Simulation study on characteristics of cylinder-shaped particles and sphere-shaped particles flow, J. Cent. South Univ. 48 (2017) 1667–1673.
- [245] L. Zhu, Z. Zhong, H. Wang, Z. Wang, Simulation of large biomass pellets in fluidized bed by DEM-CFD, Korean J. Chem. Eng. 33 (2016) 3021–3028.
- [246] F. Guo, Z. Zhong, Simulation and analysis of coal and biomass pellet in fluidized bed with hot air injection, Waste Biomass Valor. 11 (2020) 1115–1123.
- [247] F. Guo, Z. Wang, Z. Zhong, Experiment and improved simulation on heat transfer for cylindrical biomass and quartz sand, Trans. Chin. Soc. Agric. Mach. 48 (2017) 272–279.
- [248] F. Guo, Z. Zhong, CFD-DEM numerical simulation and experimental validation of heat transfer and two-component flow in fluidized bed, Int. J. Chem. React. Eng. 16 (2018) 20160207.
- [249] V.V. Mahajan, T.M.J. Nijssen, J.A.M. Kuipers, J.T. Padding, Non-spherical particles in a pseudo-2D fluidised bed: modelling study, Chem. Eng. Sci. 192 (2018) 1105–1123.
- [250] I. Mema, J.T. Padding, Fluidization of elongated particles-Effect of multi-particle correlations for drag, lift, and torque in CFD-DEM, AICHE J. 67 (2021), e17157.
- [251] B. Esgandari, S. Golshan, R. Zarghami, R. Sotudeh-Gharebagh, J. Chaouki, CFD-DEM analysis of the spouted fluidized bed with non-spherical particles, Can. J. Chem. Eng. 99 (2021) 2303–2319.
- [252] R. Zhang, X. Ku, J. Lin, Fluidization of the spherocylindrical particles: comparison of multi-sphere and bond-sphere models, Chem. Eng. Sci. 253 (2022), 117540.
- [253] T. Rosemann, S.R. Reinecke, H. Kruggel-Emden, Analysis of mobility effects in particle-gas flows by particle-resolved LBM-DEM simulations, Chem. Ing. Tech. 93 (2021) 223–236.
- [254] A.-X. Ren, T.-Y. Wang, T.-Q. Tang, Y.-R. He, Non-spherical particle mixing behaviors by spherical inert particles assisted in a fluidized bed, Pet. Sci. 17 (2020) 509–524.

- [255] O. Baran, T. Eppinger, K. Han, DEM simulation of cylinders and capsules in a fluidized bed, in: 8th World Congress on Particle Technology. Orlando, USA, 2018.
- [256] E. Abbaszadeh Molaei, A.B. Yu, Z.Y. Zhou, Particle scale modelling of solid flow characteristics in liquid fluidizations of ellipsoidal particles, *Powder Technol.* 338 (2018) 677–691.
- [257] E. Abbaszadeh Molaei, A.B. Yu, Z.Y. Zhou, Particle scale modelling of mixing of ellipsoids and spheres in gas-fluidized beds by a modified drag correlation, *Powder Technol.* 343 (2019) 619–628.
- [258] E.A. Molaei, A. Yu, Z. Zhou, CFD-DEM modelling of mixing and segregation of binary mixtures of ellipsoidal particles in liquid fluidizations, *J. Hydodyn.* 31 (2019) 1190–1203.
- [259] S. Shrestha, S. Kuang, A. Yu, Z. Zhou, Bubble dynamics in bubbling fluidized beds of ellipsoidal particles, *AICHE J.* 65 (2019), e16736.
- [260] S. Shrestha, S. Kuang, A. Yu, Z. Zhou, Particle shape effect on bubble dynamics in central air jet pseudo-2D fluidized beds: a CFD-DEM study, *Chem. Eng. Sci.* 201 (2019) 448–466.
- [261] S. Shrestha, Z. Zhou, A CFD-DEM study of single bubble formation in gas fluidization of spherical and non-spherical particles, *EPJ Web Confer.* 140 (2017) 15026.
- [262] S. Shrestha, S.B. Kuang, A.B. Yu, Z.Y. Zhou, Effect of van der Waals force on bubble dynamics in bubbling fluidized beds of ellipsoidal particles, *Chem. Eng. Sci.* 212 (2020), 115343.
- [263] S. Shrestha, S.B. Kuang, A.B. Yu, Z.Y. Zhou, Orientation of spheroidal particles in single jet bubbling fluidized beds, *Powder Technol.* 361 (2020) 363–373.
- [264] S. Yang, S. Hu, W. Zhang, Mixing and dispersion behaviours of ellipsoid particles in a bubbling fluidized bed, *Powder Technol.* 396 (2022) 210–223.
- [265] D. Peng, Y. Wang, J. Hou, T. Yu, S. Wu, Z. Wang, Distribution and motion characteristics of ellipsoidal particles in liquid-solid two-phase flow in vertical upward pipe, *Chin. Powder Sci. Tech.* 27 (2021) 94–104.
- [266] D. E., P. Zhou, S. Guo, J. Zeng, J. Cui, Y. Jiang, Y. Lu, Z. Jiang, Z. Li, S. Kuang, Particle shape effect on hydrodynamics and heat transfer in spouted bed: a CFD-DEM study, *Particulology*. 69 (2022) 10–21.
- [267] L. Zhong, D. Xu, Y. Jiang, Y. Guo, A numerical study on gas-fluidized beds of wet flexible fibers, *Powder Technol.* 399 (2022), 117094.
- [268] Y. Jiang, Y. Guo, Z. Yu, X. Hua, J. Lin, C.R. Wassgren, J.S. Curtis, Discrete element method-computational fluid dynamics analyses of flexible fibre fluidization, *J. Fluid Mech.* 910 (2021) A8.
- [269] K. Wu, E. Zhang, J. Xu, Z. Yuan, W. Zhu, B. Li, L. Wang, D. Luo, Three-dimensional simulation of gas-solid flow in a fluidised bed with flexible ribbon particles, *Int. J. Multiphase Flow* 124 (2020), 103181.
- [270] K. Wu, E. Zhang, Z. Yuan, B. Li, W. Zhu, J. Xu, L. Wang, D. Luo, Analysis of flexible ribbon particle residence time distribution in a fluidised bed riser using three-dimensional CFD-DEM simulation, *Powder Technol.* 369 (2020) 184–201.
- [271] Z. Jiang, C. Rieck, A. Bück, E. Tsotsas, Modeling of inter- and intra-particle coating uniformity in a Wurster fluidized bed by a coupled CFD-DEM-Monte Carlo approach, *Chem. Eng. Sci.* 211 (2020), 115289.
- [272] G. Wei, H. Zhang, X. An, S. Jiang, Influence of particle shape on microstructure and heat transfer characteristics in blast furnace raceway with CFD-DEM approach, *Powder Technol.* 361 (2020) 283–296.
- [273] G. Wei, H. Zhang, X. An, D. E., Numerical investigation on the mutual interaction between heat transfer and non-spherical particle dynamics in the blast furnace raceway, *Int. J. Heat Mass Transf.* 153 (2020), 119577.
- [274] G. Wei, H. Zhang, X. An, B. Xiong, S. Jiang, CFD-DEM study on heat transfer characteristics and microstructure of the blast furnace raceway with ellipsoidal particles, *Powder Technol.* 346 (2019) 350–362.
- [275] G. Wei, H. Zhang, X. An, Q. Hou, Effect of particle shape on raceway size and pressure drop in a blast furnace: experimental, numerical and theoretical analyses, *Adv. Powder Technol.* 33 (2022), 103455.
- [276] Y. You, Y. Li, Z. Luo, H. Li, Z. Zou, R. Yang, Investigating the effect of particle shape on the charging process in melter gasifiers in COREX, *Powder Technol.* 351 (2019) 305–313.
- [277] A.M. Nyembwe, R.D. Cromarty, A.M. Garbers-Craig, Simulation of the pressure drop across granulated mixtures using a coupled DEM-CFD model, *Adv. Powder Technol.* 30 (2019) 85–97.
- [278] J. Wiese, F. Wissing, D. Höhner, S. Wirtz, V. Scherer, U. Ley, H.M. Behr, DEM/CFD modeling of the fuel conversion in a pellet stove, *Fuel Process. Technol.* 152 (2016) 223–239.
- [279] H. Wu, N. Gui, X. Yang, J. Tu, S. Jiang, Parameter analysis and wall effect of radiative heat transfer for CFD-DEM simulation in nuclear packed pebble bed, *Exp. Comput. Multi. Flow.* 3 (2021) 250–257.
- [280] X. Gao, J. Yu, L. Lu, C. Li, W.A. Rogers, Development and validation of SuperDEM-CFD coupled model for simulating non-spherical particles hydrodynamics in fluidized beds, *Chem. Eng. J.* 420 (2021), 127654.
- [281] X. Gao, J. Yu, L. Lu, W.A. Rogers, Coupling particle scale model and SuperDEM-CFD for multiscale simulation of biomass pyrolysis in a packed bed pyrolyzer, *AICHE J.* 67 (2021), e17139.
- [282] M. Mohseni, B. Peters, M. Baniasadi, Conversion analysis of a cylindrical biomass particle with a DEM-CFD coupling approach, *Case Stud. Therm. Eng.* 10 (2017) 343–356.
- [283] F. Buss, S. Wirtz, V. Scherer, Simulation of a reacting agitated bed of straw pellets by a resolved coupled DEM/CFD method using a blocked-off approach, *Int. J. Therm. Sci.* 152 (2020), 106332.
- [284] P. Ostermeier, F. Fischer, S. Fendt, S. Deyoung, H. Spliethoff, Coarse-grained CFD-DEM simulation of biomass gasification in a fluidized bed reactor, *Fuel* 255 (2019), 115790.
- [285] P. Ostermeier, S. Deyoung, A. Vandersickel, S. Gleis, H. Spliethoff, Comprehensive investigation and comparison of TFM, DenseDEM and CFD-DEM for dense fluidized beds, *Chem. Eng. Sci.* 196 (2019) 291–309.
- [286] X. Xu, C. Li, X. Gao, Coarse-grained DEM-CFD simulation of fluidization behavior of irregular shape sand particles, *Ind. Eng. Chem. Res.* 61 (2022) 9099–9109.
- [287] F. Marchelli, D. Bove, C. Moliner, B. Bosio, E. Arato, Discrete element method for the prediction of the onset velocity in a spouted bed, *Powder Technol.* 321 (2017) 119–131.
- [288] G.A. Olatunde, O.O. Fasina, Influence of drag equations on computational fluid dynamic modeling of fluidization behavior of loblolly pine wood grinds, *Renew. Energy* 139 (2019) 651–660.
- [289] A. Atxutegi, P. Kieckhefen, S. Pietsch, R. Aguado, M. Olazar, S. Heinrich, Unresolved CFD-DEM simulation of spherical and ellipsoidal particles in conical and prismatic spouted beds, *Powder Technol.* 389 (2021) 493–506.
- [290] B. Kravets, D. Schulz, R. Jasevičius, S.R. Reinecke, T. Rosemann, H. Kruggel-Emden, Comparison of particle-resolved DNS (PR-DNS) and non-resolved DEM/CFD simulations of flow through homogenous ensembles of fixed spherical and non-spherical particles, *Adv. Powder Technol.* 32 (2021) 1170–1195.
- [291] P. Prakotnak, S. Wangchai, CFD-DEM simulation of fluidization of multi sphere-modeled corn particles, *Part. Sci. Technol.* 1–10 (2021).
- [292] J. Hosta, M. Čermák, J. Rozbroj, D. Žurovec, CFD-DEM numerical model of laboratory scale fluidized bed coffee roaster, *AIP Conf. Proc.* 2116 (2019), 320004.
- [293] K. Vollmari, H. Kruggel-Emden, Numerical and experimental analysis of particle residence times in a continuously operated dual-chamber fluidized bed, *Powder Technol.* 338 (2018) 625–637.
- [294] K. Vollmari, T. Oschmann, H. Kruggel-Emden, Mixing quality in mono-and bidisperse systems under the influence of particle shape: a numerical and experimental study, *Powder Technol.* 308 (2017) 101–113.
- [295] D. Han, D. Zhang, H. Jing, L. Yang, T. Cui, Y. Ding, Z. Wang, Y. Wang, T. Zhang, DEM-CFD coupling simulation and optimization of an inside-filling air-blowing maize precision seed-metering device, *Comput. Electron. Agric.* 150 (2018) 426–438.
- [296] X. Lei, Y. Liao, Q. Zhang, L. Wang, Q. Liao, Numerical simulation of seed motion characteristics of distribution head for rapeseed and wheat, *Comput. Electron. Agric.* 150 (2018) 98–109.
- [297] Y. Wang, H. Li, H. Hu, J. He, Q. Wang, C. Lu, P. Liu, D. He, X. Lin, DEM - CFD coupling simulation and optimization of a self-suction wheat shooting device, *Powder Technol.* 393 (2021) 494–509.
- [298] X. Gao, Z. Zhou, Y. Xu, Y. Yu, Y. Su, T. Cui, Numerical simulation of particle motion characteristics in quantitative seed feeding system, *Powder Technol.* 367 (2020) 643–658.
- [299] Z. Li, P. Zhang, Y. Sun, C. Zheng, L. Xu, D. E., Discrete particle simulation of gas-solid flow in air-blowing seed metering device, *Comput. Model. Eng. Sci.* 127 (2021) 1119–1132.
- [300] J. Du, Y. Heng, J. Xia, M. Hu, G. Zou, Simulation of non-spherical rice seed motion in pneumatic conveying with bend by CFD-DEM, *Int. J. Fluid Machin. Syst.* 14 (2021) 300–308.
- [301] H. Yang, F. Liu, J. Li, D. Mo, Simulation analysis of working parameters of Panax notoginseng seeder based on CFD-DEM coupling, *J. Chin. Agric. Mech.* 40 (2019) 22–25.
- [302] S. Shi, H. Liu, G. Wei, J. Zhou, S. Jian, R. Zhang, Optimization and experiment of pneumatic seed metering device with guided assistant filling based on EDEM-CFD, *Trans. Chin. Soc. Agric. Mach.* 51 (2020) 54–66.
- [303] L. Ding, L. Yang, D. Wu, Simulation and experiment of corn air suction seed metering device based on DEM-CFD coupling method, *Trans. Chin. Soc. Agric. Mach.* 49 (2018) 48–57.
- [304] Q. Lai, X. Gao, Z. Zhang, Simulation and experiment of seed-filling performance of pneumatic cylinder seed-metering device for Panax notoginseng, *Trans. Chin. Soc. Agric. Mach.* 47 (2016) 27–37.
- [305] Q. Lai, J. Zhao, W. Su, G. Jia, J. Li, Q. Lv, Design and test of air suction directional transplanting device for Panax notoginseng seedlings based on DEM-CFD coupling, *Trans. Chin. Soc. Agric. Mach.* 52 (2021) 60–70.
- [306] X. Gao, Y. Xu, L. Yang, D. Zhang, Y. Li, T. Cui, Simulation and experiment of uniformity of Venturi feeding tube based on DEM-CFD coupling, *Trans. Chin. Soc. Agric. Mach.* 49 (2018) 92–100.
- [307] L. Ding, L. Yang, D. Zhang, T. Cui, X. Gao, Design and experiment of seed plate of corn air suction seed metering device based on DEM-CFD, *Trans. Chin. Soc. Agric. Mach.* 50 (2019) 50–60.
- [308] D. Han, D. Zhang, L. Yang, K. Li, T. Zhang, Y. Wang, T. Cui, EDEM-CFD simulation and experiment of working performance of inside-filling air-blowing seed metering device in maize, *Trans. CSAE.* 33 (2017) 23–31.
- [309] D. Han, D. Zhang, L. Yang, T. Cui, Y. Ding, X. Bian, Optimization and experiment of inside-filling air-blowing seed metering device based on EDEM-CFD, *Trans. Chin. Soc. Agric. Mach.* 48 (2017) 43–51.
- [310] X. Lei, Y. Liao, W. Zhang, S. Li, D. Wang, Q. Liao, Simulation and experiment of gas-solid flow in seed conveying tube for rapeseed and wheat, *Trans. Chin. Soc. Agric. Mach.* 48 (2017) 57–68.
- [311] X. Lei, Y. Liao, L. Wang, D. Wang, L. Yao, Q. Liao, Simulation of gas-solid two-phase flow and parameter optimization of pressurized tube of air-assisted centralized metering device for rapeseed and wheat, *Trans. CSAE.* 33 (2017) 67–75.
- [312] X. Lei, Y. Liao, Q. Liao, Simulation of seed motion in seed feeding device with DEM-CFD coupling approach for rapeseed and wheat, *Comput. Electron. Agric.* 131 (2016) 29–39.

- [313] B. Liu, L. Li, R. Zhang, Study on working efficiency of pneumatic of road sweeper, *Mech. Eng.* 44 (2022) 45–50.
- [314] M. Ebrahimi, M. Crapper, J.Y. Ooi, Numerical and experimental study of horizontal pneumatic transportation of spherical and low-aspect-ratio cylindrical particles, *Powder Technol.* 293 (2016) 48–59.
- [315] W. Liu, J. Xu, X. Liu, Numerical study on collision characteristics for non-spherical particles in venturi powder ejector, *Vacuum*. 131 (2016) 285–292.
- [316] A.E. Kabeel, M. Elkelawy, H.A.-E. Mohamad, A.M. Elbanna, H. Panchal, M. Suresh, M. Israr, The influences of loading ratios and conveying velocity on gas-solid two phase flow characteristics: a comprehensive experimental CFD-DEM study, *Int. J. Ambient Energy.* 43 (2020) 2714–2726.
- [317] A.K. Olaleye, O. Shardt, G.M. Walker, H.E.A. Van Den Akker, Pneumatic conveying of cohesive dairy powder: experiments and CFD-DEM simulations, *Powder Technol.* 357 (2019) 193–213.
- [318] D. Markauskas, S. Platzk, H. Kruggel-Emden, Comparative numerical study of pneumatic conveying of flexible elongated particles through a pipe bend by DEM-CFD, *Powder Technol.* 399 (2022), 117170.
- [319] J.-W. Zhou, Y. Liu, S.-Y. Liu, C.-L. Du, J.-P. Li, Effects of particle shape and swirling intensity on elbow erosion in dilute-phase pneumatic conveying, *Wear.* 380–381 (2017) 66–77.
- [320] J.-W. Zhou, Y. Liu, C.-L. Du, S.-Y. Liu, Effect of the particle shape and swirling intensity on the breakage of lump coal particle in pneumatic conveying, *Powder Technol.* 317 (2017) 438–448.
- [321] J. Zhou, Y. Liu, C. Du, S. Liu, J. Li, Numerical study of coarse coal particle breakage in pneumatic conveying, *Particology.* 38 (2018) 204–214.
- [322] L. Chen, Z. Sun, H. Ma, G. Pan, P. Li, K. Gao, Flow characteristics of pneumatic conveying of stiff shotcrete based on CFD-DEM method, *Powder Technol.* 397 (2022), 117109.
- [323] D. Zeng, E. Zhang, Y. Ding, Y. Yi, Q. Xian, G. Yao, H. Zhu, T. Shi, Investigation of erosion behaviors of sulfur-particle-laden gas flow in an elbow via a CFD-DEM coupling method, *Powder Technol.* 329 (2018) 115–128.
- [324] X.F. Liu, J.F. Zhou, S.Q. Gao, H.L. Zhao, Z.Y. Liao, H.Z. Jin, C. Wang, Study on the impact wear characteristics of catalyst particles at 90° elbow via CFD-DEM coupling method, *J. Appl. Fluid Mech.* 15 (2022) 221–230.
- [325] J. Zhao, A. Haghnegahdar, Y. Feng, A. Patil, N. Kulkarni, G.J.P. Singh, G. Malhotra, R. Bharadwaj, Prediction of the carrier shape effect on particle transport, interaction and deposition in two dry powder inhalers and a mouth-to-G13 human respiratory system: a CFD-DEM study, *J. Aerosol Sci.* 160 (2022), 105899.
- [326] S. Ohsaki, R. Mitani, S. Fujiwara, H. Nakamura, S. Watano, Effect of particle-wall interaction and particle shape on particle deposition behavior in human respiratory system, *Chem. Pharm. Bull.* 67 (2019) 1328–1336.
- [327] M. Dauphin, M. Trofa, P.L. Maffettone, CFD-DEM Modelling: clogging of triplet particles in a microchannel with a constriction, in: IEEE 6th International Forum on Research and Technology for Society and Industry. Naples, Italy, 2021.
- [328] F. Weigler, H. Scarf, J. Mellmann, Investigation of particle and air flows in a mixed-flow dryer, *Dry. Technol.* 30 (2012) 1730–1741.
- [329] B.K. Gandhi, S.N. Singh, V. Seshadri, Performance characteristics of centrifugal slurry pumps, *J. Fluids Eng.* 123 (2001) 271–280.
- [330] R.-J. Zhao, Y.-L. Zhao, D.-S. Zhang, Y. Li, L.-L. Geng, Numerical investigation of the characteristics of erosion in a centrifugal pump for transporting dilute particle-laden flows, *J. Mar. Sci. Eng.* 9 (2021) 961.
- [331] C. Xia, R. Zhao, W. Shi, D. Zhang, X. Gao, Numerical investigation of particle induced erosion in a mixed pump by CFD-DEM coupled method, *J. Eng. Thermophys.* 42 (2021) 357–369.
- [332] W. Shao, R. Zhao, D. Zhang, Erosion of multistage mixed flow pump based on fully coupled CFD-DEM method, *Chin. J. Hydodyn.* 35 (2020) 640–648.
- [333] C. Tang, Y.-C. Yang, P.-Z. Liu, Y.-J. Kim, Prediction of abrasive and impact wear due to multi-shaped particles in a centrifugal pump via CFD-DEM coupling method, *Energies.* 14 (2021) 2391.
- [334] Y. Guan, L. Zou, H. Zheng, Y. Bian, Z. Yu, Ore particle backflow performance in the deep-sea mining slurry pump, *J. Harbin Eng. Univ.* 42 (2021) 1557–1565.
- [335] Z. Chara, CFD-DEM simulations in water channel flow, *AIP Conf. Proc.* 2293 (2020), 030018.
- [336] S. Qu, W. Ding, L. Xue, Investigating on influence of particle shape on blockage in slurry pipeline transportation by CFD-DEM, *Chin. J. Hydodyn.* 36 (2021) 499–506.
- [337] Y. Wang, Y. Xia, X. Xiao, H. Xu, P. Chen, G. Zeng, Ballast flow characteristics of discharging pipeline in shield slurry system, *Appl. Sci.* 9 (2019) 5402.
- [338] J. Qi, J. Yin, F. Yan, P. Liu, T. Wang, C. Chen, Liquid-solid flow characteristics in vertical swirling hydraulic transportation with tangential jet inlet, *J. Mar. Sci. Eng.* 9 (2021) 1091.
- [339] M.T. Ibrahim, H. Briesen, P. Först, J. Zacharias, CFD-DEM modelling approach of particle-liquid food flows in a bent pipe, in: Proceedings of the 4th World Congress on Momentum, Heat and Mass Transfer. Rome, Italy, 2019.
- [340] R. Zhao, Y. Zhao, Q. Si, X. Gao, Effects of different characteristics of the dilute liquid-solid flow on the erosion in a 90° bend, *Powder Technol.* 398 (2022), 117043.
- [341] B. Shao, Y. Yan, X. Yan, Z. Xu, A study on non-spherical cuttings transport in CBM well drilling by coupled CFD-DEM, *Eng. Appl. Comput. Fluid Mech.* 13 (2019) 579–590.
- [342] B. Shao, Y. Yan, C. Bi, X. Yan, Primary research on movement of big-size cuttings in coal-bed methane wells by parallel computing using coupled CFD-DEM, *Sci. Tech. Engrg.* 17 (2017) 42–47.
- [343] B. Shao, Y. Yan, X. Wang, F. Liao, X. Yan, Numerical investigation of a double-circulation system for cuttings transport in CBM well drilling using a CFD-DEM coupled model, *Eng. Appl. Comput. Fluid Mech.* 14 (2020) 38–52.
- [344] B. Shao, Y. Yan, C. Bi, Migration of irregular cuttings particles in big size by CFD-DEM coupled simulation model, *Sci. Tech. Engrg.* 17 (2017) 195–200.
- [345] B. Zhu, H. Tang, X. Wang, F. Zhao, X. Yuan, Coupled CFD-DEM simulation of granular LCM bridging in a fracture, *Part. Sci. Technol.* 38 (2020) 371–380.
- [346] A.N. Balachandran Nair, S. Pirker, T. Umundun, M. Saedipour, A reduced-order model for deformable particles with application in bio-microfluidics, *Comput. Part. Mech.* 7 (2020) 593–601.
- [347] M. Alihosseini, P.U. Thamsen, Experimental and numerical investigation of sediment transport in sewers, in: ASME 2018 5th Joint US-European Fluids Engineering Division Summer Meeting, Montreal, Canada, 2018.
- [348] M. Alihosseini, P.U. Thamsen, Analysis of sediment transport in sewer pipes using a coupled CFD-DEM model and experimental work, *Urban Water J.* 16 (2019) 259–268.
- [349] J. Fu, Z. Chen, L. Han, L. Ren, Review of grain threshing theory and technology, *Int. J. Agric. Biol. Eng.* 11 (2018) 12–20.
- [350] L. Zhao, L. Chen, F. Yuan, L. Wang, Simulation study of rice cleaning based on DEM-CFD coupling method, *Processes.* 10 (2022) 281.
- [351] L. Wang, C. Zhang, Z. Ding, Structure optimization of cleaning screen for maize harvester, *Trans. Chin. Soc. Agric. Mach.* 47 (2016) 108–114.
- [352] F. Dai, W. Guo, X. Song, R. Shi, J. Qu, W. Zhao, Measurement and simulation of the suspension velocity of flax threshing material using CFD-DEM, *Int. J. Agric. Biol. Eng.* 14 (2021) 230–237.
- [353] F. Dai, X. Song, R. Shi, W. Zhao, W. Guo, Y. Zhang, Migration law of flax threshing materials in double channel air-and-screen separating cleaner, *Int. J. Agric. Biol. Eng.* 14 (2021) 92–102.
- [354] L. Xu, Y. Li, X. Choi, G. Wang, Z. Liang, Y. Li, B. Li, Numerical simulation of gas-solid two-phase flow to predict the cleaning performance of rice combine harvesters, *Biosyst. Eng.* 190 (2020) 11–24.
- [355] Y. Li, Y. Xu, T. Cui, D. Zhang, H. Fan, X. Gao, Y. Su, M. Qiao, Z. Song, Improving particle dispersion characteristics with a novel cleaning screen: parameter design and numerical simulation, *Powder Technol.* 397 (2022), 116987.
- [356] X. Feng, Z. Gong, L. Wang, Y. Yu, T. Liu, L. Song, Behavior of maize particle penetrating a sieve hole based on the particle centroid in an air-screen cleaning unit, *Powder Technol.* 385 (2021) 501–516.
- [357] H. Li, Y. Li, F. Gao, Z. Zhao, L. Xu, CFD-DEM simulation of material motion in air-and-screen cleaning device, *Comput. Electron. Agric.* 88 (2012) 111–119.
- [358] J. Yuan, C. Wu, H. Li, Y. Qi, X. Xiao, X. Shi, Movement rules and screening characteristics of rice-threshed mixture separation through a cylinder sieve, *Comput. Electron. Agric.* 154 (2018) 320–329.
- [359] J. Yuan, H. Li, X. Qi, T. Hu, M. Bai, Y. Wang, Optimization of airflow cylinder sieve for threshed rice separation using CFD-DEM, *Eng. Appl. Comput. Fluid Mech.* 14 (2020) 871–881.
- [360] M.A. El-Emam, W. Shi, L. Zhou, CFD-DEM simulation and optimization of gas-cyclone performance with realistic macroscopic particulate matter, *Adv. Powder Technol.* 30 (2019) 2686–2702.
- [361] M.A. El-Emam, L. Zhou, W. Shi, C. Han, Performance evaluation of standard cyclone separators by using CFD-DEM simulation with realistic bio-particulate matter, *Powder Technol.* 385 (2021) 357–374.
- [362] M.A. El-Emam, L. Zhou, W.D. Shi, C. Han, True shape modeling of bio-particulate matter flow in an aero-cyclone separator using CFD-DEM simulation, *Comput. Part. Mech.* 8 (2021) 955–971.
- [363] M.A. El-Emam, C. Han, S. Wei Dong, L. Zhou, ROCKY DEM-CFD simulation for Realistic Granular Flow in an Aerodynamic separating device, in: 2019 ASABE Annual International Meeting. St. Joseph, USA, 2019.
- [364] H. Dang, B. Zhao, X. Ma, R. Hao, Z. Zhao, W. Cui, Simulating research on cyclone grain cleaning device based on CFD-DEM coupling, *J. Chin. Agric. Mech.* 41 (2020) 86–91.
- [365] F. Dai, X. Song, W. Guo, W. Zhao, F. Zhang, S. Zhang, Simulation and test on separating cleaning process of flax threshing material based on gas-solid coupling theory, *Int. J. Agric. Biol. Eng.* 13 (2020) 73–81.
- [366] X. Ma, L. Zhao, B. Guo, H. Dang, Simulation and experiment of rice cleaning in air-separation device based on DEM-CFD coupling method, *Int. J. Agric. Biol. Eng.* 13 (2020) 226–233.
- [367] Z. Hu, H. Zeng, Y. Ge, W. Wang, J. Wang, Simulation and experiment of gas-solid flow in a safflower sorting device based on the CFD-DEM coupling method, *Processes.* 9 (2021) 1239.
- [368] E. Jiang, Z. Sun, Z. Pan, L. Wang, Numerical simulation based on CFD-DEM and experiment of grain moving laws in inertia separation chamber, *Trans. Chin. Soc. Agric. Mach.* 45 (2014) 117–122.
- [369] F. Dai, X. Song, W. Zhao, Z. Han, F. Zhang, S. Zhang, Motion simulation and test on threshed grains in tapered threshing and transmission device for plot wheat breeding based on CFD-DEM, *Int. J. Agric. Biol. Eng.* 12 (2019) 66–73.
- [370] E. De Almeida, N. Spogis, O.P. Taranto, M.A. Silva, Theoretical study of pneumatic separation of sugarcane bagasse particles, *Biomass Bioenergy* 127 (2019), 105256.
- [371] E. De Almeida, N. Spogis, M. Silva, Computational study of the pneumatic separation of sugarcane bagasse, in: 6th International Conference on Engineering for Waste and Biomass Valorisation. Albi, France, 2016.
- [372] C. Pieper, F. Pfaff, G. Maier, H. Kruggel-Emden, S. Wirtz, B. Noack, R. Gruna, V. Scherer, U.D. Hanebeck, T. Längle, J. Beyerer, Numerical modelling of an optical belt sorter using a DEM-CFD approach coupled with particle tracking and comparison with experiments, *Powder Technol.* 340 (2018) 181–193.

- [373] J. Qiao, P. Wen, C. Duan, W. Wang, Particle behavior and parameter optimization in treatment of waste petroleum reforming catalysts based on a compound dry separator, *Adv. Powder Technol.* 31 (2020) 1181–1195.
- [374] J. Qiao, L. Huang, C. Duan, H. Jiang, Y. Zhao, H. Shao, M. Pan, Research on separation mechanism of waste palladium catalyst in a structure-optimized compound dry separator based on DEM-CFD, *Part. Sci. Technol.* 38 (2020) 131–143.
- [375] H.A. Petit, E.F. Irassar, M.R. Barbosa, Evaluation of the performance of the cross-flow air classifier in manufactured sand processing via CFD-DEM simulations, *Comput. Part. Mech.* 5 (2018) 87–102.
- [376] D. Hund, S. Antonyuk, S. Ripperger, Simulation of bridging at the static surface filtration by CFD-DEM coupling, *EPJ Web Confer.* 140 (2017) 09033.
- [377] R. Deshpande, S. Antonyuk, O. Iliev, DEM-CFD study of the filter cake formation process due to non-spherical particles, *Particuology* 53 (2020) 48–57.
- [378] Y. Zhu, D. Hu, C. Li, C. Zhuang, G. Yang, CFD-DEM simulation of the hydrodynamic filtration performance in balaenid whale filter feeding, *Sci. Total Environ.* 787 (2021), 147696.
- [379] K. Lv, F. Min, J. Zhu, B. Ren, X. Bai, C. Wang, Experiments and CFD-DEM simulations of fine kaolinite particle sedimentation dynamic characteristics in a water environment, *Powder Technol.* 382 (2021) 60–69.
- [380] V.V. Mahajan, J. Mehmood, Y.M.F. El Hasadi, J.T. Padding, Fluid medium effect on stresses in suspensions of high-inertia rod-like particles, *Chem. Eng. Sci. X* 3 (2019), 100030.
- [381] J.D. Redlinger-Pohn, L.M. König, C. Kloss, C. Goniva, S. Radl, Modeling of non-spherical, elongated particles for industrial suspension flow simulation, in: *ECCOMAS Congress 2016 - VII European Congress on Computational Methods in Applied Sciences and Engineering*, Crete Island, Greece, 2016.
- [382] J.D. Redlinger-Pohn, L.A. Jagiello, W. Bauer, S. Radl, Mechanistic understanding of size-based fiber separation in coiled tubes, *Int. J. Multiphase Flow* 83 (2016) 239–253.
- [383] M. Isoz, M.K. Sourek, O. Studenfik, P. Kočí, Hybrid fictitious domain-immersed boundary solver coupled with discrete element method for simulations of flows laden with arbitrarily-shaped particles, *Comput. Fluids* 244 (2022), 105538.
- [384] H. Xiong, H. Wu, X. Bao, J. Fei, Investigating effect of particle shape on suffusion by CFD-DEM modeling, *Constr. Build. Mater.* 289 (2021), 123043.
- [385] J.-G. Qian, C. Zhou, Z.-Y. Yin, W.-Y. Li, Investigating the effect of particle angularity on suffusion of gap-graded soil using coupled CFD-DEM, *Comput. Geotech.* 139 (2021), 104383.
- [386] D.C. Seo, J. Wang, Numerical simulation of model test in pre-sawn ice by CFD-DEM coupled method, in: *ASME 2021 40th International Conference on Ocean, Offshore and Arctic Engineering*, Virtual, Online, 2021.
- [387] L. Huang, J. Tuhkuri, B. Igrec, M. Li, D. Stagonas, A. Toffoli, P. Cardiff, G. Thomas, Ship resistance when operating in floating ice floes: a combined CFD&DEM approach, *Mar. Struct.* 74 (2020), 102817.
- [388] L. Huang, Z. Li, C. Ryan, J.W. Ringsberg, B. Pena, M. Li, L. Ding, G. Thomas, Ship resistance when operating in floating ice floes: derivation, validation, and application of an empirical equation, *Mar. Struct.* 79 (2021), 103057.
- [389] W. Guo, Q.-S. Zhao, Y.-K. Tian, W.-C. Zhang, The research on floe ice force acting on the “Xue Long” icebreaker based on synthetic ice test and virtual mass numerical method, *J. Hydronav.* 33 (2021) 271–281.
- [390] W. Guo, Q.-S. Zhao, Y.-K. Tian, W.-C. Zhang, Research on total resistance of ice-going ship for different floe ice distributions based on virtual mass method, *Int. J. Nav. Archit. Ocean Eng.* 12 (2020) 957–966.
- [391] W. Luo, D. Jiang, T. Wu, C. Guo, C. Wang, R. Deng, S. Dai, Numerical simulation of an ice-strengthened bulk carrier in brash ice channel, *Ocean Eng.* 196 (2020), 106830.
- [392] X. Nan, J. Hou, Z. Shen, Y. Tong, G. Li, X. Wang, Y. Kang, CFD-DEM coupling with multi-sphere particles and application in predicting dynamic behaviors of drifting boats, *Ocean Eng.* 247 (2022), 110368.
- [393] X. Hou, T. Ding, Z. Deng, Z. Yu, P. Xue, P. Cao, T. Tang, Study of the creeping of irregularly shaped Martian dust particles based on DEM-CFD, *Powder Technol.* 328 (2018) 184–198.
- [394] J. Hu, G. Xu, Y. Shi, L. Wu, Formation mechanism of brownout in full-scale helicopter based on CFD-DEM couplings numerical simulation, *Acta Astronaut.* 41 (2020), 123363.
- [395] D. Gou, X. An, B. Zhao, R. Yang, CFD-DEM simulations of densification of tetrahedron particles under air impact, *Powder Technol.* 361 (2020) 220–225.
- [396] H. Baghban, A. Arulrajah, G.A. Narsilio, S. Horpibulsuk, Evaluating the effective thermal conductivity of geothermal pavements constructed using demolition wastes by DEM and 3D printing techniques, *Acta Geotech.* 17 (2022) 1681–1697.
- [397] Y. Guo, X. Yu, Study of the particle shape influence on soil erodibility using coupled CFD-DEM modeling, in: *Proceedings of Geotechnical Frontiers 2017*, 2017, Orlando, USA.
- [398] Y. Guo, Y. Yang, X. Yu, Influence of particle shape on the erodibility of non-cohesive soil: insights from coupled CFD-DEM simulations, *Particuology* 39 (2018) 12–24.
- [399] S. Zhou, J. Li, H. Yang, C. Qiao, C. Lu, J. Zhang, CFD-DEM simulation of key unit in graphene production process, *Chin. Powder Sci. Tech.* 28 (2022) 87–98.
- [400] P.G. Jayathilake, B. Li, P. Zuliani, T. Curtis, J. Chen, Modelling bacterial twitching in fluid flows: a CFD-DEM approach, *Sci. Rep.* 9 (2019) 14540.
- [401] Y. Song, P.G. Ranjith, B. Wu, A study of ellipsoidal and spherical particle flow, clogging and unclogging dynamics, *Powder Technol.* 392 (2021) 424–437.
- [402] P.W. Cleary, J.E. Hilton, M.D. Sinnott, Modelling of industrial particle and multiphase flows, *Powder Technol.* 314 (2017) 232–252.
- [403] M.D. Sinnott, S.M. Harrison, P.W. Cleary, A particle-based modelling approach to food processing operations, *Food Bioprod. Process.* 127 (2021) 14–57.
- [404] M.D. Sinnott, P.W. Cleary, Particulate and water mixing in the feed box for a screen, *Miner. Eng.* 109 (2017) 109–125.
- [405] P.W. Cleary, R.D. Morrison, M.D. Sinnott, Prediction of slurry grinding due to media and coarse rock interactions in a 3D pilot SAG mill using a coupled DEM + SPH model, *Miner. Eng.* 159 (2020), 106614.
- [406] S. Cummins, P.W. Cleary, G. Delaney, A. Phua, M. Sinnott, D. Gunasegaran, C. Davies, A coupled DEM/SPH computational model to simulate microstructure evolution in Ti-6Al-4V laser powder bed fusion processes, *Metals* 11 (2021) 858.
- [407] L. Liu, J. Wu, S. Ji, DEM-SPH coupling method for the interaction between irregularly shaped granular materials and fluids, *Powder Technol.* 400 (2022), 117249.
- [408] S. Ji, X. Chen, L. Liu, Coupled DEM-SPH method for interaction between dilated polyhedral particles and fluid, *Math. Probl. Eng.* 2019 (2019) 4987801.
- [409] L. Liu, P. Zhang, P. Xie, S. Ji, Coupling of dilated polyhedral DEM and SPH for the simulation of rock dumping process in waters, *Powder Technol.* 374 (2020) 139–151.
- [410] T. Qiao, L. Liu, S. Ji, Superquadric DEM-SPH coupling method for interaction between non-spherical granular materials and fluids, *Particuology* 71 (2022) 20–33.
- [411] S.F. Sizkow, U. El Shamy, SPH-DEM simulations of saturated granular soils liquefaction incorporating particles of irregular shape, *Comput. Geotech.* 134 (2021), 104060.
- [412] B. Nassauer, T. Liedke, M. Kuna, Development of a coupled discrete element (DEM)-smoothed particle hydrodynamics (SPH) simulation method for polyhedral particles, *Comput. Part. Mech.* 3 (2016) 95–106.
- [413] S. Natsui, A. Sawada, K. Terui, Y. Kashihara, T. Kikuchi, R.O. Suzuki, DEM-SPH study of molten slag trickle flow in coke bed, *Chem. Eng. Sci.* 175 (2018) 25–39.
- [414] C. Peng, L. Zhan, W. Wu, B. Zhang, A fully resolved SPH-DEM method for heterogeneous suspensions with arbitrary particle shape, *Powder Technol.* 387 (2021) 509–526.
- [415] B.V. Derjaguin, V.M. Muller, Y.P. Toporov, Effect of contact deformations on the adhesion of particles, *J. Colloid Interface Sci.* 53 (1975) 314–326.
- [416] K.L. Johnson, K. Kendall, A.D. Roberts, D. Tabor, Surface energy and the contact of elastic solids, *Proc. Roy. Soc. London. A. Math. Phys. Sci.* 324 (1971) 301–313.
- [417] W. Nan, Y. Wang, Y. Liu, H. Tang, DEM simulation of the packing of rodlike particles, *Adv. Powder Technol.* 26 (2015) 527–536.
- [418] N. Govender, P.W. Cleary, M. Kiani-Oshtorjani, D.N. Wilke, C.-Y. Wu, H. Kureck, The effect of particle shape on the packed bed effective thermal conductivity based on DEM with polyhedral particles on the GPU, *Chem. Eng. Sci.* 219 (2020), 115584.
- [419] C.A. Radeke, B.J. Glasser, J.G. Khinast, Large-scale powder mixer simulations using massively parallel GPU architectures, *Chem. Eng. Sci.* 65 (2010) 6435–6442.